Multichannel Staggered SAR for High-Resolution Wide-Swath Imaging

Zur Erlangung des akademischen Grades eines

DOKTOR-INGENIEURS

von der Fakultät für
Elektrotechnik und Informationstechnik
des Karlsruher Instituts für Technologie (KIT)

genehmigte

DISSERTATION

von

M.Sc. Felipe Queiroz de Almeida
geb. in Goiânia, Goiás, Brasilien

Tag der mündlichen Prüfung:	18.12.2017
Referent:	Prof. Dr.-Ing. habil. Alberto Moreira
Korreferent:	Prof. Dr.-Ing. Lorenz-Peter Schmidt

Contents

Zusammenfassung

Im Kontext aktueller und zukünftiger raumgestützter Radarsysteme mit synthetischer Apertur (engl.: SAR – *Synthetic Aperture Radar*), wie z.B. dem deutschen Missionsvorschlag Tandem-L, werden kurze Aufnahmezyklen bei gleichzeitig hoher Auflösung benötigt, um dynamische Prozesse auf der Erde beobachten und zahlreiche wissenschaftliche und umweltpolitische Anwendungen bedienen zu können. Da konventionelle SAR-Systeme diese anspruchsvollen Anforderungen nicht erfüllen, sind neue Aufnahmemodi und -techniken wie die digitale Strahlformung erforderlich, um die Abbildungsleistung zukünftiger SAR-Systeme signifikant zu verbessern und den immer weiter steigenden Missionsanforderungen gerecht zu werden.

Mehrkanal-SAR-Systeme mit digitaler Strahlformung in Azimut sind eine Option, den neuen Anforderungen gerecht zu werden und eine hochaufgelöste Erdbeobachtung über breite Streifen (High-Resolution Wide-Swath – HRWS) zu ermöglichen. Allerdings benötigen diese Systeme eine sehr lange Antenne, um einen breiten Streifen abzubilden. Alternativ wurde daher die Nutzung digitaler Strahlformungstechniken in Elevation in Kombination mit einer zyklisch variierenden Pulswiederholzeit (Staggered SAR) vorgeschlagen. Hierbei ist allerdings die erzielbare Azimutauflösung durch die Antennenlänge beschränkt. Der Fokus dieser Dissertation liegt auf der Entwicklung neuer SAR-Techniken und der zugehörigen Signalverarbeitungsverfahren, die die Vorteile der digitalen Strahlformung in Azimut mit den Vorteilen des Staggered SAR kombinieren. Hierdurch ergeben sich äußerst leistungsfähige SAR-Modi, mit denen erstmals sehr breite Streifen mit sehr hoher Azimutauflösung unter Nutzung kompakter Antennen abgebildet werden können.

Die Dissertation beinhaltet sowohl neuartige Algorithmen für die Rekonstruktion von Mehrkanal-Staggered-SAR-Daten als auch Design-Beispiele für leistungsstarke HRWS-Satelliten-SAR-Systeme, die diese neue Technik nutzen. Zusätzlich werden die neuen Techniken anhand von experimentellen Daten eines bodengestützten Radars demonstriert und mögliche Fehlereinflüsse bei der Implementierung dieser neuen Klasse von raumgestützten Abbildungssystemen analysiert und diskutiert.

Abstract

In the context of state-of-the-art and next-generation spaceborne Synthetic Aperture Radar (SAR) imaging systems, such as the German *Tandem-L* mission proposal, a short revisit time coupled with high resolution presents itself as a requirement for the observation of numerous Earth dynamic processes in various scientific and environmental applications. This poses contradicting and demanding requirements on system design for whose realization digital beamforming techniques play a crucial role, in order to enable next-generation systems to significantly outperform current state-of-the-art systems and fulfil the increasingly stringent needs of applications.

Multichannel SAR systems with digital beamforming in azimuth have been proposed as an option for coping with these challenging requirements in order to achieve high-resolution wide-swath (HRWS) imaging capabilities. These systems tend however to require a very long antenna to image wide swaths. As an alternative, the use of digital beamforming in elevation, in conjunction with a varying pulse repetition interval (PRI) for the SAR system radar pulses (*Staggered* SAR), has been proposed. The best azimuth resolution in this case is nevertheless limited by the antenna dimensions. The thesis focuses on the development of new SAR techniques and corresponding processing methodologies which allow the combination of the advantages of the multichannel system architectures in azimuth with those of *staggered SAR.* This introduces new and potentially highly flexible modes of operation, enabling HRWS imaging with a compact antenna and contributing to the new developments in the field of digital beamforming techniques.

The thesis includes the proposal of novel algorithms for the resampling of multichannel staggered SAR data and examples of high-performance HRWS systems designed to make use of the technique. In addition, a proof-of-concept with experimental data from a ground-based radar system and a discussion of the possible effects of errors for the implementation of this new class of spaceborne imaging systems are presented.

Acronyms and Symbols

List of Constants

c	Speed of light in vacuum	$2.99792458 \cdot 10^{8}$ [m · s^{-1}]
g	Acceleration due to Earth's gravity	9.8 [m · s^{-1}]
k_B	Boltzmann constant	$1.3806485279 \cdot 10^{-23}$ [J · K^{-1}]
G	Universal gravitational constant	$6.67384 \cdot 10^{-11}$ [m^3 · kg^{-1} · s^{-2}]
M_E	Earth's mass	$5.9726 \cdot 10^{24}$ [kg]
R_E	Mean Earth radius	6371 [km]
π	Pi	3.14159265359

Mathematical Notations, Symbols and Functions

In this work no distinction in notation is made between real and complex quantities.

%	Integer division operator
$(.)^*$	Complex conjugate
$\arcsin(\theta)$	Inverse sine function
argmin(.)	Argument of the minimum of a function (in optimization context)
$\cos(\theta)$	Cosine function
$\sin(\theta)$	Sine function
$e^{j\cdot\theta}, \exp(j \cdot \theta)$	Complex exponential
$\mathbb{C}$	Set of complex numbers
$\mathbb{N}$	Set of natural numbers
$\mathrm{rect}\left(\frac{t-t_0}{T}\right)$	Rectangle function of duration T symmetrical around t_0
$\mathrm{sinc}(x) = \frac{\sin(x)}{x}$	Sinus Cardinalis (sinc) function
$\mathbb{Z}$	Set of integer numbers
$E[.]$	Expectation operator
$Re\{.\}, \ Im\{.\}$	Real and imaginary part of complex quantity
j	Imaginary unit
mod	Modulo (remainder of integer division) operator
$\delta[n]$	Discrete Dirac delta

Acronyms

AASR	Azimuth Ambiguity to Signal Ratio
ASI	Agenzia Spaziale Italiana (Italian Space Agency)
ATC	Air Traffic Control
BAQ	Block-Adaptive Quantization
DBF	Digital BeamForming
DLR	Deutches Zentrum für Luft und Raumfahrt (German Aerospace Center)
ESA	European Space Agency
FFT	Fast Fourier Transform
FIR	Finite Impulse Response
GCA	Ground Controlled Approach
HRWS	High Resolution Wide Swath
IR	Impulse Response

ISLR	Integrated Sidelobe (to mainlobe) Ratio
JAXA	Japan Aerospace eXploitation Agency
LCMV	Linear Constraint Minimum Variance (beamformer)
LS	Least Squares
MCRA	Multichannel Reconstruction Algorithm
MIMO	Multiple Input Multiple Output
MMSE	Minimum Mean Squared Error (multichannel reconstruction method)
MSANR	Maximum Signal to Ambiguity and Noise Ratio (multichannel reconstruction method)
MSE	Mean Squared Error
MVDR	Minimum Variance Distortionless (beamformer)
NESZ	Noise Equivalent Sigma Zero
NSOAS	National Satellite Ocean Application Service (China)
PALSAR	Phased Array based L-band Synthetic Aperture Radar
PEL	Pulse Extension Loss
PRF	Pulse Repetition Frequency
PRI	Pulse Repetition Interval
PSD	Power Spectral Density
RADAR	Radio Detection and Ranging
RASR	Range Ambiguity to Signal Ratio
RCMC	Range Cell Migration Correction
RCS	Radar Cross Section
RF	Radiofrequency
Rx	Reception
SANR	Signal to Ambiguity and Noise Ratio
SAR	Synthetic Aperture Radar
SIMO	Single Input Multiple Output
SLAR	Side Looking Airborne Radar
SNR	Signal-to-Noise Ratio
STAP	Space-Time Adaptive Processing
TOPS	Terrain Observation by Progressive Scans
TR-module	Transmit-Receive Module
Tx	Transmission
VBS	Virtual Beam Synthesis

Lower Case Letters

$\underline{\boldsymbol{c}}$	Linear constraint imposed at the same N specific angles (as many as array elements) for LCMV beamforming
d	Inter-element spacing of antenna array (generic dimension)
d_{OFF}	Feed offset in elevation, for reflector antenna
d_{az}	Spacing in azimuth for antenna array
d_{el}/d_{az}	Channel spacing in elevation/azimuth
$d_{i,k}$	Delay of order k starting from pulse index i, for a staggered PRI sequence
$d_{i,k}^1;\ d_{i,k}^2$	Delays $d_{i,k}$, highlighting the validity of the formulas in regions 1 or 2 of the index range
$d_{max}(k)$	Maximum delay (over all pulse indices i) for an order k
$d_{min}(k)$	Minimum delay (over all pulse indices i) for an order k
$\mathrm{d}A, \mathrm{d}\phi, \mathrm{d}R$	Infinitesimal area, azimuth angle, range elements
f_0	Center frequency
f_{IF}	Intermediate center frequency
f_D	Doppler frequency
f_{fund}	Fundamental frequency of simple pendulum

f_s	ADC sampling rate (real data)
$f_{sp}(\theta)$	Spatial frequency, in the context of array pattern analysis
$f_{s_{az}}$	Azimuth sampling rate. This corresponds to the PRF for unfiltered data but may be reduced if suitable processing is applied
g_0	Ground range of corner reflector
$g(t)$	Generic WSS signal
h_{el}	Antenna height above ground
h_{orbit}	Orbit height of satellite
i_{break}	Index that separates the two regions in the expression of delay $d_{i,k}$
$i_{valid}(k)$	Index of available (non-blocked) pulses for a given output grid sample k
k_c	Critical delay order used in the derivation of the single pulse gap criterion
k_c^{INT}	Discretization of $\tilde{k}_c$
k_{min}, k_{max}	Minimum and maximum orders of delay relevant for a given swath
$\tilde{k}_c$	Critical delay order as a real number, an intermediate step in the design equations
k_{FM}	Linear frequency modulation rate of chirp waveform
k_{win}	Proportionally constant between inverse of bandwidth and temporal resolution of impulse response, a property of the spectral weighting
l_{az}	Antenna aperture length in azimuth
l_{el}	Antenna aperture length in elevation
n_{MSE}, n_{SNR}	Normalization factors for MSE and SNR used in the joint MSE-SNR optimization criterion
$\underline{\boldsymbol{n}}(f_{\mathrm{D}})$	N_{ch} element column vector describing the noise over the channels
p_{G}	Goal pattern power
$p_c^{\mathrm{Tx}}, p_c^{\mathrm{Rx}}, p_c$	Phase Center position in Tx, Rx and two-way, respectively
p_n	Noise Power
p_s	Signal Power
$\underline{\boldsymbol{p}}_m^{SANR}(f_{\mathrm{D}})$	Optimal weights minimizing the SANR for the m^{th} sub-band
r_0	Slant range of corner reflector
r_{ADC}	ADC resolution
s_0	Signal magnitude in pattern uncertainty model
$s_{Rw}(\underline{\boldsymbol{w}})$	Squared norm of the weight vector $\underline{\boldsymbol{w}}$,weighted by $\underline{\boldsymbol{R}}_{\boldsymbol{v}}$
$s_{out}[k]$	Output sample of index k
$s_w(\underline{\boldsymbol{w}})$	Squared norm of the weight vector $\underline{\boldsymbol{w}}$
$\boldsymbol{s_{in}}$	Complex vector with N_{win} input samples
$\boldsymbol{s_{in}}$	Vector with N_{win} input samples
$s_{chirp}(t)$	Chirp waveform in time domain
$S_{chirp}(f)$	Spectrum of the chirp waveform
t_0, t_1	Instants defining the blockage by the Tx pulse
t_{TX}, t_{RX}	Instants of transmission and reception of signal (radar pulse)
$t_{out}[k]$	Sampling instants of the regular output grid
$t_{rx}[i]$	Sampling instants of the input grid, which depend on sequence parameters and the local range
$u_{in}(t)$	Input signal of TR-module
$u_{out}(t)$	Output signal of TR-module
v_{ground}	Beam velocity on ground
v_{plat}	Platform velocity in the azimuth (flight) direction
v_{plat}	Platform speed (e.g. orbital velocity in the case of satellites)
w_{TRM}	Complex coefficient to be applied by TR-module
w_n	n^{th} element of weight vector

$\underline{\boldsymbol{w}}_{error}$	Weight vector with phase and amplitude errors induced by the TR-module biases
$w(x)$	Theoretical continuous weight distribution over uniform array
$\boldsymbol{w}[k]$	DBF weight (column) vector for output index k
$w_{sig}(\theta)$	Signal power scaling due to azimuth compression, as a function of the look angle θ
$w_{amb}(\theta_{i,k})$	Range ambiguous signal power scaling due to azimuth compression, as a function of the look angle $\theta_{i,k}$ of the k^{th} order range ambiguity for the i^{th} pulse of the staggered PRI sequence
w_{noise}	Noise power scaling due to azimuth compression (assumes white noise with flat spectrum)
x_0	Corresponding spatial shift of the regular output time channel
x_{PH}	Desired phase center position
x_{tgt}	Target position in along-track

Capital Letters

A_{ant}	Antenna aperture area
A_{RX}	Aperture area of the Rx antenna
$A_k(f_{\mathrm{D}})$	Antenna pattern contribution to k^{th} channel's transfer function
$\underline{\boldsymbol{A}}$	Array matrix with manifold information at N specific angles (as many as array elements) for LCMV beamforming
$\boldsymbol{A}^H$	Hermitian (transpose conjugate) of complex matrix $\boldsymbol{A}$
$AF(\theta)$	Array factor resulting from uniform array excitation
A_{ill}	Illuminated area on ground
$B(f_{sp})$	Modulation of the phase-center induced phase ramp, in the context of array pattern analysis
Bw_{az}	Signal Doppler bandwidth, defined by the geometry and the antenna pattern beamwidth
Bw_{chirp}	Pulse (chirp) bandwidth
Bw_{proc}	Processed Doppler bandwidth
Bw_n	System noise bandwidth
$C(\theta,\phi)$	Two-way normalized antenna pattern
$C_{RX}(\theta,\phi)$	Normalized Rx antenna pattern ($\lvert C_{RX}(\theta,\phi)\rvert \leq 1$)
$C_{TX}(\theta,\phi)$	Normalized Tx antenna pattern ($\lvert C_{TX}(\theta,\phi)\rvert \leq 1$)
D	Diameter of reflector antenna
D_{maj}	Elliptical reflector major axis
D_{min}	Elliptical reflector minor axis
EWL	Echo window length
F	Focal length of reflector antenna
G_1, G_2, G_3, G_4	Indices of the pulses which represent the edges of the two possible gaps for a given range
$G_{DBF}(f_{\mathrm{D}})$	Achieved pattern after (generic) DBF
$G_{GOAL}(f_{\mathrm{D}})$	Goal pattern for LS pattern synthesis
$G_{actual}(f_{\mathrm{D}})$	Actual antenna patterns, disturbed by noise/uncertainty in pattern uncertainty model
$G_{com}(f_{\mathrm{D}})$	Common pattern used as design goal for the VBS methods
$G_{com}^{i}(f_{\mathrm{D}})$	Common pattern at a given iteration i, for the iterative LS pattern synthesis procedure
$\hat{G}_{com}(f_{\mathrm{D}})$	Achieved average common pattern of the output grid
$G_i(f_{\mathrm{D}})$	Pattern corresponding to element i (entry i of array manifold vector $\underline{\boldsymbol{v}}(f_{\mathrm{D}})$)
$G_{nom}(f_{\mathrm{D}})$	Nominal (error-free) antenna patterns in pattern uncertainty model

$G_{sub-set}(f_{\mathrm{D}})$	Pattern obtained from the sum of a sub-set of the array elements, a meaningful choice for the common pattern in case of planar arrays
$G_{sum}(f_{\mathrm{D}})$	Pattern obtained from the sum of all elements, a meaningful choice for the common pattern in case of reflector arrays
$\hat{G}_{GOAL}(\theta)$	Achieved pattern approximation after LS-DBF
G_{RX}	Gain of the Rx antenna
G_{TX}	Gain of the Tx antenna
$H_{az}(f_{\mathrm{D}})$	Focusing (matched) filter over azimuth
$H_k(f_{\mathrm{D}})$	Transfer function of multichannel system's k^{th} receiver in Doppler domain
$\boldsymbol{H}(f_{\mathrm{D}})$	N_{ch} x N_s system matrix describing channel transfer function over intervals I_m
I_m	Frequency interval defining m^{th}sub-band of signal with bandwidth PRF
$\boldsymbol{I}_N$	N x N identity matrix
$ISLR_{alias-free}$	ISLR of alias-free reference impulse response
$ISLR_{data}$	ISLR of resampled data
L	Length of planar array
L_1, L_2	Length in pulses of each of the possible gaps
L_f	Feed system losses
L_Ω	Feed (reflector) or antenna system (planar array) losses
L_p	Length of simple pendulum
(L_{el}, L_{az})	Feed dimensions (elevation, azimuth) of reflector antenna
$\tilde{L}_1, \tilde{L}_2$	Length in pulses of each of the possible gaps, considered as a real number for analysis purposes
MEM_{coef}	Total on board memory required to store the coefficients for resampling, considering the polarization and range variation
$\overline{MSE}_i$	Average over output samples of the achieved MSE with the given method, at iteration i
N	Number of elements of an antenna array (generic dimension)
$N_{active_{elev}}$	Number of active elements for elevation beamforming
$N_{\text{additions, Re}}$	Number of real additions
N_{ambs}	Total number of ambiguities used for RASR estimation
N_{beams}	Number of simultaneous elevation beams
N_{ch}	Number of azimuth channels of the system
N_{eff}	Effective number of pulses in the sequence (not blocked)
N_{el}/N_{az}	Number of channels in elevation/azimuth
$N_{gap\ sets}$	Total number of gap sets (summation over all orders)
$N_{gap\ sets}(k)$	Number of gap sets for a given order k_0
$N_{\text{multiplications, Re}}$	Number of real multiplications
N_p	Number of pulses in azimuth beamformer window
N_{pols}	Number of polarization-pairs to be recorded
N_{PRI}	Number of PRIs in a staggered PRI sequence
N_{rbins}	Number of range bins in echo window
N_{rg}	Number of different sets of resampling coefficients due to range variation of input manifold (a function of sampling and antenna patterns)
N_{SDL}	Number of angles in the sidelobe grid
N_s	Number of sub-bands of bandwidth PRF within Bw_{az}
$N_T(R)$	Number of traveling pulses for an arbitrary slant range
N_{win}	Number of samples in azimuth beamformer window (as many samples as channels per pulse)

$N_{PRI\,MIN}(k_{critical})$	Minimum sequence length as a function of $k_{critical}$, in the context of the sequence design equations
N_{bits}^{data}	Number of bits used for BAQ data quantization
$N_{bits}^{storage}$	Number of bits used for coefficient storage
N_{sb}^{RF}	Number of RF sub-bands
$\widetilde{N}_{PRI\,min}$	Minimum sequence length as a real number, an intermediate step in the design equations
$NESZ(\theta)$	NESZ for a given look angle θ
$\overline{PRF}$	Mean PRF of the staggered PRI sequence
$\overline{PRF}_{eff}$	Effective mean PRF of system at a given range, discounting the blocked pulses
PRF_{multi}	Multichannel PRF, considering all N_{ch} channels
$\overline{PRI}$	Mean PRI of the staggered sequence
PRI_0	Initial PRI in a staggered PRI sequence
P_{TX}	Peak transmit power
$\bar{P}_{TX}$	Average transmit power
P_{signal}	Total signal power
$P_{sidelobe}$	Signal power within the sidelobe region are of the impulse response
$P_{mainlobe}$	Signal power within the mainlobe region are of the impulse response
$P_{ambiguity}$	Ambiguous power (azimuth ambiguities), concentrated in the sidelobe region
$P_{s,comp}(\theta)$	Signal power after azimuth compression, for a given range/look angle
$P_{n,comp}(\theta)$	Noise power after azimuth compression, for a given range/look angle
$P_k(f_{\mathrm{D}})$	Filter applied to the k^{th} channel for multichannel reconstruction
$\boldsymbol{P}(f_{\mathrm{D}})$	N_s x N_{ch} reconstruction filter matrix
R	Generic slant range from radar to target
$R(\theta,\phi), R(\theta)$	Slant range to the area element
$R(t_{az})$	Slant range history of target in along-track
R_0	Slant range of minimum approximation for a given target
R_1 , R_2	Slant range region delimiting pulse extension
$R_{amb}(k)$	Slant range of the range ambiguity of order k, for constant PRI SAR
$R_{amb}(i,k)$	Slant range of the range ambiguity of order k and pulse index i, for Staggered SAR
R_{data}	Total system data rate
$R_{data_{min}}$	Minimum data rate, i.e., considering possibility of reducing the azimuth sampling rate up to $f_{s_{az}} = \gamma_{az} \cdot Bw_{proc}$, which requires on-board resampling and an anti-alias filter
$R_{data_{orig}}$	Original data rate, i.e., with azimuth sampling rate corresponding to $f_{s_{az}} = PRF$ and no reduction
R_{max}	Maximal slant range of interest in the swath
R_{min}	Minimal slant range of interest in the swath
$R(\tau)$	Autocorrelation function of a WSS signal
$\boldsymbol{R}(f_{\mathrm{D}})$	Covariance matrix of signal vector $\underline{\boldsymbol{Y}}(f_{\mathrm{D}})$
$\underline{\boldsymbol{R}}_{\boldsymbol{noise}}$	Covariance matrix of noise affecting elements of antenna array
$\underline{\boldsymbol{R}}_{\boldsymbol{v}}$	Array manifold autocorrelation matrix
$\widetilde{\boldsymbol{R}}(f_{\mathrm{D}})$	Modified covariance matrix of signal vector $\underline{\boldsymbol{Y}}(f_{\mathrm{D}})$, introducing intentional SNR over- or underestimation according to parameter q
$\boldsymbol{R}_m^{interf}(f_{\mathrm{D}})$	Interference covariance matrix (based on signal vector $\underline{\boldsymbol{Y}}(f_{\mathrm{D}})$ for m^{th} sub-band
$RASR(\theta_s)$	Range ambiguity to signal ratio for a given signal look angle θ_s
$S(f_{\mathrm{D}}), S(\theta, f_{\mathrm{D}})$	Azimuth signal power spectral density
$SANR_m$	Signal to Ambiguity and Noise Ratio for m^{th} sub-band

$SNR_{DBF}(\underline{\boldsymbol{w}})$	SNR figure of pattern after DBF, as a function of DBF weights $\underline{\boldsymbol{w}}$
$SNR_{comp}(\theta)$	SNR of the SAR signal after azimuth compression
$S_m(f)$	m^{th}*look* of signal spectrum, i.e. $U(f_\mathrm{D})$ within I_m
$\underline{\boldsymbol{S}}(f_\mathrm{D})$	N_s element column vector describing the signal to be reconstructed (concatenation of *looks*)
$\underline{\widehat{\boldsymbol{S}}}(f_\mathrm{D})$	N_s element column vector describing the reconstructed signal
T_{PRI}	Period of the staggered PRI sequence
T_{dc}	Duty cycle
T_{ill}	Illumination time over which a target is visible within the synthetic aperture
T_{noise}	System noise temperature
T_p	Pulse length (duration)
$U(f_\mathrm{D})$	Signal spectrum in Doppler domain
W_g	Swath width on ground
$Y_k(f_\mathrm{D})$	Sampled signal available at multichannel system's k^{th} receiver
$\underline{\boldsymbol{Y}}(f_\mathrm{D})$	N_{ch} element column vector describing the sampled signal

Greek Symbols

α	SNR sensitivity factor in the range [0,1] in the joint MSE-SNR optimization criterion
β	Phase step in excitation for uniform array
γ_{az}	Oversampling rate in azimuth, accounting for a margin in the signal sampling.
γ_{rg}	Oversampling rate in range, accounting for a margin in the signal sampling, as well as guard times, data headers, etc.
γ_0	Proportionality constant between power spectral density and pattern gain
δ_{az}	(Goal) azimuth resolution
δt	Arbitrary delay in output grid, a degree of freedom used to minimize the shifts
δt_{IR}	Time domain resolution of impulse response after pulse compression
Δf	Uncertainty in the definition of frequency
Δi	Step in pulse index causing complete decorrelation of the range ambiguity of a given order due to migration of the illuminated area over range
Δ_{PRI}	Step between adjacent PRIs in a staggered PRI sequence
Δb	Duration of the blockage event
ΔMSE	$\overline{MSE_i}$ step between subsequent iterations
$\Delta R_{block}(k_0)$	Span of the blockage diagram for a given order k_0
$\Delta R(t_{az})$	Cross-track platform motion as a function of slow time, which generates another contribution to the phase error
ΔSNR	$\overline{\Phi_{SNR}}$ step between subsequent iterations
Δt	Uncertainty in the definition of time
Δt_1, Δt_2	Set of time shifts created by the choices $\delta t = \delta t_1$ and $\delta t = \delta t_2$, respectively
Δt_k	Channel delay in k^{th} channel's transfer function, related to phase center position
Δx	Phase center shift in azimuth direction
Δx_{eq}	Maximum phase center shift from input to output grid, assuming δt is chosen to equalize $\lvert\min\{\Delta x\}\rvert = \max\{\Delta x\}$
Δx_{max}	Maximum phase center shift from input to output grid
$\Delta\phi_k$	Constant phase term in k^{th} channel's transfer function, related to imaging

	geometry and phase center position
$\Delta\theta(\epsilon)$	Maximum phase error magnitude
$\Delta w_{amb}(\theta_{i,k})$	Ratio of $w_{amb}(\theta_{i,k})$ calculated from PSD and using flat spectrum assumption
ϵ	Normalized noise magnitude in pattern uncertainty model
ϵ_0	Noise magnitude in pattern uncertainty model (no normalization)
ϵ_k	Amplitude error of TR-module
ϵ_{SDL}	Elevation beamforming sidelobe constraint (refers to Dolph-Chebyshev weighting in the planar case)
η	Generic incidence angle
η_i	Incidence angle corresponding to i^{th} range ambiguity
η_{min}/η_{max}	Swath minimum/maximum incidence angle
θ	Generic elevation angle in antenna coordinate system
θ_1, θ_2	Elevation angle region delimiting pulse extension
θ_0	Goal scan angle for the uniform array steering
$\theta_0(\Delta x)$	Mapping from baseline to scan angle, as an intermediate step in the azimuth phase center steering method
θ_{az}, ϕ	Azimuth angle between antenna reference system and target position
$\theta_{i,k}$	Look angle of the k^{th} order range ambiguity, for pulse index i in Staggered SAR
$\theta_{min}/\theta_{max}$	Swath minimum/maximum look angle
θ_s	Look angle for the main signal, in the discussion of range ambiguities
θ_{tilt}	Elevation tilt angle w.r.t. nadir
Θ_{SDL}	Sidelobe grid for beamforming
γ	Eigenvalue of $\underline{\boldsymbol{R}}_{\boldsymbol{v}}$
λ	(Carrier) wavelength
λ_0	Nominal wavelength, in the analysis of the pattern deviation due to the RF bandwidth
λ_{offset}	Worst-case deviation of wavelength within the bandwidth, in the analysis of the pattern deviation due to the RF bandwidth
$\underline{\boldsymbol{v}}(f_{\mathrm{D}})$	Array manifold vector as a function of Doppler frequency
$\xi_{MSE}, \xi_{SNR}, \xi_J$	Cost functions for optimal MSE, optimal SNR and Joint MSE-SNR optimization criterions, respectively
$\sigma(\theta,\phi), \sigma_0, \sigma_0(\theta)$	Radar Cross Section (RCS) per unit area
σ_n^2	Noise power
σ_s^2	Signal power for each *look*
$\underline{\boldsymbol{\sigma}}_{\boldsymbol{G}}$	Cross-correlation vector between goal pattern and array manifold
ϕ_{AZ}	Azimuth beamwidth
ϕ_{hamm}	Hamming window coefficient
ϕ_k	Phase error of k^{th} TR-module
$\phi_k(t_{az})$	Phase error of corner reflector response with respect to ideal trajectory in k^{th} channel
$\phi_{pattern}(k, \theta_{az}(t_{az}))$	Contribution of the uncompensated antenna pattern differences to the phase error
$\phi_{uni}(f_{\mathrm{D}})$	Uniform distributed random phase of pattern uncertainty
$\Phi_{SNR}(\underline{\boldsymbol{w}})$	SNR scaling with respect to the sum pattern
$\overline{\Phi_{SNR_i}}$	Average over output samples of the achieved SNR scaling with the given method, at iteration i
ψ_n	Argument of the arcsin function in discussion of steering of a phased array

Subscripts and Superscripts

$\{.\}_{amb}$	(Range) Ambiguities
$\{.\}_{az}$	Azimuth
$\{.\}_{el}$	Elevation
$\{.\}_{mainlobe}$	Mainlobe region (of impulse response)
$\{.\}_{max}$	Maximum
$\{.\}_{min}$	Minimum
$\{.\}_{noise}$	Noise
$\{.\}_{rg}$	Range (as opposed to azimuth dimension)
$\{.\}_{sidelobe}$	Sidelobe region (of impulse response)
$\{.\}_{sig}$, $\{.\}_{signal}$	Signal
$\{.\}_{comp}$	After azimuth compression
$\{.\}_{orig}$	Original (uncompensated)

1 Introduction

Radio Detection and Ranging (RaDAR) is a technology whose development started already on the eve of the XXth century [1]. Its development followed the theoretical and experimental framework on electromagnetism laid in the XIXth century by notorious physicists such as Michael Faraday (1791-1867), James Clarke Maxwell (1831-1879), and Heinrich Hertz (1857-1894). Faraday developed in 1836 the concept of an electromagnetic field, whereas in 1865 Maxwell described mathematically its behavior, which would be experimentally demonstrated by Hertz in 1888. Building on Hertz's work on the reflectivity of metal surfaces, Christian Hülsmeyer (1881-1957) proposed in 1904 the *Telemobiloscope* [2], which is considered the first radar system, conceived for ship collision avoidance.

Whereas the *Telemobiloscope* was not widely implemented at the time due to technological limitations, radio communications found a fast development and wide acceptance in the first decades of the XXth century. The radio pioneer Gugliermo Marconi (1874-1937) demonstrated wireless telegraphy in 1886 and achieved transatlantic communication in 1902, being also responsible for the development of commercial applications of the technology. The worldwide interest in radio communications brought important advancements in RF technology, paving the way to a resurrection of RADAR research in the 1930s, motivated mostly by military applications. By 1939, Germany, Italy, Japan, the United States, the United Kingdom and also the Soviet Union had developed early radar systems, which were considerably enhanced and matured during World War Two.

The principle of Synthetic Aperture Radar (SAR) was invented by Carl Wiley (1918-1985) in 1951, while working at Goodyear Aerospace [3]. The technique was further developed in the 1950s and 1960s [4], [5], [6], also pursuing military applications. Meanwhile, RADAR systems also found an increasing interest in civil aviation, with the development of Air Traffic Control (ATC) and Ground Controlled Approach (GCA) systems, matured in the 1970s and co-responsible for the safety and feasibility of mass air transportation. This decade also saw the early developments in short-range

automotive radar [7], initially intended for collision avoidance. The systems evolved to offer features such as automatic cruise control and parking aid, present in high-end automobiles of several manufactures by the end of the 1990s. Currently, boosted by advancements in radiofrequency and digital technology, automotive radars are expected to experience a boom and become fairly widespread in some decades, as they represent a key technology for the intended autonomous-driving cars of the future [8]. Several more advanced radar applications are expected to be available for everyday automobile usage [9], some of which include the usage of SAR [10]. SAR techniques are also currently employed for state-of-the-art short-range radars in non-destrutive testing applications [11], [12] (e.g. analysis of materials and body scanning).

The history of spaceborne SAR for remote sensing, in particular, begins with the United States National Reconnaissance Office's (NRO) QUILL program [13], on the frame of which an experimental satellite was launched in 1964. National Aeronautics and Space Administration (NASA)'s Seasat Mission [14], [15] in 1978 is a pioneering example for civilian applications. The Space shuttle Imaging Radar (SIR) program followed with SIR-A [16] in 1981 and SIR-B [17] in 1984. In the following years, other agencies developed and launched their own radar satellites as well, including ESA's ERS-1 [18] (1991), the Soviet system ALMAZ-1 [19] (1991) and the Japanese System JERS-1 [20] (1992). The SIR-C Mission [21] in 1994 – a cooperation between NASA, the German Aerospace Center (DLR) and the Italian Space Agency (ASI) – is also an important benchmark, and already envisioned interferometric applications. It's success lead to the Shuttle Radar Topography Mission (SRTM) [22] in 2000, which provided a first world-wide Digital Elevation Model (DEM) with pixel spacing ranging from 30 to 90 m. In 2016, DLR's Tandem-X Mission [23] completed a second world-wide DEM [24] with considerably improved coverage and resolution (up to 12 m pixel spacing and 1 m height accuracy).

As described in [25], great improvements were made in SAR processing techniques in the 1980s and 1990s, progressively turning SAR into a mature remote sensing technique [26], [27]. An increasing number of applications [28] followed in the 1990s

and 2000s, including SAR interferometry [29], and more recently polarimetric interferometry [30], high-accuracy deformation through permanent scatterers [31] and SAR tomography [32]. In this context, SAR images and related products are increasingly accepted and employed by the scientific community. As before, the advances in processing techniques and applications go hand in hand with the development and the lessons learned from new spaceborne SAR missions. An overview of the state-of-the-art in terms of spaceborne SAR missions is provided next in Section. 1.1.

1.1 State-of-the-Art Spaceborne Synthetic Aperture Radar Missions

A survey of ESA's Earth Observation Satellite Mission Database (Stand of July 2017) [33], [34] reveals a total of 28 currently operational or planned spaceborne SAR missions, which also speaks for the interest on SAR image products. The projects are from 14 space agencies encompassing 11 countries (Argentina, China, Germany, India, Italy, Japan, Korea, Russia, Spain and the United States), plus the international European Space Agency (ESA). From these, the majority consists of X-band missions, followed by C-band and L-band, as illustrated in **Figure 1**.

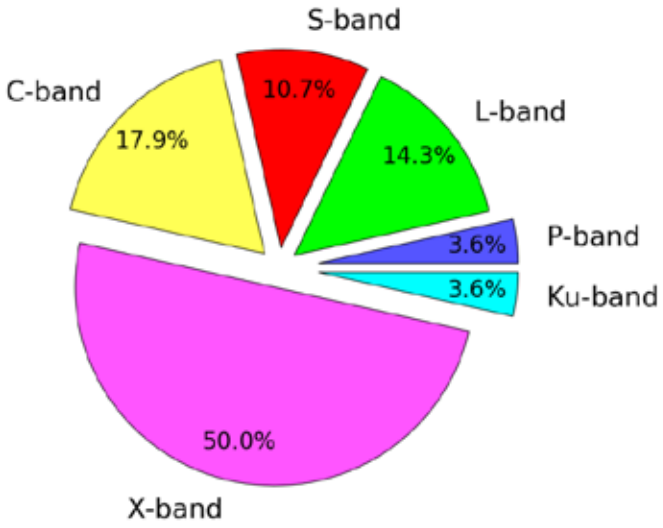

Figure 1. RF bands of the 28 current and planned Spaceborne SAR Missions, as of July 2014 [33].

To assess the High-Resolution Wide Swaths (HRWS) capabilities of these missions, the most important parameters are the swath width W_g and the azimuth resolution δ_{az}. The parameters of some example systems are represented in the W_g - δ_{az} plane in **Figure 2 (a)**.

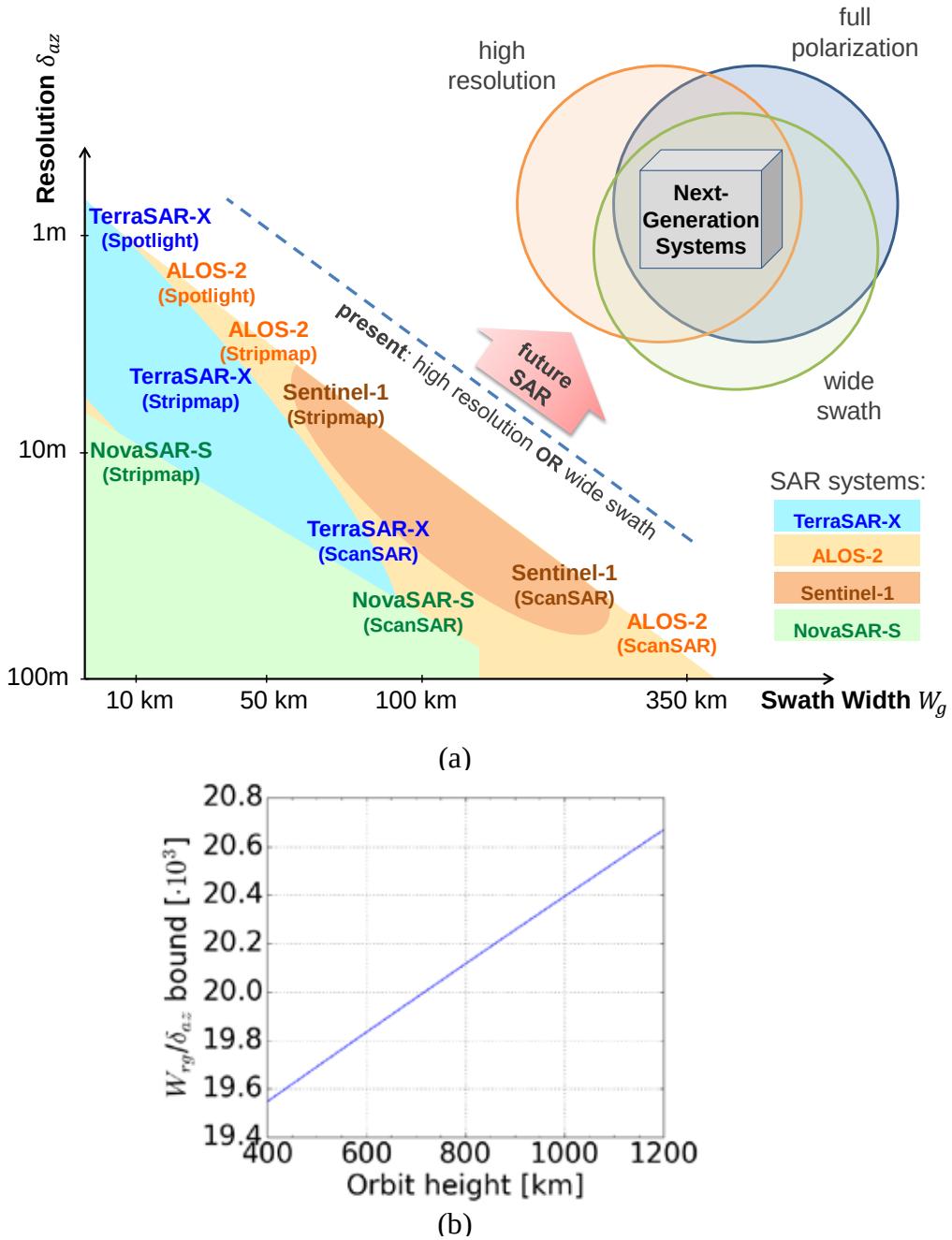

Figure 2. Azimuth resolution and swath width of example spaceborne SAR missions [33].

The ratio of W_g in kilometers to δ_{az} in meters may be considered as a figure of merit for each of the imaging modes. As will be explained in Section 2.3.1, this ratio has an upper bound for a conventional single-channel SAR which is mainly a property of the orbit height. The variation of the upper bound on W_g / δ_{az} with this parameter is shown in **Figure 2 (b)**.

The parameters of the missions in the database which show W_g / δ_{az} greater than $15 \cdot 10^3$ are listed in TABLE I.

TABLE I
OVERVIEW OF CURRENT AND PLANNED HIGH-RESOLUTION WIDE-SWATH SAR MISSIONS

Mission	Agency	Mode	Azimuth resolution δ_{az}	Swath width W_g	Ratio W_g / δ_{az}	RF Band	Orbit height h_{orbit}
COSMO-SkyMed 2nd Generation (CSG)	ASI (Italy)	Spotlight	0.35 m	7.3 km	$20.9 \cdot 10^3$	X	620 km
HRWS DBF SAR	DLR (Germany)	VHR Mode	0.25 m	10 km	$40.0 \cdot 10^3$	X	-
		HR Stripmap	0.5 m	20 km	$40.0 \cdot 10^3$		
		Stripmap	1 m	70 km	$70.0 \cdot 10^3$		
		ScanSAR	25 m	800 km	$32.0 \cdot 10^3$		
NISAR	NASA (US) and ISRO (India)	Stripmap	10 m	240 km	$24.0 \cdot 10^3$	L	747 km
ALOS/ PALSAR-2	JAXA (Japan)	Spotlight	1 m	25 km	$25.0 \cdot 10^3$	L	628 km
		Stripmap	3 m	50 km	$16.7 \cdot 10^3$		
RADARSAT-2	CSA (Canada)	Wide Fine	8 m	150 km	$18.8 \cdot 10^3$	C	798 km
WSAR	NSOAS/ CAST (China)	High Resolution	1 m	40 km	$40.0 \cdot 10^3$	X	-
		Medium Resolution	5 m	80 km	$16.0 \cdot 10^3$		
		Wide Swath	10 m	150 km	$15.0 \cdot 10^3$		
Tandem-L	DLR (Germany)	Stripmap "B"	7 m	350 km	$50.0 \cdot 10^3$	L	745 km
Sentinel-1	ESA	Stripmap	5 m	80 km	$16.0 \cdot 10^3$	C	693 km

For the span of relevant orbit heights, the W_g / δ_{az} bound is around $19 \cdot 10^3$, effectively indicating that the state-of-the-art system requirements are either already on the limit or beyond of what a single channel system can provide. It should be noted that spotlight[1] modes may also provide high resolution and high W_g / δ_{az} ratios, but the acquisition is confined to narrow swaths in both range and azimuth (a parameter which this metric does not consider), whereas multichannel stripmap modes are responsible for truly HRWS operation. With respect to this metric, HRWS, Tandem-L, WSAR and NISAR show the best performance.

The swath width W_g is a crucial performance parameter since it determines the temporal resolution (or update rate) of the data in a continuous observation scenario. Near-future spaceborne missions, as e.g. DLR's Tandem-L [35], [36], envision the imaging of ever-increasing swaths with the highest possible resolution. This allows delivering applications high-quality data at a high update rate, needed to observe dynamic Earth processes. This bears the potential to fill the gaps in the scientific understanding of many processes with relevance on a global scale, such as the evolution of glaciers, changes in ocean currents and the contribution of the biomass distribution to the carbon cycle [35].

For instance, Tandem-L's intended 350 km swath allows global coverage in 8 days, whereas Tandem-X [23]'s 30 km swath in Stripmap mode requires roughly one year to achieve global coverage (though at a finer 3 m resolution). The increasingly demanding HRWS requirements of SAR Missions pose system design with a challenging task that requires new processing techniques and mission concepts able to deliver unpresented performance in terms of high resolution coverage. This serves as main motivation for this thesis, as will be addressed next in Section 1.2.

[1] In spotlight the illumination is changed over azimuth time to maximize the observation time and thus the acquired Doppler beamwidth over a particular area, which allows a finer resolution but limits the swath extension in both azimuth and range dimensions.

1.2 Motivation

As discussed in the previous section, HRWS SAR imaging [37]-[53] has become an active research field, in order to provide next generation spaceborne SAR Systems with next-level imaging capabilities. These are required by the current and projected demand for remote sensing inputs for the scientific understanding of global-scale processes. The demands for simultaneously fine geometric and temporal resolution cannot be fulfilled by conventional single-channel SAR systems and different alternatives have been investigated, as a rule involving the use of multiple channels in elevation and/or azimuth, and suitable digital beamforming (DBF) techniques[2].

This thesis is inserted in this context, and more specifically addresses the problem of achieving higher W_g / δ_{az} ratios than those made possible by the current state-of-the-art monostatic systems, while keeping the swath continuous. In fact, current techniques allow either reducing δ_{az} at the price of gaps in the swath (in other words, with a limit on the continuous W_g) or increasing W_g for a given δ_{az} which is bounded by the capabilities of a single azimuth channel. The solution to this problem will be shown to be a hybrid between two HRWS approaches.

On one hand, a system with multiple channels in azimuth [39], [47], [48], [49], [51] allows imaging with very fine resolution over a moderately wide swath. The limitiation is due to the upper bound on the size of an antenna deployable in space, as discussed in [44]. Conceptually, the multichannel architecture system provides Doppler and/or phase center variety[3][37], which can be exploited to increase the Doppler bandwidth and improve the azimuth resolution of the SAR signal. This class of system shows in addition a sampling rate which is increased with respect to the pulse repetition frequency (PRF) by a factor equal to the number of azimuth channels N_{ch}. This feature

[2] Digital beamforming is a technique that also plays an important role in improving the performance of state-of-the-art short-range radar for automobile [54] and non-destructive testing [12] applications.

[3] In the case of planar arrays, the different azimuth channels observe the same Doppler spectrum with different phase centers [39]; whereas in the case of systems with reflectors antennas [40], the channels observe different portions of the Doppler spectrum, and their number is directly linked to the total bandwidth.

in general allows acquiring a wide Doppler spectrum (required for fine azimuth resolution) with a lower PRF in comparison to a conventional system. The technique is being considered for a follow-on mission of ESA's Sentinel-1 [55], [56] – Sentinel Next Generation (NG) – as well as the German *HRWS* mission [57] and has been implemented in a hardware demonstrator [58], [59], [60]. This solution relies on digitization of the azimuth channels as separate data streams and frequency-domain digital beamforming (DBF) for reconstruction of the signal at the higher sampling rate of $N_{ch} \cdot PRF$.

On the other hand, Staggered SAR [41], [50], [53]-[64] is a promising solution to image wide swaths without gaps, currently the baseline mode in the Tandem-L mission proposal [35]. The solution relies on two important concepts. First, multiple channels and time-variant digital beamforming in elevation (an extension of the Scan-on-Receive (SCORE) technique [46], [65]) to form multiple simultaneous elevation beams [37], [43], [44], [45] and second on PRI variation, which allows spreading the gaps due to Tx events over range in a way that enables posterior interpolation over azimuth to yield a swath without blind ranges. The technique is currently an alternative to the multichannel architecture in azimuth, of special interest when a wide gapless swath is desired. It was however developed for a single azimuth channel, which limits its maximum resolution.

Even though complementary in their characteristics, these imaging modes cannot be straightforwardly combined, since the frequency-domain DBF used in the multichannel systems requires a constant PRF, which is incompatible with Staggered SAR. The multichannel Staggered SAR technique developed in this thesis relies on a novel beamforming perspective in time domain, combining the temporal (staggered PRI pulses) and spatial (different azimuth channels) sampling in order to reconstruct the signal into a regular grid with a higher sampling rate. The technique, which is applicable to both planar and reflector antennas, is furthermore verified by means of simulations and an experiment. Part of the results presented in this Thesis has been published as part of [66], [67], [68], [69], and the concept has been awarded a patent [70].

1.3 Scope and Structure

The scope of this work thus includes as first main aspect the presentation of the mathematical framework for the modeling and solution of the multichannel staggered SAR resampling problem. To establish the necessary background, Chapter 2 reviews the characteristic of conventional SAR systems with emphasis on their limitations (cf. Section 2.3), leading to the trade-off between swath width and azimuth resolution – a fundamental system property at the core of the HRWS imaging problem – and the effect of blind ranges – which motivates Staggered SAR. The chapter closes with an overview of spaceborne SAR imaging modes, which illustrate the aforementioned trade-off and introduces the basic rationale of existing HRWS alternatives. Chapter 3 completes the background by examining more closely systems with multiple channels in azimuth as well as formally introducing Staggered SAR and developing mathematical expression for the timing of this class of systems, which will be useful for the following chapters.

Chapter 4 describes the multichannel Staggered SAR concept and different algorithms for calculating the resampling weights, establishing the Virtual Beam Synthesis (VBS) technique. Important aspects affecting performance are identified and discussed, to enable the understanding of properties and trades of this new class of system, both for reflector and planar antennas. In Chapter 5, the algorithms are compared in a step-by-step implementation of the discussed technique, providing examples to aid the understanding of the problem and the trade-offs involved.

Chapter 6 shifts focus to system performance and the promising capabilities of the new technique. Design examples in single polarization as well as fully polarimetric acquisition scenarios are considered, both for reflector and planar antennas. The systems show unprecedented HRWS performance, with azimuth resolutions in the order of 1.0 to 3.0 m and swaths of width 350 km to 500 km (cf. TABLE IV for an overview). Section 6.5 considers an important aspect for the implementation of such systems, namely the trade-off between the onboard implementation complexity and the data rates. The first is alongside the implicit calibration requirements the main

obstacle for on-board implementation, though the time-domain nature of the DBF for the VBS techniques leads to a relatively low-cost solution in comparison to constant-PRF frequency domain techniques (cf. Section 3.2). The second is a crucial and challenging practical aspect for high-performance HRWS modes [71], [72] with current technology and the main obstacle for on-ground processing of multichannel systems in azimuth.

Chapter 7 provides a proof-of-concept of the techniques employing the ground-based multiple-input multiple output (MIMO) radar demonstrator [73], [74] developed at the Microwaves and Radar Institute of DLR. The system is operated with a reflector antenna and a multichannel feed [75], and measurements of an example scene acquired in X-band are employed to show the feasibility of the technique with experimental radar data.

Chapter 8 provides a first analysis of various possible sources of errors causing a mismatch between the modelled and the actual antenna array manifold and therefore performance degradation. The material has as main goal the identification of the critical sources of errors and a first-order estimation of the acceptable error levels, which can be translated into hardware and calibration requirements for future systems of this class.

Chapter 9 concludes the thesis providing a summary of the discussed material and an outlook for further research. Appendix A to Appendix B address relevant complementary topics, including elevation beamforming for staggered SAR systems and the estimation of the SAR performance indices, which also show peculiarities in this case [64].

1.4 Main Contributions

The main contributions of this work include:

- Novel interpretation and modelling of the multichannel staggered SAR signal, allowing the resampling to be cast as a beamforming or pattern synthesis problem.

- Solution to the resampling problem in the form of the Virtual Beam Synthesis (VBS) algorithm, which allows introducing parameters to induce an ambiguity-suppression/noise-scaling trade-off.
- Extension of the concept, initially based on a reflector antenna architecture, to planar arrays, alongside a discussion of the differences and implications for the design of such systems.
- Exemplification of the capability of the techniques with different system designs and prediction of their performance through simulations, as well as a proof-of-concept with measured data.
- First-order analysis of the impact of several sources of errors and derivation of corresponding calibration requirements, in support of the analysis of the on-board vs. on-ground implementation options.

2 Conventional SAR

2.1 Chapter Overview

This chapter briefly examines the principle of Synthetic Aperture Radar in Section 2.2 and the limitations of conventional single-channel SAR imaging systems, in Section 2.3. Next, Section 2.4 discusses conventional spaceborne SAR imaging modes, illustrating the trade-offs with respect to SAR performance, and presents an overview of alternative system designs and techniques to push the performance beyond the limits of this class of system.

2.2 Synthetic Aperture Radar: Basic Principle

Pulse Compression

A waveform which is very widely used in radar systems is the linearly frequency modulated *chirp* [26], [27], [76], of duration T_c

$$s_{chirp}(t) = \text{rect}\left(\frac{t}{T_c}\right) \cdot \exp(\text{j} \cdot \pi \cdot k_{FM} \cdot t^2), \quad (1)$$

with instantaneous frequency $f(t) = k_{FM} \cdot t$ within $\left[-\frac{T_c}{2}, \frac{T_c}{2}\right]$ and a total bandwidth $B = k_{FM} \cdot T_c$. Using the principle of stationary phase, the spectrum of a chirp can be shown to also be a *chirp* [27]

$$S_{chirp}(f) = \text{rect}\left(\frac{f}{B}\right) \cdot \exp(-\text{j} \cdot \pi \cdot \frac{f^2}{k_{FM}}), \quad (2)$$

so that compression of the waveform with the matched filter $S^*_{chirp}(f)$ removes the phase modulation and yields a *sinus cardinalis* (sinc) response with 3 dB resolution proportional to the inverse of the bandwidth

$$\delta t_{IR} \cong 0.89 \cdot \frac{1}{B}, \quad (3)$$

in a process known as *pulse compression*, since a longer linearly modulated radar pulse yields a finer resolution.

Basics of Synthetic Aperture Radar

Whereas many radar systems in different geometries apply pulse compression over range, the defining characteristic of a Synthetic Aperture Radar (SAR) [25], [26], [27] system is exploitation of the Doppler history of a target in a side-looking geometry to achieve pulse compression over azimuth, which dramatically increases the resolution in comparison to the system's real antenna aperture. In the simplified flat-Earth geometry of **Figure 3**, in which the platform is flying with speed v_{plat} and the nearest slant range of the target is R_0,

$$R(t) = \sqrt{R_0^2 + \left(v_{plat} \cdot t\right)^2} \cong R_0 + \frac{{v_{plat}}^2}{2 \cdot R_0} \cdot t^2 \,, \tag{4}$$

assuming $R_0 >> v_{plat} \cdot t$ over the whole time T_{ill} the target is observed, which is defined by the azimuth antenna pattern.

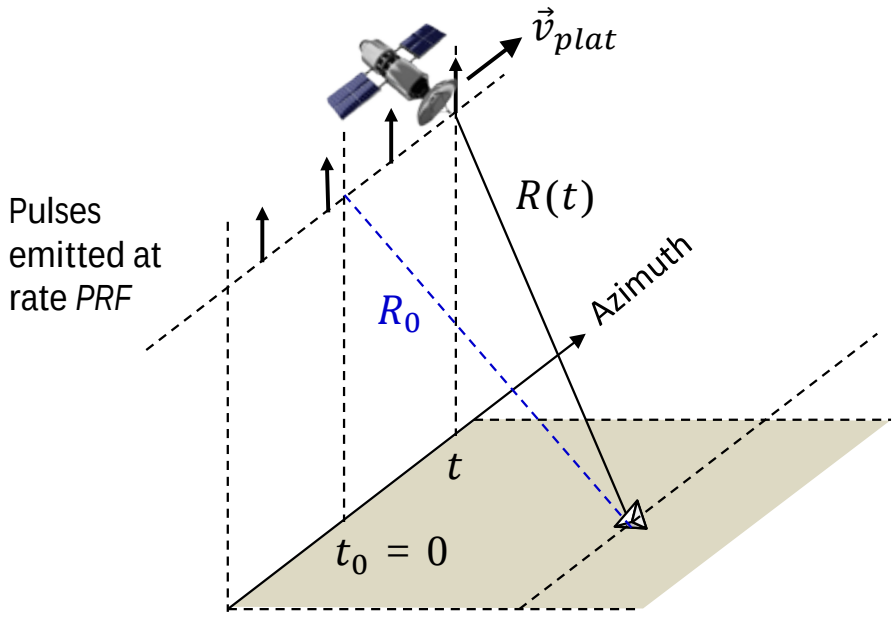

Figure 3. Simplified geometry over azimuth to illustrate origin of the geometry-induced azimuth chirp over Doppler frequency, for a SAR system observing a point target located at closest approach R_0 by emiting pulses at the Pulse Repetition Frequency (PRF).

The SAR signal over azimuth has thus an instantaneous Doppler shift

$$f_{\mathrm{D}}(t) \triangleq -\frac{2}{\lambda} \cdot \frac{\mathrm{d}R(t)}{\mathrm{d}t} = -2 \cdot \frac{{v_{plat}}^2}{\lambda \cdot R_0} \cdot t, \tag{5}$$

where λ is the wavelength. This frequency variation is recognized to be that of a *chirp* of rate $k_{FM} = -2 \cdot \frac{{v_{plat}}^2}{\lambda \cdot R_0}$, and total bandwidth

$$Bw_{az} = 2 \cdot \frac{{v_{plat}}^2}{\lambda \cdot R_0} \cdot T_{ill}. \tag{6}$$

For a directive antenna, the half power beamwidth θ_{az} relates to the aperture length l_{az} as

$$\theta_{az} \cong \frac{\lambda}{l_{az}}, \tag{7}$$

and assuming $T_{ill} = R_0 \cdot \theta_{az} / v_{plat}$ yields

$$Bw_{az} \cong 2 \cdot \frac{v_{plat}}{l_{az}}, \tag{8}$$

highlighting that this quantity is range independent.

The SAR signal – after compensation for the migration of the target position over the range resolution cells as $R(t)$ varies, which is known as Range Cell Migration Correction (RCMC) – can therefore be compressed using a matched filter[4] into an impulse response with spatial resolution

[4] Even though the model presented here is on purpose kept very simple, matched filtering in range Doppler domain is in fact the basic concept behind one of the most classical SAR processors, the Range Doppler algorithm [77].

$$\delta_{az} = v_{plat} \cdot \delta t_{IR} = k_{win} \cdot \frac{v_{plat}}{Bw_{az}} \cong k_{win} \cdot \frac{l_{az}}{2}, \quad (9)$$

a fundamental equation for SAR systems, in which k_{win} is a proportionality constant[5] depending on the shape of the spectrum, which is weighted by the azimuth antenna pattern. The relation (9) is important for the understanding of the trade-off between the swath width and azimuth resolution presented in Section 2.3.1, and shows that a larger Doppler bandwidth (provided by a wider antenna beamwidth or equivalently a smaller aperture) yields a better resolution after focusing. This contrasts to the case of real aperture radar, for which the resolution is proportional to beamwidth and a fine resolution requires large apertures. Moreover, the region of length $L_{sa} = T_{ill} \cdot v_{plat}$ over which the echoes are integrated in azimuth by the focusing (matched) filter is known as *synthetic aperture*. This nomenclature is motivated by the fact that a real aperture radar with an antenna of length L_{sa} would in fact present a resolution

$$R_0 \cdot \left(\frac{\theta_{sa}}{2}\right) \cong R_0 \cdot \left(\frac{\lambda}{2 \cdot L_{sa}}\right) \cong \delta_{az}, \quad (10)$$

i.e., in the order of the one achieved by the SAR system after processing (ignoring here the proportionally constant k_{win}). That is to say, a possible interpretation of the focusing in azimuth is the combination of the signals over the synthetic aperture to form the equivalent of a very large array with fine resolution capabilities.

2.3 Limitations and Constraints

2.3.1 Ambiguities and the Trade-off between Swath Width and Azimuth Resolution

[5] In (3), $k_{win} \cong 0.89$, since the spectrum is rectangular.

A fundamental limitation of pulsed radar systems [76] is ambiguity (a form of uncertainty) in terms of the determination of a target's range delay and its Doppler shift. This can be addressed formally by the analysis of the radar system's *ambiguity function*. A crucial result in this context is known as the *Radar Uncertainty Relation* [77], which states that a target's range delay and Doppler shift cannot be known simultaneously with arbitrary precision, but rather the combined delay-Doppler resolution [6] is subject to a limit. This property echoes Heisenberg's Uncertainty Principle from quantum mechanics, which also states that the uncertainty in the definition of time Δt and the uncertainty in the definition of frequency Δf are subject to a relation of the form

$$\Delta f \cdot \Delta t \approx 1, \tag{11}$$

and cannot be reduced simultaneously to an arbitrary level.

In the case of Synthetic Aperture Radar [26], the same concept applies and a compromise between two forms of ambiguities (over range and over azimuth) leads to a trade-off between swath width and azimuth resolution.

Range ambiguities arise in a pulsed radar system due to the simultaneous reception of the returns from different pulses, which are repeated every Pulse Repetition Interval (PRI). A simplified swath geometry in **Figure 4** illustrates the concept. The return of the i^{th} pulse of a target located at slant range R from the radar occurs simultaneously with the return of the $(i-k)^{th}$ pulse located at $R_{amb}(k) = R + k \cdot \frac{c}{2} \cdot PRI$, $k \in \mathbb{Z}$. This signal is known as the k^{th} order range ambiguity. The figure also illustrates the

[6] Note that the radar system's *resolution* in the context of [76], [77] is understood as the capability of *unambiguously* separating targets, which is slightly different than the usual concept used in the field of imaging radar. In the latter, resolution is associated with the bandwidth of the signal in range and azimuth dimensions and translates into the image's information content. The bandwidth has to be supported by the sampling, thus inherently relating this property to the "fineness" of the 2D grid forming the image. Following the usual interpretation, the range and azimuth resolution of a radar image depend respectively on the chirp bandwidth (supported by the ADC rate) and the Doppler bandwidth (supported by the PRF) and can be set independently. They cannot however be set independently of the range and azimuth ambiguity levels, which are considered part of the (wide-sense) *resolution* concept addressed in this context.

design guideline for a single-channel system: the antenna pattern, which determines the swath extension $[R_{min}, R_{max}]$ should be designed to exclude the first order range ambiguities of the antenna's main beam, for every $R \in [R_{min}, R_{max}]$.

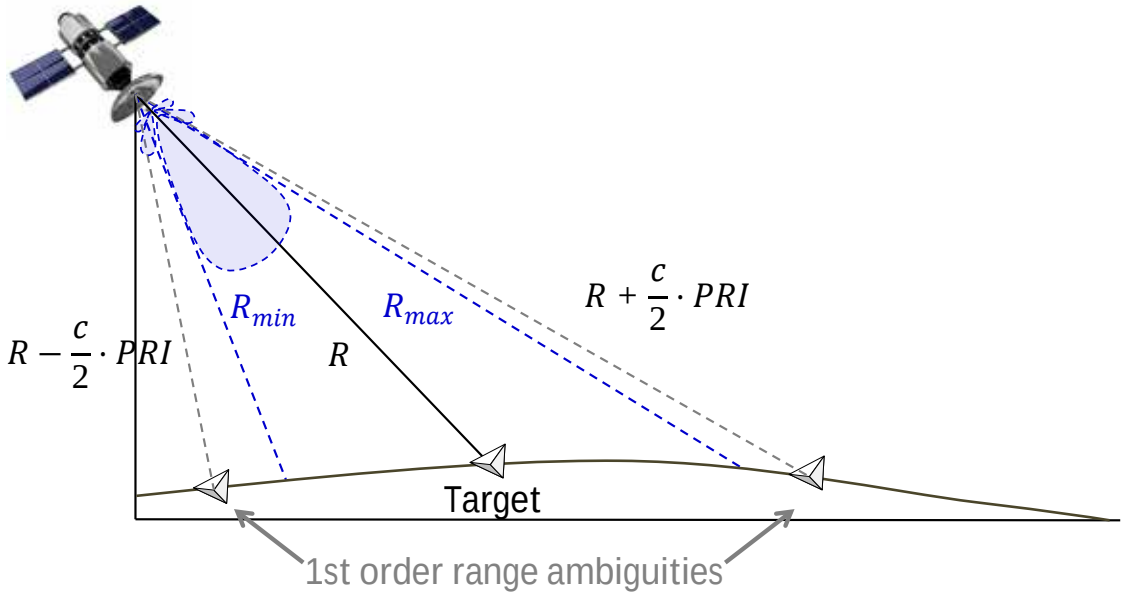

Figure 4. Simplified swath geometry illustrating the position of first order range ambiguities. The Tx antenna patterns should be designed so that they lie outside of the interval $[R_{min}, R_{max}]$.

One may express an upper bound [7]for the extension of non-ambiguous swath as

$$R_{max} - R_{min} < \frac{c}{2} \cdot PRI, \tag{12}$$

where c is the speed of light, and the projection to ground range assuming an incidence angle η yields

$$W_g < \frac{\mathrm{c}}{2} \cdot \frac{PRI}{\sin(\eta)} = \frac{\mathrm{c}}{2} \cdot \frac{1}{PRF \cdot \sin(\eta)}. \tag{13}$$

[7] Note that this expression doesn't consider the effects of the pulse duration nor the need for guard times. In practice a tighter bound could be expressed as $R_{max} - R_{min} < \frac{c}{2} \cdot (PRI - 2 \cdot T_p - \Delta t_{guard})$., where T_p is the pulse duration and Δt_{guard} accounts for guard times before and after the transmission of the pulse. The factor two multiplying T_p accounts first for the incapability of recording while transmitting and second for the need to observe a given target for an interval of duration T_p to achieve full range resolution.

Figure 5 (a) and **(b)** illustrate the timing for non-ambiguous and ambiguous swaths, respectively. In the first case the echo window length (which is proportional to PRI) is enough to accommodate the echo, whereas in the second the PRF is too high for the swath dimensions. This leads to overlaps between the received echoes, which means that returns from more than one angle of arrival [8]within the transmit antenna main beam are expected simultaneously, causing range ambiguity. Overlaps between the received echoes and the transmission of pulses are also seen to occur, which lead to blind ranges, discussed next in Section 2.3.2.

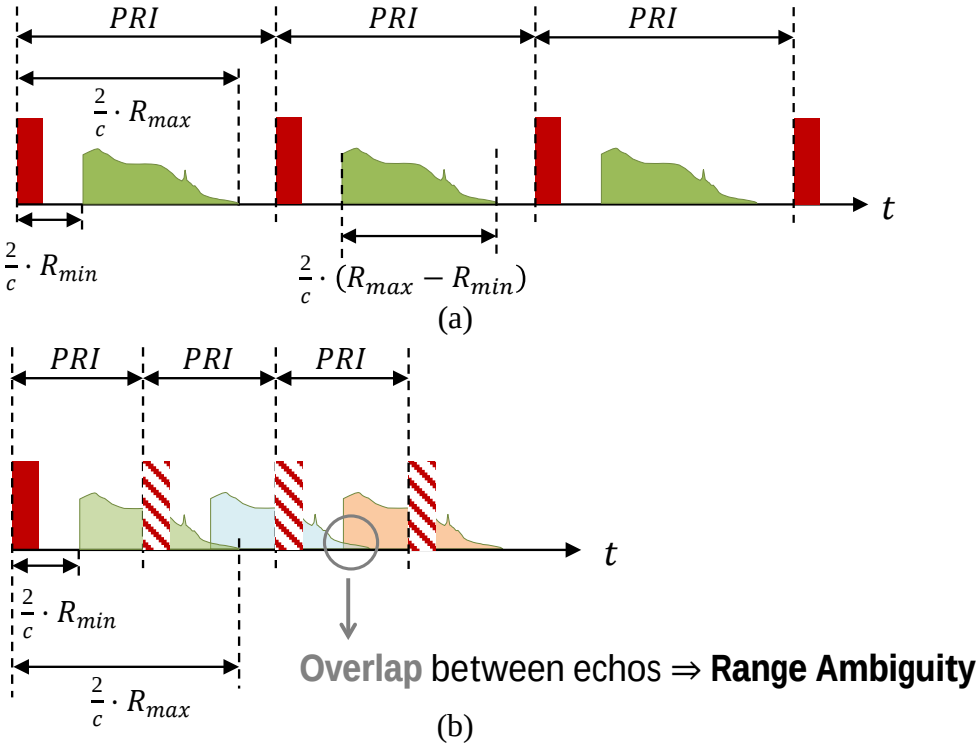

Figure 5. Pulse and echo timing with respect to range ambiguities. (a) Non-ambiguous swath: the echo window length is enough to accommodate the swath. (b) Ambiguous swath: the overlap between echoes indicates that signals from different directions of arrival within the swath are received simultaneously.

[8] The range ambiguous returns arising from different angles of arrival within the wide swath can be separated by the simultaneous formation of multiple elevation beams [38], [37], as will be better explained in Section 2.4. This is one possible configuration allowing the imaging of a swath wider than the bound discussed in this section, relying on a multichannel system with digital beamforming capabilities.

The other form of ambiguity present in SAR systems is azimuth ambiguity, which relates to the sampling of the Doppler spectrum. The azimuth spectrum of SAR data is complex and takes the shape of the azimuth antenna pattern (cf. [26], Appendix B), with a bandwidth Bw_{az} in the main beam. The pulsed operations means the signal for a given range is inherently discrete and sampled at the rate PRF. To ensure Nyquist sampling, $PRF \geq Bw_{az}$. From (9),

$$\frac{1}{PRI} = PRF \geq k_{win} \cdot \frac{v_{plat}}{\delta_{az}}. \tag{14}$$

Combining (14) and (36) and assuming $k_{win} \cong 1$ yields the upper bound

$$\frac{W_g}{\delta_{az}} \leq \frac{c}{2 \cdot v_{plat} \cdot \sin(\eta)} \leq \frac{c}{2 \cdot v_{plat}}. \tag{15}$$

This expression can be re-written, by using (9) and relating W_g to the aperture length in elevation l_{el} (cf. (30)) as

$$A_{ant} = l_{az} \cdot l_{el} > \frac{4 \cdot \lambda \cdot R_0 \cdot v_{plat} \cdot \tan(\eta)}{c}, \tag{16}$$

which is known in the literature as the *minimum antenna area constraint*[9] [26], [27], [77], [78].

For spaceborne SAR, v_{plat} is the orbit velocity, which is a function of the orbit height. It can be determined from the Law of Universal Gravitation as [79]

$$v_{plat}(h_{orbit}) = \sqrt{\frac{G \cdot M_E}{R_E + h_{orbit}}}. \tag{17}$$

[9] As highlighted in [78], it should be kept in mind that (15) and (16) assume a single channel stripmap system illuminating the complete swath at all times with the best possible azimuth resolution. This means that the relation is neither a hard constraint on the physical SAR antenna dimensions nor means that W_g/δ_{az} ratios higher than the bound cannot be achieved by special techniques. Illuminating a reduced swath at a time (either in ScanSAR or SCORE modes) for instance is a way to overcome the limitation, which however requires as a rule the use of a multichannel antenna (at least in elevation) instead of a simple aperture. The use of multiple channels in azimuth is also a possibility to overcome the limitation (cf. Section 3.2).

In **Figure 6**, this bound is illustrated using the spaceborne SAR mission parameters of TABLE I. The dashed line indicates the bound (15) for h_{orbit} = 800 km (also an upper bound for the systems shown in TABLE I), which yields $W_g / \delta_{az} < 19 \cdot 10^3$ in this case. The table only includes systems with W_g / δ_{az} greater than $15 \cdot 10^3$ and, in the plot, systems with W_g / δ_{az} less than $19 \cdot 10^3$ are marked by crosses, whereas the remaining systems, which show higher HRWS performance, are marked by filled symbols (circles, triangles, squares, etc.) as indicated in the subtitle.

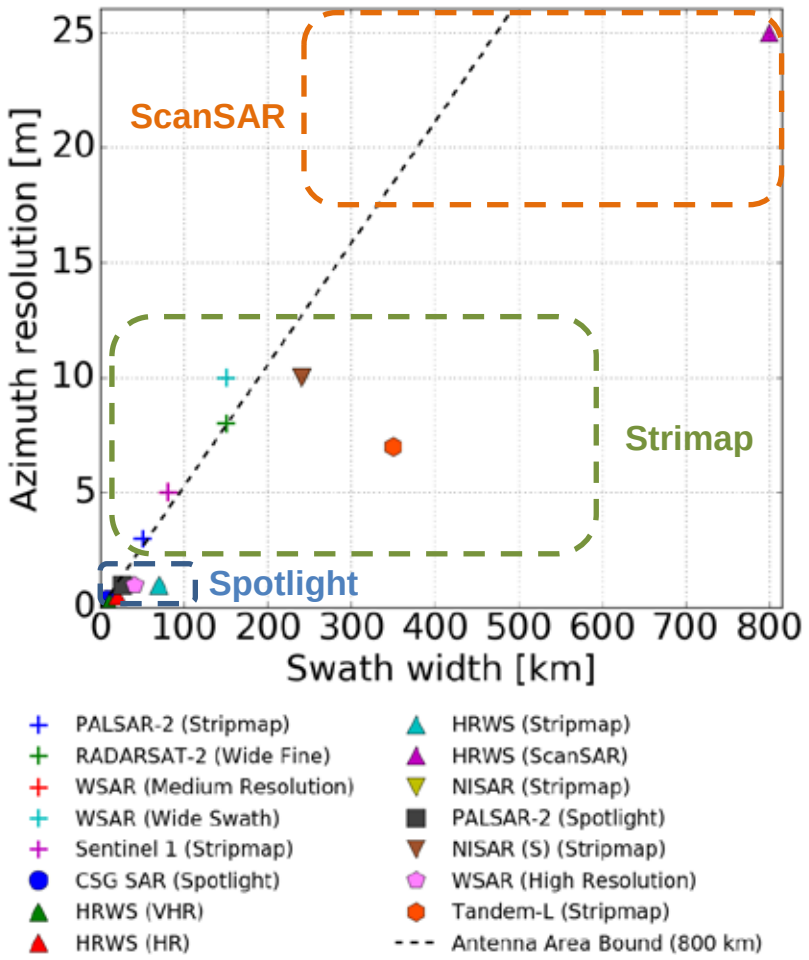

Figure 6. HRWS mission from ESA's Earth Observation Satellite Mission Database (State: July, 2017) and the upper bound of (15), considering (17) with an orbit height of 800 km. Each mission is represented by its swath width (abscissa) and azimuth resolution (ordinate), and missions to the right of the line are beyond the bound (15).

Systems below the curve have parameters in excess of the bound (15) and are either spotlight modes with narrow swaths or Stripmap/ScanSAR modes which rely on

special techniques (such as SCORE, Staggered-SAR or multiple azimuth channels) to deliver this level of performance, as a rule requiring multiple channels and DBF. The loci of Spotlight, Stripmap and ScanSAR modes – of which an overview which will be provided next in Section 2.4 – is indicated qualitatively by the dashed lines shapes in the figure.

2.3.2 Blind Ranges

In monostatic SAR systems, blind ranges are a consequence of the periodical transmission of pulses, in light of the fact that simultaneous recording of the received echoes and transmission of a new pulse is not possible. This leads to a pattern of ranges which the system cannot image, since their two way delays $\frac{2}{c} \cdot R$ coincide with transmission events. This is depicted in **Figure 7 (a)** for an example swath of interest extending from R_{min} to R_{max}. It should be highlighted that, for conventional SAR systems with a constant PRI, all returns from the aforementioned ranges suffer from this blockage effect and the backscatter information is therefore lost, as represented in **Figure 7 (b)**.

The occurrence of a pulse transmission (Tx) inhibits the reception (Rx) of the signal at least during the duration of the pulse, plus possibly a guard interval. Assuming a given Tx event begins at time $t = 0$, the blockage is assumed to occur from instants t_0 to t_1, with duration $\Delta b = t_1 - t_0$. In the simplest case, ignoring guard intervals and pulse length effects (which lead to partial correlation in the range compression [53], [63]), $t_0 = 0$ and $t_1 = T_p$, where T_p is the pulse length. Extending the time vector to several pulses and assuming Tx events begin at every instant $n \cdot PRI$, $n \in \mathbb{N}$, one may formulate the blockage condition for an instant of reception time t as

$$t_0 \leq t - n \cdot PRI \leq t_1, \tag{18}$$

which translates into blind ranges following

$$\frac{c}{2} \cdot (t_0 + n \cdot PRI) \leq R \leq \frac{c}{2} \cdot (t_1 + n \cdot PRI). \quad (19)$$

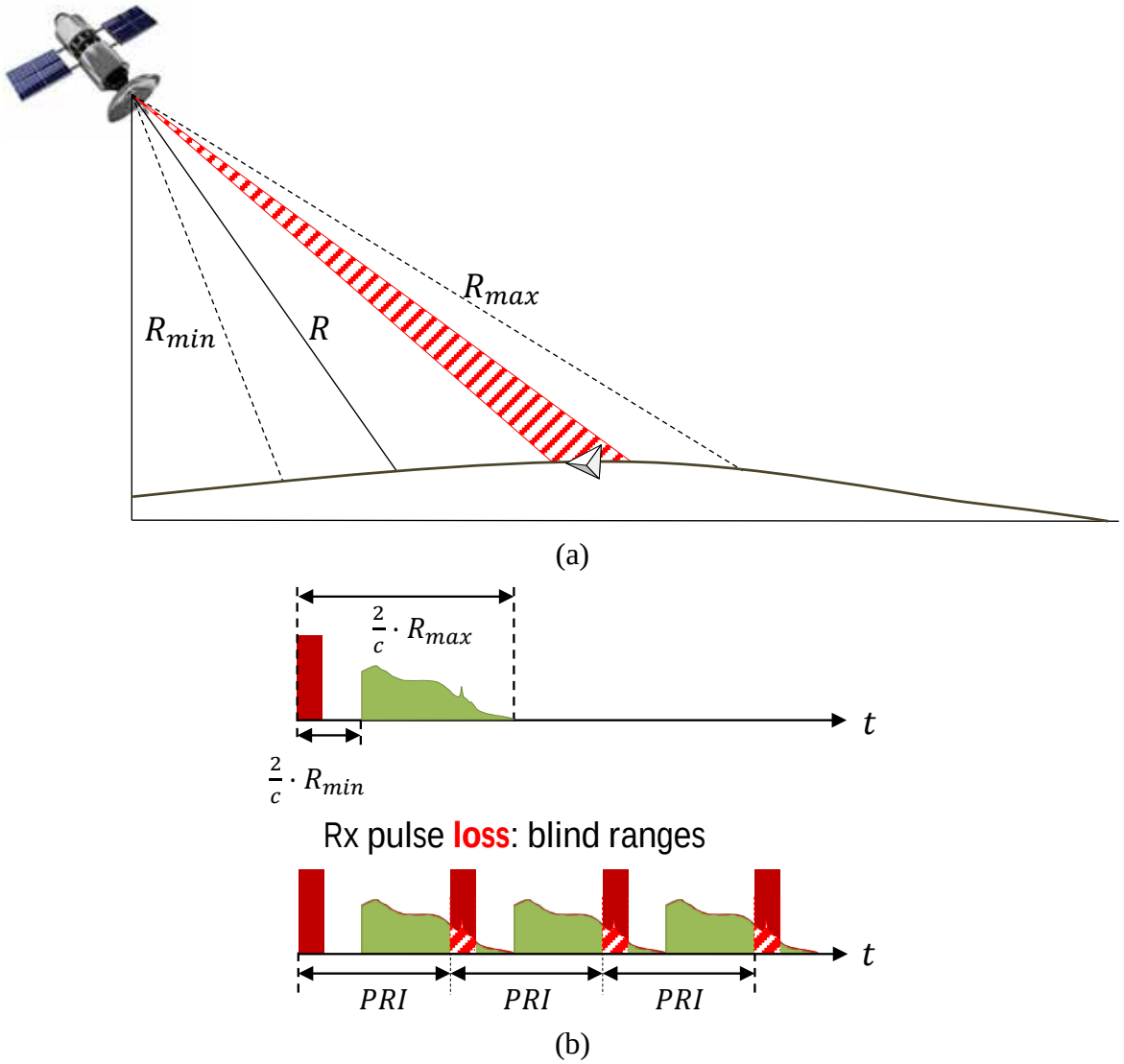

Figure 7. Conceptual illustration of blind ranges in an example swath (a). Due to the regular transmit events (b), all returns from the highlighted interval of ranges are not recorded.

Blind ranges play an important role in the design of the (sub-)swaths of interest of a spaceborne SAR system, and are closely related to the operational PRF. This relationship is often represented as a timing diagram of the imageable swaths – in terms of range or corresponding look angle – against the PRF, also known as a

diamond diagram. An example of timing diagram for a system with an orbit height of 745 km is shown in **Figure 8**. Notice that a SAR system in this configuration would have 3 sub-swaths separated by blind ranges (blue regions). These appear as gaps in the SAR image and represent a disadvantage in terms of ground coverage which serves as motivation for the concept of Staggered SAR (cf. Section 3.3).

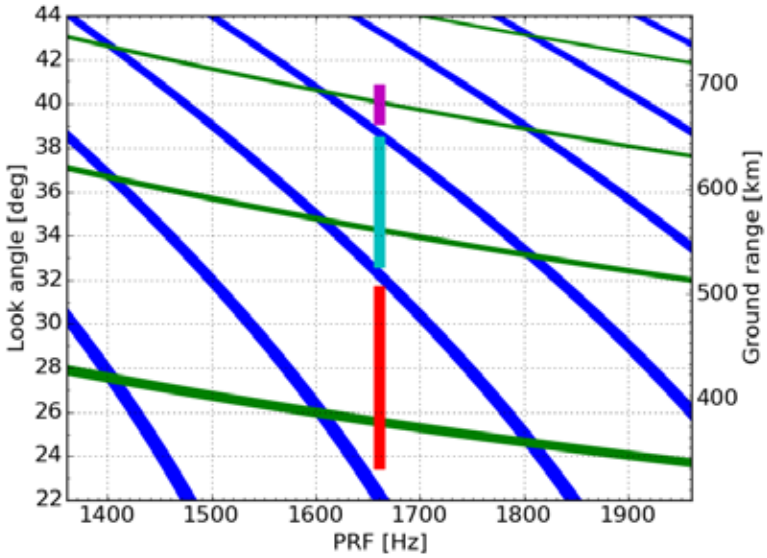

Figure 8. Example timing diagram, showing blind ranges in blue and nadir returns in green. The later are here considered as returns from incidence angles of less than 5°, disturbing due to the specular nature of the reflection. The blind ranges separate possible imageable sub-swaths, for instance the 3 shown in different colors for a PRF of 1660 Hz.

2.4 Overview of Spaceborne SAR Modes and High-Resolution Wide-Swath (HRWS) SAR Techniques

The classic spaceborne SAR modes [25] are described conceptually in **Figure 9**. As will be explained, their characteristics illustrate the trade-off discussed in Section 2.3.1.

Stripmap

The Stripmap mode [26] (cf. **Figure 9 (a)**) is the most conventional SAR imaging mode, dating back to SEASAT. Based on the geometry of the Side Looking Airborne Radar (SLAR), it presents a fixed illumination over elevation, away from Nadir. The mode is subject to the compromise between azimuth resolution and swath width

described in 2.3.1, and the performance of both parameters is intermediate in comparison to the Spotlight and ScanSAR modes.

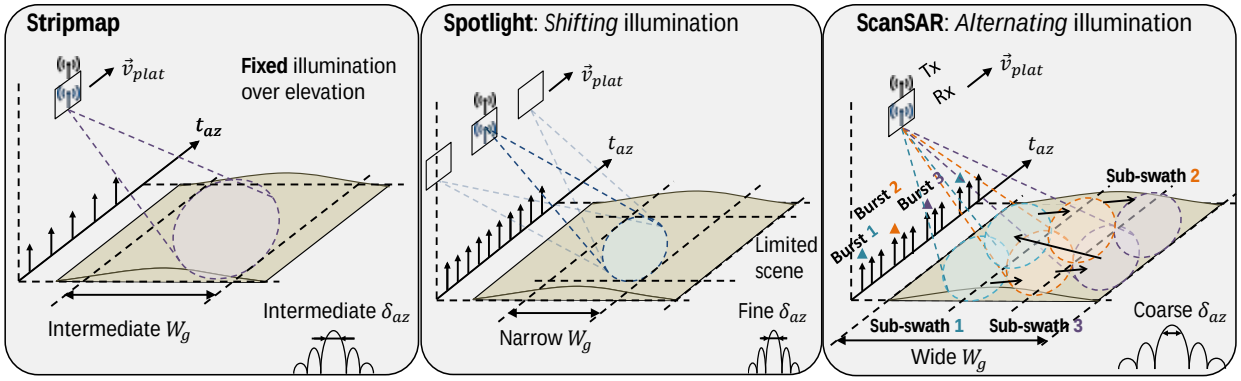

(a) (b) (c)

Figure 9. Basic overview and comparison of classical spaceborne SAR imaging modes. (a) Stripmap mode with fixed illumination over elevation, an "all-rounder" with intermediate swath width and azimuth resolution. (b) Spotlight mode with shifting illumination in azimuth to observe a given region for a longer time: resolution is improved at the cost of a narrower swath in range and scene limitation in azimuth. (c) ScanSAR with cyclically alternating illumination of different sub-swaths. The instantly illuminated swath changes in slow time as indicated by the arrows and the operation introduces both restrictions on the illumination time (and thus azimuth resolution) and Doppler spectral gaps due to the partial illumination over time.

Spotlight (and Sliding Spotlight)

The Spotlight mode [26], [80] (cf. **Figure 9 (b)**) prioritizes azimuth resolution over coverage. The mode's name is based on the behavior of the antenna pattern in azimuth over the platform trajectory: steering is applied to shift the illumination so a region on ground is tracked by the azimuth antenna pattern. The rationale is to maximize the target observation time, allowing a higher azimuth resolution to be supported. The swath extension is however limited in range and azimuth. As the Doppler bandwidth is increased, processing usually requires more advanced focusing algorithms [80], able to cope with the highly squinted geometry.

An interesting observation scenario which takes the rationale of tracking a region on ground to maximize the acquired bandwidth to the limit is *Circular SAR* [81], [82], [83]. In this case, a (typically) airborne platform flies a circular path whereas keeping

the illumination fixed at a certain region on ground and the synthetic aperture is formed over the whole or part of the circular path. Though the geometry and signal properties differ, the extended illumination allows improving the resolution up to $\lambda/4$, thought the covered area is limited by the antenna footprint.

A more recent mode related to Spotlight is the *Sliding*[10] *Spotlight* [84], [85], [86], in which the steering rate is not fast enough to track a given area on ground (the pattern thus "slides" with respect to the imaged region), but still increases the illumination time and thus the maximum resolution. The properties of this mode are intermediate between the Spotlight and the Stripmap cases.

ScanSAR (and TOPS)

In contrary to Spotlight, the ScanSAR mode [87], [88] prioritizes swath width over azimuth resolution. The rationale is to alternately illuminate several sub-swaths in elevation, to get the combined swath width W_g, as seen in **Figure 9 (c)**. The illumination cycle timing has to be designed so that sufficient overlap in the azimuth illumination occurs between adjacent cycles. However, each sub-swath is covered by a burst of pulses whose PRF can be set independently, which allows a design in which the blind ranges of any given swath are covered by the other(s).

For each sub-swath, the illumination is restricted over slow time to a part of the cycle time, which introduces gaps in the Doppler spectrum, depending on the target position. This results in two important effects: first, reduced Doppler bandwidth due to the reduced illumination time in comparison to a Stripmap system, reducing the maximum azimuth resolution. Second, targets which are closest to the platform during the illumination of the other sub-swaths are only observed with squint, which introduces scalloping and has a negative impact on the overall performance.

[10] The original Spotlight mode is also referred to in the literature as *Staring Spotlight* mode, when the distinction is necessary.

The second effect can be countered by applying the Terrain Observation by Progressive Scans (TOPS) mode [89]. In this case, the azimuth antenna pattern's maximum is steered over slow time within each sub-swath in the opposite direction of a Spotlight. The beam is initially squinted to point backwards with respect to the trajectory and ends the cycle pointing forward. The goal is no longer to track a region on ground but to ensure every target in the sub-swath is illuminated by the main beam of the steered azimuth pattern at some point of the cycle, to equalize the performance and reduce the squint-induced scalloping. Thought more uniform over slow time, the SAR performance still presents a lower resolution in comparison to a Stripmap.

Advanced Concepts for HRWS: Overview

The imaging modes discussed so far explore the trade-off of Section 2.3.1 by prioritizing either swath width or azimuth resolution. Different alternatives described in [37], [38], [43], [44] show how a good performance in both aspects can be achieved simultaneously, generally requiring acquisition of the signal through multiple channels (at least in elevation), their independent digitization and suitable Digital Beamforming (DBF) techniques. In particular, [90] extends the aforementioned ScanSAR and TOPS to the multichannel configuration in azimuth, using the technique described in Section 3.2.

The most important concepts in the context of this thesis are briefly described in **Figure 10**. In **Figure 10 (a)**, a multichannel antenna in elevation allows the simultaneous formation of several beams through DBF. Each of them images a given sub-swath of the system, which allows extending the swath width without the downsides of the burst-mode operation of ScanSAR. The concept is especially suitable for combination with the Scan-on-Receive (SCORE) [46], [65] – also referred to as SweepSAR [91] – technique. The latter concept is related to [92], [93] and was further developed in [94], [95], [96]. The rationale is using a wide Tx beam, which is low-gain and prone to range ambiguity (cf. Section 2.3.1), but narrow high-gain time-variant Rx beams, following the position of the return echo on ground and ensuring a

better signal to noise ratio (SNR) than a fixed-beam system. In a single elevation beam system, the swath width (determined by the Tx pattern) is limited by the range ambiguity level. However, the range ambiguous returns (received simultaneously from different angles of arrival) may be distinguished by forming though DBF different narrow Rx beams, one for each of the relevant returns. These beams possess not only high gain but also low levels at the position of the range ambiguities, allowing the rejection of the range-ambiguous returns. The technique is referred to as Multi-SCORE [37], [44].

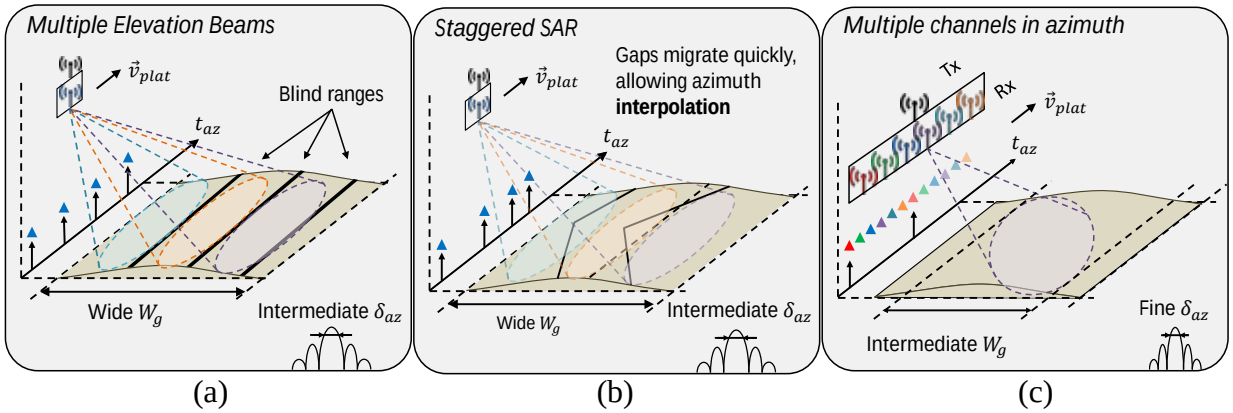

Figure 10. Overview of concepts for HRWS SAR imaging modes. (a) Multiple elevation beams allow simultaneous imaging of sub-swaths separated by blind ranges. This requires a multichannel antenna in elevation and a DBF-capable system but eliminates the downsides of the burst-mode operation (as e.g. in ScanSAR). (b) Staggered SAR in combination with multiple elevation beams allows spreading the regions whose echoes are blocked by Tx events over range in an azimuth-dependent form, so that interpolation may take place and fill the gaps over azimuth, yielding a wide continuous swath. (c) A system with multiple channels in azimuth has increased azimuth sampling for the same PRF, which relaxes the trade-off with the swath width by a factor the number of channels.

Multi-SCORE with a constant PRI still suffers from blind ranges (cf. Section 2.3.2), which separate the sub-swaths. Staggered SAR (cf. **Figure 10 (b)**) [41], [50], [53]-

[64] is a solution to eliminate the blind ranges[11]. The concept will be better explained in Section 3.3, but the rationale is to vary the PRI so as to induce a migration of the gaps due to Tx events (black lines in the figure) over azimuth. Even though the gaps still occur, they are located at different ranges for different pulses. For a fixed range the gap has a limited duration and can be filled by interpolation, given that the mean PRF provides enough oversampling. The concept allows imaging very wide swaths, though the best azimuth resolution is subject to limitations, since a single channel in azimuth is available.

Another important HRWS system concept – described in Section 3.2 in more detail – is based on the use of multiple azimuth channels, independently digitized on receive [39], [47], [51]. As represented in **Figure 10 (c)**, a system with N_{ch} channels in azimuth gathers as many samples per transmitted pulse, and thus the sampling rate becomes $PRF_{multi} = N_{ch} \cdot PRF$.Fulfilling the Nyquist sampling thus requires that $PRF \geq Bw_{az}/N_{ch}$, which relaxes (14) by a factor of N_{ch}. The PRF can thus be set lower without affecting the resolution, allowing a wider swath to be imaged in Stripmap mode (cf. (13), which is still valid for each channel). In practice however the PRF cannot be set arbitrarily low, as a lower PRF requires a larger azimuth antenna (cf. [43], [44], (27)), and the system concept is better suited to provide high resolution over moderately wide swaths.

Starting from the next chapter, the two latter alternatives will be described in more detail, aiming at the development of Multichannel Staggered SAR in Azimuth (cf. Chapter 4), which combines the strengths of both methods to fulfill unprecedented HRWS imaging requirements.

[11] In general , PRI variation is the key to eliminate blind ranges, though several strategies are possible. In the conventional ScanSAR system, the PRI changes over a very limited set of values. Staggered SAR represents a fast variation of the PRI following a more sophisticated strategy, though intermediate solutions such as a slow PRI variation (cf. [97]) are possible.

2.5 Remarks on Conventional SAR

This chapter introduced the basics of SAR (Section 2.2) and discussed some limitations of conventional SAR systems (Section 2.3) which are important for the understanding of HRWS techniques. In particular, range and azimuth ambiguities (and their implications for the trade-off between azimuth resolution and swath width) were addressed (Section 2.3.1); alongside blind ranges (Section 2.3.2).

In the following, an overview of the classical Stripmap, Spotlight and ScanSAR modes (Section 2.4) was presented, to illustrate the trade-offs in system design. Finally, a basic description of alternatives to overcome the aforementioned limitations by design of more advanced multichannel systems relying on DBF was discussed. This description will be deepened next in Chapter 3, focusing on multichannel SAR in azimuth and Staggered SAR, which will be combined in Chapter 4.

3 HRWS SAR

3.1 Chapter Overview

This chapter discusses in more detail techniques suitable to overcome the compromise between swath-width and azimuth resolution, which is imposed on single channel SAR systems (cf. Sections 2.3 and 2.4). SAR with multiple channels in azimuth and Staggered SAR are presented separately in a first step. The goal is to establish the concepts necessary to posteriorly combine both techniques into the proposed Multichannel Staggered SAR operation (cf. Chapter 4).

Section 3.2 presents techniques for the use of multiple channels in azimuth: acquiring the signal over multiple receivers decouples the signal's sampling rate (and therefore the best achievable resolution) and the PRF. This in turn allows, under certain limits, to achieve a fine azimuth resolution with a low PRF, which eases the constraint on the non-ambiguous swath width. The techniques rely on DBF to obtain an equivalent single-channel signal sampled at a higher rate from the multichannel data, so that conventional focusing can be applied after resampling.

Section 3.3 describes the Staggered SAR technique, with emphasis on an analysis of staggered PRI sequences and their timing. The timing analysis discussed in Section 3.3.2 is important for the resampling techniques discussed in Chapter 4. Sequence design is the topic of [41], [53], [62], [63]. Section 3.3.3 briefly presents the most important criterion, which will be used in order to design the PRI sequences according to the swath parameters in the examples in Chapters 5, 6 and 7.

3.2 Multichannel SAR in Azimuth

In the following, a system with one Tx and N_{ch} Rx azimuth channels is considered. As described in [39], [47]-[49], [51] in detail, if the sampling of each of the individual channels occurs at a rate of PRF, the effective sampling of the equivalent monostatic system is $PRF_{multi} = N_{ch} \cdot PRF$, as N_{ch} samples are recorded for each received pulse. Thus, a complex bandlimited signal spectrum $U(f_{\mathrm{D}})$ may be recovered

unambiguously, as long as the Doppler bandwidth is $Bw_{az} \leq N_{ch} \cdot PRF$. This is achieved by proper combination of the aliased spectra of each of the channels in the frequency domain, as illustrated in **Figure 11**. In the block diagram, the channels are described by transfer functions $H_k(f_\mathrm{D})$ and the (sub-)sampled signals from the individual channels $Y_k(f_\mathrm{D})$ are processed using the filters $P_k(f_\mathrm{D})$, for $1 \leq k \leq N_{ch}$. The rationale of increased sampling by means of multichannel systems is first described in [98], [99].

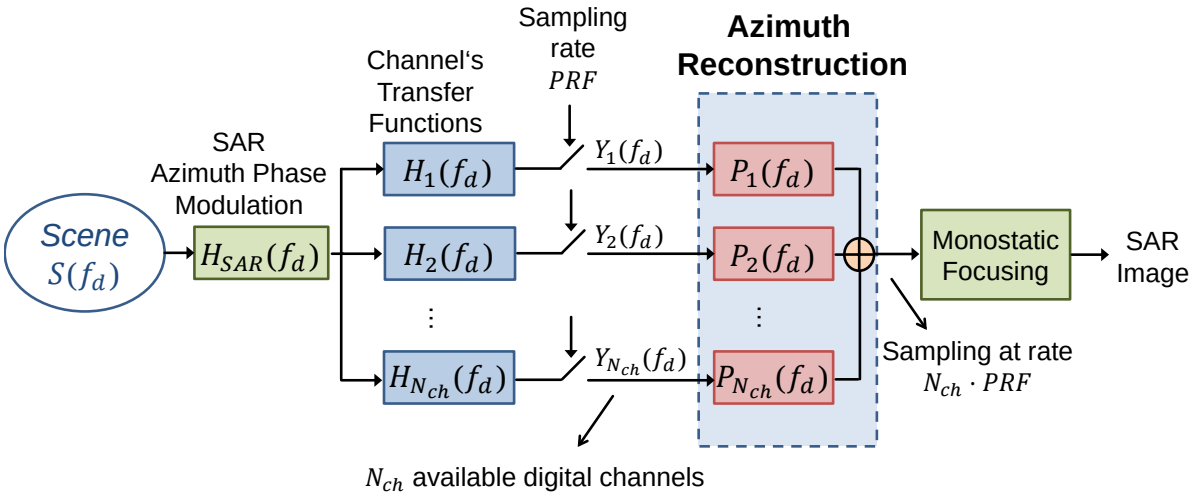

Figure 11. Basic system configuration for multichannel reconstruction in azimuth. N_{ch} channels sampled individually at rate PRF are combined in frequency domain to generate an equivalent single-channel signal in a finer grid, sampled at $N_{ch} \cdot PRF$.

The k-th azimuth channel is considered to be described by the transfer function $H_k(f_\mathrm{D})$ and the complete spectrum of the scene is denoted $U(f_\mathrm{D})$, with frequency support in $[-N_s \cdot \frac{PRF}{2}, N_s \cdot \frac{PRF}{2}]$. For generality, assume the total signal bandwidth $Bw_{az} = N_s \cdot PRF \leq N_{ch} \cdot PRF$ to be divided into N_s contiguous sub-bands I_m of bandwidth PRF, with $N_s \leq N_{ch}$ (thus allowing for oversampling). The first sub-band is $I_1 = [-N_s \cdot \frac{PRF}{2}, -N_s \cdot \frac{PRF}{2} + PRF]$, so that $I_m = I_1 + (m-1) \cdot PRF$, $1 \leq m \leq N_s$. Due to the aliasing, the signal spectrum of the channels may be represented in any interval of length PRF, taken here to be I_1. Correspondingly, let the N_s signals of bandwidth PRF be denoted $S_m(f) = U(f_\mathrm{D} + (m-1) \cdot PRF)$, for f_D in I_1. These

signals can be regarded as azimuth *looks* of the SAR image, in accordance with typical SAR processing nomenclature.

Considering that the *k*-th azimuth channel is positioned at $\Delta x_{k,}$ and that the platform velocity in along-track is v_{plat}, the channel transfer function in frequency domain after a Taylor expansion may be approximated by [51]:

$$H_k(f_\mathrm{D}) = A_k(f_\mathrm{D}) \cdot \exp(-\mathrm{j} \cdot \Delta\phi_k) \cdot \exp(-\mathrm{j} \cdot 2 \cdot \pi \cdot \Delta t_k \cdot f_\mathrm{D}), \tag{20}$$

where $\Delta t_k = \frac{\Delta x_k}{2 \cdot v_{plat}}$ are the delays induced by the phase center baselines; $\Delta\phi_k$ is a constant phase term given by

$$\Delta\phi_k = \frac{v_{ground}}{v_{plat}} \cdot \frac{\pi \cdot \Delta x_k^2}{2 \cdot \lambda \cdot R_0} \tag{21}$$

and $A_k(f_\mathrm{D})$ accounts for possibly different antenna patterns for each element. Typically, for planar antenna arrays, the patterns $A_k(f_\mathrm{D})$ are the same for all elements and can be factored out of the description ($A_k(f_\mathrm{D}) = 1$ is used), even though this is not mandatory. Thus, the elements spacing and the resulting phase center position define the channels. In contrast, for reflector systems with a multichannel feed, the phase centers coincide for all elements (cf. Section 4.3, [100]) and no baseline between elements is expected ($\Delta x_k = 0$ is used), whereas $A_k(f_\mathrm{D})$ are different from element to element and must be taken into account.

Considering the sub-band division, the multichannel system may be described in frequency domain by the N_{ch} x N_s matrix $\boldsymbol{H}(f_\mathrm{D})$ with elements $H_{kl}(f_\mathrm{D}) = H_k(f_\mathrm{D} + (l-1) \cdot PRF)$ and the sub-sampled signal at each channel *k* by

$$Y_k\ (f) = \sum_{m=1}^{N} H_k(f_\mathrm{D} + (m-1) \cdot PRF)\ \cdot S_m(f_\mathrm{D}), \tag{22}$$

accounting for the aliasing with respect to PRF. Consequently, in matrix notation,

$$\begin{bmatrix} Y_1\ (f_\mathrm{D}) \\ Y_2\ (f_\mathrm{D}) \\ \vdots \\ Y_{N_{ch}}(f_\mathrm{D}) \end{bmatrix}_{N_{ch}x1} = \boldsymbol{H}(f_\mathrm{D})_{N_{ch}xN_s} \cdot \begin{bmatrix} S_1(f_\mathrm{D}) \\ S_2(f_\mathrm{D}) \\ \vdots \\ S_{N_s}(f_\mathrm{D}) \end{bmatrix}_{N_s x1} \tag{23}$$

$$\underline{\boldsymbol{Y}}(f_\mathrm{D})_{N_{ch}x1} = \boldsymbol{H}(f_\mathrm{D})_{N_{ch}xN_s} \cdot \underline{\boldsymbol{S}}(f_\mathrm{D})_{N_s x1}.$$

Reconstruction can be regarded as an estimator

$$\widehat{\underline{\boldsymbol{S}}}(f_\mathrm{D})_{N_s x1} = \boldsymbol{P}(f_\mathrm{D})_{N_s xN_{ch}} \cdot \underline{\boldsymbol{Y}}(f_\mathrm{D})_{N_{ch}x1}, \tag{24}$$

where the filter matrix has entries

$$P_{mk}(f_\mathrm{D}) = P_k(f_\mathrm{D} + (m-1) \cdot PRF) \tag{25}$$

and hence each *look* $S_m(f_\mathrm{D})$ is recovered by means of row m of matrix $\boldsymbol{P}(f_\mathrm{D})$, and each column of it is applied to a particular channel k.

Different reconstruction schemes are analyzed and compared in [48], [49], from which an overview is provided. Taking $\boldsymbol{P}(f_\mathrm{D}) = \boldsymbol{H}^H(f_\mathrm{D})$ is referred to as the Maximum Signal Method and guarantees a coherent sum of the signal, however not cancelling the ambiguities. In the planar antenna case (with phase-only transfer functions), this can be interpreted as a phase compensation by the baseline and amounts to interleaving the samples.

In particular, if $N_s = N_{ch}$, then $\boldsymbol{P}(f_\mathrm{D}) = \boldsymbol{H}(f_\mathrm{D})^{-1}$, which is the Multichannel Reconstruction Algorithm (MCRA) as proposed in [51], yielding ideal reconstruction of the bandlimited signal in the noiseless case. This configuration makes complete usage of the multichannel sampling and can be shown to be optimal in a mean square error (MSE) sense even in the presence of noise and a non-bandlimited spectrum [101], [102]. The limitation is that the matrix $\boldsymbol{H}(f_\mathrm{D})$ must be invertible, which translates into non-coinciding (or not too similar) channels. In practice, however, invertibility is not the major concern. Since the signal model (22) is noiseless, the

noise scaling of the reconstruction filter (described in [51] and [101], [102] in different but equivalent terms) is usually the limiting factor. The performance degradation can nonetheless be kept under certain bounds by proper design of the system parameters, what usually translates into bounds for the maximum allowable deviation from the uniform sampling condition. The latter is given by

$$\Delta x_k = k \cdot \frac{2 \cdot v_{plat}}{N_{ch} \cdot PRF}, \tag{26}$$

and represents a particular case in which the spatial sampling due to the baselines directly generates regular samples at a rate $N_{ch} \cdot PRF$. These can be simply interleaved to generate the equivalent single channel with a finer grid. Note that (5) implies that the total aperture length is of size

$$l_{az} = \frac{2 \cdot v_{plat}}{PRF}. \tag{27}$$

Since in practice multichannel systems in azimuth do not deviate too strongly from the uniform condition, to avoid severe SNR degradation, (27) may be used to estimate the antenna size for this class of system [44]. Combining (27) and (13) yields

$$W_g < \frac{c \cdot l_{az}}{4 \cdot v_{plat} \cdot \sin(\eta_{inc})}, \tag{28}$$

showing that the minimum PRF (and thus the maximum swath width) is subject to a bound of practical nature, as the deployment of a very long antenna in space can be impractical or too costly. For instance, to keep the antenna length smaller than 20 m, assuming $v_{sat} = 7$ km/s and $\eta_{inc} = 45°$, the maximum swath width becomes limited to 303 km. Conversely, a 26.4 m long antenna operated at $PRF = 433$ Hz would be required to achieve a swath of 400 km.

In the non-square case, $N_s < N_{ch}$, particular sub-bands can be retrieved by Gram-Schmitt orthogonal projection or equivalently using the Moore-Penrose

pseudoinverse[12], $\boldsymbol{P}(f_{\mathrm{D}}) = \boldsymbol{H}^{\dagger}(f_{\mathrm{D}})$, which is referred to in [49] as the projection method.

In [48], [49], the model (22), (23) is augmented to account for noise by taking

$$\underline{\boldsymbol{Y}}(f_{\mathrm{D}})_{N_{ch}x1} = \boldsymbol{H}(f_{\mathrm{D}})_{N_{ch}xN_s} \cdot \underline{\boldsymbol{S}}(f_{\mathrm{D}})_{N_s x1} + \underline{\boldsymbol{n}}(f_{\mathrm{D}})_{N_s x1} \,. \tag{29}$$

Assuming the signal to be uncorrelated between non-overlapping *looks* (which is a default assumption in SAR literature [26]) and the noise $\underline{\boldsymbol{n}}(f_{\mathrm{D}})$ to be white and uncorrelated between channels, the normalized (divided by σ_s^2) covariance matrix of $\underline{\boldsymbol{Y}}$ can be shown to be [48]

$$\boldsymbol{R}(f_{\mathrm{D}}) = \boldsymbol{R}_{\underline{\boldsymbol{Y}}\underline{\boldsymbol{Y}}}(f_{\mathrm{D}}) = \boldsymbol{H}^{H}(f_{\mathrm{D}}) \cdot \boldsymbol{H}(f_{\mathrm{D}}) + \frac{\sigma_n^2}{\sigma_s^2} \cdot \boldsymbol{I}_{N_{ch}}, \tag{30}$$

where σ_n^2 is the noise power, σ_s^2 is the signal power within each look (assumed to be the same for all of them) and $\boldsymbol{I}_{N_{ch}}$ is the N_{ch} by N_{ch} identity matrix. Notice the first term is the contribution from the signal, whereas the second is the noise covariance matrix.

The Minimum Mean Square Error (MMSE) approach proposed in [48] is to select the filters $\boldsymbol{P}(f_{\mathrm{D}})$ so that $\left\|\underline{\widehat{\boldsymbol{S}}}(f_{\mathrm{D}}) - \underline{\boldsymbol{S}}(f_{\mathrm{D}})\right\|^2$ is minimized, which in principle does not require the signal to be bandlimited (i.e. $N_s > N_{ch}$ could also be accommodated by the formulation). The solution is found to be

$$\boldsymbol{P}(f_{\mathrm{D}}) = \boldsymbol{H}^{H}(f_{\mathrm{D}}) \cdot \boldsymbol{R}^{-1}(f_{\mathrm{D}}) = \boldsymbol{H}^{H}(f_{\mathrm{D}}) \cdot \left(\boldsymbol{H}^{H}(f_{\mathrm{D}}) \cdot \boldsymbol{H}(f_{\mathrm{D}}) + \frac{\sigma_n^2}{\sigma_s^2} \cdot \boldsymbol{I}_{N_{ch}}\right)^{-1}. \tag{31}$$

In particular, if $\frac{\sigma_n^2}{\sigma_s^2} \to 0$ (the noiseless case), $\boldsymbol{P}(f_{\mathrm{D}}) = \boldsymbol{H}^{\dagger}(f_{\mathrm{D}})$ and therefore the solution is equivalent to the Multichannel Reconstruction Algorithm (or the Projection

[12] $\boldsymbol{H}^{\dagger}(f_d) = \boldsymbol{H}^{\mathrm{H}}(f_d) \cdot \left(\boldsymbol{H}(f_d) \cdot \boldsymbol{H}^{\mathrm{H}}(f_d)\right)^{-1}$, as long as $\boldsymbol{H}(f_d) \cdot \boldsymbol{H}^{\mathrm{H}}(f_d)$ is invertible.

Method, if the matrix is not square). Otherwise, the channel's covariance matrix is seen to be a combination of the signal and the noise components, weighted by the inverse of the signal to noise ratio (SNR). A variation of the MMSE method proposed in the same paper is:

$$\boldsymbol{P}(f_{\mathrm{D}}) = \boldsymbol{H}^{H}(f_{\mathrm{D}}) \cdot \widetilde{\boldsymbol{R}}^{-1}(f_{\mathrm{D}}), \tag{32}$$

analogous to (31), with the modified covariance matrix

$$\widetilde{\boldsymbol{R}}(f_{\mathrm{D}}) = \boldsymbol{H}^{H}(f_{\mathrm{D}}) \cdot \boldsymbol{H}(f_{\mathrm{D}}) + \frac{1-q}{q} \cdot \frac{\sigma_n^2}{\sigma_s^2} \cdot \boldsymbol{I}_{N_{ch}}, \tag{33}$$

where $0 \leq q \leq 1$ is a degree of freedom to allow obtaining a solution either closer to the optimal ambiguity suppression (the Multichannel Reconstruction Algorithm) or rejecting more noise at the price of worst ambiguity levels. Changing q is analogous to over- or underestimating the signal to noise ratio $\frac{\sigma_s^2}{\sigma_n^2}$.

The Maximum Signal to Ambiguity and Noise Ratio (MSANR) approach proposed in [49] applies Space-Time Adaptive Processing (STAP) concepts, specifically interference rejection, to the reconstruction problem. Let $\underline{\boldsymbol{h}}_m(f_{\mathrm{D}})$ and $\underline{\boldsymbol{p}}_m(f_{\mathrm{D}})$ be N_{ch} element column vectors describing respectively the m^{th} column of the N_{ch} x N_s system matrix $\boldsymbol{H}(f_{\mathrm{D}})$ and the m^{th} row of the N_{ch} x N_s filter matrix $\boldsymbol{P}(f_{\mathrm{D}})$. The index m within $1 \leq m \leq N_s$ denotes the sub-band. Then, (29) can be rewritten as

$$\hat{s}_m(f_{\mathrm{D}}) = \underline{\boldsymbol{p}}_m^{H}(f_{\mathrm{D}}) \cdot \underline{\boldsymbol{h}}_m(f_{\mathrm{D}}) \cdot s_m(f_{\mathrm{D}}) + \sum_{\substack{i=1 \\ i \neq m}}^{N_s} \underline{\boldsymbol{p}}_i^{H}(f_{\mathrm{D}}) \cdot \underline{\boldsymbol{h}}_i\ (f_{\mathrm{D}}) \cdot s_i(f_{\mathrm{D}}) + n_m(f_{\mathrm{D}}) \tag{34}$$

where $\hat{s}_m(f_{\mathrm{D}})$, $s_m(f_{\mathrm{D}})$ and $n_m(f_{\mathrm{D}})$ are entries of the column vectors $\underline{\widehat{\boldsymbol{S}}}(f_{\mathrm{D}})$, $\underline{\boldsymbol{S}}(f_{\mathrm{D}})$ and $\underline{\boldsymbol{n}}(f_{\mathrm{D}})$, respectively, for $1 \leq m \leq N_s$. Note that the first term in the summation (34) gives the signal of interest, the second the ambiguities (signal corresponding to the wrong sub-bands), and the third represents the noise. The second and third terms are

undesired and can be regarded as interferences. Defining the normalized (again divided by σ_s^2) interference covariance matrix, for the m^{th} sub-band as

$$\boldsymbol{R}_m^{interf}(f_{\mathrm{D}}) = \boldsymbol{H}^H(f_{\mathrm{D}}) \cdot \boldsymbol{H}(f_{\mathrm{D}}) - \underline{\boldsymbol{h}}_m(f_{\mathrm{D}}) \cdot \underline{\boldsymbol{h}}_m(f_{\mathrm{D}}), \tag{35}$$

one may write the following expression for the reconstructed signal power:

$$E\left[\hat{s}_m^* \cdot \hat{s}_m\right](f_{\mathrm{D}}) = \sigma_s^2 \cdot \left|\underline{\boldsymbol{p}}_m^H(f_{\mathrm{D}}) \cdot \underline{\boldsymbol{h}}_m(f_{\mathrm{D}})\right|^2 + \underline{\boldsymbol{p}}_m^H(f_{\mathrm{D}}) \cdot \boldsymbol{R}_m^{interf}(f_{\mathrm{D}}) \cdot \underline{\boldsymbol{p}}_m(f_{\mathrm{D}}), \tag{36}$$

using the assumption that the signals $s_m(f_{\mathrm{D}})$ are mutually uncorrelated and also uncorrelated with the noise.

The first term in the summation (36) can be identified as the unambiguous signal power, whereas the second term is the power of ambiguities plus noise. The criterion proposed for the choice of the weights at the m^{th} sub-band is to maximize the ratio

$$SANR_m = \frac{\left|\underline{\boldsymbol{p}}_m^H(f_{\mathrm{D}}) \cdot \underline{\boldsymbol{h}}_m(f_{\mathrm{D}})\right|^2}{\underline{\boldsymbol{p}}_m^H(f_{\mathrm{D}}) \cdot \boldsymbol{R}_m^{interf}(f_{\mathrm{D}}) \cdot \underline{\boldsymbol{p}}_m(f_{\mathrm{D}})}. \tag{37}$$

As derived in the same paper, the solution is to apply the Cauchy-Schwartz inequality to the vector inner product $\langle \underline{\boldsymbol{x}}, \underline{\boldsymbol{y}} \rangle = \underline{\boldsymbol{x}}^H \cdot \boldsymbol{R}_m^{interf}(f_{\mathrm{D}}) \cdot \underline{\boldsymbol{y}}$, yielding the optimum weights for each sub-band, $1 \leq m \leq N_s$:

$$\underline{\boldsymbol{p}}_m^{SANR}(f_{\mathrm{D}}) = \frac{1}{\sqrt{\underline{\boldsymbol{h}}_m^H(f_{\mathrm{D}}) \cdot \left(\boldsymbol{R}_m^{interf}(f_{\mathrm{D}})\right)^{-1} \cdot \underline{\boldsymbol{h}}_m(f_{\mathrm{D}})}} \cdot \left(\boldsymbol{R}_m^{interf}(f_{\mathrm{D}})\right)^{-1} \cdot \underline{\boldsymbol{h}}_m(f_{\mathrm{D}}). \tag{38}$$

The result can be conceptually understood as a projection in the subspace orthogonal to the interference's (ambiguities plus noise) subspace, which is spanned by the eigenvalues of the interference covariance matrix of (35). The method is thus in essence related to the previous ones and also coincides with the Projection / MCRA methods in the noiseless case.

This concludes the overview of multichannel techniques, which are seen to assume a constant PRF and also to involve filters modeled and applied in frequency domain to achieve signals sampled at $N_{ch} \cdot PRF$, following different criteria. Next, Section 3.3 turns focus to another HRWS technique, namely Staggered SAR, paving the way to the combination of both techniques in Chapter 4.

3.3 Staggered SAR

3.3.1 Rationale and Motivation

In the discussion of blind ranges in Section 2.3.2, it became apparent that the regular repetition of pulse transmissions according to PRF leads to a pattern of blockage of pulses backscattered by specific ranges along the swath, effectively separating it into multiple sub-swathes. Moreover, the regularity of the transmit events means the blocked ranges are the same for every pulse, and hence no information is retrieved from these, which then become *blind ranges*. The blockage in fact cannot be avoided in monostatic systems. However, by avoiding the PRF regularity, one would be able to change the position of the blocked ranges from pulse to pulse, and thus avoid complete loss of information from specific ranges along the swath. This concept is the basic rationale for Staggered SAR [41], [50], [53]-[64], and is illustrated for a simple example sequence of variable PRIs in **Figure 12**. For an arbitrary swath geometry, in **Figure 12 (a)**, the regions of pulse blockage migrate from pulse to pulse, as highlighted in **Figure 12 (b).** Moreover, the rate of migration is determined by how fast the change in the PRIs occurs, as suggested by **Figure 12 (c)**. The blockage and corresponding loss of information after each pulse is unavoidable, but the loss may be distributed along the ranges of the swath so that e.g. ranges for which all pulses are lost no longer exist. For instance, in the case of **Figure 12 (c),** the range corresponding to the vertical dashed line is blocked for the second pulse but not for the first or the third ones and thus data from this range can be obtained in spite of the local gap. Note that the gaps caused by Tx still exist but no longer cause a *blind range*.

In the next section, the PRI sequences will be formally defined and mathematical properties of their delays, which are useful as tools for timing analysis, will be derived.

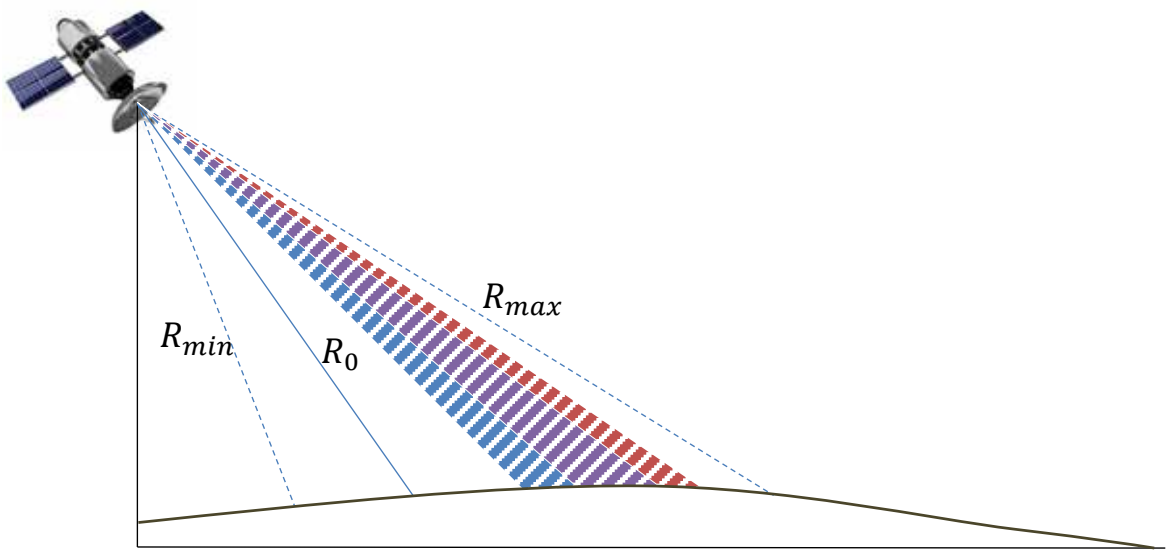

(a)

Rx pulse **loss** is pulse dependent: migration of *blocked ranges*

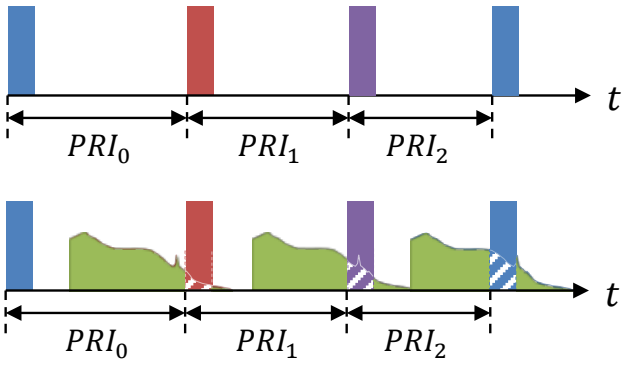

(b)

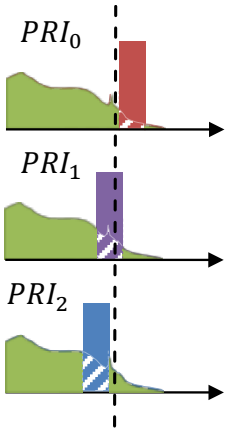

(c)

Figure 12. Conceptual illustration of blind range migration in the case of operation with varying PRIs in an arbitrary swath geometry (a). Due to the irregular transmit events, the interval of ranges which are not recorded changes from pulse to pulse (b), meaning that returns from specific ranges are lost for some but not all pulses (c) and therefore some information from all ranges in the swath can be retrieved.

3.3.2 Definition and Timing Analysis of PRI Sequences

Definition of Sequences and Notation

Basically, the Staggered SAR technique consists in the use of variable PRIs instead of a uniform PRI for all pulses. Even though a myriad of possible choices for the PRI present themselves – including even random PRIs [61], the choice of a linearly varying PRI is of particular interest due to its simplicity, and will be adopted in the following analysis.

Assume a linearly varying PRI sequence of length N_{PRI}, with an initial PRI_0 and a step Δ_{PRI} (positive or negative) between adjacent PRIs, leading to the expression

$$PRI_n = PRI_0 + n \cdot \Delta_{PRI} \tag{39}$$

for the n^{th} PRI, $0 \leq n \leq N_{PRI} - 1$. For other values of the pulse index n, the sequence of PRI's repeats itself with period

$$T_{PRI} = \sum_{n=0}^{N_{PRI}-1} PRI_n = N_{PRI} \cdot PRI_0 + N_{PRI} \cdot \frac{(N_{PRI} - 1)}{2} \cdot \Delta_{PRI} \tag{40}$$

and is characterized by a mean PRI given by

$$\overline{PRI} = \frac{T_{PRI}}{N_{PRI}} = PRI_0 + \frac{N_{PRI}-1}{2} \cdot \Delta_{PRI}. \tag{41}$$

Such a definition leads to a sampling scheme in azimuth which is referred to in the literature as *periodic (recurrent) non-uniform sampling* [102], [103].

Delays between Pulses and Basic Properties

At this point, it is useful to define the time elapsed between pulses i and $i + k$ as

$$d_{i,k} = \sum_{n=i-1}^{i+k-2} PRI_n, \tag{42}$$

a quantity which represents the delay of order k starting from the begin of pulse i of the PRI sequence. For clarity, this definition is illustrated by means of examples in **Figure 13**, where **Figure 13 (a)** gives a simple example in the beginning of a sequence, whereas **Figure 13 (b)** illustrates an example in the end of a PRI cycle. The latter illustrates two important effects: the cyclical repetition of the PRIs and also the property that $d_{i,k}$ is not monotonic with i, but suffers a discontinuity when the window of k pulses enters the next cycle.

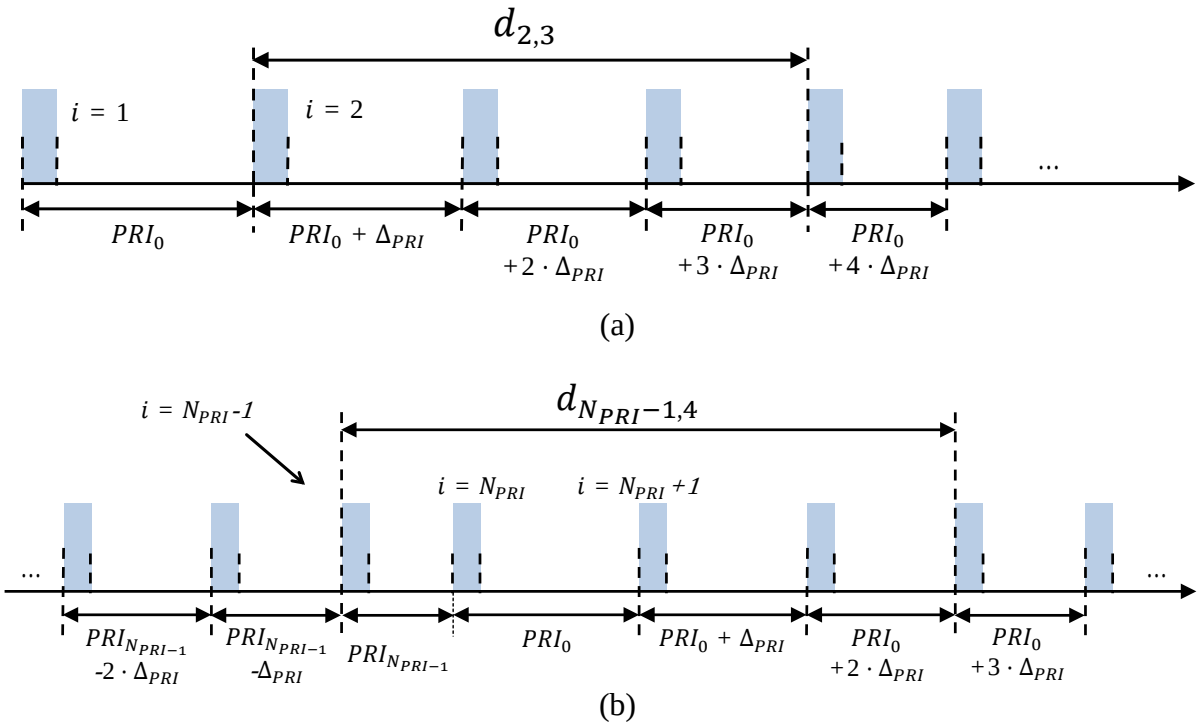

Figure 13. Examples illustrating the definition of $d_{i,k}$.(a) Delay of order 3 starting from pulse index 2, i.e. $d_{2,3}$. (b) Delay of order 4 starting from pulse index $N_{PRI} - 1$, $d_{N_{PRI}-1,4}$, illustrating sequence repetition in a new cycle.

In the following, this and other mathematical properties of the delays $d_{i,k}$ will be derived. These properties are an important tool for timing analysis, since these delays translate directly into the position of the gaps caused by Tx events in the case of staggered SAR, as will be explained.

Due to the periodicity of the PRI sequence, it is enough to analyze the cases $1 \leq i,k \leq N_{PRI}$, since for integer n and m

$$d_{i+n\cdot N_{PRI},\ k+m\cdot N_{PRI}} = d_{i,k} + m \cdot T_{PRI}. \tag{43}$$

To perform the summation in (42), it is helpful to consider two distinct cases. If $i + k - 2 \leq N_{PRI} - 1$, the summation index *n* is always within a cycle of PRIs, and no folding of the sequence occurs. Hence,

$$d_{i,k} = \sum_{n=i-1}^{i+k-2} PRI_0 + n \cdot \Delta_{PRI} = k \cdot PRI_0 + \frac{\Delta_{PRI}}{2} \cdot (2 \cdot i + k - 3) \cdot k, \tag{44}$$

for $i + k \leq N_{PRI} + 1$.

However, when $i + k - 2 > N_{PRI} - 1$, summation occurs over the next PRI sequence as well, so that the sum can be split into two terms, the first covering a first interval from the pulse *i* until the end of the sequence and another from the beginning of the next sequence until the end of the count, determined by *i* and *k*. This is equivalent to the sum of the whole sequence minus a summation between the aforementioned intervals. One can therefore write

$$d_{i,k} = \sum_{n=i-1}^{N_{PRI}} PRI_n + \sum_{n=0}^{i+k-2-N_{PRI}} PRI_n = T_{PRI} - \sum_{n=i+k-1-N_{PRI}}^{N_{PRI}-1} PRI_0 + n \cdot \Delta_{PRI}$$

$$d_{i,k} = T_{PRI} - (N_{PRI} - k) \cdot PRI_0 - \frac{\Delta_{PRI}}{2} \cdot (2 \cdot i + k - N_{PRI} - 3) \cdot (N_{PRI} - k) \tag{45}$$

To summarize the results, one may write

$$d_{i,k} = \begin{cases} k \cdot PRI_0 + \dfrac{\Delta_{PRI}}{2} \cdot (2 \cdot i + k - 3) \cdot k, \\ \text{for } 1 \leq i \leq N_{PRI} + 1 - k; \\ T_{PRI} - (N_{PRI} - k) \cdot PRI_0 - \dfrac{\Delta_{PRI}}{2} \cdot (2 \cdot i + k - N_{PRI} - 3) \cdot (N_{PRI} - k), \\ \text{for } N_{PRI} + 2 - k \leq i \leq N_{PRI}. \end{cases} \tag{46}$$

A similar analysis was performed in [50], in which emphasis is however placed on the recurrence relations leading to (46). A schematic plot of the delays $d_{i,k}$ is depicted in **Figure 14** to highlight their expected behavior and illustrate some properties discussed in the following.

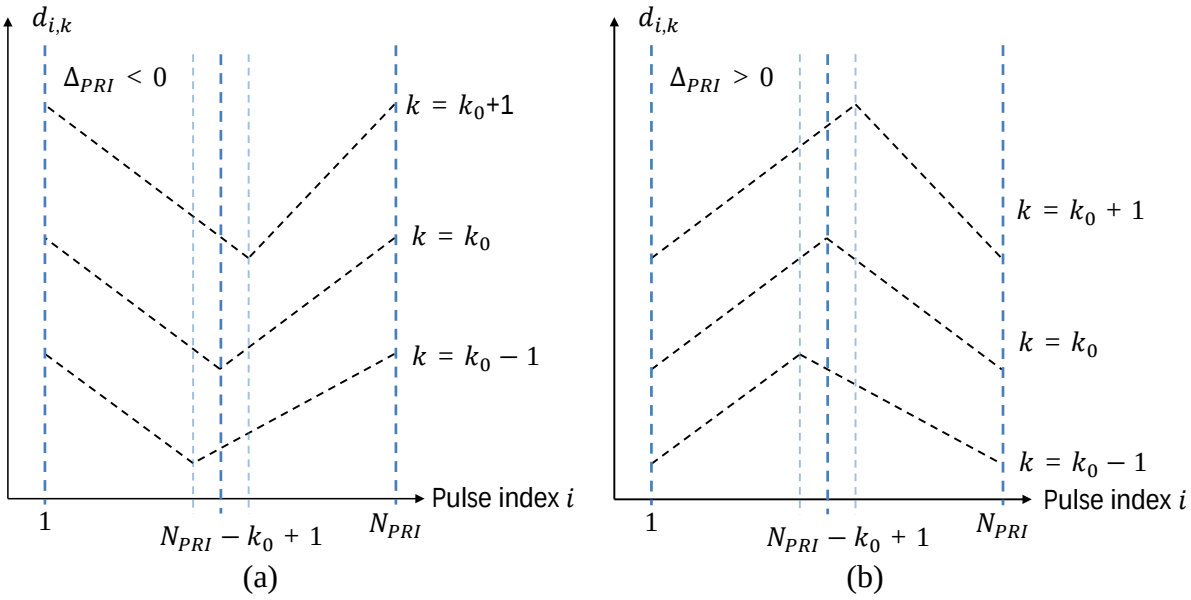

Figure 14. Schematic representation of $d_{i,k}$ over all sequence indices of i for neighboring orders around a fixed k_0, highlighting the behavior of the delay term. (a) $\Delta_{PRI} < 0$. (b) $\Delta_{PRI} < 0$.

As visible from **Figure 14**, there is a discontinuity between $i + k = N_{PRI} + 1$ and $i + k = N_{PRI} + 2$, which corresponds to the begin of a new period of the PRI sequence and hence a jump in the delay value (cf. **Figure 13 (b)**). Thus the pulse index immediately before the discontinuity, $i_{break} = N_{PRI} - k + 1$, thus defines two distinct regions for the delay pattern $d_{i,k}$. For a given delay of order k one may also note that

$$d_{i+1,k} - d_{i,k} = \begin{cases} k \cdot \Delta_{PRI}, & \text{for } 1 \le i \le i_{break} - 1; \\ -\Delta_{PRI} \cdot (N_{PRI} - k), & \text{for } i_{break} \le i \le N_{PRI}. \end{cases} \quad (47)$$

Inserting i_{break} into (47) yields $d_{i_{break}+1,k} - d_{i_{break},k} = -\Delta_{PRI} \cdot (N_{PRI} - k)$, hence the delay variation between pulses in the discontinuity is the same as in the second region. Next, (47) will be used to obtain the minimum and maximum of $d_{i,k}$.

Since the delay variation in (47) follows the sign of the step Δ_{PRI}, one may conclude that if $\Delta_{PRI} < 0$, the delay $d_{i,k}$ decreases with the pulse index *i* until it starts increasing again, after the discontinuity. Therefore, $d_{i_{break},k} = d_{N_{PRI}-k+1,k}$ is a minimum for the delays of order *k*. In turn, the maximum must lie in one of the extremes $d_{1,k}$ or $d_{N_{PRI},k}$. From (46) and (40) one has

$$d_{1,k} - d_{N_{PRI},k} = k \cdot PRI_0 + \frac{\Delta_{PRI}}{2} \cdot (k-1) \cdot k +$$

$$(-k) \cdot PRI_0 + \frac{\Delta_{PRI}}{2} \cdot \left(-N_{PRI} \cdot (N_{PRI} - 1) + (k + N_{PRI} - 3) \cdot (N_{PRI} - k)\right)$$

$$d_{1,k} - d_{N_{PRI},k} = \frac{\Delta_{PRI}}{2} \cdot (N_{PRI} - k) \cdot (-2)$$

$$d_{1,k} - d_{N_{PRI},k} = -\Delta_{PRI} \cdot (N_{PRI} - k), \quad (48)$$

which has the opposite sign as Δ_{PRI}, meaning $d_{1,k} > d_{N_{PRI},k}$ for negative Δ_{PRI}. This allows the conclusion that $d_{1,k}$ is the maximum in this case.

Conversely, for $\Delta_{PRI} > 0$, a similar analysis can be performed, with the opposite signs, yielding that $d_{N_{PRI}-k+1,k}$ is a maximum, and $d_{1,k}$, a minimum. These relations can be consolidated for later reference as

$$d_{min}(k) = \min_i \{d_i, k\} = \begin{cases} d_{N_{PRI}-k+1,k} & \Delta_{PRI} < 0 \\ d_{1,k} & \Delta_{PRI} > 0 \end{cases}, \quad (49)$$

$$d_{max}(k) = \max_i \{d_i, k\} = \begin{cases} d_{1,k} & \Delta_{PRI} < 0 \\ d_{N_{PRI}-k+1,k} & \Delta_{PRI} > 0 \end{cases}.$$

$$d_{min}(k) = \begin{cases} k \cdot PRI_0 + \frac{\Delta_{PRI}}{2} \cdot (2 \cdot N_{PRI} - k - 1) \cdot k & \Delta_{PRI} < 0 \\ k \cdot PRI_0 + \frac{\Delta_{PRI}}{2} \cdot (k-1) \cdot k & \Delta_{PRI} > 0 \end{cases},$$

$$d_{max}(k) = \begin{cases} k \cdot PRI_0 + \frac{\Delta_{PRI}}{2} \cdot (k-1) \cdot k & \Delta_{PRI} < 0 \\ k \cdot PRI_0 + \frac{\Delta_{PRI}}{2} \cdot (2 \cdot N_{PRI} - k - 1) \cdot k & \Delta_{PRI} > 0 \end{cases}. \quad (50)$$

Obviously, the maximum variation of the delay for a given order k is the difference of these two extremes,

$$\Delta d(k) = |\Delta_{PRI}| \cdot (N_{PRI} - k) \cdot k. \quad (51)$$

A special case of the delay equation is the order $k = N_{PRI}$, for which

$$d_{i,N_{PRI}} = \sum_{n=i-1}^{i+N_{PRI}-2} PRI_n = T_{PRI}, \quad (52)$$

which is also obtained by substitution in (46). This indicates that staggered SAR systems actually always have an order of delay that shows pulse-independent behavior, exactly like the uniform PRI case.

Timing of Rx Gaps due to Tx Events: Blocked Ranges

As is the case for monostatic constant PRI SAR systems, pulse transmissions prohibit the reception of the signal (cf. Section 2.3.2). Nonetheless, in staggered PRI systems, the time instants for Tx events are no longer uniform, but vary according to the adopted PRI sequence. Their position with respect to the echoes is closely related to the delays $d_{i,k}$ already analyzed, as will be explained in the following by using the example in **Figure 15**. As represented in **Figure 15 (a)**, the delays which define the beginning and end of the echo of any given pulse are determined by the geometric

parameters of the swath of interest[13], considered to be between the slant ranges R_{min} and R_{max}.

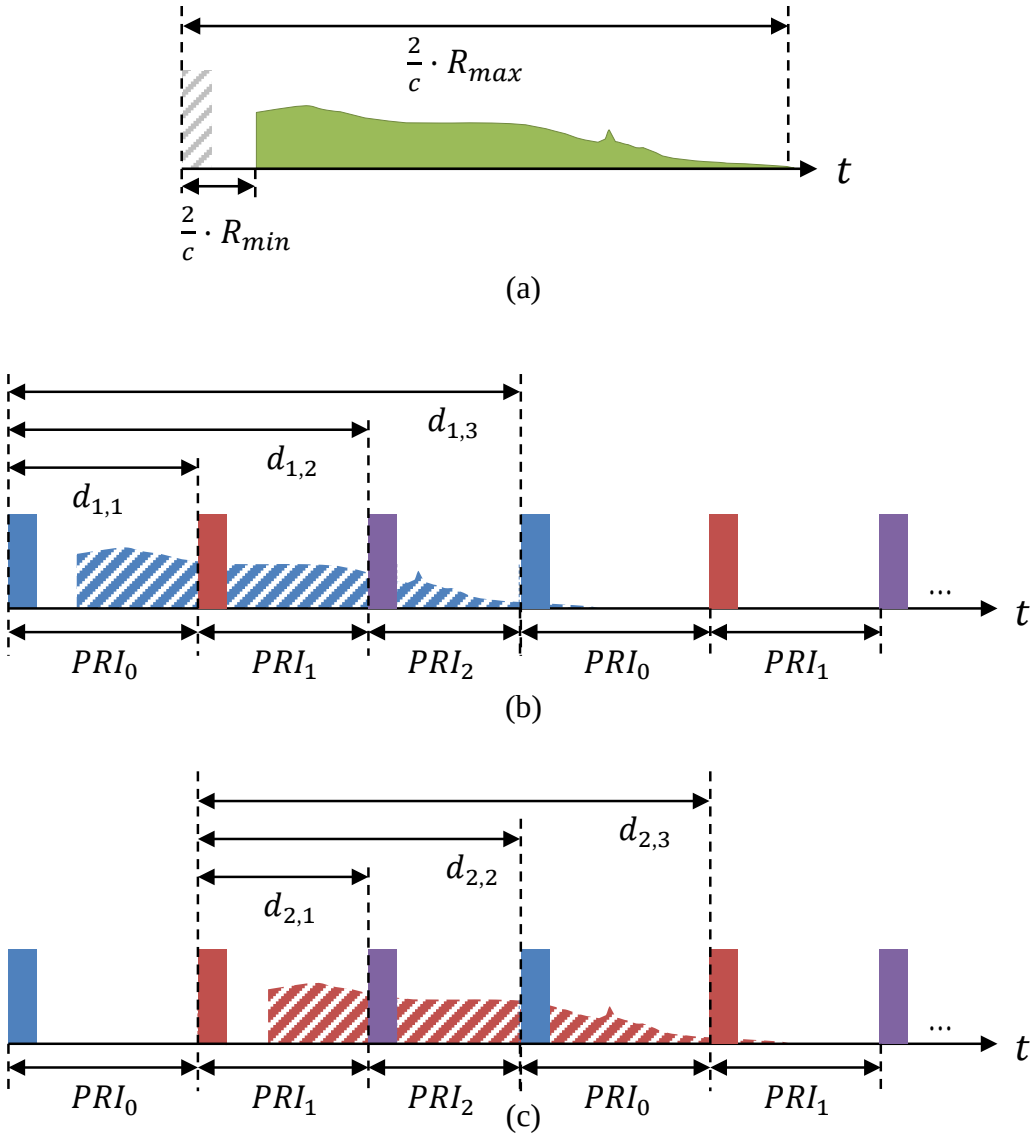

Figure 15. Position of gaps due to Tx events in Staggered SAR, defined in terms of $d_{i,k}$.(a) Echo from arbitrary pulse, defined by the geometry (R_{min}, R_{max}). (b) Echo of pulse i = 1 and corresponding blockage regions as a function of $d_{1,k}$. (c) Echo of pulse i = 2 and corresponding blockage regions as a function of $d_{2,k}$.

[13] The swath of interest is the region illuminated by the Tx antenna pattern's main beam.

Assume, to fix ideas, a very simple PRI sequence with $N_{PRI} = 3$. The corresponding Tx instants are illustrated in **Figure 15 (b)** by pulses with different colors, according to the local PRI_n. In the same figure, the echo from the first pulse ($i = 1$) is represented by the blue waveform, and it is clear that the beginning of the Tx windows, and therefore the gaps (*blockage* regions), are given by the delays $d_{1,1}$, $d_{1,2}$ and $d_{1,3}$. The same is true for the echo of the second pulse ($i = 2$) in **Figure 15 (c)**. There, the red echo has gaps defined by the delays (with respect to the time of transmission of the second pulse) $d_{2,1}$, $d_{2,2}$ and $d_{2,3}$.

It is clear from the example that, for a pulse of index i within the sequence, the timing of Tx events causing gaps is closely related to the delays $d_{i,k}$. In order to determine when blockage occurs for the i^{th} pulse, one has therefore to compare the range delays of the swath to $d_{i,k}$ for a suitable set of orders k (1 to 3 in the previous example). The orders which have to be considered are defined by R_{min} and R_{max}, since these parameters define the begin and end of the echo of each pulse. The orders are also closely related to the number of *traveling pulses*, i.e., the number of pulses which are transmitted before the echo signal of a particular range is received. In fact, the number of traveling pulses in the example is $N_T(R_{min}) = 0$ for R_{min} and $N_T(R_{max}) = 2$ for R_{max}, and the corresponding orders of interest for the swath are in the interval $k \in [N_T(R_{min}) + 1, N_T(R_{max}) + 1]$.

Repeating the analysis for all the sequence, i.e. $1 \leq i \leq N_{PRI}$, thus fully determines the position of the Tx pulse-dependent gaps. It turns out that the timing analysis for locating the gaps of a staggered PRI sequence can be formulated as an analysis of $d_{i,k}$ for all i (cf. **Figure 14**) and the set of ks dictated by the geometry. Assuming a slant range R (limited to the interval $R_{min} \leq R \leq R_{max}$ within the swath) one may reformulate the blockage condition in the staggered case (cf. (18) for the constant PRI case) as

$$t_0 \leq t - d_{i,k} \leq t_1,$$
$$t_0 \leq \frac{2 \cdot R}{c} - d_{i,k} \leq t_1. \tag{53}$$

which may also be written as

$$\frac{2 \cdot R}{c} - t_1 \leq d_{i,k} \leq \frac{2 \cdot R}{c} - t_0, \tag{54}$$

$$\frac{c}{2} \cdot \left(t_0 + d_{i,k}\right) \leq R \leq \frac{c}{2} \cdot \left(t_1 + d_{i,k}\right), \tag{55}$$

the equivalent of the constant PRI blockage condition (19) in this case. Recall t_0 and t_1 indicate the blockage times: in the simplest case, without any guard intervals, $t_0 = 0$ and $t_1 = T_p$, the pulse length.

Equation (53) and the delay definition (46) may thus be used as an analysis tool for staggered PRI systems. The form (54) is useful to determine which Tx pulse indices i will cause blockage of a given range of interest, while form (55) allows to determine the blind ranges as a function of the Tx pulse index for a given delay order. These can be seen to be regions centered around the ranges corresponding to the delays $d_{i,k}$ of (46), whose configuration translates directly into the blockage diagram of the given sequence in slant range (cf. **Figure 16** for an schematic representation and **Figure 30** for an example).

In order to perform the analysis, the relevant orders k of the delays – determined by the ranges R_0 within the swath of interest and the sequence parameters – need to be estimated. Given the limitation of the swath of interest, typically only a few orders $k_{min} \leq k \leq k_{max}$ are relevant. Unless the sequence is very short (a case considered in [62]), the range leading to blockage for all pulses identified by (52) is indeed seldom observed within the swath of interest. Since $d_{i,k}$ is a summation of k PRIs within the

bounds $PRI_{min} \leq PRI_n \leq PRI_{max}$, clearly $k \cdot PRI_{min} < d_{i,k} < k \cdot PRI_{max}$, and the region of interest is given by

$$\frac{2 \cdot R_{min}}{c} - t_1 \leq d_{i,k} \leq \frac{2 \cdot R_{max}}{c} - t_0. \tag{56}$$

Therefore, one may derive the bounds:

$$k_{min} > \frac{2 \cdot R_{max}}{c \cdot PRI_{min}},$$
$$k_{max} < \frac{2 \cdot R_{min}}{c \cdot PRI_{max}}. \tag{57}$$

For instance, for an orbit height h_{orbit} = 700 km and a swath defined between the look angles θ_{min} = 25° and θ_{max} = 45°, (which correspond to W_{ground} = 415 km) one has R_{min} = 782 km and R_{max} = 1051 km. If the sequence has PRIs corresponding to a PRF variation between 2000 Hz and 3000 Hz, then k_{min} > 5 and k_{max} < 14. The *blind range* $d_{i,N_{PRI}}$ of (52) is in the order of $N_{PRI} \cdot \overline{PRI}$, which for a (relatively short) sequence of N_{PRI} = 20 and $\overline{PRF}$ = 2500 Hz lies at a slant range of 2400 km (look angle of 64°), thus outside a typical swath.

A more precise interval can, nonetheless, be obtained by employing the extrema of the delay equation, namely $d_{N_{PRI}-k+1,k}$ and $d_{1,k}$, in combination with the blockage condition (55). Solving for *k* allows to identify the orders which have the potential to cause blockage in the extremes R_{min}, R_{max} of the swath.

The first order of interest k_{min} is such that the most distant ranges of the blockage diagram are within the swath, which can be expressed as

$$R_{min} \leq \frac{c}{2} \cdot (\, t_1 + d_{max}(k_{min})), \tag{58}$$

while the maximum order k_{max} still has some of its least distant ranges within the swath and satisfies the condition

$$\frac{c}{2} \cdot (t_0 + d_{min}(k_{max})) \leq R_{max.} \tag{59}$$

For instance, for $\Delta_{PRI} < 0$, $d_{max}(k) = d_{1,k}$ and $d_{min}(k) = d_{N_{PRI}-k+1,k}$, (cf. (49)) so that

$$\begin{aligned} & R_{min} \cdot \frac{2}{c} - t_1 \leq k_{min} \cdot PRI_0 + \frac{\Delta_{PRI}}{2} \cdot (k_{min} - 1) \cdot k_{min} \\ & -\frac{\Delta_{PRI}}{2} \cdot k_{min}^2 - \left(PRI_0 - \frac{\Delta_{PRI}}{2}\right) \cdot k_{min} + R_{min} \cdot \frac{2}{c} - t_1 \leq 0 \\ & k_{min} = \left\lceil \frac{-\left(PRI_0 - \frac{\Delta_{PRI}}{2}\right) + \sqrt{\left(PRI_0 - \frac{\Delta_{PRI}}{2}\right)^2 + 2 \cdot \Delta_{PRI} \cdot \left(R_{min} \cdot \frac{2}{c} - t_1\right)}}{\Delta_{PRI}} \right\rceil \end{aligned} \tag{60}$$

and

$$\begin{aligned} & k_{max} \cdot PRI_0 + \frac{\Delta_{PRI}}{2} \cdot (2 \cdot N_{PRI} - k_{max} - 1) \cdot k_{max} \leq R_{max} \cdot \frac{2}{c} - t_0 \\ & -\frac{\Delta_{PRI}}{2} \cdot k_{max}^2 + \left(PRI_0 + \frac{\Delta_{PRI}}{2} \cdot (2 \cdot N_{PRI} - 1)\right) \cdot k_{max} - R_{max} \cdot \frac{2}{c} + t_0 \leq 0 \\ & k_{max} = \left\lfloor \frac{\left(PRI_0 + \frac{\Delta_{PRI}}{2} \cdot (2 \cdot N_{PRI} - 1)\right) + \sqrt{B}}{\Delta_{PRI}} \right\rfloor, \end{aligned} \tag{61}$$

where

$$B = \left(PRI_0 + \frac{\Delta_{PRI}}{2} \cdot (2 \cdot N_{PRI} - 1)\right)^2 - 2 \cdot \Delta_{PRI} \cdot \left(R_{max} \cdot \frac{2}{c} - t_0\right)$$

Similarly, if $\Delta_{PRI} > 0$, one can show that

$$k_{min} = \left\lceil \frac{\left(PRI_0 + \frac{\Delta_{PRI}}{2} \cdot (2 \cdot N_{PRI} - 1) \right) - \sqrt{B_1}}{\Delta_{PRI}} \right\rceil$$

where

$$B_1 = \left(PRI_0 + \frac{\Delta_{PRI}}{2} \cdot (2 \cdot N_{PRI} - 1) \right)^2 - 2 \cdot \Delta_{PRI} \cdot \left(R_{min} \cdot \frac{2}{\mathrm{c}} - t_1 \right) \tag{62}$$

and

$$k_{max} = \left\lfloor \frac{-\left(PRI_0 - \frac{\Delta_{PRI}}{2} \right) + \sqrt{\left(PRI_0 - \frac{\Delta_{PRI}}{2} \right)^2 + 2 \cdot \Delta_{PRI} \cdot \left(R_{max} \cdot \frac{2}{\mathrm{c}} - t_0 \right)}}{\Delta_{PRI}} \right\rfloor.$$

With this information, the blockage ranges of the sequence can identified, and the blockage diagram fully determined.

Timing of Rx Gaps due to Tx Events: Lost Pulses and Gap Extension

Up to this point, the definition of $d_{i,k}$ and the blockage condition have been used to establish the blockage diagram against the pulse index and obtain the orders k of interest for a given swath. A further critical aspect of the analysis of Staggered SAR sequences is determining the indices of the pulses in the sequence whose returns are blocked for a given slant range, which will be analyzed in the following.

From (54), (55), the positions of the blocked ranges are proportional to the delays $d_{i,k}$ defined in (46), according to the parameters t_0 and t_1, which define the blockage interval and are determined by the pulse duration and eventual guard intervals. Furthermore, as derived, the delays vary linearly from pulse to pulse, with a minimum or a maximum (according to the sign of Δ_{PRI}, cf. (50)) at the discontinuity $i_{break} = N_{PRI} - k + 1$ and steps of opposite signs in the two regions separated by the breakpoint (cf. **Figure 14**). It is thus clear that, for a given order k, blockage may occur simultaneously at both regions of the delay pattern $d_{i,k}$. Therefore, a maximum

of two gaps, one between indices G_1 and G_2 – located in the first region of (46) – and another between indices G_3 and G_4 – located in the second region – is expected, as depicted schematically in **Figure 16**. There, the ordinates indicate the Tx pulse index whereas the abscissas show slant range, linearly related to the delays, for a given order k_0. The plot is equivalent to **Figure 14** with scaling of the delays to ranges by $\frac{c}{2}$ and inversion of the order of the co-ordinates. The Tx pulse indices causing blockage at the fixed slant range R_0 belong to the intervals $[G_1, G_2]$ and $[G_3, G_4]$, at opposite sides of the discontinuity i_{break} .

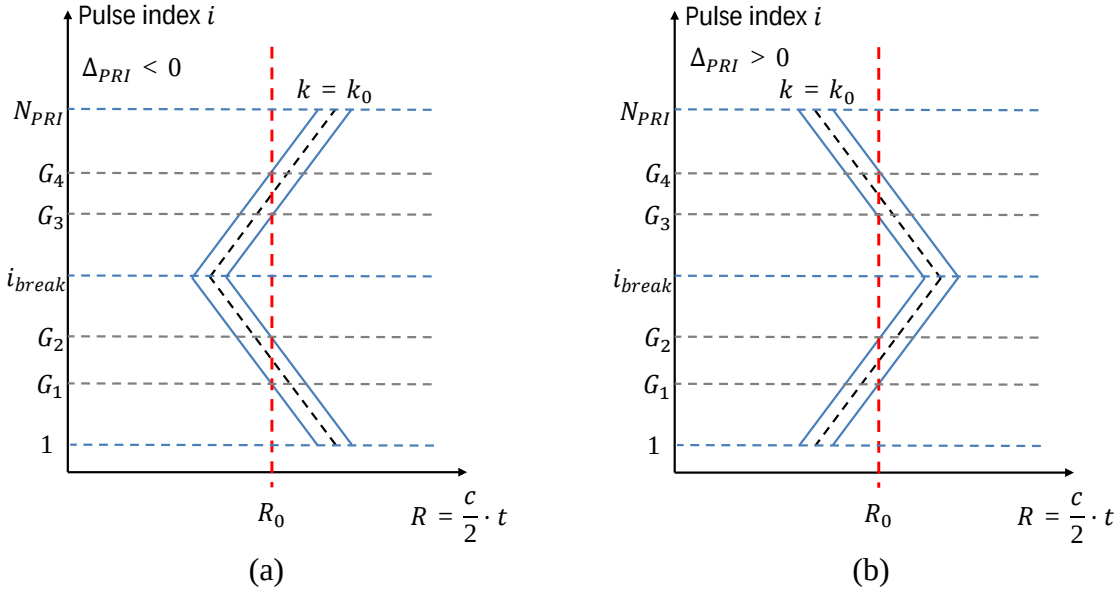

Figure 16. Schematic representation of gaps at a given range R_0 for a delay order k_0, considering (a) $\Delta_{PRI} < 0$ and (b) $\Delta_{PRI} > 0$.

Applying (53) and (46) for the appropriate regions, and solving for the index leads to the following expressions for the gap extrema, i.e., the first and last lost pulse indices:

for $1 \leq i \leq N_{PRI} + 1 - k$: (first region)

$$(\Delta_{PRI} \cdot k) \cdot G_1 \leq \left(\frac{2 \cdot R_0}{c} - t_0 - k \cdot PRI_0 - \frac{\Delta_{PRI}}{2} \cdot k \cdot (k-3) \right) \tag{63}$$

$$(\Delta_{PRI} \cdot k) \cdot G_2 \geq \left(\frac{2 \cdot R_0}{c} - t_1 - k \cdot PRI_0 - \frac{\Delta_{PRI}}{2} \cdot k \cdot (k-3) \right)$$

for $N_{PRI} + 2 - k \leq i \leq N_{PRI}$: (second region)

$$\left(\Delta_{PRI} \cdot (N_{PRI} - k)\right) \cdot G_3 \geq$$

$$\left(\frac{2 \cdot R_0}{\mathrm{c}} - t_0 - T_{PRI} + (N_{PRI} - k) \cdot PRI_0 + \frac{\Delta_{PRI}}{2} \cdot (k - N_{PRI} - 3) \cdot (N_{PRI} - k)\right) \quad (64)$$

$$\left(\Delta_{PRI} \cdot (N_{PRI} - k)\right) \cdot G_4 \leq$$

$$\left(\frac{2 \cdot R_0}{\mathrm{c}} - t_1 - T_{PRI} + (N_{PRI} - k) \cdot PRI_0 + \frac{\Delta_{PRI}}{2} \cdot (k - M - 3) \cdot (N_{PRI} - k)\right)$$

which can be adapted to the appropriate integer solution for the indexes using the floor ($\lfloor \ \rfloor$) and ceil ($\lceil \ \rceil$) operators on the indices L_n according to the sign of Δ_{PRI}. For $\Delta_{PRI} < 0$, e.g:

$$G_1 = \left\lceil \left(\frac{2 \cdot R_0}{\mathrm{c}} - t_0 - k \cdot PRI_0 - \frac{\Delta_{PRI}}{2} \cdot k \cdot (k - 3)\right) \cdot \frac{1}{\Delta_{PRI} \cdot k} \right\rceil$$

$$G_2 = \left\lfloor \left(\frac{2 \cdot R_0}{\mathrm{c}} - t_1 - k \cdot PRI_0 - \frac{\Delta_{PRI}}{2} \cdot k \cdot (k - 3)\right) \cdot \frac{1}{\Delta_{PRI} \cdot k} \right\rfloor$$

$$G_3 =$$

$$\left\lceil \left(\frac{2 \cdot R_0}{c} - t_0 - T_{PRI} + (N_{PRI} - k) \cdot PRI_0 + \frac{\Delta_{PRI}}{2} \cdot (k - N_{PRI} - 3) \cdot (N_{PRI} - k)\right) \cdot \frac{1}{\Delta_{PRI} \cdot (N_{PRI} - k)} \right\rceil \quad (65)$$

$$G_4 =$$

$$\left\lfloor \left(\frac{2 \cdot R_0}{c} - t_1 - T_{PRI} + (N_{PRI} - k) \cdot PRI_0 + \frac{\Delta_{PRI}}{2} \cdot (k - M - 3) \cdot (N_{PRI} - k)\right) \cdot \frac{1}{\Delta_{PRI} \cdot (N_{PRI} - k)} \right\rfloor$$

The gap lengths in unit of pulses for the two regions are given by $L_1 = G_2 - G_1 + 1$ and $L_2 = G_4 - G_3 + 1$, in which the index restriction to integer values is taken into account. The gap lengths without considering this discretization are given by the expressions

$$\tilde{L}_1 = \frac{t_1 - t_0}{k \cdot |\Delta_{PRI}|} \triangleq \frac{\Delta b}{k \cdot |\Delta_{PRI}|}$$
$$\tilde{L}_2 = \frac{\Delta b}{(N_{PRI} - k) \cdot |\Delta_{PRI}|}, \tag{66}$$

which highlight the dependence of the gap length on the blockage interval $\Delta b = t_1 - t_0$ and the rate of variation of the delays for a given order (cf. (47)). It is clear that, the faster the PRIs change, the narrower the gaps become, since the Rx blockage windows – the Tx events – migrate faster and tend to overlap less between adjacent pulses. This fact can be understood intuitively from the discussion in the beginning of Section 3.3.1 (cf. **Figure 12**), and plays an important role in the formulation of criteria for staggered PRI sequence design, to be considered in Section 3.3.3. In the case of constant PRI SAR, $\Delta_{PRI} = 0$ and the gap length tends to infinity, describing the formation of arbitrarily long blind ranges in azimuth, to be expected since no echo signals whatsoever can be recorded.

In Section 5.2, the blockage analysis discussed here is illustrated for an example Multichannel Staggered SAR system (cf. TABLE II, **Figure 30** and **Figure 32**).

3.3.3 A Brief Discussion of Sequence Design

The design of sequence parameters following different criteria has been analyzed in [41], [53] in detail and is not the main topic of this work. However, for completeness in light of the frequent use of this criterion in upcoming Chapters, and in order to

provide an example of the employment of the analysis framework developed in Section 3.3.2, the *fast PRI variation* criterion will be briefly described.

As apparent from (66), gap lengths and the rate at which the PRIs in the sequence vary, embodied by the parameter Δ_{PRI}, are intimately related properties of the sequence. As expected, the gap length is also determined by the duration Δb of each blockage event, accounting for the pulse length and including possible guard intervals. The gap lengths $\tilde{L}_1$ and $\tilde{L}_2$ cannot vanish for a given $\Delta b > 0$, but a sensible criterion is to limit the gap length to a single pulse [53], whenever it occurs. This corresponds to the smallest possible gap, which facilitates the recovery of the signal by interpolation. The condition can be stated as

$$\begin{aligned} \tilde{L}_1 &= \frac{\Delta b}{k \cdot |\Delta_{PRI}|} \leq 1 \\ \tilde{L}_2 &= \frac{\Delta b}{(N_{PRI} - k) \cdot |\Delta_{PRI}|} \leq 1, \end{aligned} \tag{67}$$

and leads to an effective number of non-blocked pulses $N_{eff} \geq N_{PRI} - 2$ over all ranges in the swath, since $N_{eff} = N_{PRI} - (\tilde{L}_1 + \tilde{L}_2)$.

This condition has to be enforced for all orders k within the swath of interest. Assuming relevant orders $k_{min} \leq k \leq k_{max}$ for the swath, it suffices to require that

$$\begin{aligned} \frac{\Delta b}{k_{min} \cdot |\Delta_{PRI}|} \leq 1 \;\Rightarrow\; k_{min} &\geq \frac{\Delta b}{|\Delta_{PRI}|} \\ \frac{\Delta b}{(N_{PRI} - k_{max}) \cdot |\Delta_{PRI}|} \leq 1 \;\Rightarrow\; k_{max} &\leq N_{PRI} - \frac{\Delta b}{|\Delta_{PRI}|}. \end{aligned} \tag{68}$$

By defining the sequence parameter

$$k_c = \frac{\Delta b}{|\Delta_{PRI}|}, \tag{69}$$

and letting $k_{min} = k_c$, $k_{max} = N_{PRI} - k_c$, i.e. the critical case for satisfying (68), one may resort to an analysis based on the blockage condition (55) in order to derive the required relationship between the sequence parameters for this criterion.

Given that $k_{min} = k_c$ is defined as the first order of delay whose blockage pattern interferes with the swath, assumed to extend from $R_{min} \leq R_0 \leq R_{max}$, for the order $k_c - 1$, the delays should be such that no interference occurs at the beginning of the swath, $R = R_{\min}$, i.e.,

$$R_{min} \geq \frac{\mathrm{c}}{2} \cdot (\, t_1 + d_{max}(k_c - 1)), \tag{70}$$

whereas the order beyond the maximum, $k_{max} + 1 = N_{PRI} - k_c + 1$ should no longer have its blockage pattern within the swath, meaning that

$$\frac{\mathrm{c}}{2} \cdot \left(t_0 + d_{min}(N_{PRI} - k_c + 1)\right) \geq R_{max.} \tag{71}$$

Assuming the case $\Delta_{PRI} < 0$ and using the extrema relations (49) alongside the definition of the delays (42), these relations can be expanded as

$$R_{min} \geq \frac{\mathrm{c}}{2} \cdot \left(t_1 + \sum_{n=0}^{k_c-2} PRI_n \right)$$

$$\sum_{n=0}^{k_c-2} PRI_n \leq \frac{2 \cdot R_{min}}{\mathrm{c}} - t_1, \tag{72}$$

and

$$\frac{\mathrm{c}}{2} \cdot \left(t_0 + \sum_{n=k_c-1}^{N_{PRI}-1} PRI_n \right) \geq R_{max}$$

$$\sum_{n=k_c-1}^{N_{PRI}-1} PRI_n \geq \frac{2 \cdot R_{max}}{c} - t_0$$

$$PRI_{k_c-1} + \sum_{n=k_c}^{N_{PRI}-1} PRI_n \geq \frac{2 \cdot R_{max}}{c} - t_0$$

$$\sum_{n=k_c}^{N_{PRI}-1} PRI_n \geq \frac{2 \cdot R_{max}}{c} - t_0 - PRI_0 - (k_c - 1) \cdot \Delta_{PRI}.$$

Noting that $-\Delta_{PRI} = |\Delta_{PRI}|$ is a positive number and using (69), the condition above can be replaced by the more restrictive one

$$\sum_{n=k_c}^{N_{PRI}-1} PRI_n \geq \frac{2 \cdot R_{max}}{c} - t_0 - PRI_0 - (k_c) \cdot \Delta_{PRI}$$

$$\sum_{n=k_c}^{N_{PRI}-1} PRI_n \geq \frac{2 \cdot R_{max}}{c} - t_0 - PRI_0 + \Delta b. \quad (73)$$

In [41], [53] a pulse interference analysis for the case $\Delta_{PRI} < 0$ with parameters $t_0 = 0$ and $t_1 = \Delta b = T_P$ yields analogous conditions for the *fast PRI variation* criterion (single pulse gaps, as in (67)).

In practice, in order to design a sequence according to this criterion, the sequence parameters PRI_0, N_{PRI} and Δ_{PRI} are the quantities of interest to be determined. As in [41], [53], the goal is also to minimize Δ_{PRI} and N_{PRI} in order to simplify the sequence, while still achieving the design $\overline{PRI}$. The swath limits R_{min} and R_{max}, as well as the mean pulse repetition interval $\overline{PRI}$ and the blockage model – pulse duration T_P, instants of begin t_0 and end t_1 of the blockage (Rx) window and its duration Δb – are typically known. In the following a strategy to obtain the sequence parameters fulfilling the conditions (68), (72) and (73) is presented. The first step is to rewrite the conditions in terms of $\overline{PRI}$ by employing (41).

From (68), one may write

$$|\Delta_{PRI}| \geq \left|\Delta_{PRI}^{min}\right| = \frac{\Delta b}{k_{min}} \tag{74}$$

Since (72) and (73) will be used in the derivation, the hypotheses $\Delta_{PRI} < 0$, $k_{min} = k_c$ and $k_{max} = N_{PRI} - k_c$ are assumed to hold. One can thus write

$$(i) \quad |\Delta_{PRI}| \geq \left|\Delta_{PRI}^{min}\right| = \frac{\Delta b}{k_c}, \tag{75}$$

where the inequality with respect to Δ_{PRI} is kept to highlight the fact that using a larger step than the critical one is a possibility that still satisfies the criterion.

(72) may be expanded as

$$(ii) \quad \sum_{n=0}^{k_c-2} PRI_n < \frac{2 \cdot R_{min}}{\mathrm{c}} - t_1$$

$$(k_c - 1) \cdot PRI_0 - (k_c - 1) \cdot (k_c - 2) \cdot \frac{\Delta_{PRI}}{2} \leq \frac{2 \cdot R_{min}}{\mathrm{c}} - t_1$$

$$\frac{\Delta_{PRI}}{2} \cdot (k_c)^2 - k_c \cdot \left(PRI_0 + \frac{3 \cdot \Delta_{PRI}}{2}\right) + \left(PRI_0 + \frac{2 \cdot R_{min}}{\mathrm{c}} - t_1\right) \geq 0.$$

From (41),

$$PRI_0 = \overline{PRI} + \frac{N_{PRI} - 1}{2} \cdot \Delta_{PRI.} \tag{76}$$

Substituting in the above equation yields

$$\frac{\Delta_{PRI}}{2}\cdot(k_c)^2 - k_c\cdot\left(\overline{PRI} + \frac{N_{PRI}+2}{2}\cdot\Delta_{PRI}\right) + \left(\overline{PRI} + \frac{N_{PRI}-1}{2}\cdot\Delta_{PRI} + \frac{2\cdot R_{min}}{\mathrm{c}} - t_1\right) \geq 0$$

$$\frac{\Delta_{PRI}}{2}\cdot(k_c)^2 - \frac{\Delta_{PRI}}{2}\cdot k_c\cdot N_{PRI} - (\overline{PRI} + \Delta_{PRI})\cdot k_c + \frac{\Delta_{PRI}}{2}\cdot N_{PRI} + \left(\overline{PRI} - \frac{\Delta_{PRI}}{2} + \frac{2\cdot R_{min}}{\mathrm{c}} - t_1\right) \geq 0. \tag{77}$$

In the particular case of the minimum PRI step (75), one may write

$$\frac{\Delta b}{2\cdot k_c}\cdot(k_c)^2 - \frac{\Delta b}{2\cdot k_c}\cdot k_c\cdot N_{PRI} - k_c\cdot\left(\overline{PRI} + \frac{\Delta b}{k_c}\right) + \frac{\Delta b}{2\cdot k_c}\cdot N_{PRI} + \left(\overline{PRI} - \frac{\Delta b}{2\cdot k_c} + \frac{2\cdot R_{min}}{\mathrm{c}} - t_1\right) \geq 0$$

$$k_c\cdot\left(-\overline{PRI} + \frac{\Delta b}{2}\right) + \left(\overline{PRI} + \frac{2\cdot R_{min}}{\mathrm{c}} - t_1 - \frac{\Delta b}{2}\cdot N_{PRI}\right) + \frac{\Delta b}{2\cdot k_c}\cdot(N_{PRI}-1) \geq 0.$$

Multiplying by k_c, which is positive, and inverting the side of the inequation leads to

$$\left(\overline{PRI} - \frac{\Delta b}{2}\right)\cdot(k_c)^2 - \left(\overline{PRI} + \frac{2\cdot R_{min}}{\mathrm{c}} - t_1 - \frac{\Delta b}{2}\cdot N_{PRI}\right)\cdot k_c - \frac{\Delta b}{2}\cdot(N_{PRI}-1) \leq 0. \tag{78}$$

Finally, from (73)

$$(iii) \quad \sum_{n=k_c}^{N_{PRI}-1} PRI_n > \frac{2\cdot R_{max}}{\mathrm{c}} - t_0 - PRI_0 + \Delta b$$

$$(N_{PRI} - k_c) \cdot PRI_0 - (N_{PRI} - k_c) \cdot (N_{PRI} + k_c - 1) \cdot \frac{\Delta_{PRI}}{2} \geq \frac{2 \cdot R_{max}}{\mathrm{c}} - t_0 - PRI_0 + \Delta b$$

$$\frac{\Delta_{PRI}}{2} \cdot (k_c)^2 - \frac{\Delta_{PRI}}{2} \cdot N_{PRI}{}^2 - k_c \cdot \left(PRI_0 + \frac{\Delta_{PRI}}{2}\right) + N_{PRI} \cdot \left(PRI_0 + \frac{\Delta_{PRI}}{2}\right) - \left(\frac{2 \cdot R_{max}}{\mathrm{c}} - t_0 - PRI_0 + \Delta b\right) \geq 0.$$

Using (76) and rearranging,

$$\frac{\Delta_{PRI}}{2} \cdot (k_c)^2 - \frac{\Delta_{PRI}}{2} \cdot N_{PRI}{}^2 - k_c \cdot \left(\overline{PRI} + N_{PRI} \cdot \frac{\Delta_{PRI}}{2}\right) + N_{PRI} \cdot \left(\overline{PRI} + N_{PRI} \cdot \frac{\Delta_{PRI}}{2}\right) - \left(\frac{2 \cdot R_{max}}{\mathrm{c}} - t_0 - \overline{PRI} - \frac{N_{PRI} - 1}{2} \cdot \Delta_{PRI} + \Delta b\right) \geq 0$$

$$\frac{\Delta_{PRI}}{2} \cdot (k_c)^2 - \frac{\Delta_{PRI}}{2} \cdot k_c \cdot N_{PRI} - \overline{PRI} \cdot k_c + \left(\overline{PRI} + \frac{\Delta_{PRI}}{2}\right) \cdot N_{PRI} - \left(\frac{2 \cdot R_{max}}{\mathrm{c}} - t_0 - \overline{PRI} + \frac{\Delta_{PRI}}{2} + \Delta b\right) \geq 0. \quad (79)$$

Taking (77) and (79) in the limit case, i.e., as equations, and subtracting leads to

$$-\Delta_{PRI} \cdot k_c - \overline{PRI} \cdot N_{PRI} + \left(\frac{2 \cdot R_{min}}{\mathrm{c}} + \frac{2 \cdot R_{max}}{\mathrm{c}} + \Delta b - t_1 - t_0\right) = 0.$$

Using (75) – i.e., the minimum PRI step – and considering blockage intervals as $t_0 = 0$, $t_1 = \Delta b$ the equation simplifies to

$$-\frac{\Delta b}{k_c} \cdot k_c - \overline{PRI} \cdot N_{PRI} + \left(\frac{2 \cdot R_{min}}{\mathrm{c}} + \frac{2 \cdot R_{max}}{\mathrm{c}}\right) = 0$$

$$\widetilde{N}_{PRI_{min}} = \frac{1}{\overline{PRI}} \cdot \left(\frac{2}{c} \cdot (R_{min} + R_{max}) + \Delta b\right),$$
$$N_{PRI} \geq \lceil \widetilde{N}_{PRI_{min}} \rceil. \tag{80}$$

yielding the minimum sequence length for design, under the minimum Δ_{PRI} condition. The notation $\widetilde{N}_{PRI_{min}}$ highlights the fact that this quantity is a real number, in consequence of taking the limit case of the inequations. In practice, $N_{PRI} \geq \lceil \widetilde{N}_{PRI_{min}} \rceil$ gives the limit on the shortest PRI sequence length.

To complete the design, the parameter k_c, which defines Δ_{PRI} through (75) must also be known. Considering N_{PRI} as a parameter, (78) can be solved as

$$k_c \leq \tilde{k}_c \Rightarrow k_c^{INT} = \lfloor \tilde{k}_c \rfloor,$$

with

$$\tilde{k}_c = \frac{B + \sqrt{(B)^2 + 2 \cdot (N_{PRI} - 1) \cdot \Delta b \cdot \left(\overline{PRI} - \frac{\Delta b}{2}\right)}}{2 \cdot \left(\overline{PRI} - \frac{\Delta b}{2}\right)}, \tag{81}$$

$$B = \left(\overline{PRI} + \frac{2 \cdot R_{min}}{\mathrm{c}} - t_1 - \frac{\Delta b}{2} \cdot N_{PRI}\right);$$

where $\tilde{k}_c$ is a real number representing the maximum value of the order k_c and k_c^{INT} the discretization of this limit order to integer values.

To achieve a simple design procedure, in light of the need of discretization of the real parameters respecting the given relations to fulfil the criterion, the following strategy is proposed. Use of (80) gives $\widetilde{N}_{PRI_{min}}$ (and it's rounding) which may be used as a "first-guess" of the sequence length to specify the integer k_c^{INT} via (81), eliminating this parameter and defining the minimal Δ_{PRI} by means of (75). To ensure the fulfillment of the criterion, consider k_c as a parameter in (79). Enforcing (75) leads to

$$\frac{\Delta b}{2 \cdot k_c} \cdot (k_c)^2 - \frac{\Delta b}{2 \cdot k_c} \cdot k_c \cdot N_{PRI} - \overline{PRI} \cdot k_c + \left(\overline{PRI} + \frac{\Delta b}{2 \cdot k_c}\right) \cdot N_{PRI} - \left(\frac{2 \cdot R_{max}}{\mathrm{c}} - t_0 - \overline{PRI} + \frac{\Delta b}{2 \cdot k_c} + \Delta b\right) \geq 0$$

$$\left(\frac{\Delta b}{2} - \overline{PRI}\right) \cdot k_c + \left(\overline{PRI} + \frac{\Delta b}{2 \cdot k_c} - \frac{\Delta b}{2}\right) \cdot N_{PRI} - \left(\frac{2 \cdot R_{max}}{\mathrm{c}} - t_0 - \overline{PRI} + \frac{\Delta b}{2 \cdot k_c} + \Delta b\right) \geq 0$$

$$N_{PRI} \geq \frac{\left(\frac{2 \cdot R_{max}}{\mathrm{c}} - t_0 - \overline{PRI} + \frac{\Delta b}{2 \cdot k_c} + \Delta b\right) - \left(\frac{\Delta b}{2} - \overline{PRI}\right) \cdot k_c}{\left(\overline{PRI} + \frac{\Delta b}{2 \cdot k_c} - \frac{\Delta b}{2}\right)}$$

$$N_{PRI\,MIN}(k_c) = \left\lceil \frac{\left(\frac{2 \cdot R_{max}}{\mathrm{c}} - t_0 - \overline{PRI} + \frac{\Delta b}{2 \cdot k_c} + \Delta b\right) - \left(\frac{\Delta b}{2} - \overline{PRI}\right) \cdot k_c}{\left(\overline{PRI} + \frac{\Delta b}{2 \cdot k_c} - \frac{\Delta b}{2}\right)} \cdot \right\rceil \tag{82}$$

Therefore, using Δ_{PRI} and k_c^{INT} determined in the step before into (82) allows a choice of sequence length N_{PRI} which satisfies the criterion. The use of a longer sequence remains a possibility, while adding complexity to the system. Finally, given N_{PRI} and Δ_{PRI}, (76) yields a PRI_0 satisfying the design $\overline{PRI}$, concluding the design.

In [41], [53], [62] and [63], additional strategies for sequence design are provided, including options for variations of the *fast PRI variation* criterion.

One noteworthy extension which will be used later in this thesis is the design of *quad-pol* sequences, necessary for fully polarimetric acquisitions. The basic idea is to design the sequence for the *full* mean PRF (i.e. twice the mean PRF of each polarization pair) and then repeat each PRI twice, to account for the interleaving of transmit pulses. The relevant delays defining the Tx (and thus blockage) positions, in terms of (46) and the full interleaved PRI sequence, are then $d_{2 \cdot i, 2 \cdot k}$ for the first polarization and $d_{2 \cdot i+1, 2 \cdot k}$ for the second. The concepts and timing analysis tools

described in this chapter can still be applied, with adaptations. The main difference which should be taken into account is that the transmission events of the opposite polarization also cause blockage.

3.4 Remarks on HRWS SAR

This chapter described in more detail the HRWS alternatives represented by multichannel systems in azimuth (Section 3.2) and Staggered SAR (Section 3.3). The usefulness of multichannel systems in increasing the sampling rate of the signal in azimuth was made clear, as well of the capability of the techniques to resample the multichannel data to a finer regular grid in azimuth.

In the case of Staggered SAR, a detailed analysis of sequence timing was presented, since it is necessary to determine the position of the received pulses in azimuth, as well as the blockage effects expected for a particular range. As will become clear next, this information is crucial in the modeling and solution of the problem of resampling multichannel Staggered SAR data to a regular grid.

The following Chapter 4 introduces the combination of the methods from Sections 3.2 and 3.3 into a Multichannel Staggered SAR concept.

4 Multichannel Staggered SAR in Azimuth

4.1 Chapter Overview

This chapter introduces the resampling problem found in the operation of a multichannel staggered SAR system (Section 4.2), and analyses possible solutions mathematically. A first method applicable for reflector antennas is presented in Section 4.3, and a novel method is introduced in Section 4.4. Section 4.5 shows that the method is applicable to planar antenna arrays as well, under certain limitations. The algorithms discussed here represent the core of the Thesis. Part of the material in this chapter is present in [67], [69], [70].

4.2 Problem Overview

Until this point, the HRWS techniques (cf. Sections 3.2 and 3.3) have been described as separate alternatives. As a first step in order to combine the staggered PRI technique with multichannel system architectures – thus introducing new and potentially highly flexible modes of operation – this section describes and briefly develops a signal model for a multichannel staggered SAR system. A multichannel system in azimuth (cf. Section 3.2) which is capable of recording the output of N_{ch} samples per received pulse by means of an equal number of receiver channels is assumed.

The system is operated with a staggered PRI sequence with linear PRI variation and parameters PRI_0, N_{PRI} and Δ_{PRI}, as described in Section 3.3. As apparent from the last sections, the staggered PRI operation leads to a received signal in azimuth which is sampled in a periodically non-uniform manner. In turn, the pulse sequence is subject to range-dependent gaps induced by blockage (cf. Section 3.3.2), and N_{eff} out of N_{PRI} samples are actually available within each cycle of PRIs at a given range. The ultimate goal is to develop suitable processing techniques allowing one to obtain from the effective N_{eff} staggered PRI pulses, each sampled at N_{ch} receiver channels, a

regularly sampled output at an increased rate of $PRF_{multi} = N_{ch} \cdot \overline{PRF}_{eff}$, where $\overline{PRF}_{eff}$ is the effective average sampling rate of the pulses, i.e.

$$\overline{PRF}_{eff} = \frac{N_{eff}}{N_{PRI}} \cdot \overline{PRF}, \tag{83}$$

and $\overline{PRF}$ is the average system pulse repetition frequency. The final output is a regularly sampled signal which can be processed using conventional SAR algorithms.

Assume the return of the first pulse to be at time instant $t_{rx}[1] = 0$. Then, before blockage is taken into consideration, each pulse of index $1 \leq n \leq N_{PRI}$ is received at time instants given by the cumulative sum of the PRI intervals, i.e.

$$t_{rx}[n] = \sum_{m=0}^{n-1} PRI_m \overset{\text{using (42)}}{=} d_{1,n}$$

$$t_{rx}[n] \overset{\text{using (46)}}{=} (n) \cdot PRI_0 + \frac{\Delta_{PRI}}{2} \cdot (n-1) \cdot (n)\,. \tag{84}$$

Depending on the particular range R_0 and the PRI sequence parameters, blockage due to Tx events (cf. Section 3.3.2) leaves N_{eff} pulses out of the N_{PRI} available. The indices of the pulses lost at a particular range can be evaluated by solving the blockage condition (54).

The desired regular output grid has $N_{ch} \cdot N_{eff}$ samples over a cycle at the time instants described by

$$t_{out}[k] = \frac{(k-1)}{N_{ch} \cdot \overline{PRF}_{eff}} + \delta t, \qquad 1 \leq k \leq N_{out} = N_{ch} \cdot N_{eff}; \tag{85}$$

where the arbitrary constant shift parameter δt is included to highlight the fact that the output grid may be shifted arbitrarily without losing the regularity property, and its importance will be made clear in following sections. Note that this grid is a resampling of the original multichannel non-uniform grid preserving the number of

samples per cycle, and can be converted to other sampling rates – e.g. the full $N_{ch} \cdot \overline{PRF}$ compensating the pulse blockage – by conventional interpolation methods, e.g. zero-padding in frequency domain. The desired resampling operation is represented schematically for a cycle of pulses in **Figure 17**.

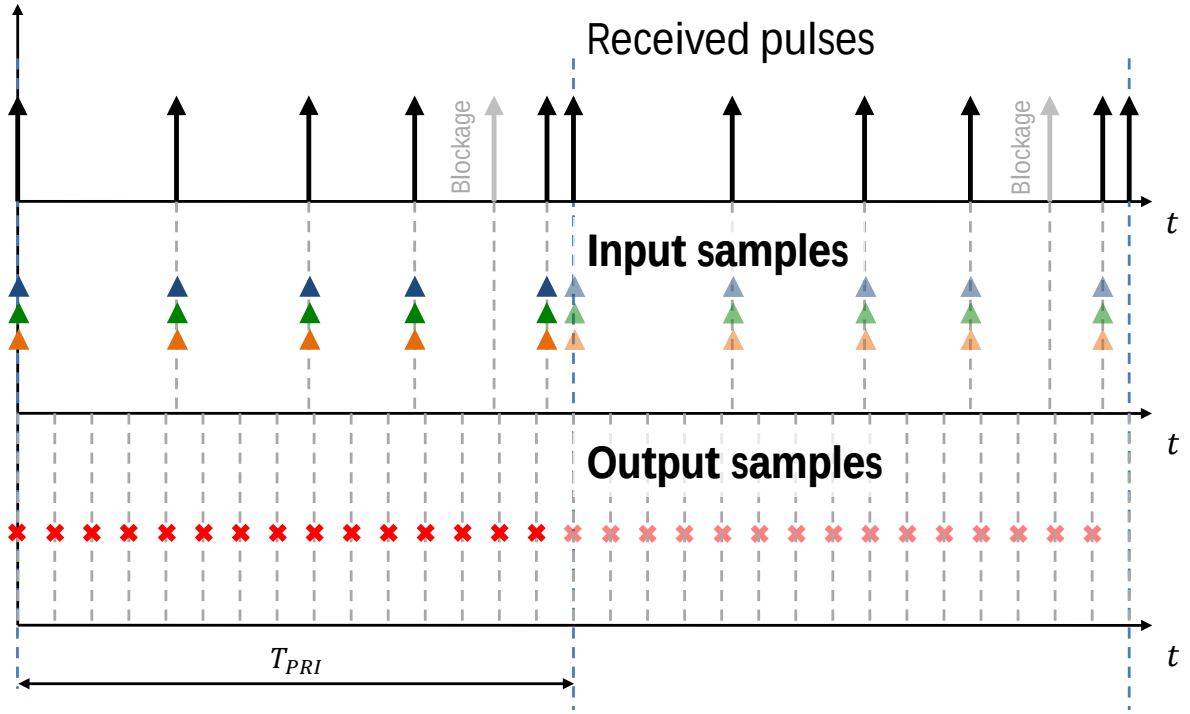

Figure 17. Schematic representation of resampling operation over a cycle of pulses of duration T_{PRI}, assuming δt = 0. The received pulses are received over a periodically non-uniform grid due to Staggered PRI operation, and for each pulse several input samples are gathered (3 in this example) owing to the multiple receiver channels. The goal is to resample the input into a finer regular grid, both regularizing the samples and increasing the sampling rate by a factor of the number of channels.

As was the case for constant-PRI multichannel systems (cf. Section 3.2) the acquisition of the azimuth signal through multiple phase centers [37], [38] is the key to the uniform signal reconstruction capability. Different methods offering this capability will be considered in the following sections.

4.3 Azimuth Phase Steering

Steering the Main Beam of a Phased Array towards a Desired Angle

The *uniform array steering* [100] method – widely used in phased arrays – is a well-known technique applied in order to shift the angular position of the main beam of the resulting pattern of an antenna array within a certain scan angle range. In [104], application of this technique to the feed (primary) beams of a reflector system is investigated as a possibility to obtain far field (secondary) beams on the ground with different phase centers, while still observing the same Doppler spectrum. This is analogous to the behavior of the (primary) far field patterns of a multichannel planar system and is achieved by illuminating different regions of the reflector's surface. Illuminating only part of the reflector's surface broadens the resulting secondary patterns. Nonetheless, the ability to continuously vary the primary beam's position allows adjusting the phase centers' position. Thus a reflector with a multichannel feed concept as suggested in [104] is equivalent to a planar system with the great benefit of an adjustable inter-element spacing within certain limits. Amongst other application envisioned in [104] is the staggered PRI SAR sample regularization.

In the following, the technique will be reviewed and a more detailed explanation of its application to the staggered SAR sample regularization problem will be described.

A uniform array [100] of N elements with inter-element spacing d is depicted in **Figure 18**. The array, the impinging waves and the angle θ are assumed to lie in the xy-plane. For such a system, it is assumed that a phase shift β is applied in the excitation between adjacent elements. Thus, for a given angle θ with the positive y axis (in this example in the xy-plane), the array factor $AF(\theta)$ after normalization by the number of elements N, is given by [100]

$$AF(\theta) = \frac{1}{N} \cdot \sum_{i=1}^{N} \exp\left(\mathrm{j} \cdot (i-1) \cdot \left(-\frac{2 \cdot \pi \cdot d}{\lambda} \cdot \sin(\theta) + \beta \right) \right), \tag{86}$$

where j is the imaginary unit.

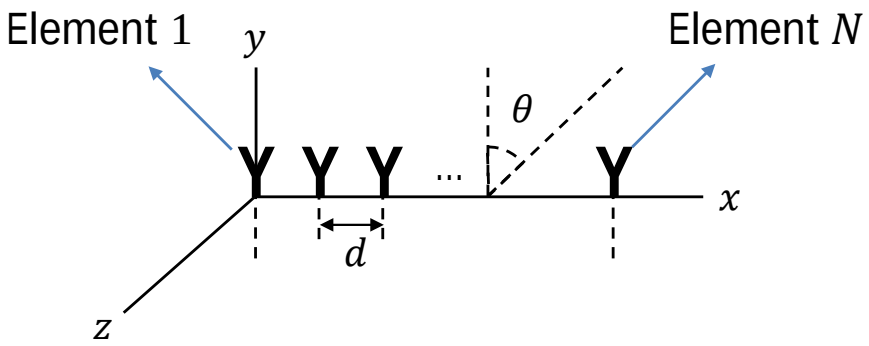

Figure 18. Basic geometry of an uniform array with N elements and inter-element spacing d.

This well-known factor is equal to the resulting pattern for isotropic elements, and is to be superimposed on the element pattern otherwise, describing the contribution of the array geometry to the final patterns. In order to achieve a maximum at a given scan angle θ_0, the phase step of the excitation is chosen as

$$\beta(\theta_0) = \frac{2 \cdot \pi \cdot d}{\lambda} \cdot \sin(\theta_0), \tag{87}$$

thus realizing a maximum by forcing constructive interference at the desired scan angle. For a given β_0, taking into account the $2 \cdot \pi$ phase ambiguity, the resulting pattern has maxima at

$$\theta_n = \arcsin\left(\frac{\lambda}{2 \cdot d} \cdot \frac{(\beta_0 + n \cdot 2 \cdot \pi)}{\pi}\right) = \arcsin\left(\frac{\lambda}{2 \cdot d} \cdot \frac{\beta_0}{\pi} + \frac{n \cdot \lambda}{d}\right), \tag{88}$$

where it should be noted that in this context only angles within $-\pi < \theta_n \leq \pi$ have a physical meaning. These correspond to arguments of the arcsin function, denoted $\psi_n = \frac{\lambda}{2 \cdot d} \cdot \frac{\beta_0}{\pi} + \frac{n \cdot \lambda}{d}$, within $[-1,1]$. From (88) it can be seen that, if $d \leq \lambda/2$, all scan angles $-\pi < \theta_0 \leq \pi$ are possible and the first-order steering ambiguities θ_{-1}, θ_1 lie outside the physical angle range, since $\psi_{-1} < -1$ and $\psi_1 > 1$, which is an ideal

situation from a steering perspective. In fact, $\lambda/2$ can be interpreted as the Nyquist limit on the spatial sampling frequency (cf. Section 4.5).

If $d > \lambda/2$, $|\psi_n| < 1$ is possible for $n \neq 0$, meaning maxima other than the intended one at θ_0 are visible. These are known as *grating lobes* and their position with respect to the desired range of θ_0 should be taken into account during the array design. In practice, the desired range of θ_0 is $|\theta_0| < \theta_{max}$ and often $\theta_{max} \ll 2 \cdot \pi$, so that the presence of *grating lobes* does not prevent the usage of $d > \lambda/2$, as long as the first grating lobes are always outside of the region of interest of the scanning.

The resulting N x 1 beamformer complex weight column vector is given by

$$w(\theta_0) = [1 \quad e^{j\cdot\beta\cdot\theta_0} \quad \dots \quad e^{j\cdot(N-1)\cdot\beta\cdot\theta_0}]^T. \tag{89}$$

Steering of a Reflector's Primary Beam: Conceptual Discussion

The method described in [104] for a reflector system with a multichannel feed consists fundamentally in applying the array steering method to the N_{ch} recorded feed channels to obtain N_{ch} linear combinations with unique phase centers. The concept is illustrated in **Figure 19,** in which the different scan angles θ_{GOAL} and corresponding weights lead to different illuminated portions of the reflector surface. The phase center position is expected to be approximately in the center of the induced current distribution, thus relating to its spatial properties. The initial phase center position for each of the recorded channels – represented by triangles in the figure – is expected to be similar since as a rule the beam patterns are designed to illuminate the whole of the reflector in order to make full use of its area to maximize gain. The phase centers of the linear combinations of the channels – represented by crosses – vary according to the appropriate illuminated portion. As expected, a primary beam narrowing results from the combination of additional array elements. It is also interesting to note that the process can be understood to represent in essence a resampling of phase centers, taking the initial channels as inputs and the linear combinations as outputs. The resampling, which is usually portrayed as an interpolation problem, is achieved by

proper beamforming of the channels. The equivalence between beamforming and interpolation for the solution of this problem will be further explored in Section 4.4.

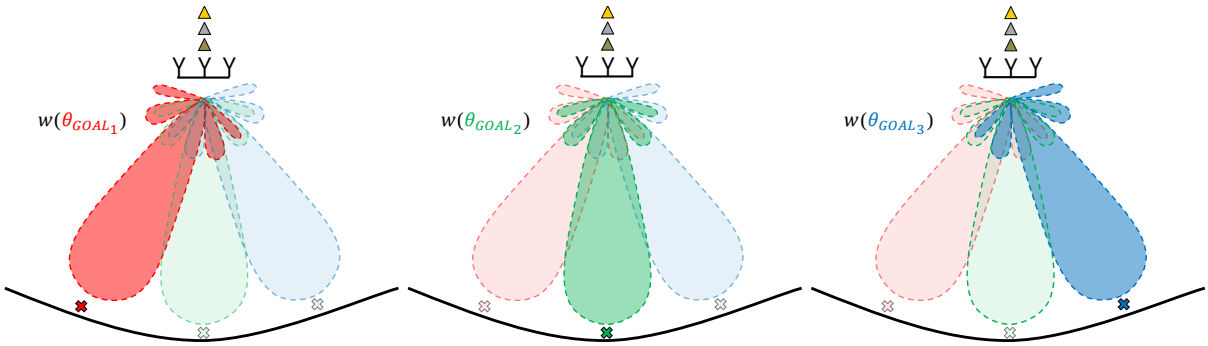

Figure 19. Uniform array steering applied to the feed array of a reflector system, highlighting the use of different weights to shift the illumination to different positions of the reflector. The phase centers of the input channels are represented by triangles – initially very close since all patterns illuminate the whole reflector – and the phase centers of the linear combinations by crosses, indicating that a phase center resampling operation is in place.

An important result in antenna theory is that the current distribution and the induced far field pattern form a Fourier transform pair [100], and some further insight into the method can be obtained by use of basic properties of this transform [105]. As depicted in **Figure 20 (a)**, the primary beam patterns of the individual elements create broad current distributions over the whole reflector, with the same phase center positions for all elements (the displacement in the figure is merely for visualization and has no physical meaning). The spatial shift between the elements is expected to create a phase ramp between the primary illumination patterns, in accordance with the property of the Fourier transform. The induced current on the reflector surface and the far field pattern on ground form in turn another Fourier pair, and thus the broad primary illumination translates into a narrow pattern, whereas the phase ramps translates into physical displacement with respect to the azimuth angle. The resulting secondary patterns are depicted in **Figure 20 (b)**.

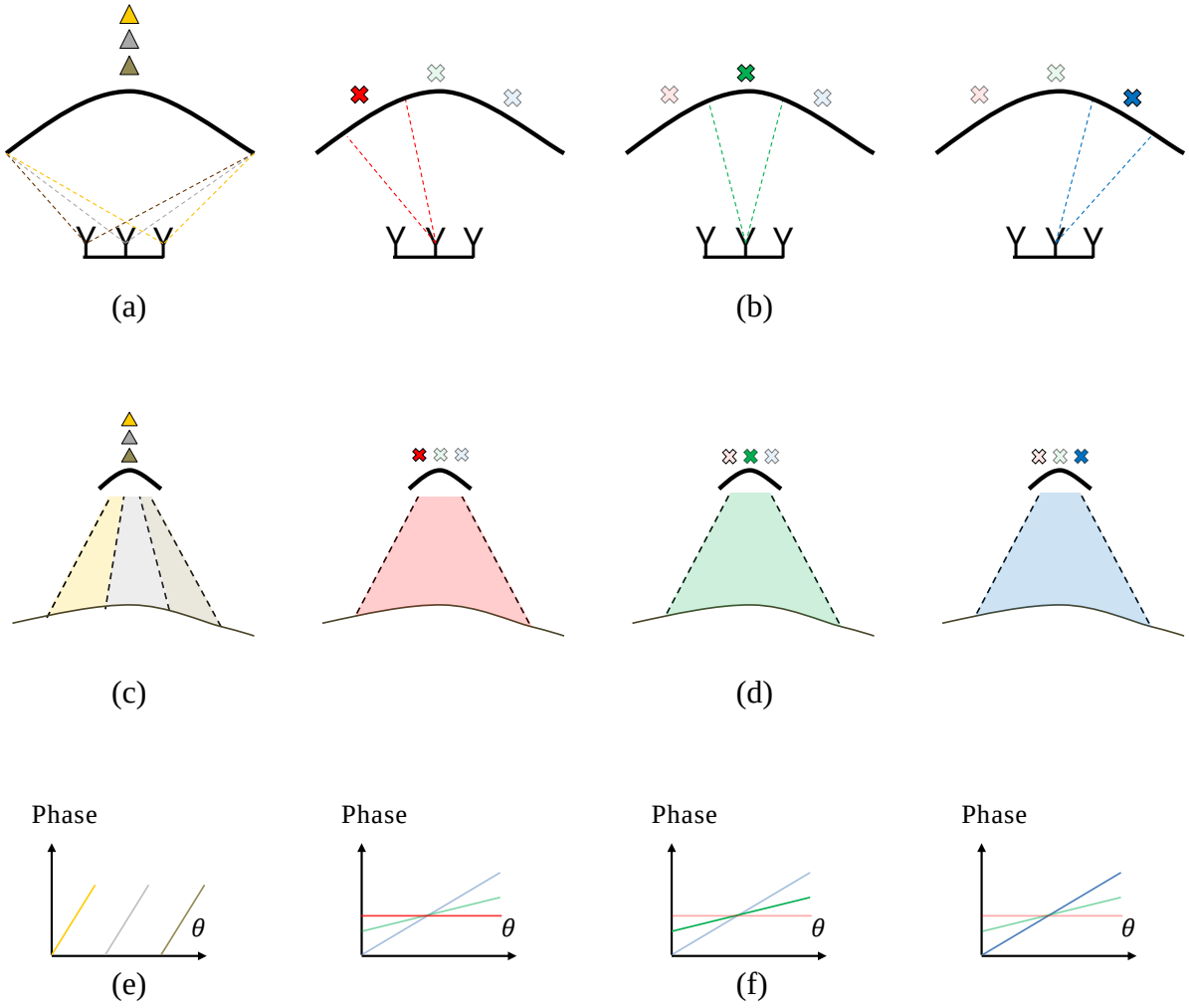

Figure 20. Illustration of the relationship between the feed (primary) patterns and the far field (secondary) patterns, according to the steering of the feed beams. The first row shows an example multichannel feed with three elements, the reflector and the phase centers of the induced current distribution. In (a), the individual feed elements – all of which illuminate the same area – are activated and the azimuth phase center (triangle) is therefore the same for all of them. In (b) steering of the primary beam by combination of the feed elements is applied, highlighting that different phase centers can be achieved. The second row illustrates the far field patterns. In (c) the element's far field patterns are shown, highlighting the common phase center but distinct (Doppler) regions illuminated on ground. In (c) the secondary patterns resulting from steering are considered, showing illumination of the same angular region with different phase centers. The third row shows a schematic plot of phase with an arbitrary reference, to illustrate the angular support and the expected phase relations. In (e) the different angular support of the patterns is highlighted, whereas in (f) the steering leads to a phase ramp difference between the patterns, as a consequence of the phase center shift.

Due to the relationship between the azimuth angle and the Doppler frequency [26], complementary parts of the spectrum of the scene are imaged by the channels. The phase plot on **Figure 20 (c)** highlights this distinct angle support.

When the linear combinations resulting from the steering example in **Figure 19** are considered – as depicted in **Figure 20 (d)** – the broader feed current distribution resulting from the use of more elements creates narrow primary beams spatially shifted by the steering process. Notice that in each case, a different portion of the reflector's surface is illuminated. The far field patterns resulting from the different steering weights – seen in **Figure 20 (e)** – are correspondently broader, and the phase difference between them is approximately a ramp, as represented schematically in **Figure 20 (f)**. Each linear combination thus results in a broader far-field secondary pattern with a different phase center, which translates into an equivalent along-track baseline. This allows the system to be portrayed as an equivalent direct radiating array system which illuminates a wider Doppler spectrum. This is an important result of [104] and is the reason interferometry and HRWS techniques based on phase center diversity may be accordingly applied. Note that the price for the phase center diversity and the broadening of the patterns is a corresponding reduction in their gain, with respect to the patterns of the individual feed elements. A scaling of the SNR is thus to be expected and has to be included as part of the analysis of the technique's performance.

Use of the Technique for Multichannel Staggered SAR Resampling

In order to apply the technique as a suitable processing step to fulfil the needs of a multichannel staggered SAR system, we focus on the phase center resampling interpretation. Indeed, as the phase centers are closely related to the spatial-temporal properties of the channel, they can be directly linked to the position of the samples recorded by the various channels. Recalling the discussion from Section 4.2, the output grid of interest should follow (85). The parameter δt translates into an arbitrary original of the axis in which the equation is defined, and can be incorporated as an

equally arbitrary shift in the output channel position $x_0 = v_{plat} \cdot \delta t$, where v_{plat} is the platform speed. The reason why this parameter is kept is that, since it doesn't change the regularity of the output, it remains as a degree of freedom in the design which can be exploited to minimize the magnitude of the required baseline shift and thus enhance performance, as will be elaborated shortly.

Recalling the input sample position – due to the staggered PRI pulses – from (84) one may write the required baseline shift for the k^{th} output sample in the grid, $1 \leq k \leq N_{ch} \cdot N_{eff}$ as

$$\Delta x[k] = v_{plat} \cdot \left(\frac{k-1}{N_{ch} \cdot \overline{PRF}_{eff}} - t_{rx}[\mathrm{i}_{valid}(k)] \right) + x_0. \tag{90}$$

where $i_{valid}(k)$ denotes a particular pulse in the subset of N_{eff} non-blocked pulses for a given range, and changes according to the index k of the output sample. The resampling operation is illustrated in **Figure 21**.

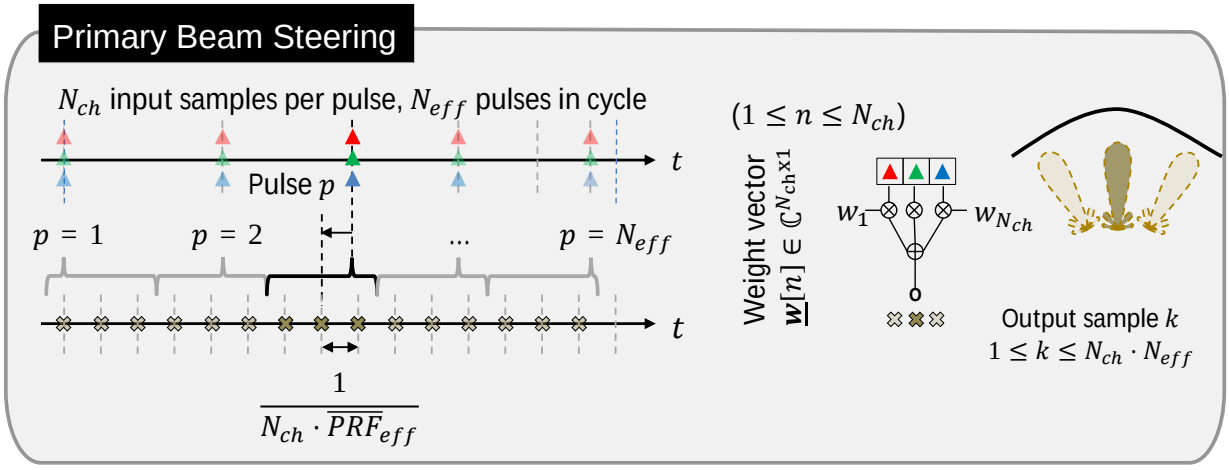

Figure 21. Usage of primary beam steering for multichannel staggered SAR resampling in azimuth. N_{ch} samples of the input grid with the same starting position are used to form a subset of N_{ch} samples of the output grid at each time, using beamforming weights of dimension N_{ch}. For each available pulse, $1 \leq p \leq N_{eff}$, the required phase center shift is different, dependent on the sequence timing.

The indexes $i_{valid}(k)$ assume N_{eff} values within the range $[1, N_{PRI}]$ (recall that not all of the pulses are available for a particular range) and are basically a mapping which

selects the pulse which is used to obtain a given set of N_{ch} output samples in the output grid. Due to the reflector system properties, all N_{ch} physical channels for a given pulse have the same starting position.

The phase center diversity in this case relies on changing the position of the illuminated region of the reflector's surface, thus the available span of phase center shifts in (90) is inherently limited by the physical dimensions of the reflector in azimuth. Border effects contribute further to pattern degradation and performance loss for large phase center shifts, meaning it is desirable to reduce their maximum extent. This can be achieved in the stage of PRI sequence design, by increasing the mean PRF. In the case of a one-pulse gap, the maximum phase center shift $\Delta x_{max}$is half of the maximum distance between samples, i.e.

$$\Delta x_{max} < \frac{2 \cdot v_{plat} \cdot PRI_{max}}{2} = v_{plat} \cdot PRI_{max}. \tag{91}$$

For instance, for an orbit velocity of $7 \cdot 10^3$ m/s and a minimum PRF of 2 kHz, a maximum required shift of around $\Delta x = \pm 3.5$ m is expected, which in turn already requires a rather large reflector of diameter 15 m. Recall that the phase center $p_c = (p_c^{\mathrm{Tx}} + p_c^{\mathrm{Rx}})/2$ is not changed on transmit, meaning that only half of the geometrical change translates into a phase center shift. Since the mean PRF cannot be increased without other implications on the system performance, such as e.g. degradation of range ambiguity levels, the azimuth performance of such a system is in last consequence subject to a compromise between the mean PRF and the reflector size, in the sense that a larger reflector supports a wider range of shifts and allows the usage of a lower PRF, though at increased hardware costs.

Regarding the choice of the degree of freedom δt, a possible criterion is to minimize the worst-case required shifts in terms of absolute value. This can be achieved by a simple two-step procedure, better understood by comparing two possible choices of δt, leading to two different output grids illustrated schematically in **Figure 22**. Evaluating (90) with $\delta t_1 = 0$ yields the grid shown in red, in which $min\{\Delta t_1\} = 0$, as

the first samples coincide, but a given maximum shift $max\{\Delta t_1\}$ is needed in the worst-case. However, choosing the value $\delta t_2 = 0.5 \cdot (min\{\Delta t_1\} + max\{\Delta t_1\})$, based on the shifts of the first grid, equalizes the largest and smallest shifts in absolute value. In fact, $|min\{\Delta t_2\}| = max\{\Delta t_2\} = max\{\Delta t_1\}/2$, half of the worst-case original value. This will lead to a shift of the resulting channel by δt_2 with respect to the reference system of the pulses in (84), an effect which nonetheless may be easily compensated if necessary in posterior processing steps by a phase ramp in Doppler domain, since the output grid is regular. The corresponding phase shift following this equalization approach is a property of the input and output grids, and will be denoted by Δx_{eq} for future reference.

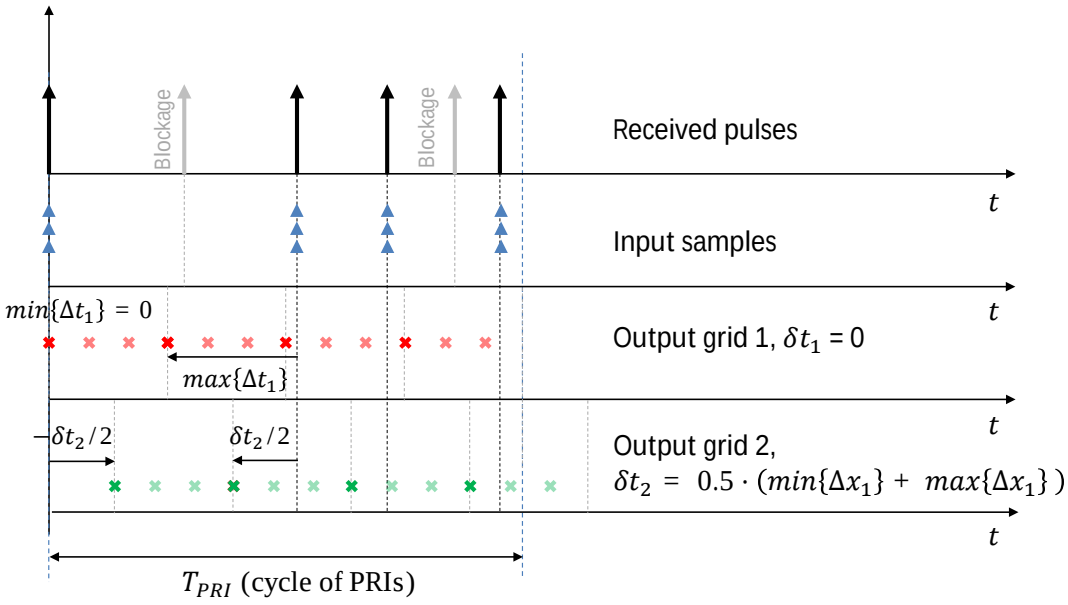

Figure 22. Relevance of the degree of freedom δt in minimizing the absolute value of the worst case required sample (phase center) shift. In the first (red) grid, $\delta t = 0$, leading to a set of shifts Δt_1. As the first sample of the input and output coincide, $min\{\Delta t_1\} = 0$, which is optimal for this sample, but a given $max\{\Delta t_1\}$ will result as a consequence of the parameters. In the second grid, the parameter is chosen based on the results of the first grid, with $\delta t_2 = 0.5 \cdot (min\{\Delta t_1\} + max\{\Delta t_1\})$, and although a larger shift occurs for the first sample, the worst case shift for the sequence is minimized in absolute value. This causes a shift of δt_2 in the output axis with respect to the input, which nonetheless can be easily compensated in posterior processing steps.

In order to use (87) to determine the required phase step $\beta(\theta_{GOAL}[k])$ between the feed elements for the desired output sample k (and hence obtain the beamforming

weights using (89)) one requires a relation between the baseline shift Δx and the scan angle θ_{GOAL}. A method described in [104] to obtain the baseline from a fit of the phase difference between two antenna patterns, for small azimuth angles, may be used to this effect. Taking the sum of the manifold elements – which is also the pattern achieved for a scan angle of zero – as a reference for the baseline measurement, the baseline shift obtained for a given scan angle can be measured. Considering a sweep of possible scan angles according to the particular feed-reflector geometry, an inverse mapping $\theta_{GOAL}(\Delta x)$ from the scan angle to baseline shift can be derived. Letting the complex secondary patterns of the N_{ch} azimuth channels be denoted by $G_n(\theta)$, $1 \leq n \leq N_{ch}$, the antenna system is described by an array manifold vector [106]

$$\underline{\boldsymbol{v}}(\theta) = [G_1(\theta) \quad \ldots \quad G_{N_{ch}}(\theta)]^T \tag{92}$$

which collects the N_{ch} complex antenna patterns $G_i(\theta)$ as a function of the azimuth angle θ.

In an ideal steering scenario, for small scan angles, the patterns resulting from steering correspond to the *sum pattern*

$$G_{sum}(f_\mathrm{D}) = \frac{1}{N_{ch}} \cdot \sum_{i=1}^{N_{ch}} G_i(f_\mathrm{D}), \tag{93}$$

including a linear phase shift. Due to the correspondence between the azimuth angle θ and the Doppler frequency f_D [26], both may be used interchangeably as independent variables of the array manifold. The formation of the output grid is therefore equivalent to the formation of a set of $N_{ch} \cdot N_{eff}$ patterns

$$G_k(f_\mathrm{D}) = \underline{\boldsymbol{w}}[k]^H \cdot \underline{\boldsymbol{v}}(f_\mathrm{D}) \cong G_{sum}(f_\mathrm{D}) \cdot \exp(-\mathrm{j} \cdot 2 \cdot \pi \cdot t_{out}[k] \cdot f_\mathrm{D}), \tag{94}$$

$1 \leq k \leq N_{ch} \cdot N_{eff}$, with suitable phase relations implied by the grid in (85). This interpretation is helpful for the understanding of the method described in the next section.

One should keep in mind that the antenna factor model (86) accounts only for the effect of an isotropic element antenna array, whereas real-world scenarios show non-isotropic patterns. For reflectors e.g. tapering of the feed beam at the borders of the reflector surface is expected. In this context, such a scan angle sweep also offers the opportunity to compensate for the attenuation of the steered pattern's main beam, which inevitably occurs due to the feed element pattern and also due to border effects, for large scan angles. Hence (89) may be augmented by a real multiplicative factor $A(\theta_{GOAL})$ in order to account for this attenuation, yielding in last analysis, for each k in the output grid,

$$w[k] = A\big(\theta_{GOAL}(\Delta x[k])\big) \cdot [1 \quad e^{\mathrm{j}\cdot\beta\cdot\theta_{GOAL}(\Delta x[k])} \quad \dots \quad e^{\mathrm{j}\cdot(N_{ch}-1)\cdot\beta\cdot\theta_{GOAL}(\Delta x[k])}]^T, \qquad (95)$$

where $\theta_{GOAL}(\Delta x[n])$ describes the relation between the scan angle and the required baseline shift, as derived from the fit analysis.

In the next section, a novel method for azimuth resampling will be introduced, employing optimal beamforming concepts. Understanding of the phase center resampling concepts introduced during the description of this section will prove helpful for the understanding of the underlying physical principle.

4.4 The Virtual Beam Synthesis (VBS) Method

4.4.1 General Framework

The method described in Section 4.3 introduces the physical principle behind the change in phase centers, alongside some of its limitations and the involved compromises. It also represents first example of resampling of the signal in azimuth by means of beamforming techniques. In this section, a more general framework for

the resampling is considered, and the novel virtual beam synthesis method is introduced.

In **Figure 23**, the resampling problem is re-examined, considering multiple cycles of the PRI sequence.

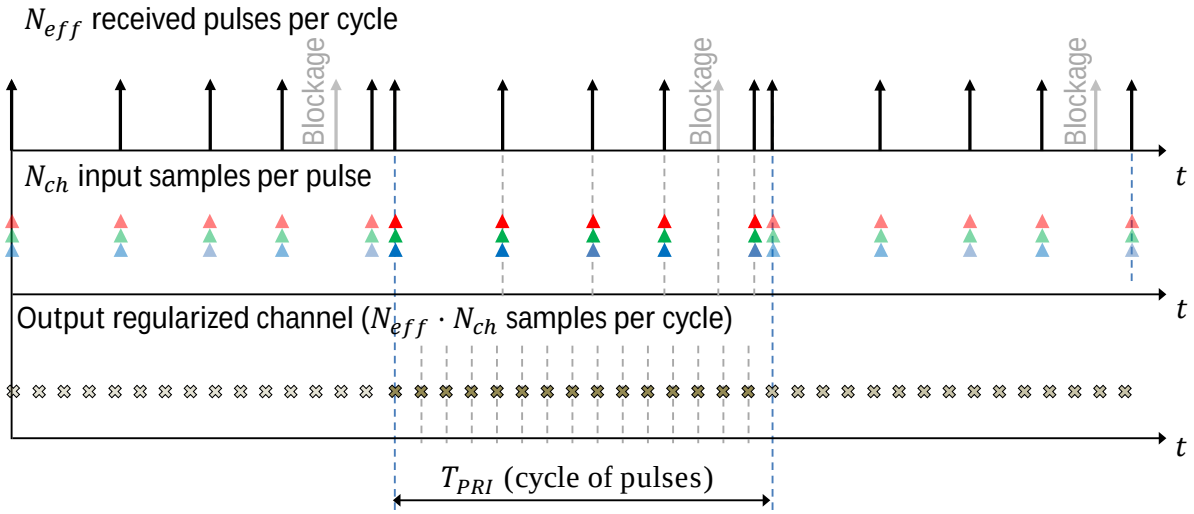

(a)

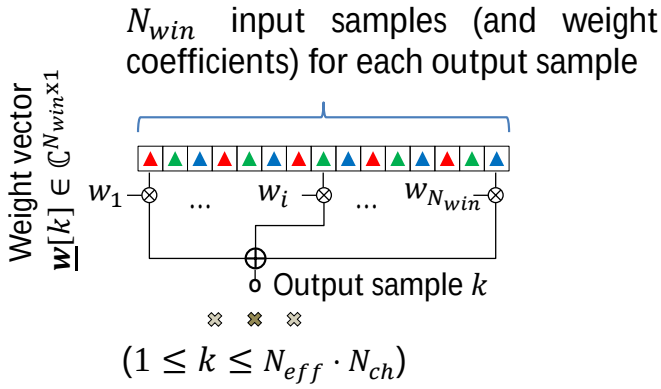

(b)

Figure 23. Required resampling operation focusing on a cycle of pulses of duration T_{PRI}. (a) Overview showing the input grid composed of a set of N_{eff} staggered PRI pulses received per cycle, in a multichannel configuration yielding N_{ch} samples per pulse. The overall sampling results in $N_{eff} \cdot N_{ch}$ samples per cycle, to be rearranged uniformly in the output grid, which is equivalent to a single channel system at a higher sampling rate. (b) Formation of a single sample of index k in the output grid, which is derived from the combination of N_{win} input samples with complex weights.

Figure 23 (a) shows the intended resampling and **Figure 23 (b)** the linear combination of N_{win} samples from various channels in time domain to constitute each output sample. In general, $N_{win} = N_p \cdot N_{ch}$, indicating that the samples of each of the N_{ch} channels are combined over a region of N_p pulses to yield each output sample. In the particular case of $N_p = 1$, conventional beamforming takes place for each pulse separately. This was the case for the primary beam steering of Section 4.3, even though the previous method is based on a different beamforming concept. When $N_p > 1$, interpolation between different pulses is introduced. **Figure 24** illustrates both methods schematically, highlighting their difference.

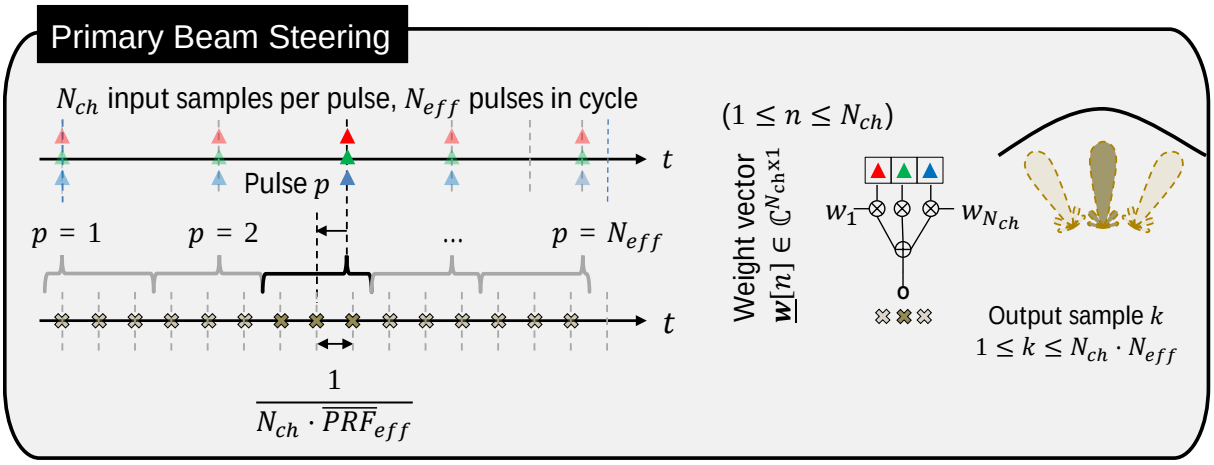

(a)

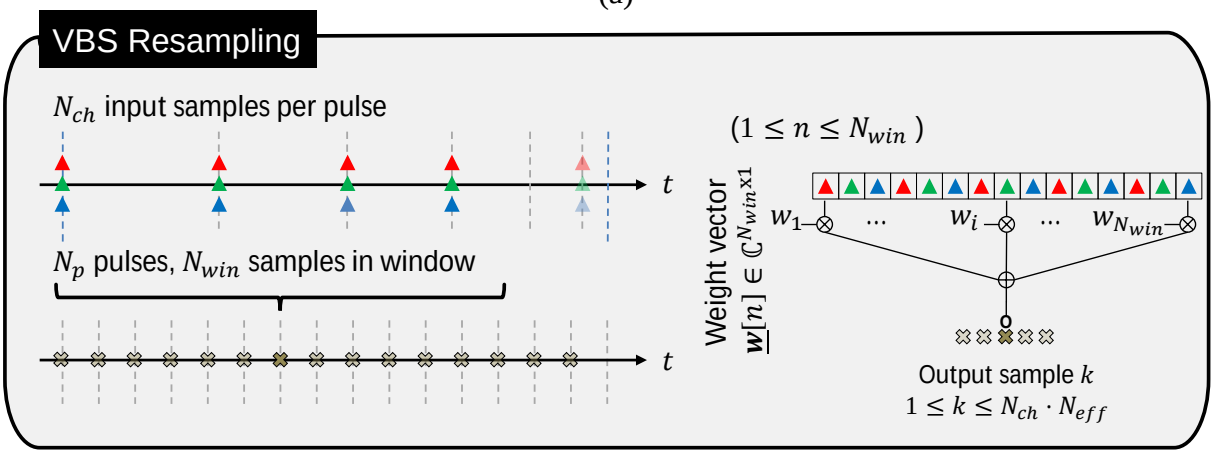

(b)

Figure 24. Multichannel staggered SAR resampling methods. (a) Steering method of Section 4.3, applying beamforming over the N_{ch} channels one pulse at a time. (b) Proposed framework, combining beamforming and interpolation over N_p pulses in a single step.

In general, the weights for the linear combination are, as before, dependent on the output sample's position within the regular grid. One may write

$$s_{out}[k] = \boldsymbol{w}[k]^T \cdot \boldsymbol{s_{in}}, \tag{96}$$

where $1 \leq k \leq N_{eff} \cdot N_{ch}$ is a sample in a cycle of the output grid with index k and $\boldsymbol{w}[k]$ and $\boldsymbol{s_{in}}$ are N_{win}-element complex column vectors representing respectively a set of resampling weights and the signal samples gathered over the input window.

Due to the periodical nature of the sampling of the inputs, a consequence of the cyclical PRI variation, the same set of weights may be applied over several cycles and it is thus sufficient to analyze the outputs over a single period. Note that in the case $N_{win} < N_{ch} \cdot N_{eff}$ a sliding neighborhood consisting of a position dependent subset of the cycle of pulses is employed as input for the uniformly sampled signal recovery. In the case $N_{win} \geq N_{ch} \cdot N_{eff}$ either the full cycle of pulses or more – introducing an overlap between cycles – are employed as inputs.

In order to design the weight vectors $\underline{\boldsymbol{w}}[k]$, it is necessary to describe the input and output grids. The approach followed here is to model each input or output sample by means of an equivalent antenna pattern. We thus interpret the samples at different channels and time positions as part of a "virtual" array manifold, combining the spatial (physical antenna channels) and temporal (different pulses) sampling. In other words, though only N_{ch} physical channels exist, an extended array manifold vector of length $N_{win} = N_p \cdot N_{ch}$ can be considered for the system, augmenting the manifold vector of the physical channels (92) with a phase ramp describing the pulse position in the sampling over the window. We keep the notation $t_{RX}[i]$, $1 \leq i \leq N_p$ for the time instants of the received pulses, and now express the complex (secondary, in case of reflectors) patterns of the N_{ch} azimuth channels by $G_n(f_\mathrm{D})$, $1 \leq n \leq N_{ch}$. The elements of the extended manifold vector $\boldsymbol{v}(f_\mathrm{D})$, which models the input samples over all virtual elements, may then be written as

$$v_m(f_\mathrm{D}) = G_{k_1[m]}(f_\mathrm{D}) \cdot \exp(-\mathrm{j} \cdot 2 \cdot \pi \cdot t_{RX}[k_2[m]] \cdot f_\mathrm{D}), \quad (97)$$

for $1 \leq m \leq N_{win}$, where $k_1[m] = 1 + (m \bmod N_{ch})$ and $k_2[m] = m \,\%\, N_{ch}$. Here, mod denotes the modulo (integer division remainder) operator, and % denotes the quotient of integer (Euclidean) division. This expresses mathematically that, as m varies, the pattern indices $k_1[m]$ vary cyclically from 1 to N_{ch}, and the sample indices $k_2[m]$ repeat themselves N_{ch} times before being incremented by one. This ensures that all azimuth channels for a given pulse position are taken as part of the manifold. Note that the pulse positions thus translate into an equivalent baseline for the virtual patterns of the extended manifold vector.

It should be recalled that a total of $N_{ch} \cdot N_{eff}$ unique sample positions per cycle exist, but samples from neighboring cycles may also be modelled as part of the manifold by considering input sampling instants $t_{RX}[i] \pm n \cdot T_{PRI}$, $1 \leq i \leq N_{eff}$ and integer n. Thus, arbitrary choices of the input window can be considered by proper implementation of (97).

The desired output samples form, as before, a regular grid at the increased sampling rate of $N_{out} = N_{ch} \cdot N_{eff}$ samples per cycle. This can also be described by a set of N_{out} output patterns $G_{GOAL}(f_\mathrm{D}, k)$, one for each sample $1 \leq k \leq N_{out}$, with phase relations implied by

$$G_{GOAL}(f_\mathrm{D}, k) = G_{com}(f_\mathrm{D}) \cdot \exp(-\mathrm{j} \cdot 2 \cdot \pi \cdot t_{out}[k] \cdot f_\mathrm{D}), \quad (98)$$

where $G_{com}(f_\mathrm{D})$ is the common (i.e. k-invariant) component of the patterns of the output samples (which can be considered to be the desired azimuth pattern of the equivalent single-channel system sampled at $N_{ch} \cdot \overline{PRF}_{eff}$ which the multichannel system with azimuth beamforming seeks to emulate) and $t_{out}[k]$ (cf. (85)) denotes the sampling instants of the output grid, being regular by definition. Note that the parameter δt in (85), which doesn't change the regularity property of the grid, can be chosen using the criterion explained in Section 4.3 (cf. **Figure 22**).

It should be noted that $\overline{PRF}_{eff}$ varies with range according to the timing of the PRI sequence, and that range-dependent interpolation needs to be applied. At each range, $\overline{PRF}_{eff} = \frac{N_{eff}}{N_{PRI}} \cdot \overline{PRF}$, where $\overline{PRF}$ is the mean PRF of the sequence. As a constant $PRF_{multi} \leq N_{ch} \cdot \overline{PRF}$ across the swath is desirable, one may either resample each range to its particular $PRF_{multi}(R)$ and introduce an interpolation to $N_{ch} \cdot \overline{PRF}$ (for the simulation results in Chapters 6 and 8 this was done by zero-padding before azimuth compression) or use the method to resample directly to $N_{ch} \cdot \overline{PRF}$ at every range.

The desired output patterns in (98) should be similar to the patterns expected in the case of Section 4.3 (cf. (94)), although the number of elements in the manifold vector is different, since now several pulses are used instead of one. In that case, the phase relations are determined by the scan angle θ_{GOAL} to which the feed pattern is steered to, and the resulting illuminated area on the reflector, implicitly defined by the mapping $\theta_{goal}(\Delta x)$. Moreover, the common component can be assumed to be invariant for small phase center shifts, meaning the pattern is not distorted. This means that $G_{com}(f_{\mathrm{D}})$ is under certain conditions equal to the *sum pattern* $G_{sum}(f_{\mathrm{D}})$ (cf. (93)) of all physical channels. This pattern effectively corresponds to a primary beam steering to the center of the reflector and results in a broader secondary pattern that illuminates approximately the combined beamwidth of the individual elements. The sum pattern of the physical channels remains a reasonable choice for the design of $G_{com}(f_{\mathrm{D}})$ in (98), at least for reflector systems. Particularities of planar systems are addressed in Section 4.5. This parameter remains however a degree of freedom which may also be exploited, as detailed in Section 4.4.5.

It should be noted that the proposed modeling of each sample by means of an equivalent pattern through (97) and (98) effectively transforms the initial resampling problem of Section 4.2 into a more tractable pattern synthesis problem. The method is for this reason referred to as the virtual beam synthesis (VBS) method, and has as main feature the representation of the input and output samples by means of their

corresponding patterns, which are considered to be elements of an extended manifold vector. The patterns may be referred to as "virtual" in the sense that they do not represent physical array antenna elements, but rather mathematical constructs incorporating the information of the antenna patterns alongside the timing of the pulses.

To determine the weights that map the input samples modeled by (97) into the output samples modeled by (98), we propose to apply optimal beamforming which minimizes a cost function of the form

$$\xi(G_{GOAL}(f_{\mathrm{D}},\, k), v_i(f_{\mathrm{D}})), \qquad 1 \le i \le N_{win}, 1 \le k \le N_{out}. \tag{99}$$

Particular choices of the cost function will give rise to variants of the method, which allow emphasizing certain properties of the solution and introducing compromises if necessary, as will be made clear in the next sections. In the flow chart of **Figure 25**,

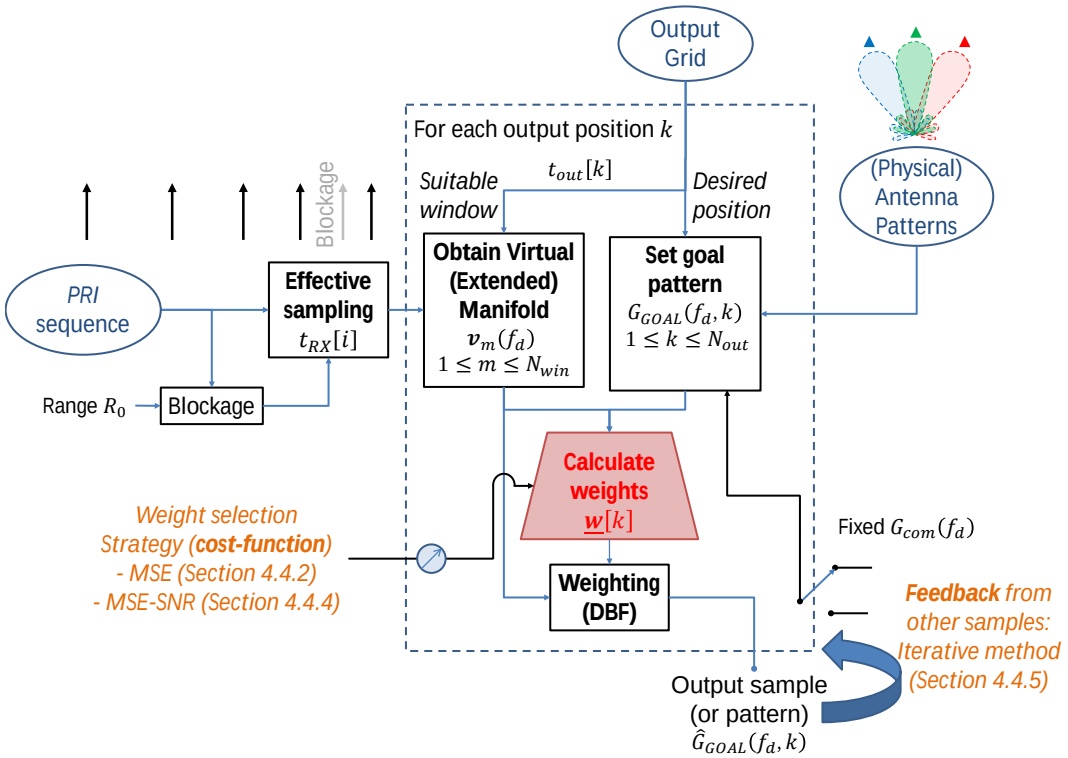

Figure 25. Flow chart highlighting the information needed for the weight calculation. Knowledge of the antenna patterns and sampling conditions is common for all the variations of the VBS method. The choice of the cost function (cf. Sections 4.4.2 and 4.4.4) determines the weight calculation strategy, whereas the iterative method of Section 4.4.5 is a possibility to introduce feedback from other samples in the output grid into the weight calculation.

an overview of the common inputs and the different methods is provided. In all cases, knowledge of the PRI sequence (which leads to the input sample position information according to the timing analysis in Section 3.3.2), the physical antenna patterns and the desired output grid is necessary. For each output position of the grid, a goal pattern is set reflecting the regularity of the grid and the pattern of the equivalent channel $G_{com}(f_{\mathrm{D}})$, which is typically a fixed pre-selected pattern, but can also be iteratively updated as described in Section 4.4.5. The extended manifold is then used to implement this pattern with weights, obtained by minimizing a cost function, generically described in (99). Sections 4.4.2 to 4.4.5 analyse different options of cost functions, starting with the best possible implementation of the regular grid, and later allowing for a compromise between that approach and rejection of noise.

4.4.2 Optimal Mean Square Error (MSE) Criterion

The first choice of the cost function (98) is based on the *least-squares (LS) pattern synthesis* technique discussed in [106]. The original LS pattern synthesis problem may be described as follows: given an arbitrary N_{win}-element array manifold vector $\underline{\boldsymbol{v}}(\theta)$, derive the beamforming weight vector $\underline{\boldsymbol{w}}$ that leads to the closest approximation

$$\hat{G}_{GOAL}(\theta) = \underline{\boldsymbol{w}}^{H} \cdot \underline{\boldsymbol{v}}(\theta) \tag{100}$$

of a desired pattern $G_{GOAL}(\theta)$. The pattern's azimuth angle θ and the instantaneous Doppler frequency f_{D} are related by the well know mapping [26]

$$f_{\mathrm{D}} = \frac{2}{\lambda} \cdot v_{plat} \cdot \sin(\theta), \tag{101}$$

where λ is the carrier wavelength. One can therefore equivalently consider the patterns a function of Doppler frequency, which will be the adopted notation in the following. Furthermore, with the aim of solving (98), the notation is adapted to consider a set of goal patterns. We thus write $G_{GOAL}(f_{\mathrm{D}}, k)$, and correspondingly $\underline{\boldsymbol{w}}[k]$ and $\hat{G}_{GOAL}(f_{\mathrm{D}}, k)$, for $1 \leq k \leq N_{out}$.

The solution is achieved by minimizing a cost function that measures the integral of the mean squared error (MSE) between the goal pattern and the approximation, namely,

$$\xi_{MSE}[k] = \int_{f_1}^{f_2} \left(G_{GOAL}(f_\mathrm{D}, k) - \hat{G}_{GOAL}(f_\mathrm{D}, k) \right)^2 \mathrm{d}f_\mathrm{D}, \tag{102}$$

where the region of integration has to be appropriately chosen, and a Doppler-frequency dependent weighting of the integral may also be applied. In the multichannel resampling context, PRF_{multi} is for instance a meaningful choice. Additional weights in the integration can also be introduced, even though the squared error magnitude is inherently proportional and hence weighted by the squared pattern magnitude itself.

Expanding (102) using the adapted, i.e. k-dependent, (100) leads to

$$\xi_{MSE}[k] = p_G[k] - \underline{\boldsymbol{w}}[k]^H \cdot \underline{\boldsymbol{\sigma}}_{\boldsymbol{G}}[k] - \underline{\boldsymbol{w}}[k]^T \cdot \underline{\boldsymbol{\sigma}}_{\boldsymbol{G}}^*[k] + \underline{\boldsymbol{w}}[k]^H \cdot \underline{\boldsymbol{R}}_{\boldsymbol{v}} \cdot \underline{\boldsymbol{w}}[k], \tag{103}$$

where

$$\underline{\boldsymbol{R}}_{\boldsymbol{v}} \triangleq \int_{f_1}^{f_2} \underline{\boldsymbol{v}}(f_\mathrm{D}) \cdot \underline{\boldsymbol{v}}(f_\mathrm{D})^H \mathrm{d}f_\mathrm{D} \tag{104}$$

is the N_{win} x N_{win} array manifold autocorrelation matrix, which only depends on the inputs;

$$\underline{\boldsymbol{\sigma}}_{\boldsymbol{G}}[k] \triangleq \int_{f_1}^{f_2} G_{GOAL}^*(f_\mathrm{D}, k) \cdot \underline{\boldsymbol{v}}(f_\mathrm{D}) \mathrm{d}f_\mathrm{D} \tag{105}$$

is an N_{win} x 1 vector, describing the cross-correlation between the goal pattern $G_{GOAL}(f_\mathrm{D}, k)$ and the manifold, and

$$p_G \triangleq \int_{f_1}^{f_2} \left| G_{GOAL}(f_\mathrm{D}) \right|^2 \mathrm{d}f_\mathrm{D} \tag{106}$$

is a scalar describing the goal pattern's power.

The solution to the optimal weights problem is obtained by applying the complex gradient operator [107] with respect to the conjugate $\underline{\boldsymbol{w}}[k]^H$ of the weights and equating the result to the null vector, treating the weights $\underline{\boldsymbol{w}}[k]$ themselves as a constant in the derivation. This leads to the optimal weights with respect to the MSE, $\underline{\boldsymbol{W}}_{MSE}[k]$ as

$$\nabla \underline{\boldsymbol{w}}^H (\xi_{MSE}[k])|_{\underline{\boldsymbol{w}}[k]=\underline{\boldsymbol{w}}_{MSE}[k]} = \underline{\boldsymbol{R}}_{\boldsymbol{v}} \cdot \underline{\boldsymbol{w}}_{MSE}[k] - \underline{\boldsymbol{\sigma}}_G[k] = \underline{\mathbf{0}}$$

$$\underline{\boldsymbol{w}}_{MSE}[k] = \underline{\boldsymbol{R}}_{\boldsymbol{v}}{}^{-\mathbf{1}} \cdot \underline{\boldsymbol{\sigma}}_G[k], \tag{107}$$

a solution with the desirable property of achieving the closest possible implementation of the desired set of output patterns.

A particular case which serves as a sanity check for this result is that of a goal pattern which represents one of the elements of the array manifold, i.e. $G_{GOAL}(f_\mathrm{D}, k) = v_i(f_\mathrm{D})$ for a particular i. In this case, $\underline{\boldsymbol{\sigma}}_G[k]$ becomes the i^{th} column of the matrix $\underline{\boldsymbol{R}}_{\boldsymbol{v}}$ and consequently the weights are $\delta[i]$ – where $\delta[n]$, $n \in \mathbb{Z}$ is the discrete Dirac delta. This means that the i^{th} element is appropriately selected as a solution and the other weight elements are null.

Evaluation of (103) with the optimal weights of (107) leads to the minimum of the cost function,

$$\xi_{MSE_{min}}[k] = \underline{\boldsymbol{w}}_{MSE}[k]^H \cdot (\underline{\boldsymbol{R}}_{\boldsymbol{v}} \cdot \underline{\boldsymbol{w}}_{MSE}[k] - \underline{\boldsymbol{\sigma}}_{\boldsymbol{G}}[k]) - \underline{\boldsymbol{w}}_{MSE}[k]^T \cdot \underline{\boldsymbol{\sigma}}_{\boldsymbol{G}}^*[k] + p_G[k]$$

$$\xi_{MSE_{min}}[k] = p_G[k] - \underline{\boldsymbol{\sigma}}_{\boldsymbol{G}}^T[k] \cdot \left(\underline{\boldsymbol{R}}_{\boldsymbol{v}}{}^{-\mathbf{1}}\right)^T \cdot \underline{\boldsymbol{\sigma}}_{\boldsymbol{G}}^*[k], \tag{108}$$

which is a property of the array manifold and the goal pattern, describing how well the pattern can be approximated by a combination of the manifold elements.

The structure of (107), notably the dependence on $\underline{\boldsymbol{\sigma}}_G[k]$, implies that the method automatically selects – from the physical channels in different positions during the pulse cycles – the elements with higher correlation to a particular output position. Even though the pulse separation induced baselines introduce decorrelation between the elements of the proposed extended manifold, no degradation in terms of MSE ensues from the use of additional channels. Should they be too distant from the desired sample position and thus uncorrelated, the corresponding weights are accordingly very low in magnitude, according to the corresponding element of $\underline{\boldsymbol{\sigma}}_G[k]$. This small gain avoids therefore a possible degradation from uncorrelated samples. In fact, (108) implies that the MSE corresponding to the best approximation (which is in general nonzero) is given by the goal pattern's power minus the norm of $\underline{\boldsymbol{\sigma}}_G[k]$ weighted by $\underline{\boldsymbol{R}}_{\boldsymbol{v}}^{-1}$. This means that extending the manifold (and thus getting a longer $\underline{\boldsymbol{\sigma}}_G[k]$) in principle cannot reduce the quality of the approximation, since it causes $\xi_{MSE_{min}}$ to get smaller [14]. Clearly, the entries of $\underline{\boldsymbol{\sigma}}_{\boldsymbol{G}}[k]$ show lower and lower magnitudes with increasing distance from the goal pattern's phase center position, leading to a saturation effect in the sense that additional elements start having little impact. The fact that for a staggered SAR system an overall oversampling in azimuth is expected means that some correlation and therefore performance gain is however possible from the usage of neighboring pulses.

The method introduced in this section will be referred to as Mean Square Error Virtual Beam Synthesis (MSE-VBS), to emphasize the choice of the cost function. An alternative cost function is examined in the two following sections.

[14] This is true as long as the model (97) holds, though in practice the delay (phase ramp) is not an adequate representation for the relationship between arbitrarily distant pulses, as effects like range cell migration (RCM) and scene decorrelation come into play if the corresponding baseline is too large, resulting in an effective limitation of the feasible pulse neighborhood.

4.4.3 Optimal Signal to Noise Ratio (SNR) Criterion

A complementary approach is to combine the array manifold elements so as to maximize the SNR of the achieved pattern $G_{DBF}(f_\mathrm{D}) = \boldsymbol{w}^H \cdot \underline{\boldsymbol{v}}(f_\mathrm{D})$. The SAR signal in azimuth has a power spectral density which is proportional to the squared magnitude of the antenna patterns[15] [108], [109], i.e. $S(f_\mathrm{D}) = \gamma_0 \cdot |G_{DBF}(f_\mathrm{D})|^2$, where γ_0 is a constant. The signal power within the spectral region $[f_1, f_2]$ (usually chosen to reflect the processed bandwidth Bw_{proc}) can thus be calculated as

$$p_s = \int_{f_1}^{f_2} S(f_D)\,\mathrm{d}f_\mathrm{D} = \gamma_0 \cdot \int_{f_1}^{f_2} |G_{DBF}(f_\mathrm{D})|^2 \mathrm{d}f_\mathrm{D}$$
$$p_s = \gamma_0 \cdot \underline{\boldsymbol{w}}^H \cdot \left(\int_{f_1}^{f_2} \underline{\boldsymbol{v}}(f_\mathrm{D}) \cdot \underline{\boldsymbol{v}}^H(f_\mathrm{D})\,\mathrm{d}f_\mathrm{D}\right) \cdot \underline{\boldsymbol{w}} = \gamma_0 \cdot \underline{\boldsymbol{w}}^H \cdot \underline{\boldsymbol{R}}_{\boldsymbol{v}} \cdot \underline{\boldsymbol{w}}. \tag{109}$$

The noise however is assumed to be white, uncorrelated between receivers and with equal variance for all elements, with spectral density $\eta_0(f_\mathrm{D}) = \eta_0$ on each array element and total power $\sigma_0^2 = \eta_0 \cdot Bw_{proc}$ over the processed bandwidth. The noise power in the output signal is hence

$$p_n = \underline{\boldsymbol{w}}^H \cdot \underline{\boldsymbol{w}} \cdot \int_{Bw_{proc}} \eta_0 \cdot \mathrm{d}f_\mathrm{D} = \sigma_0^2 \cdot \underline{\boldsymbol{w}}^H \cdot \underline{\boldsymbol{w}}. \tag{110}$$

This leads to an SNR after beamforming – evaluated over the processed bandwidth – given by

$$SNR_{DBF}(\underline{\boldsymbol{w}}) = \frac{p_s}{p_n} = \frac{\gamma_0}{\sigma_0^2} \cdot \frac{\underline{\boldsymbol{w}}^H \cdot \underline{\boldsymbol{R}}_{\boldsymbol{v}} \cdot \underline{\boldsymbol{w}}}{\underline{\boldsymbol{w}}^H \cdot \underline{\boldsymbol{w}}} \tag{111}$$

[15] The spectrum is proportional to the two-way antenna pattern. In this derivation, the weights are implicitly assumed to be the same for Tx and Rx. In the case of DBF on receive only, the Tx pattern cannot be influenced by the DBF weights and that pattern introduces an additional spectral weighting which influences the signal power p_s. The result obtained here is thus only optimal with respect to a flat Tx pattern, but nonetheless still relevant for improvement of the SNR.

In order to remove the system-parameter dependent constants and generate a figure which depends only on the array manifold and the given weights, one may consider normalizing (111), which is the SNR of the achieved pattern $G_{DBF}(f_\mathrm{D})$, to the SNR of the common pattern $G_{com}(f_\mathrm{D})$. Recalling the interpretation of $G_{com}(f_\mathrm{D})$ as the pattern of the equivalent single-channel system the multichannel staggered system should emulate after DBF, the normalized (111) thus becomes the SNR scaling with respect to an ideal system which is regularly sampled and has the pattern $G_{com}(f_\mathrm{D})$. Thus, the quantity may be interpreted as the impact of the (imperfect) resampling over the SNR.

If, as discussed in Section 4.4.1, $G_{com}(f_\mathrm{D}) = G_{sum}(f_\mathrm{D})$ (a meaningful choice of common pattern for reflector systems to re-examined for planar antennas in Section 4.5), one has the special case of unitary weights $\underline{\boldsymbol{w}}_{sum} = [1, 1, \ldots, 1]^T$ – leading to the sum pattern (93) – as a reference:

$$SNR_{sum} = \frac{\gamma_0}{\sigma_0^2} \cdot \frac{1}{N_{win}} \cdot \int_{f_1}^{f_2} |G_{sum}(f_\mathrm{D})|^2 \mathrm{d}f_\mathrm{D} = \frac{\gamma_0}{\sigma_0^2} \cdot \frac{1}{N_{win}} \cdot \int_{f_1}^{f_2} \left| \sum_{i=1}^{N_{win}} v_i(f_\mathrm{D}) \right|^2 \mathrm{d}f_\mathrm{D}. \tag{112}$$

Let the SNR scaling with respect to the sum pattern[16] be defined as

$$\Phi_{SNR}(\underline{\boldsymbol{w}}) = \frac{SNR_{DBF}(\underline{\boldsymbol{w}})}{SNR_{sum}}$$

$$\Phi_{SNR}(\underline{\boldsymbol{w}}) = \frac{N_{win}}{\int_{f_1}^{f_2} \left| \sum_{i=1}^{N_{win}} v_i(f_\mathrm{D}) \right|^2 \mathrm{d}f_\mathrm{D}} \cdot \frac{1}{\underline{\boldsymbol{w}}^H \cdot \underline{\boldsymbol{w}}} \cdot \int_{f_1}^{f_2} \left| \hat{G}_{GOAL}(f_\mathrm{D}, k) \right|^2 \mathrm{d}f_\mathrm{D}$$

$$\Phi_{SNR}(\underline{\boldsymbol{w}}) = \frac{N_{win}}{\int_{f_1}^{f_2} \left| \sum_{i=1}^{N_{win}} v_i(f_\mathrm{D}) \right|^2 \mathrm{d}f_\mathrm{D}} \cdot \frac{\underline{\boldsymbol{w}}^H \cdot \underline{\boldsymbol{R}}_{\boldsymbol{v}} \cdot \underline{\boldsymbol{w}}}{\underline{\boldsymbol{w}}^H \cdot \underline{\boldsymbol{w}}}. \tag{113}$$

[16] In general, the noise scaling should be defined with respect to the *common pattern*, should the common pattern differ from the sum pattern.

Therefore, in order to maximize the SNR of the resulting pattern, one may propose the cost function

$$\xi_{SNR} = \frac{\underline{\boldsymbol{w}}^H \cdot \underline{\boldsymbol{R}}_{\boldsymbol{v}} \cdot \underline{\boldsymbol{w}}}{\underline{\boldsymbol{w}}^H \cdot \underline{\boldsymbol{w}}}, \tag{114}$$

corresponding to the normalized SNR of the pattern. Denoting the elements of the N_{win} by N_{win} matrix $\underline{\boldsymbol{R}}_{\boldsymbol{v}}$ by r_{ij} and the elements of the N_{win}-element weight vector $\underline{\boldsymbol{w}}$ by w_i, one may rewrite (114) as

$$\xi_{SNR} = \frac{\sum_{i=1}^{N_{win}} r_{ii} \cdot |w_i|^2 + \sum_{j=1}^{N} \sum_{\substack{i=1 \\ j \neq i}}^{N} r_{ji} \cdot w_i^* \cdot w_j}{\sum_{i=1}^{N_{win}} |w_i|^2} \tag{115}$$

a form in which some SNR properties of the manifold and pattern after beamforming may be highlighted. Recalling that r_{ii} is proportional to the power in each manifold element and r_{ji}, $j \neq i$ is the cross-correlation between the manifold element's patterns, it is apparent that, for a given set of weights, a better SNR is obtained if the manifold elements are more correlated, whereas a completely uncorrelated manifold yields poor gain. Conversely, given a manifold, the solution to optimize the SNR involves activating the elements to the extent that the additional signal power brought by their self and cross-correlation outweighs the penalty for activating additional elements (more entries w_i and thus a larger denominator). In contrast to the MSE cost function $\xi_{MSE}[k]$ in (103), which as discussed in the previous section tends to always improve as more elements are added to the manifold (as visible from (108)), ξ_{SNR} is seen to be adversely affected by the manifold extension beyond a certain correlation threshold, as more noise is gathered for little contribution to the signal power.

The optimum weights with respect to the SNR cost function $\underline{\boldsymbol{w}}_{SNR}$ may be obtained by applying to (114) the same optimization procedure as in Section 4.4.2. This corresponds to

$$\nabla \underline{\boldsymbol{w}}^{H}(\xi_{SNR})|_{\underline{\boldsymbol{w}}=\underline{\boldsymbol{w}}_{SNR}} = \underline{\mathbf{0}}$$

$$\left.\frac{\left(\underline{\boldsymbol{w}}^{\boldsymbol{H}} \cdot \underline{\boldsymbol{w}}\right) \cdot \left(\underline{\boldsymbol{R}}_{\boldsymbol{v}} \cdot \underline{\boldsymbol{w}}\right) - \left(\underline{\boldsymbol{w}}^{\boldsymbol{H}} \cdot \underline{\boldsymbol{R}}_{\boldsymbol{v}} \cdot \underline{\boldsymbol{w}}\right) \cdot \underline{\boldsymbol{w}}}{\left(\underline{\boldsymbol{w}}^{\boldsymbol{H}} \cdot \underline{\boldsymbol{w}}\right)^{2}}\right|_{\underline{\boldsymbol{w}}=\underline{\boldsymbol{w}}_{\boldsymbol{SNR}}} = \underline{\mathbf{0}}$$

$$\underline{\boldsymbol{R}}_{\boldsymbol{v}} \cdot \underline{\boldsymbol{w}}_{SNR} = \frac{\left(\underline{\boldsymbol{w}}_{SNR}{}^{H} \cdot \underline{\boldsymbol{R}}_{\boldsymbol{v}} \cdot \underline{\boldsymbol{w}}_{SNR}\right)}{\left(\underline{\boldsymbol{w}}_{SNR}{}^{H} \cdot \underline{\boldsymbol{w}}_{SNR}\right)} \cdot \underline{\boldsymbol{w}}_{SNR} \triangleq \gamma \cdot \underline{\boldsymbol{w}}_{SNR}, \tag{116}$$

where γ is a scalar, since $\underline{\boldsymbol{w}}_{SNR}$ is an N_{win}x 1 vector and $\underline{\boldsymbol{R}}_{\boldsymbol{v}}$ a N_{win}x N_{win} matrix. In fact, (116) represents an eigenvalue problem with respect to the matrix $\underline{\boldsymbol{R}}_{\boldsymbol{v}}$. The output SNR is given by the eigenvalue γ, from which it is clear that the desired solution $\underline{\boldsymbol{w}}_{SNR}$ is the eigenvector of $\underline{\boldsymbol{R}}_{\boldsymbol{v}}$ corresponding to the largest eigenvalue. The same result is obtained in [106] using norm-constrained optimization of (114). It should be noted that this beamformer cannot be directly applied to the resampling problem of Section 4.2 since the weights do not account for the phase center positions. Nonetheless, the formulation discussed here – especially (113) and (114) – and the SNR properties of the extended manifold are of interest for the extension proposed in the next section 4.4.4.

4.4.4 Joint MSE-SNR Optimization Criterion

The weights obtained in Section 4.4.2 achieve the closest implementation of a desired pattern $G_{GOAL}(f_{\mathrm{D}}, k)$ without any regard for the output SNR, while those of 4.4.3 maximize the resulting SNR of the output beam but have no constraint linking them to a given pattern $G_{GOAL}(f_{\mathrm{D}}, k)$. For improved flexibility, one can think of a compromise between the two methods, so that fidelity to the goal patterns (and thus to the regular grid) – described by means of the MSE – and the resulting SNR can be simultaneously considered, countering the possibly negative impact of the manifold extension in terms of output SNR.

We propose to achieve this by means of the joint MSE-SNR cost function[17]

$$\xi_J[k] = (1-\alpha)\cdot\frac{\xi_{MSE}[k]}{n_{MSE}} + \alpha\cdot\frac{n_{SNR}}{\xi_{SNR}[k]}, \tag{117}$$

where n_{MSE} and n_{SNR} are normalization factors which allow the MSE and SNR to be matched in terms of numerical values and the parameter α is a SNR sensitivity factor[18] in the interval [0,1] which controls how much emphasis is given to the SNR in the joint optimization. The limit-case cost functions $\xi_{MSE}[k]$ and $\xi_{SNR}[k]$ are defined by (102) and (114) (augmented by the output sample index k), respectively.

We seek to minimize (117) using the aforementioned gradient technique, leading to

$$\nabla_{\underline{\boldsymbol{w}}^H}(\xi_J)|_{\underline{\boldsymbol{w}}=\underline{\boldsymbol{w}}_J[k]} = \underline{\mathbf{0}}$$

$$\frac{(1-\alpha)}{n_{MSE}}\cdot\left(\underline{\boldsymbol{R}}_{\boldsymbol{v}}\cdot\underline{\boldsymbol{w}}-\underline{\boldsymbol{\sigma}}_G\right) + \alpha\cdot n_{SNR} \cdot\frac{\left(\underline{\boldsymbol{w}}^H\cdot\underline{\boldsymbol{R}}_{\boldsymbol{v}}\cdot\underline{\boldsymbol{w}}\right)\cdot\underline{\boldsymbol{w}}-\left(\underline{\boldsymbol{w}}^H\cdot\underline{\boldsymbol{w}}\right)\cdot\left(\underline{\boldsymbol{R}}_{\boldsymbol{v}}\cdot\underline{\boldsymbol{w}}\right)}{\left(\underline{\boldsymbol{w}}^H\cdot\underline{\boldsymbol{R}}_{\boldsymbol{v}}\cdot\underline{\boldsymbol{w}}\right)^2}\Bigg|_{\boldsymbol{w}=\underline{\boldsymbol{w}}_J[k]} = \underline{\mathbf{0}}$$

$$\left[\left(\frac{(1-\alpha)\cdot\left(s_{Rw}(\underline{\boldsymbol{w}})\right)^2}{n_{MSE}} - \alpha\cdot n_{SNR}\cdot s_w(\underline{\boldsymbol{w}})\right)\cdot\underline{\boldsymbol{R}}_{\boldsymbol{v}} + \alpha\cdot n_{SNR}\cdot s_{Rw}(\underline{\boldsymbol{w}})\cdot\underline{\boldsymbol{I}}\right]\cdot\underline{\boldsymbol{w}} - \frac{(1-\alpha)}{n_{MSE}}\cdot\left(s_w(\underline{\boldsymbol{w}})\right)^2\cdot\underline{\boldsymbol{\sigma}}_G\Bigg|_{\boldsymbol{w}=\underline{\boldsymbol{w}}_J[k]} = \underline{\mathbf{0}}, \tag{118}$$

where $s_{Rw}(\underline{\boldsymbol{w}}) = \underline{\boldsymbol{w}}^H\cdot\underline{\boldsymbol{R}}_{\boldsymbol{v}}\cdot\underline{\boldsymbol{w}}$ is the squared norm of the weight vector $\underline{\boldsymbol{w}}$ and $s_{Rw}(\underline{\boldsymbol{w}}) = \underline{\boldsymbol{w}}^H\cdot\underline{\boldsymbol{R}}_{\boldsymbol{v}}\cdot\underline{\boldsymbol{w}}$ is the squared norm of $\underline{\boldsymbol{w}}$ weighted by $\underline{\boldsymbol{R}}_{\boldsymbol{v}}$. Clearly, (118)

[17] A similar strategy is adopted in [48], though in a different optimization context.

[18] Numerically speaking only the ratio of the weights between the coefficients of the two cost functions in (117) matters for the solution, so that a single parameter would suffice. The separation into the three parameters is however preferred to enable a more obvious interpretation of the design goal of the algorithm.

represents a non-linear system of equations on the N_{win} complex weights sought. It can nonetheless be solved numerically by Newton-like methods using $\underline{\boldsymbol{w}}_{MSE}[k]$ or $\underline{\boldsymbol{w}}_{SNR}[k]$ – the limit-case solutions – as first guesses. Alternatively, a simple iterative method to solve (118) could be to fix the scalars $s_{Rw}\left(\underline{\boldsymbol{w}}_i[k]\right)$ and $s_w\left(\underline{\boldsymbol{w}}_i[k]\right)$ as constants at iteration i and solve the resulting *linear* system of equations to obtain $\underline{\boldsymbol{w}}_i[k]$, updating the squared norms $s_w\left(\underline{\boldsymbol{w}}_{i+1}[k]\right)$ and $s_{Rw}\left(\underline{\boldsymbol{w}}_{i+1}[k]\right)$ with the new solution in order to start iteration $i + 1$. According to the magnitude of α, one could start from either $\underline{\boldsymbol{w}}_0 = \underline{\boldsymbol{w}}_{MSE}[k]$ (closer to the solution for small α) or $\underline{\boldsymbol{w}}_0 = \underline{\boldsymbol{w}}_{SNR}[k]$ and monitor the magnitude of the update of the solution $\left\|\underline{\boldsymbol{w}}_i[k] - \underline{\boldsymbol{w}}_{i-1}[k]\right\|$ as a stopping criterion. This is illustrated in the flow chart of **Figure 26**.

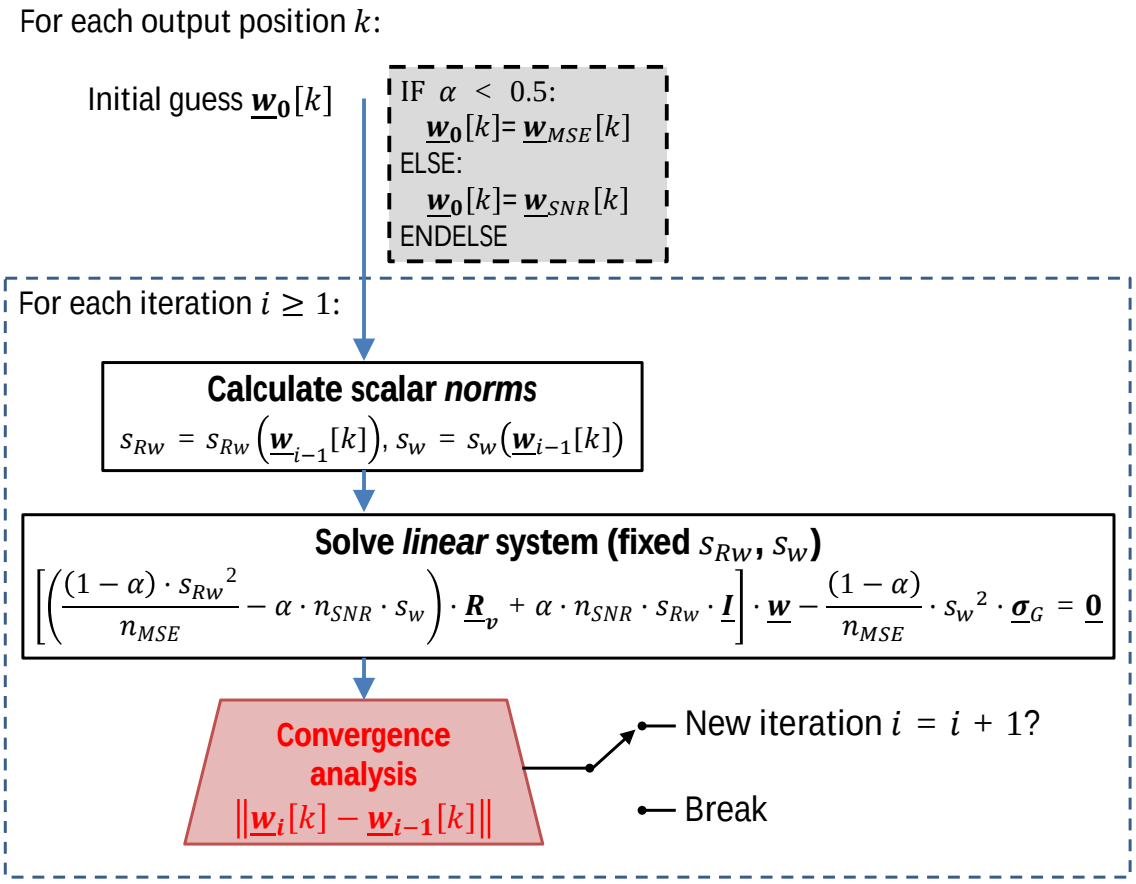

Figure 26. Block diagram describing fixed-norm algorithm for iterative solution of (118).

The method described in this section, whose goal is to introduce a compromise between signal-to-noise ratio and mean squared error, will be referred to, in short, as

the joint MSE-SNR Virtual Beam Synthesis (MSE-SNR-VBS) method, and can be interpreted as an extension that complements the MSE-VBS method of Section 4.4.2.

The next section — in contrast to this and the previous one — does not introduce a new cost function, but rather addresses the so far neglected issue of equalizing the performance over the output grid by introducing an iterative technique that may be applied regardless of the cost function.

4.4.5 Iterative Pattern Synthesis: Update of the Goal Patterns to Equalize Performance over the Grid

The optimality of the MSE method (cf. Section 4.4.2) in the least-squares sense means that the implemented patterns $\hat{G}_{GOAL}(f_\mathrm{D}) = \underline{w}^H \cdot \underline{v}(f_\mathrm{D})$ are as close as possible to the goal patterns

$$G_{GOAL}(f_\mathrm{D},\, k) = G_{com}(f_\mathrm{D}) \cdot \exp(-\mathrm{j} \cdot 2 \cdot \pi \cdot t_{out}[k] \cdot f_\mathrm{D}\,). \tag{119}$$

Nonetheless, as a rule, the implemented patterns are imperfect approximations of the goals, since residual distortions occur. Note that this is true even in an error-free environment in which the patterns are known with arbitrary precision. The MSE of the approximation in (108) is $\xi_{MSE_{min}}[k] \geq 0$ but $\xi_{MSE_{min}}[k] = 0$ cannot be achieved except for very particular cases. As the procedure is repeated over all samples to form the output grid, owing to the irregularity of $t_{RX}[i]$, some pattern approximations are less successful than others. This is especially true for the output samples that span the Tx blockage-induced gaps, as these require larger shifts of the phase centers.

Moreover, regardless of whether (102) or (108) are minimized, the optimization takes place using information from a single output sample k at a time, thus the knowledge of the other desired outputs over the grid is not used in the design and their varying degree of success cannot be accounted for. Conceptually, means to use the information from other output samples in the grid to implement a given pattern

$G_{GOAL}(f_{\mathrm{D}}, k)$ are desirable, since they may be used to better equalize the performance over the output samples.

A simple way of doing this is to exploit the degree of freedom represented by the choice of $G_{com}(f_{\mathrm{D}})$ in (98). As long as the phase relations regarding $t_{out}[k]$ hold, the output grid remains regular, and enforcing $G_{com}(f_{\mathrm{D}}) = G_{sum}(f_{\mathrm{D}})$ is not strictly necessary, though physically meaningful for reflector systems, as pointed out in Section 4.3. The rationale is to shape the common pattern so that the output grid is more readily implementable by the given input manifold, in the sense of improving the worst-case implementation. Changing the common component of the design goals may lead to more readily achievable patterns without violating the regularity, the main objective of the resampling. Moreover, if the determination of $G_{com}(f_{\mathrm{D}})$ is done iteratively, the information from the other patterns in the grid is readily available at the end of each iteration. The following logic for the common pattern design is thus proposed. The previous choice is maintained for the first iteration, i.e.,

$$G_{com}^{0}(f_{\mathrm{D}}) = G_{sum}(f_{\mathrm{D}}). \tag{120}$$

However, at iteration $i \geq 1$, the common pattern in (98) is updated to

$$G_{com}^{i}(f_{\mathrm{D}}) = \frac{1}{N_{win}} \cdot \sum_{k=1}^{N_{win}} (\underline{\boldsymbol{w}}^{\boldsymbol{i}}[k])^{\boldsymbol{H}} \cdot \underline{\boldsymbol{v}}(f_{\mathrm{D}}) \cdot \exp(+\mathrm{j} \cdot 2 \cdot \pi \cdot t_{out}[k] \cdot f_{\mathrm{D}}), \tag{121}$$

where $\underline{\boldsymbol{w}}^{\boldsymbol{i}}[k]$ denotes the weights for the k^{th} pattern in the grid at the iteration under consideration and both the manifold and the weights have dimension N_{win}. This effectively means that the *mean* common complex pattern $\hat{G}_{com}(f_{\mathrm{D}})$ effectively achieved by the implementation is calculated, and passed on as a less strict design goal to the next iteration. This allows lower (better) MSEs to be achieved in the worst cases over the grid and thus improves the overall approximation. It should be noted that, if (120) and (121) are used in combination with the MSE cost function of (102), lower MSEs than those of the MSE-VBS method in Section 4.4.2 may be obtained because of the change in the design goal, and hence without contradiction to the

optimality of that method. A degradation of $G_{com}(f_\mathrm{D})$ in comparison to the initial sum pattern is possible, but the impact is small as long as the worst-case distortions are not excessive. The effect can be controlled by proper design of the PRI sequence.

A stop criterion for the iteration is may be the improvement of the average MSE over the grid, i.e.

$$\overline{MSE_i} = \frac{1}{N_{out}} \cdot \sum_{k=1}^{N_{out}} \int_{f_1}^{f_2} \left(G_{GOAL}(f_\mathrm{D}, k) - \underline{\boldsymbol{w}}[k]^H \cdot \underline{\boldsymbol{v}}(f_\mathrm{D}) \right)^2 \mathrm{d}f_\mathrm{D} \,. \tag{122}$$

The iteration can be stopped for instance when the step between iterations $\Delta MSE = \overline{MSE_i} - \overline{MSE_{i-1}}$ is too low to justify further calculations, or when $\overline{MSE_i}$ reaches a design goal.

If the SNR-VBS cost function (108) is used, it is also possible to use an average of the SNR figure of (113), i.e.

$$\overline{\Phi_{SNR_i}} = \frac{1}{N_{out}} \cdot \sum_{k=1}^{N_{out}} \Phi_{SNR}^{i}\left(\underline{\boldsymbol{w}}[k]\right), \tag{123}$$

as an additional stop criterion, again either in the form of an analogous step $\Delta SNR = \overline{\Phi_{SNR_i}} - \overline{\Phi_{SNR_{i-1}}}$ or a design goal. Iteration also brings the possibility of adapting the sensitivity parameter α according to the results of the previous iteration, either for all or for specific output patterns.

In the case that the iterative method is combined with the SNR-VBS method, a feedback of the parameter α into the design goal is introduced. This tends to enhance the emphasis on the SNR and improve the performance with this regard, though increasing the minimum achievable MSE and possibly slowing convergence to lower MSE values. Indeed, in the limit case of $\alpha = 1$, the output pattern solution is always the same and the iteration is meaningless.

An example illustrating the application of the regularization methods discussed in this section is provided in Section 5.4.1. For the iterative method, plots of the behavior of the common patterns $G_{com}^{i}(f_{\mathrm{D}})$ as a function of the iteration number i, as well as grid performance indices are depicted in **Figure 37**. The next section turns focus to planar direct radiating arrays.

4.5 Peculiarities of Planar Direct Radiating Arrays

The primary beam steering technique in Section 4.3 clearly requires the usage of a reflector antenna. Interestingly, even though conceptually motivated by the former one, the resampling strategy of Section 4.4 does not. Knowledge of the array manifold vector is assumed, but no special structure is imposed on it, meaning the application can be readily extended to non-reflector antennas. In particular, planar direct-radiating antenna systems, so far the default in civilian SAR satellite technology [110], represent a natural candidate. Moreover, as discussed in [104], a certain equiavalency between reflectors and planar arrays exists, from which intuitively the technique should also be applicable in this case, provided that the differences are understood and adaptations are performed accordingly.

Starting from the modeling of the input patterns, an important difference for planar systems that impacts the manifold extension discussed in Section 4.4.1 is the contribution of the geometry to the phase centers. This means that, in (97), the phase ramp defining the input sample position is also influenced by the array elements geometrical position, thus combining the temporal and spatial sampling. In contrast, for reflector systems, the relative position between samples is determined exclusively by $t_{RX}[i]$. This is in fact exploited as part of the VBS method formulation (cf. Section 4.4) by using different pulses as input to the beamformer ($N_p > 1$) in order to provide a phase center *diversity* that the receive channels alone do not possess in the reflector case. In contrast, the planar antenna system's channels already show a variety of phase center positions (corresponding to the position of each element) and thus adding several pulses to the extended manifold has a smaller impact with respect to the resampling.

Another critical aspect for the successful application of the technique is a proper choice of the goal patterns $G_{com}(f_{\mathrm{D}})$ in (98), since the optimum approximation is not necessarily a good one, if the desired patterns are poorly chosen in the sense of not being realizable, as also implied by the discussion in Section 4.4.5. Whereas for the reflector systems the physical principle described in 4.3 motivated the choice of the common patterns, an analysis of the phase center resampling capabilities of planar systems is desirable in this context. The aim is to provide a better understanding of how realizable a set of patterns of the form in (98) is in the planar case, considering beamforming on receive. In [111] and [112] a technique to modify the phase centers of planar antennas on transmit is described.

We start by considering the phase centers of a uniform linear array of N isotropic elements spaced by d_{az}within the region $[0, L]$, $L = (N-1) \cdot d_{az}$, as illustrated in **Figure 27**.

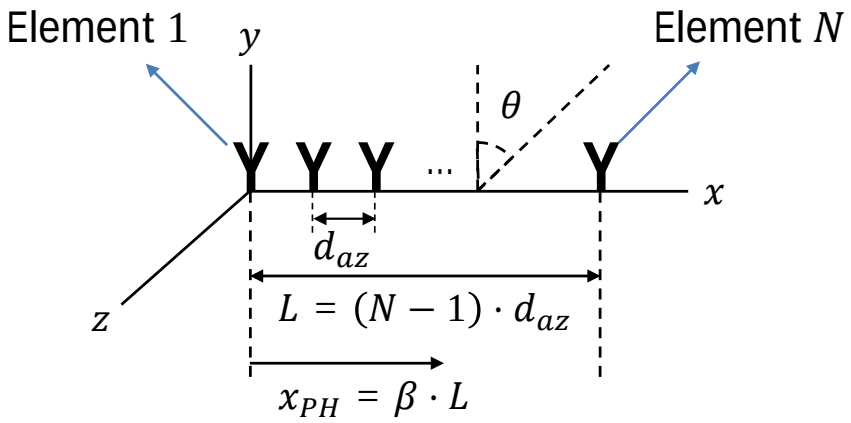

Figure 27. Geometry of a general N-element uniform linear array of inter-element spacing d_{az} and total distance between outermost elements $L = (N-1) \cdot d_{az}$. The goal is to obtain a phase center in the intermediate position $x_{PH} = \beta \cdot L$, $0 \leq \beta \leq 1$ within the array.

The goal is to obtain, by linear combination of the individual elements on receive, a phase center lying at the position $x_{PH} = \beta \cdot L$, with $0 \leq \beta \leq 1$. In particular, $x_{PH} = n \cdot d_{az}$, with integer n, are trivial cases corresponding to the usage of single

elements. The description is general, though clearly the phase centers in the azimuth direction are the main focus.

The linear combination of the received signals of the antenna array, applying the complex weight w_n for the n^{th} element, yields a resulting pattern which can be approximated in the far field by the well-known array factor [100], [106]

$$AF(\theta) = \sum_{n=0}^{N-1} w_n \cdot \exp\left(\mathrm{j} \cdot n \cdot \frac{2 \cdot \pi \cdot d_{az}}{\lambda} \cdot \sin(\theta)\right), \tag{124}$$

where θ is the off-boresight angle in **Figure 27**.

Defining the auxiliary spatial frequency $f_{sp}(\theta) = \sin(\theta)/\lambda$ — which is closely related to the Doppler frequency in the case of azimuth — one may write the conjugate complex of (124) as

$$\begin{aligned} AF^*(f_{sp}) &= \sum_{n=0}^{N-1} w_n^* \cdot \exp\left(-\mathrm{j} \cdot 2 \cdot \pi \cdot f_{sp} \cdot (n \cdot d_{az})\right) \\ AF^*(f_{sp}) &= \sum_{n=0}^{N-1} \int_{-\infty}^{\infty} w^*(x) \cdot \delta(x - n \cdot d_{az}) \cdot \exp\left(-\mathrm{j} \cdot 2 \cdot \pi \cdot f_{sp} \cdot x\right) \mathrm{d}x. \end{aligned} \tag{125}$$

where, in the last equation, the summation is changed to an integral by defining the auxiliary continuous weight function $w(x)$, sampled at $n \cdot d_{az}$ by the Dirac deltas. Taking the complex conjugate and changing the integration variable to –*x* yields

$$AF(f_{sp}) = \sum_{n=0}^{N-1} \int_{-\infty}^{\infty} w(-x) \cdot \delta(-x - n \cdot d_{az}) \cdot \exp\left(-\mathrm{j} \cdot 2 \cdot \pi \cdot f_{sp} \cdot x\right) \mathrm{d}x, \tag{126}$$

which is the Fourier Transform of the (theoretical) space-reversed continuous weight distribution $w(-x)$, considered to be non-zero only over the interval $x \in [0, -(N-1) \cdot d]$ (the negative sign comes from the inversion), and sampled at

$x = n \cdot d_{az}$, i.e. the position of the elements (and thus of their respective phase centers). Clearly (126) may also be written in terms of the Discrete-Time Fourier Transform of the sequence $w[n] = w_n$ [106] showing that the properties of the array factor rely on those of the Fourier Transform [105].

The desired phase center position is x_{PH}, meaning the array factor is expected to take the form

$$AF(f_{sp}) \triangleq \exp(\mathrm{j} \cdot 2 \cdot \pi \cdot (\beta L) \cdot f_{sp}) \cdot B(f_{sp}), \tag{127}$$

where the exponential term is related to the position of the phase center $x_{PH} = \beta \cdot L$ (using the analogy to time Fourier analysis, x_{PH} represents a "spatial-delay" with respect to the spatial frequency f_{sp}); and $B(f_{sp})$ is a complex modulation of the phase ramp.

A particular case of interest is the well-known uniform weighting, corresponding to $w_n = 1/N$ in (124), and equivalent to

$$w(x) = \frac{1}{N} \tag{128}$$

which yields [100]

$$AF_{UNI}(f_{sp}) = \exp\left(\mathrm{j} \cdot 2 \cdot \pi \cdot \frac{(N-1) \cdot d_{az}}{2} \cdot f_{sp}\right) \cdot \frac{\sin(N \cdot \pi \cdot d_{az} \cdot f_{sp})}{\sin(\pi \cdot d_{az} \cdot f_{sp})} \cdot \frac{1}{N} \tag{129}$$

showing by inspection and comparison to (127) that the phase center is located in the position of the geometric center of the array, and the amplitude modulation $B(f_{sp})$ in this case is approximately sinc-like for small angles/spatial frequencies.

In general, the cases of interest are namely the ones in which the modulation $B(f_{sp})$ is real for all f_{sp}, in order to avoid phase distortions with respect to the position-induced phase ramp. This is considered an "exact" implementation of the phase center, in the

sense that the pattern behaves as a single element positioned at $x_{PH} = \beta \cdot L$. Equating (126) to (127) and moving the term $\exp\left(\mathrm{j} \cdot 2 \cdot \pi \cdot (\beta L) \cdot f_{sp}\right)$ inside the integral allows the modulation to be expressed as

$$B\left(f_{sp}\right) = \sum_{n=0}^{N-1} \int_{-\infty}^{\infty} w(-x) \cdot \delta(-x - n \cdot d_{az}) \cdot \exp\left(-\mathrm{j} \cdot 2 \cdot \pi \cdot f_{sp} \cdot (x + \beta L)\right) \mathrm{d}x \tag{130}$$

and by changing the integration variable to $x' = x - \beta L$,

$$B\left(f_{sp}\right) = \sum_{n=0}^{N-1} \int_{-\infty}^{\infty} w(-x' + \beta L) \cdot \delta(-x' + \beta L - n \cdot d_{az}) \cdot \exp\left(-\mathrm{j} \cdot 2 \cdot \pi \cdot f_{sp} \cdot x'\right) \mathrm{d}x'. \tag{131}$$

By using conjugation and reversal of the x' axis one may also write,

$$B^{*}\left(f_{sp}\right) = \sum_{n=0}^{N-1} \int_{-\infty}^{\infty} w^{*}(x' + \beta L) \cdot \delta(x' + \beta L - n \cdot d_{az}) \cdot \exp\left(-\mathrm{j} \cdot 2 \cdot \pi \cdot f_{sp} \cdot x'\right) \mathrm{d}x' \tag{132}$$

A real $B\left(f_{sp}\right)$ requires

$$Im\{B\left(f_{sp}\right)\} = \frac{B\left(f_{sp}\right) - B^{*}\left(f_{sp}\right)}{2} = 0. \tag{133}$$

In turn, from (131) and (132), this condition requires that

$$\sum_{n=0}^{N-1} \int_{-\infty}^{\infty} [w(-x' + \beta L) \cdot \delta(-x' + \beta L - n d_{az}) - w^{*}(x' + \beta L) \cdot \delta(x' + \beta L - n d_{az})] \cdot \exp\left(-\mathrm{j} \cdot 2 \cdot \pi \cdot f_{sp} \cdot x'\right) \mathrm{d}x' = 0. \tag{134}$$

To make the integral identically null for all f_{sp}, it is thus required that

$$w(-x' + \beta L) \cdot \delta(-x' + \beta L - n \cdot d_{az}) = w^{*}(x' + \beta L) \cdot \delta(x' + \beta L - n \cdot d_{az}); \tag{135}$$

for $n \in [0, N_{el} - 1]$, which is a Hermitian symmetry relation [105], applied to the continuous weight distribution with respect to the desired phase center position at $x_{PH} = \beta \cdot L$. Note that the only relevant positions are the "samples" of this distribution at $x_n = n \cdot d_{az}$, which correspond to the positions of the array elements, every other point being merely a mathematical construct. In particular (135) is satisfied when

$$w(-x' + \beta \cdot L) = w^*(x' + \beta \cdot L), \tag{136}$$

for all x'. This condition is sufficient but not necessary, since the points outside $x_n = n \cdot d_{az}$ can take arbitrary values without changing the integrals in (131) and (132), but is preferred to simplify the notation.

The relationship between Hermitian symmetry (cf. **Figure 28 (a)**) and a real valued transform is indeed a well-known property in Fourier analysis, but the implication in this case is that a given phase center position x_{PH} can only be achieved if the weights are Hermitian-symmetric with respect to that point. This also shows that the phase center is always located in the geometrical center of the (sub-)array (cf. **Figure 28 (b)**)). The problem of locating the possible phase centers of a planar antenna array (under the conditions (127) and (133), implying no phase distortion) is thus a combinatorial one, since it only depends on the location of the active elements.

Since the array is finite and sampled at the element positions, this narrows down the possible phase centers considerably. Namely, if an odd number of elements is taken (including the trivial case of one element), the possible phase centers coincide with the element positions, whereas if an even number of elements is taken, they coincide with the positions in-between adjacent elements. In any case, the achievable phase centers are the geometrical center of the array and of any sub-arrays contained therein. Any other positions cannot be exactly obtained (in the sense of satisfying (133)) over the whole set of angles. Therefore, planar systems show an inherent *discretization* of the

achievable phase centers[19], due to the fact that the choice of the output phase centers is implemented by directly activating portions of the azimuth aperture.

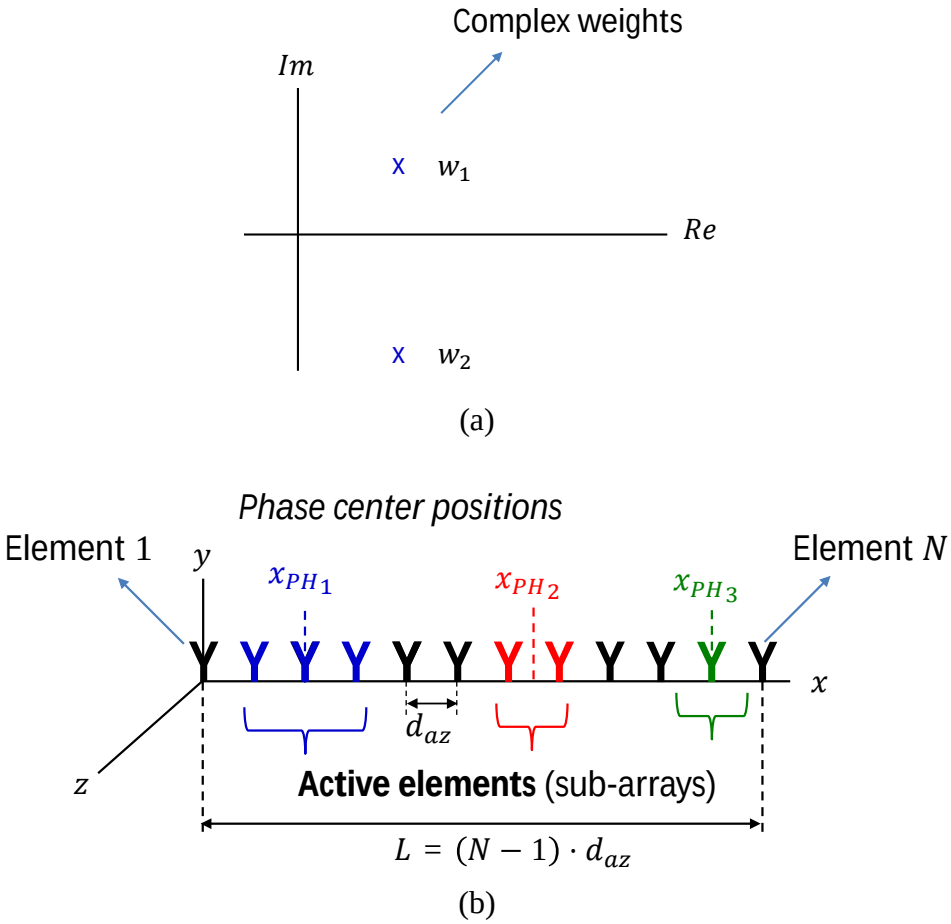

Figure 28. (a) Illustration of Hermitian symmetry of the complex weights w_1 and w_2. (b) Sub-arrays and the corresponding phase center positions at their respective geometrical center.

Moreover, so far only the implementation of a *single* phase center with an arbitrary amplitude modulation $B(f_{sp})$ as in (127) was considered. The regularization of the samples requires however that several of them — forming the regular grid — be obtained. In that case, it is important that $B(f_{sp})$ — which plays the role of the common pattern $G_{com}(f_{\mathrm{D}})$ of (98) in this case — remains stable for *all* of the required phase centers. Achieving all of the required phase centers with different amplitude

[19] In contrast, in the reflector case no such restrictions apply, and the phase center can be varied continuously within certain bounds.

modulations is indeed not a solution to the resampling problem, as the resulting output grid would present a time-varying power spectrum, and would not be equivalent to a single (constant) channel sampled at a higher rate, as is intended. As the previous analysis shows, the patterns obtained from sub-sets of a planar array will show amplitude modulations which depend strongly on the number of active elements (revealing a second form of *discretization*, with respect to the available amplitude modulations). Uniform weighting for instance imposes a sinc-like modulation parametrized by that number, as seen from (129). Therefore it is desirable that a fixed number of elements be activated to synthesize every output phase center, to achieve the desired pattern stability.

A solution is to design the azimuth antenna so that the combination of an integer number of neighboring elements yields the aperture size required by the resolution and then set $G_{com}(f_{\mathrm{D}}) = G_{sub-set}(f_{\mathrm{D}})$, the pattern of this sub-set of the antenna array elements. The resulting weights will always combine this fixed number of elements, but to choose the combination with a geometric center (determined in this case by both array geometry and pulse sampling) closest to the desired phase center ($t_{out}[k]$ in (98)). The length of the active aperture is thus set, but the maximum extent of the phase center shift remains a function of the total antenna size, whereas the granularity or "resolution" of the phase center shift is determined by the inter-element spacing (alongside the PRF, when $N_p > 1$ and several pulses are used). As before (cf. Section 3.3.2), the mean PRF still defines the maximum gap size and thus the maximum required phase center shift. Clearly, a better performance is expected for higher PRFs and a finer division of the aperture through a larger number of elements, but the more complex interdependency between geometry and PRI-sequence should be considered in the design. A possible approach is to fix the antenna size and choose the lowest possible mean PRI and number of elements which lead the shifts to be small enough to achieve the required performance level.

The antenna design is thus the most important aspect which ensures the resampling performance. Regarding the choice of beamforming parameters, the approach of

combining a smaller number of pulses than in the reflector case is favored, since the manifold extension bears the possible disadvantage of reducing the signal's SNR (cf. Section 4.4.4). Moreover, even though some level of SNR emphasis ($\alpha > 0$ in (117), (118)) can still be applied, the solution that maximizes the SNR becomes namely the addition of all array elements $G_{sum}(f_{\mathrm{D}})$ [106], which as discussed is not practical. In conclusion, a limited success of the SNR-MSE compromise is expected in this case. Some SNR gain is nevertheless possible with moderately low levels of α, leaving the control of the baseline decorrelation effect in the extended manifold to the aforementioned restriction in the number of pulses N_p used as input.

In summary, the argumentation in this section shows that the design and processing strategy requires adaptations in the planar case. The main differences in the design guidelines with respect to the reflector case can be listed as:

- The common pattern $G_{com}(f_{\mathrm{D}})$ should be the pattern $G_{sub-set}(f_{\mathrm{D}})$ of the combination of a sub-set of the antenna array elements. A single element is the simplest case, but in general a combination of several neighboring elements is necessary. $G_{sub-set}(f_{\mathrm{D}})$ must achieve the Doppler bandwidth required by the resolution and defines the length of the active aperture.
- The phase center deviations required by the resampling should be minimized by means of the joint design of the azimuth antenna and the PRI-sequence. The total antenna size and the number of azimuth channels should be chosen under the constraint that the combination of an integer number of neighboring elements yields the active aperture length. For instance, the total antenna length can be fixed and then N_{ch} set to the smallest number of channels which yields appropriate performance, using for each geometrical configuration a favorable mean PRI.
- The number of pulses N_p in the input sample window should be reduced (thus limiting $N_{win} = N_p \cdot N_{ch}$ and improving SNR performance) and a small emphasis $\alpha \cong 0$ set, to improve ambiguity suppression.

A design example following these guidelines is presented in Section 6.4.

4.6 Remarks on Multichannel Staggered SAR in Azimuth

This chapter discussed the challenge of resampling the data of a multichannel staggered SAR system (cf. Section 4.2) and detailed its solution. Section 4.3 introduced a first alternative, based on steering of the primary beam of a reflector system, which introduces the physical principle behind the multichannel resampling for reflectors, and also serves as a conceptual basis for the extended method in Section 4.4, which is new and one of the innovative contributions of this thesis.

A flow chart of the inputs employed for the weight calculations in Section 4.4 is provided in **Figure 25**, comparing the different alternatives described in the subsections therein.

Finally, Section 4.5 analyzed the case of a system with a planar direct radiating array antenna and showed that this class of systems suffers from a *discretization* of the phase centers, as well as some limitations imposed by the need of a stable pattern modulation for all of the output phase centers. Some adaptations in the strategy of Section 4.4 were found to be required, namely:

- Choice of $G_{com}(f_{\mathrm{D}}) = G_{sub-set}(f_{\mathrm{D}})$, pattern from a sub-set of the antenna array elements.
- Joint design of the PRI-sequence and the azimuth antenna to *minimize* the deviations required by the resampling.
- Reduction of the number of pulses N_p in the input sample window and $\alpha \cong 0$.

The methods described here will be used throughout the thesis. In particular, Chapter 5 will show simulation examples to better illustrate the methods, focusing on particular cases with reflector antennas to aid understanding. Chapter 6 will turn focus

to the achievable SAR performance, with examples of HRWS spaceborne SAR systems designed to make use of the multichannel staggered SAR architecture, for both reflector and planar antennas. Chapter 7 will show a proof of concept with a ground based MIMO radar demonstrator, whereas Chapter 8 addresses the impact of possible errors.

5 Simulation Examples: Analysis and Comparison of Methods

5.1 Chapter Overview

The previous chapter provided the theoretical description of the proposed methods for processing of multichannel staggered SAR data. The goal of this chapter is to provide simulation examples which illustrate the application of the methods and allow a better understanding of some of the trade-offs involved in the choice of parameters. Section 5.2 describes the simulation scenario, performace requirements and system parameters. The focus is on a particular range of a HRWS multichannel staggered SAR acquisition. In Section 5.3, the synthesis of a particular goal pattern (a certain sample of the output grid) is considered, to allow insight into the behavior of the algorithm in dependence of the SNR emphasis parameter α. In Section 5.4 the synthesis of the whole output grid is considered for this range, analyzed both in terms of the output patterns (Section 5.4.1) and the focused impulse responses (Section 5.4.2), from which the usual SAR performance figures (cf. Appendix B) are derived. Part of the material contained herein was presented in [36], [66] and [67].

5.2 Description of Simulation Scenario

In order to analyze and compare the performance of the different methods, an illustrative scenario is considered, taking as reference one of the high azimuth resolution modes of the Tandem-L mission proposal [35], [36]. The goal is to image from an orbit height of 745 km a swath of 350 km with 3.0 m azimuth resolution in L-band, using a parabolic reflector antenna architecture [40]. A visualization of the reflector and the feed system, generated using the TICRA GRASP software [113], is depicted in **Figure 29 (a)**. The feed elements in these and all other patterns simulated throughout this thesis are assumed to be patch antennas following the radiation model of [114].

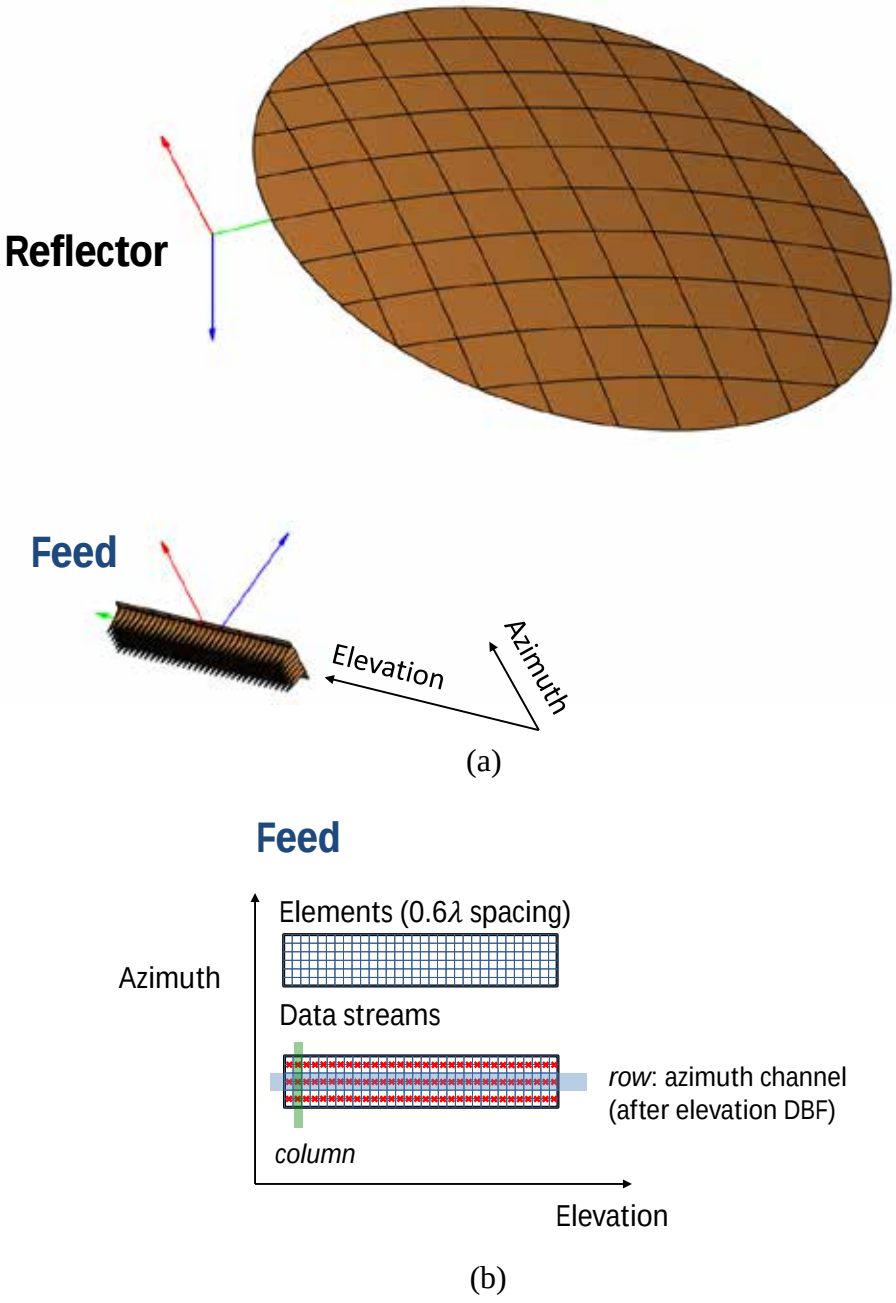

Figure 29. Antenna system configuration and geometry. (a) 3D visualization highlighting multichannel feed and reflector rim. (b) Detailed view of feed showing elements and data streams (red 'x' symbols) after digitization. The feed system consists of 32 elements in elevation and 6 in azimuth, combined pairwise and digitized to form 3 azimuth data streams per column, which are then combined into 3 channels after row-dependent elevation beamforming.

The finest required resolution in the case of Tandel-L is 7 m, which is achieved by analog combination of the three elements in azimuth into a single channel with fixed

weights (described in [36] in detail). The analog beamforming is done independently for each collumn of the feed in elevation, yielding $N_{el} = 32$ channels, each of which are digitized for DBF in elevation. As will be shown, the system can also achieve an azimuth resolution of 3 m, provided that each azimuth element corresponds to a channel which is digitized independently, yielding $N_{el} \cdot N_{az} = 96$ data streams, represented by the 'x' symbol in **Figure 29 (b)** before elevation beamforming and finally 3 azimuth channels.

In particular, a simulated point target in the center of the scene is considered as an example. A periodically non-uniformly sampled multichannel signal as discussed in Section 4.2 results from the use of a staggered PRI sequence on a system with 3 channels on receive in azimuth. In this case, the 6 azimuth feed elements spaced at 0.6λ in azimuth are combined pairwise [36] and digitized, for each column of the feed in elevation. After DBF in elevation, 3 azimuth channels result, each corresponding to a row of the feed. The relevant system parameters are summarized in TABLE II.

TABLE II
SIMULATION SCENARIO PARAMETERS

Platform and swath parameters		
Parameter	Symbol	Value
Orbit height	h_{orbit}	745 km
Swath width on ground	W_g	350 km
Minimum/maximum look angle	$\theta_{min}/\theta_{max}$	23.4 /40.9 deg
Reflector and feed parameters		
Parameter	Symbol	Value
Diameter	D	15.0 m
Focal length	F	13.5 m
Feed offset in elevation	d_{OFF}	9.0 m
Center frequency	f_0	1.2575 GHz
Number of channels in elevation/azimuth	N_{el}/N_{az}	32 / 3
Channel spacing in elevation/azimuth	d_{el}/d_{az}	0.68 λ / 1.2 λ
Elevation tilt angle w.r.t. nadir	θ_{tilt}	32.4 deg

Pulse sequence parameters		
Parameter	Symbol	Value
Average PRF	$\overline{PRF}$	2700 Hz
Initial PRI	PRI_0	386 μs
PRI sequence step	Δ_{PRI}	-0.98 μs
PRI sequence length	N_{PRI}	33
Pulse length	T_P	14.8 μs
Duty cycle	T_{dc}	4%
Processing parameters		
Parameter	Symbol	Value
Goal azimuth resolution	δ_{az}	3 m
Processed Doppler bandwidth	Bw_{proc}	2494 Hz
Number of pulses in azimuth beamformer window	N_p	31

The target is located at a (ground) range of $g_0 = 485$ km. The description of the PRI sequence and the physical antenna patterns provides the basis for the characterization of the extended manifold used as input for the resampling. With respect to the former, timing analysis (cf. Section 3.3.2) shows that for this particular range the 3rd and the 32nd pulse from the sequence of $N_{PRI} = 33$ pulses are lost due to transmission events. This leads to an effective number of pulses $N_{eff} = 31$. The blocked pulses and the resulting azimuth sampling are depicted in **Figure 30**. In **Figure 30 (a)**, the blockage diagram over the swath is provided: For each ground range, red boxes indicate the indices of the lost pulses. The fact that two consecutive losses never occur for the considered ranges — a consequence of the sequence design criterion (cf. Section 3.3.3) — can be observed. The vertical dashed line highlights the ground range under consideration, for which the resulting sampling configuration, notably the gaps, are visible in **Figure 30 (b)**. Note that the grid is non-uniform, even without considering the gaps, however the non-uniformity is not visible due to the small PRI step, Δ_{PRI} = -0.98 μs.

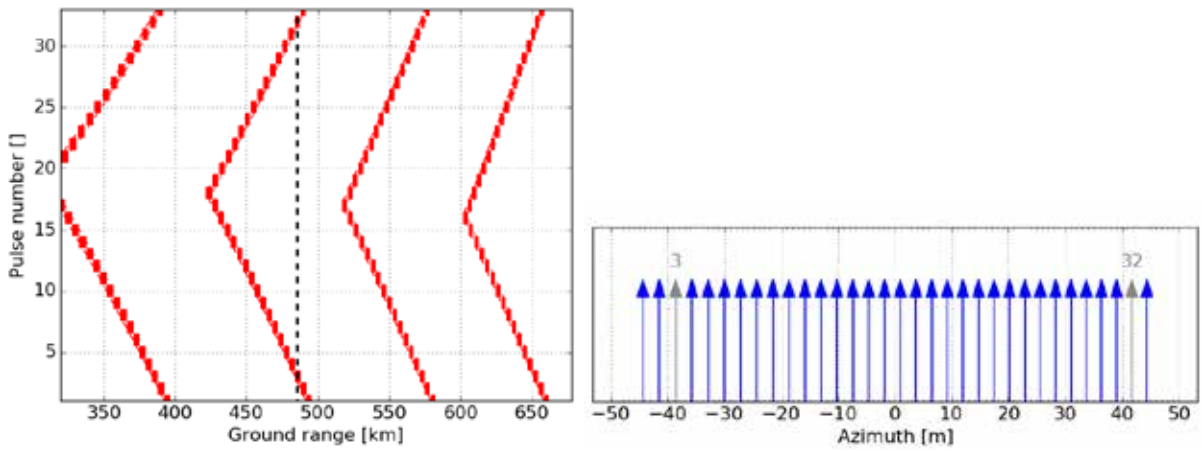

(a) (b)

Figure 30. Analysis of the transmit-event induced loss of pulses over range. (a) Blockage diagram for the whole swath, with ground range as abscissa and the pulse index as ordinate. (b) Azimuth (non-uniform) sampling instants (in blue) and blocked pulses (in grey) over one PRI sequence cycle at the particular ground range of 485 km, roughly at the center of the swath.

As discussed in Chapter 4, applying the VBS technique requires knowledge of the antenna patterns the azimuth channels (cf. the definition of the extended manifold in (97)). **Figure 31** shows the magnitude of the far-field (secondary) antenna patterns $G_i(f_\mathrm{D})$ of the 3 azimuth channels, as well as the corresponding $G_{sum}(f_\mathrm{D})$ (defined in (93)), chosen here as the desired common pattern of the regular grid. The patterns were simulated using the TICRA GRASP software [113]. The simulation takes into account the effect of blockage of the incident waves over the reflector's surface due to the feed (its "shadow"). As expected for an ideal reflector, the phase centers coincide but the Doppler region covered by each element differs. The sum pattern (dashed line) is seen to be much broader, and its width is approximately given by the combined beamwidth of all elements. The outer vertical dashed lines highlights the limits of the effective multichannel sampling rate PRF_{multi} = 7609 Hz and the inner ones the processed bandwidth Bw_{proc}.

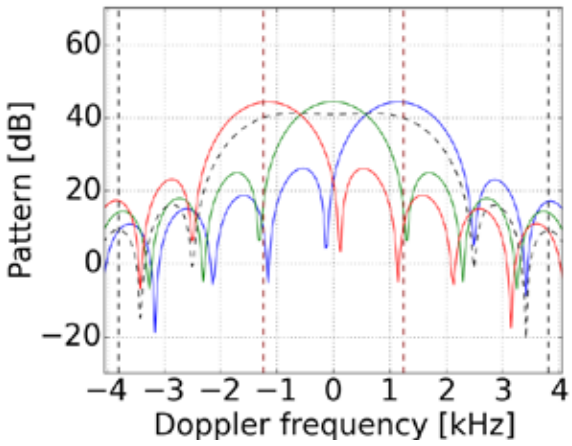

Figure 31. Antenna pattern magnitude for the 3 Rx physical channels $G_i(f_\mathrm{D})$ (solid lines) and corresponding sum pattern $G_{sum}(f_\mathrm{D})$ (dashed line).

In the following, the three channels of **Figure 31**, initially sampled at the grid of **Figure 30 (b)**, will be combined to reconstruct a regular grid sampled at the rate of PRF_{multi} = 7609 Hz. Zhe particular case of $N_{win} = N_{ch} \cdot N_{eff}$, meaning the window of inputs for formation of the output grid is chosen to be a cycle of the PRI sequence, is considered as a first example.

5.3 Synthesis of a Single Goal Pattern: The Impact of the SNR Sensitivity Parameter $\boldsymbol{\alpha}$

As a first example, the synthesis of $G_{GOAL}(f_\mathrm{D},\ 0)$, i.e., the pattern corresponding to the first sample of the output grid (cf. definition of $G_{GOAL}(f_\mathrm{D},\ k)$ in (98)) is considered. **Figure 32** shows the sampling configuration of the extended manifold (input sampling instants defined in (84)) as well as the desired phase center position (cf. regular grid $t_{out}[k]$ in (85), for $k = 1$). Since $N_{win} = N_{ch} \cdot N_{eff}$, the extended manifold has $N_{manifold} = 93$ elements, whose phase center positions are represented by blue circles. These correspond to the position of the physical channels over the whole cycle of received pulses, shown as arrows. The output regular grid samples, represented by the symbol ‘x’, has as well $N_{out} = 93$ samples over a PRI cycle.

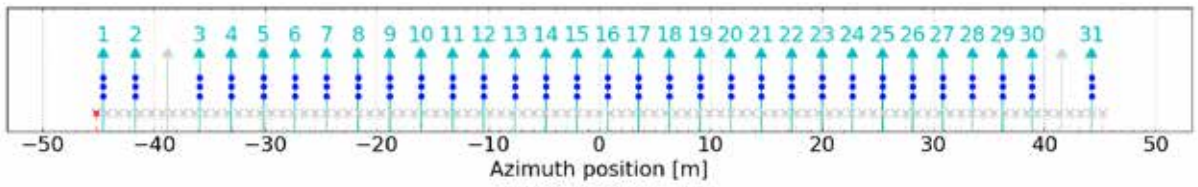

Figure 32. Sampling configuration for extended manifold and desired regular grid over a PRI sequence. Arrows represent the received pulse position, highlighting the 31 available pulses. The blue circles represent the phase center position of the samples from the different azimuth channels. The desired regular grid positions are represented by an "x", and the particular phase center position for the pattern under analysis is highlighted in red.

The first output sample is highlighted in red. In this case, a shift of -0.65 m is required with respect to the position of the nearest pulse, namely, the first one of the cycle. In order to illustrate the performance of the methods in Section 4.4, as well as to provide a better understanding of the inherent MSE-SNR trade-off involved, the implementation of this particular pattern with varying values of the sensitivity parameter α in the interval [0, 1] is considered in the following. The joint cost function of Section 4.4.4 is used with the following parameters: n_{MSE} is taken to be the power of the sum pattern $G_{sum}(f_{\mathrm{D}})$ given by (93) and n_{SNR} is equal to the normalized SNR figure of the same sum pattern,

$$k_{sum} = \frac{1}{N_{win}} \cdot \int_{f_1}^{f_2} |G_{sum}(f_{\mathrm{D}})|^2 \mathrm{d}f_{\mathrm{D}} = \frac{1}{N_{win}} \cdot \int_{f_1}^{f_2} \left| \sum_{i=1}^{N_{win}} v_i(f_{\mathrm{D}}) \right|^2 \mathrm{d}f_{\mathrm{D}} \tag{137}$$

divided by 100[20]. The correlations between the manifold elements, as well as the MSE measurement $\xi_{MSE}[k]$ (defined in (102), (105)) are computed by integration over PRF_{multi}.

[20] This choice of values is motivated by the fact that the normalized MSE figure for this example was found to be in the order of -20 to -30 dB, while the normalized SNR figure Φ_{SNR} (defined in (113)) is in the order of 0.0 to -10 dB, and hence the factor 100 was chosen to better match numerically the values of the two figures and thus adjust the sensitivity to α.

Firstly, **Figure 33** shows examples of the achieved patterns for five equally spaced values of α from 0.0 to 1.0. The abscissa values represent Doppler frequency, and the inner and outer dashed lines delimitate Bw_{proc} and PRF_{multi}, respectively. The patterns are represented in terms of normalized gain (**Figure 33** (a)) and phase error (**Figure 33** (b)), the latter with respect to the phase ramp dictated by the required phase center position $t_{out}[0]$.

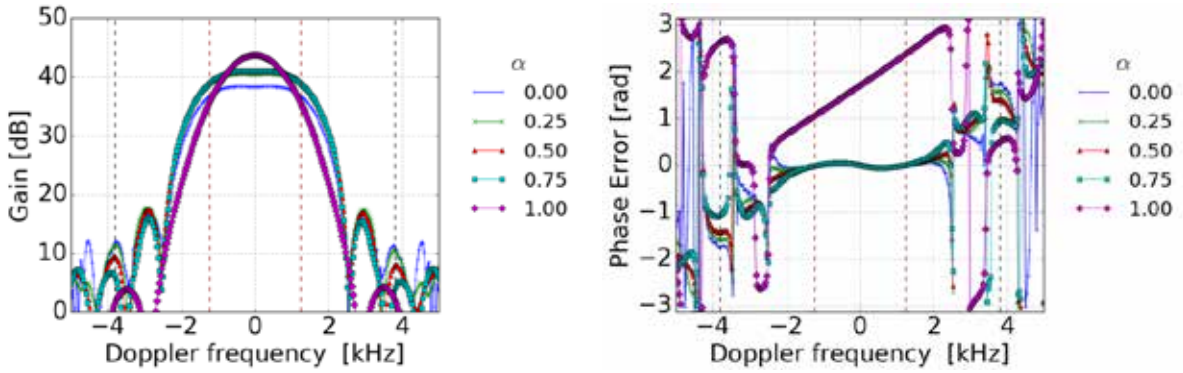

(a) (b)

Figure 33. Analysis of achieved patterns $\hat{G}_{GOAL}(f_{\mathrm{D}}, \alpha) = \underline{\boldsymbol{w}}(\alpha)^{\boldsymbol{H}} \cdot \underline{\boldsymbol{v}}(f_{\mathrm{D}})$ as a function of α, in terms of gain and phase. (a) Pattern gain. (b) Error with respect to the desired phase center position, modelled by a phase ramp in Doppler domain.

It should be highlighted that the normalized gain mentioned here refers to the usual definition in [106], i.e.

$$Q(f_{\mathrm{D}}, \alpha) = \frac{\left\| \underline{\boldsymbol{w}}(\alpha)^{H} \cdot \underline{\boldsymbol{v}}(f_{\mathrm{D}}) \right\|^2}{\underline{\boldsymbol{w}}(\alpha)^{H} \cdot \underline{\boldsymbol{w}}(\alpha)}, \tag{138}$$

as relevant for the SNR. The normalized gain should not be confused with the (achieved) pattern $\hat{G}_{GOAL}(f_{\mathrm{D}}, \alpha) = \underline{\boldsymbol{w}}(\alpha)^{\boldsymbol{H}} \cdot \underline{\boldsymbol{v}}(f_{\mathrm{D}})$. This distinction is important in this context as the pattern (here understood as the mere linear combination, without normalization of the weight magnitude) influences the MSE, while the gain in (138) influences the SNR. It can be seen from the plots that, as α increases, the pattern's normalized gain also does, leading to an improved SNR. Correspondingly, the phase errors are also seen to increase, which leads to an MSE worsening. However, the shape of most patterns is seen to be stable and resemble very closely that of $G_{sum}(f_{\mathrm{D}})$,

visible in **Figure 31**. An exception occurs for α = 1.0, a case of more theoretical than practical interest leading to the best achievable SNR without actually implementing any resampling: in this case, the shape of the pattern is unrelated to the previous one. Another interesting aspect is the considerable change in the gain when α changes from 0.0 to 0.25, even though neither the shape of the pattern nor the phase error changes abruptly.

A more detailed characterization follows from an analysis shown in **Figure 34**, where the normalized MSE and Φ_{SNR} of the achieved approximation $\hat{G}_{GOAL}(f_{\mathrm{D}}, \alpha)$ are plotted against the value of α.

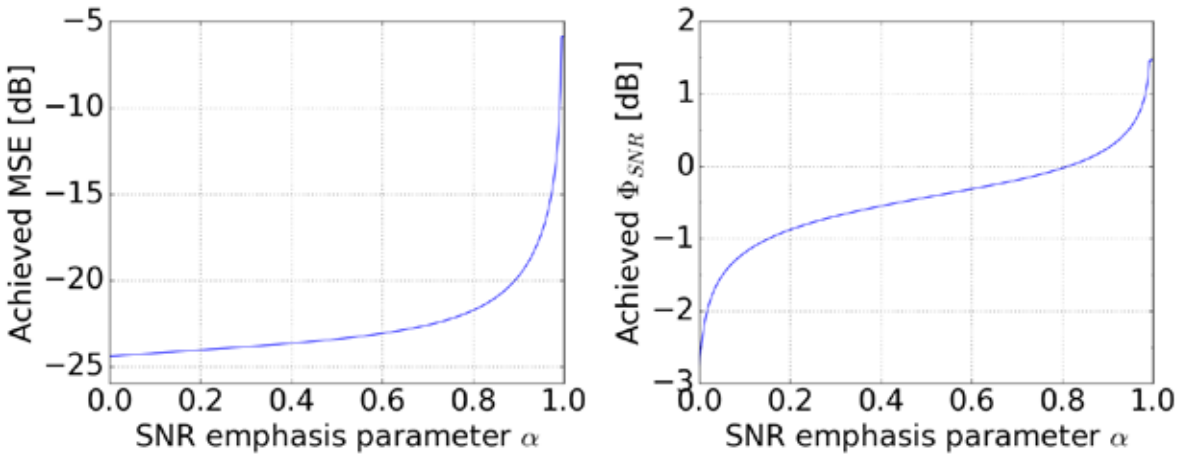

(a) (b)

Figure 34. Analysis of the performance as a function of α, in terms of normalized MSE and SNR figures. (a) Pattern MSE with respect to the goal pattern, normalized to the power of the sum pattern. (b) SNR figure Φ_{SNR}.

As expected, both the MSE and the SNR increase with increasing values of α, highlighting the compromise between the two parameters. It is nonetheless interesting to note that the sensitivity of the two curves is different. The MSE varies slowly with α up to values of circa 0.8 and then increases abruptly, indicating the increasing disregard of the sampling conditions by the cost function. On the other hand, the SNR increases

quickly with α for values up to 0.2, remains fairly stable up to 0.8 and then quickly increases again up to the maximum value[21]. The numerical values of the boundaries of the α regions identified above clearly depend on the normalization parameters n_{MSE} and n_{SNR}, which adjust the sensitivity of the cost function to α. However, as the extreme cases do not change, a change in these parameters represents a mere scaling of the curve with respect to the abscissa values, not changing the general behavior.

In terms of pattern design, the interesting point is that a considerable increase in the SNR can be achieved without a great degradation of the MSE by increasing α up to certain threshold[22].

5.4 Synthesis of Full Output Grid: Comparison between Methods

5.4.1 Output Pattern Analysis

In this section, the achieved patterns are analyzed over the whole output grid (i.e. instants $t_{out}[k]$ (85) for all k), to complete the resampling process and achieve the final goal of the method.

First of all, the MSE-VBS method described in Section 4.4.2 (or equivalently the MSE-SNR-VBS one of Section 4.4.4 with $\alpha = 0$, i.e., given all emphasis to the grid regularity) is considered as a solution to the resampling problem, so as to assess the closest possible implementation of the patterns.

[21] This behavior also explains what was visualized in **Figure 32**: the change from 0.0 to 0.25 kept the pattern shape and phase errors (and hence the MSE) fairly constant while causing a visible difference in the gain (and hence the SNR); the changes from 0.25 up to 0.75 had visually little effect in both regards; and the final change to 1.0 led to a high-gain pattern (the best SNR figure) which is however completely different from the goal and shows a correspondingly high phase error (hence the high MSE).

[22] This can be explained by the fact that the optimum MSE solution incurs a relatively high SNR penalty by using all possible extended manifold elements, including fairly uncorrelated ones (corresponding to distant pulses). These do not contribute to a great improvement of the MSE, while degrading the SNR considerably. With moderately low values of α, very similar patterns are achieved with a lower weight magnitude, what can be interpreted as a better distribution of the activation energy, made possible by disregarding such extended manifold elements.

The optimal MSE weights where obtained for every output sample, using as commom pattern $G_{com}(f_{\mathrm{D}}) = G_{sum}(f_{\mathrm{D}})$ as design goal. The output grid has per PRI cycle 93 patterns, depicted in **Figure 35**. The abscissa values correspond again to Doppler frequency, and Bw_{proc} and PRF_{multi} are marked by red and black dashed lines, respectively, in both plots. **Figure 35 (a)** shows the pattern's power gain whereas **Figure 35 (b)** depicts the phase error with respect to the goal phase ramp (defined in (98) for each outputs sample's phase center $t_{out}[k]$ of (85)).

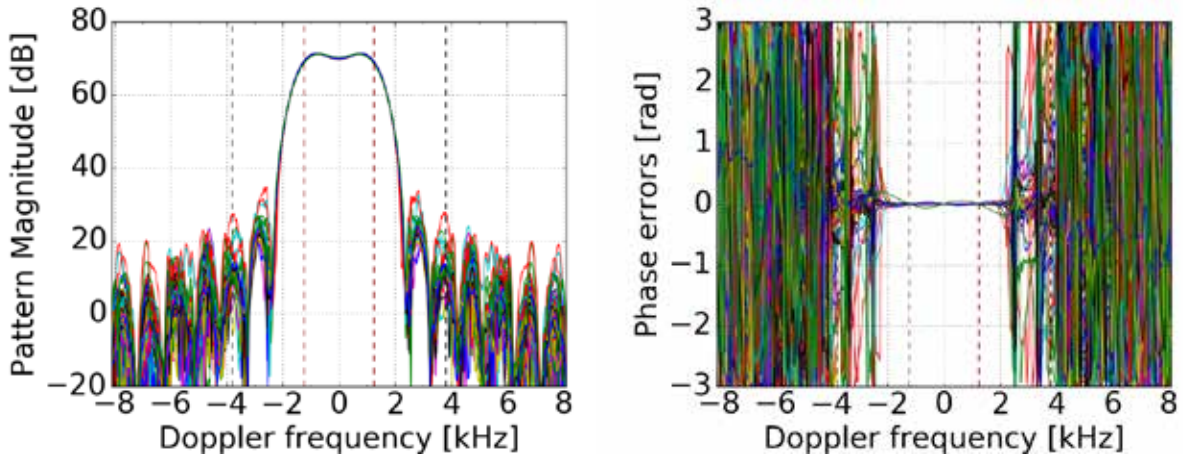

Figure 35. Set of output patterns obtained from the optimal MSE method against Doppler frequency. (a) Magnitude of patterns. (b) Phase after removal of the sample-specific linear phase ramp (cf. (98) and (85)), highlighting residual phase errors with respect to ideal regular sampling.

The similarity between the amplitude of the patterns in **Figure 35** and the sum pattern in **Figure 31** is clear, indicating that the implementation is close to the desired patterns. Within the main beam, the patterns show stable magnitudes and very low residual phase errors with respect to the desired phase center positions, further indicating that successful regularization was achieved over the grid.

Given the advantages of using the MSE-SNR-VBS method (cf. Section 4.4.4), the implementation of the grid using (117), (118) with $\alpha = 0.6$ is also considered, both directly and with the addition of the iterative method explained in Section 4.4.5.

The normalized MSE $\xi_{MSE}[k]/p_G$ and the SNR scaling $\Phi_{SNR}\left(\underline{\boldsymbol{w}}[k]\right)$ are shown over the output patterns for the three aforementioned methods in **Figure 36**.

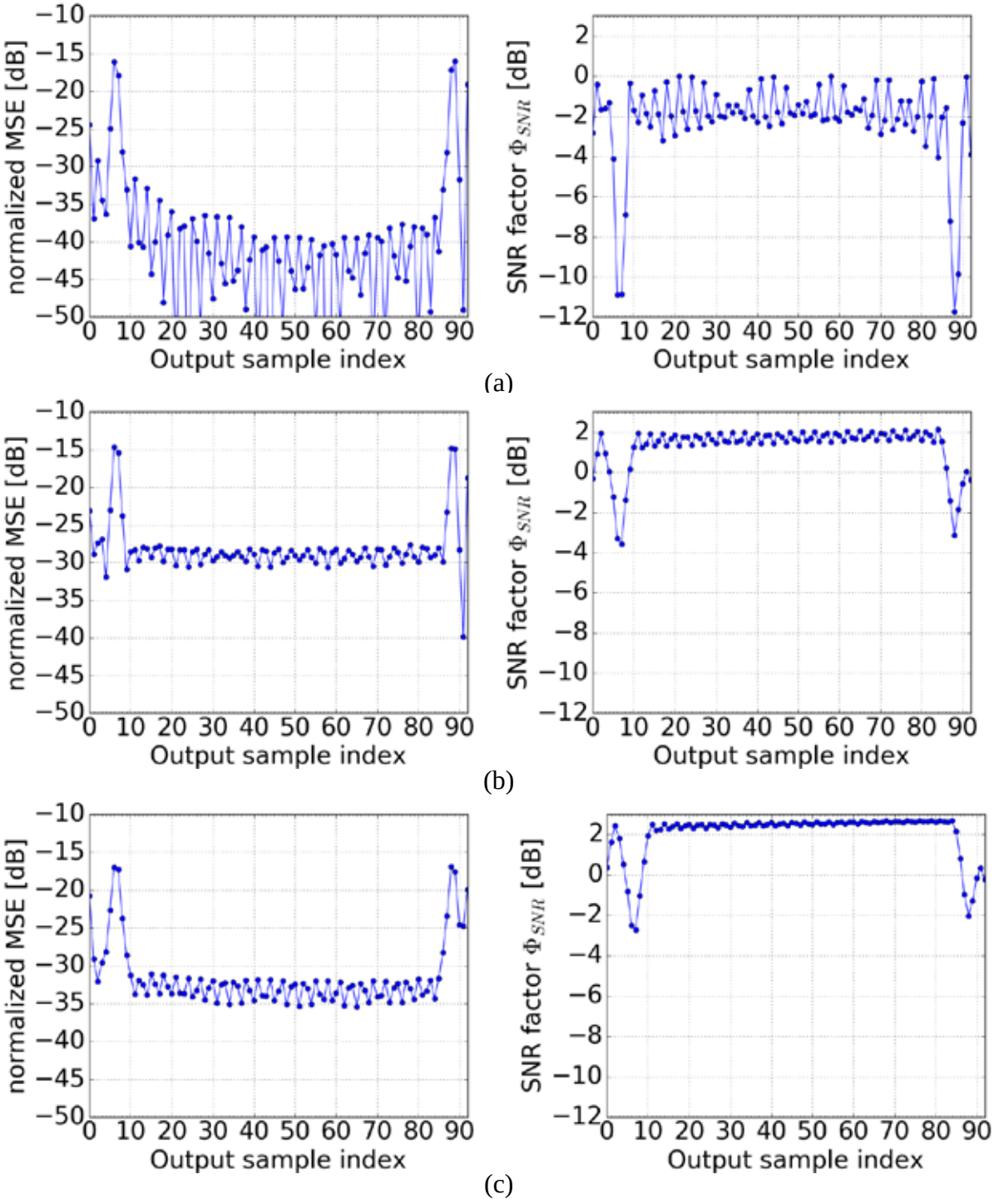

Figure 36. Normalized MSE (left column) and Φ_{SNR}(right column) over output patterns/samples for different regularization methods. (a) MSE-VBS. (b) Non-iterative MSE-SNR-VBS. (c) Iterative MSE-SNR-VBS. For the last two methods, $\alpha = 0.6$ was adopted.

The plots in **Figure 36 (a)** refer to the MSE-VBS method of Section 4.4.2. The ones in **Figure 36 (b)** were obtained with the MSE-SNR-VBS method of Section 4.4.4, evaluated with α = 0.6. Finally, the plots in **Figure 36 (c)** show the results for the iterative method of Section 4.4.5, again using the cost function $\xi_J[k]$ of (117) with α = 0.6. For all cases, performance is worse for the samples near the gaps (indices 5 to 8, and 87 to 90) and around the edges of the sequence (indices 0 and 92), which is a consequence of the choice of using only the samples within a PRI cycle for resampling.

A comparison of the results in **Figure 36 (a)** and **(b)** highlights once again the compromise between the MSE and the SNR described in Section 4.4, embodied by the design parameter α. Introducing the iterative procedure (compare **Figure 36 (b)** and **(c)**) enhances, on average, both MSE and SNR, with a larger improvement for the worst cases, as was the goal.

The ripple in Φ_{SNR} over the samples is also reduced, indicating that a more uniform performance was achieved. In all cases, the performance for the samples within the region of the blockage-induced gaps is clearly worse. This is expected and due to the larger phase center shift with respect to the input grid required to fill those gaps.

Further illustration of the iterative method is provided in **Figure 37**. In this case, the convergence criterion is an average MSE step $\Delta MSE = \overline{MSE}_i - \overline{MSE}_{i-1}$ of less than 0.05 dB, which requires a total of 11 iterations. The magnitude of the common patterns $G_{com}^{i}(f_{\mathrm{D}})$ is seen in **Figure 37 (a)** for different iteration numbers. The gradual modification of the patterns consists mostly of a change in the first sidelobes and attenuation at the borders of the main beam. This is the result of two effects: first, the incorporation of the mean residual distortion as a part of the design goal and second, the feedback of the SNR emphasis parameter α into the design goal. **Figure 37 (b)** shows how the MSE evolves with the iterations. Iteration i = 0 is equivalent to the non-iterative MSE-SNR-VBS method. The blue line shows $\overline{MSE}_i$, which is monitored for the convergence criterion, whereas the red one shows the worst-case over the grid,

which is also reduced, as intended, indicating a better approximation is achieved over the grid. **Figure 37 (c)** shows the average SNR scaling $\overline{\Phi_{SNR_i}}$, which is also seen to improve, reflecting the feedback of the SNR emphasis parameter α.

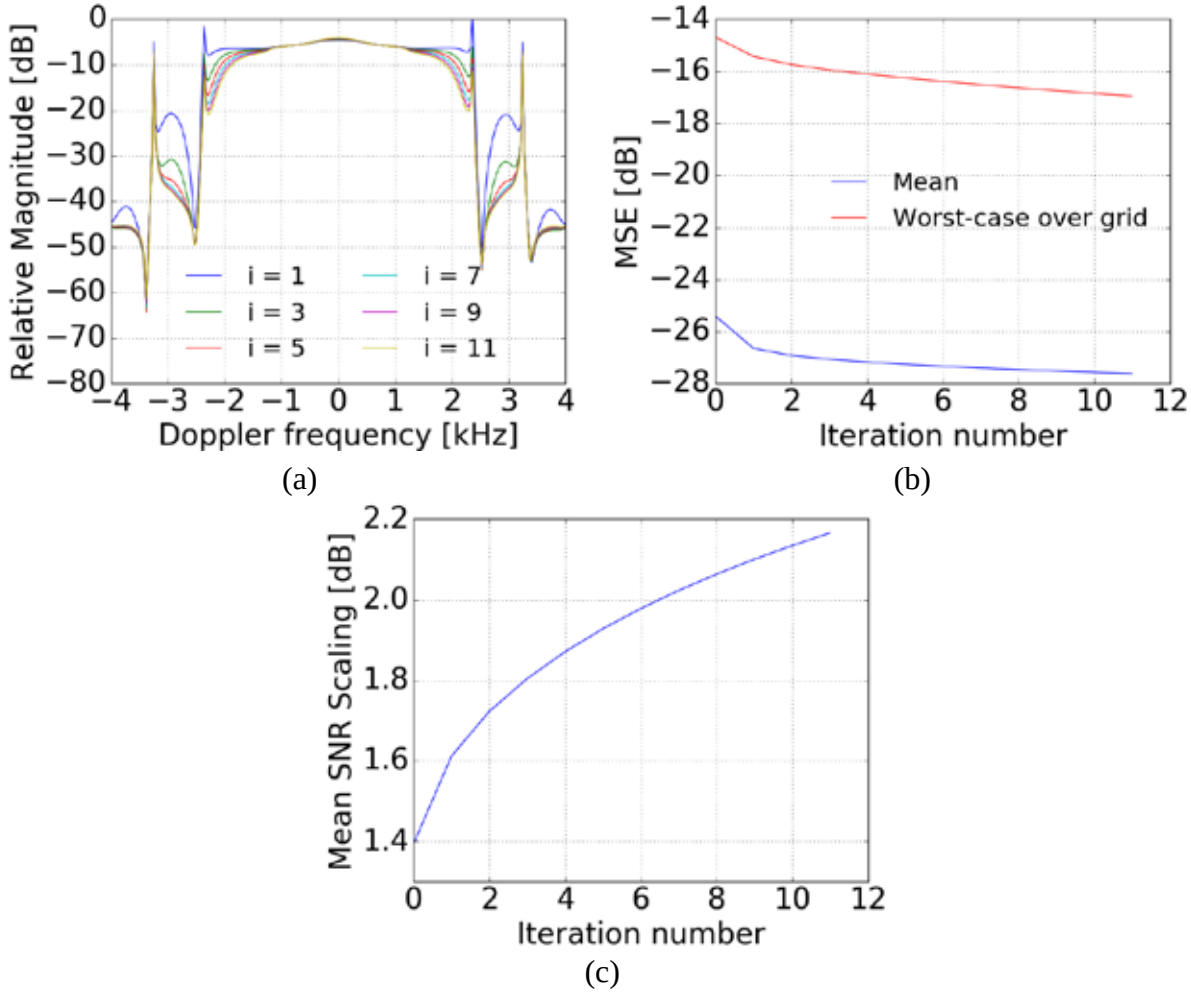

Figure 37. Iterative MSE-SNR-VBS method with $\alpha = 0.6$. (a) Magnitude of common patterns $G_{com}^{i}(f_{\mathrm{D}})$ for different iterations i. (b) MSE (mean over grid $\overline{MSE_i}$ in blue and worst-case over grid in red) as a function of iteration number. (c) Mean SNR Scaling $\overline{\Phi_{SNR_i}}$ as a function of iteration number.

As a final illustration of the method's characteristics, the actual illumination of the reflector's surface induced by the beamforming weights is plotted in **Figure 38**. The MSE-SNR-VBS weights with $\alpha = 0.6$ (cf. **Figure 36 (b)**) are chosen as an example. In each sub-figure (**(a)-(d)**), the abscissa values correspond to azimuth position, and two sub-plots are shown.

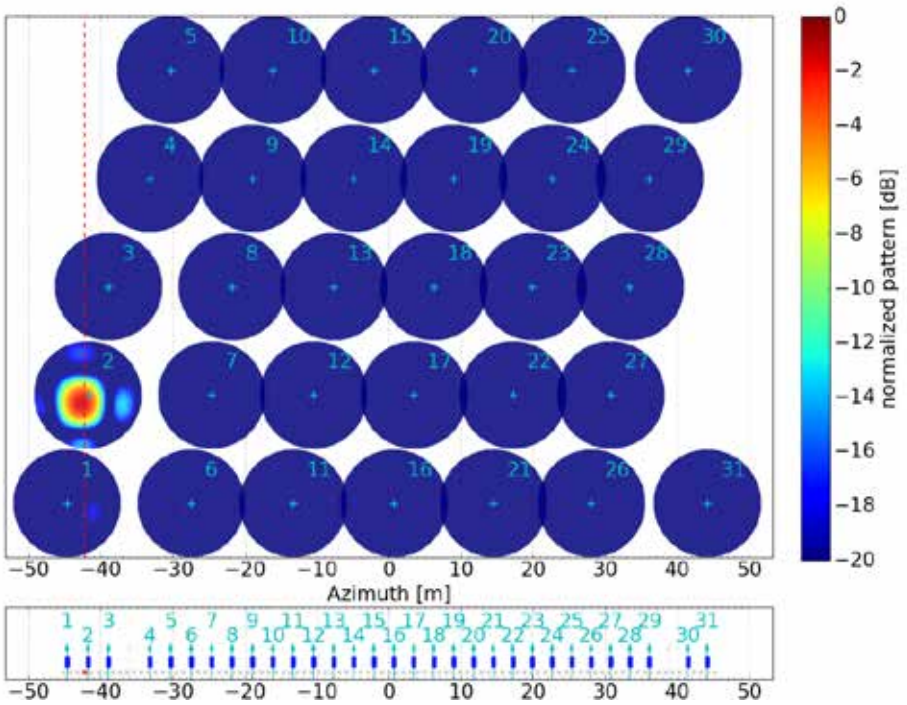
Azimuth [m]
normalized pattern [dB]
0
−2
−4
−6
−8
−10
−12
−14
−16
−18
−20
−50 −40 −30 −20 −10 0 10 20 30 40 50

(a)

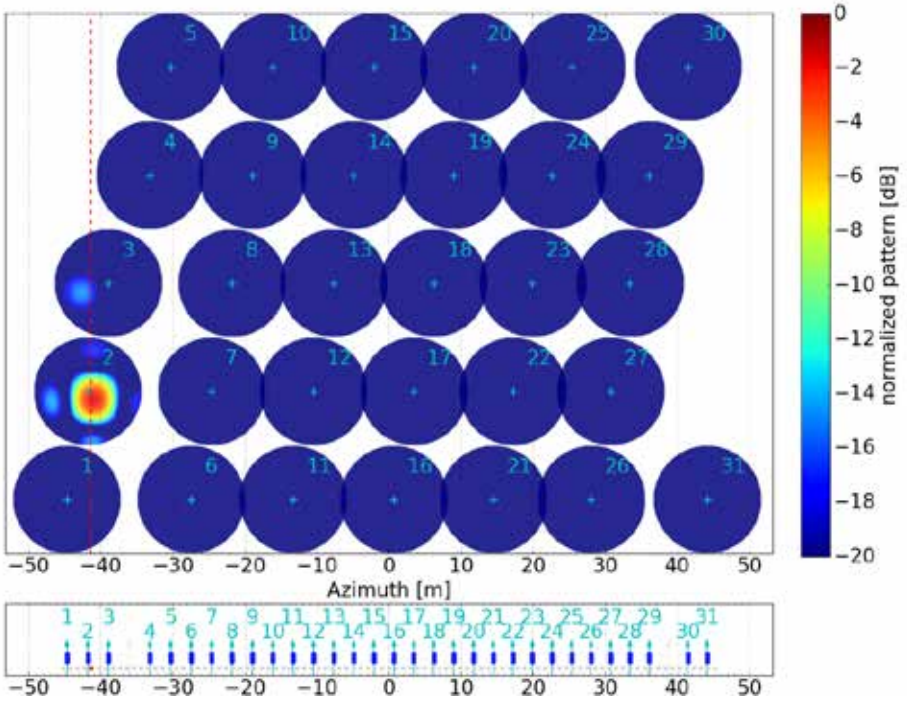
Azimuth [m]
normalized pattern [dB]
0
−2
−4
−6
−8
−10
−12
−14
−16
−18
−20
−50 −40 −30 −20 −10 0 10 20 30 40 50

(b)

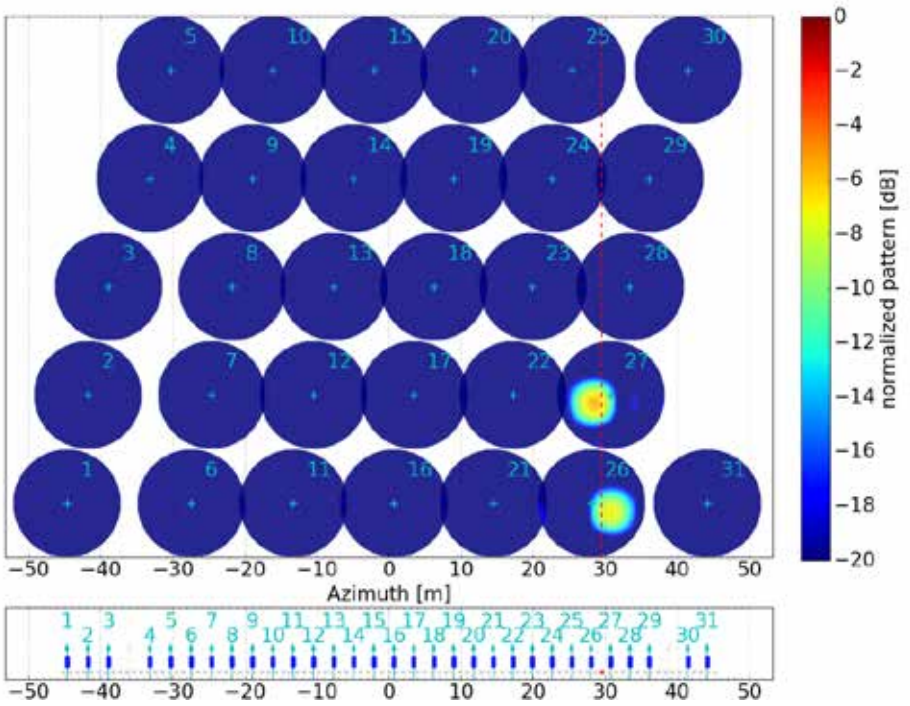

(c)

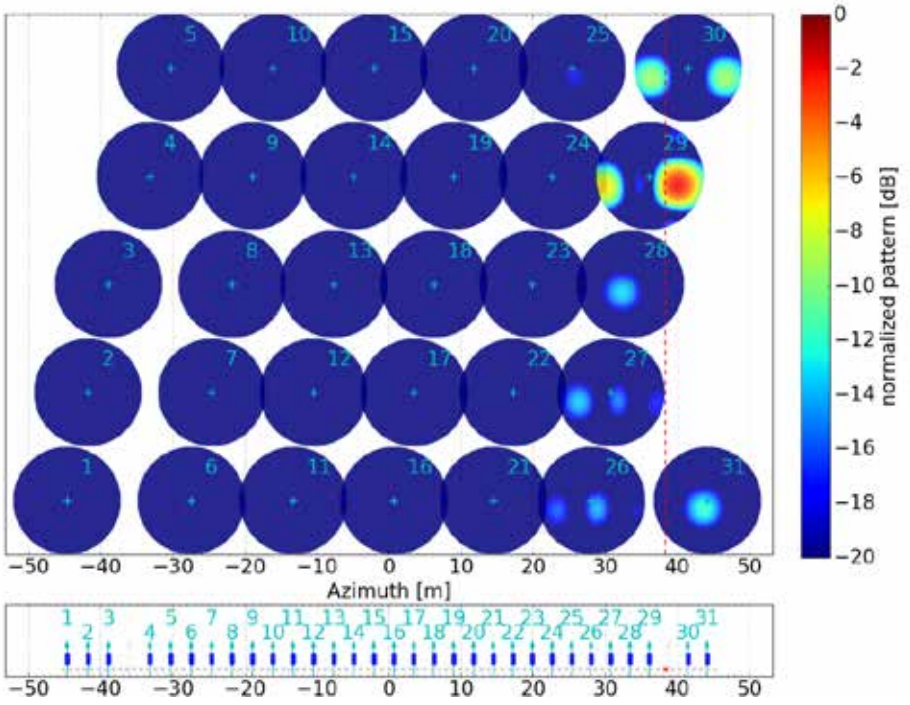

(d)

Figure 38. Illustration of reflector illumination for the MSE-SNR method with $\alpha = 0.6$. (a) Output sample of index $k = 4$: minor phase center shift is achieved with little contribution from other pulses. (b) Neighbor sample $k = 5$: notice gradual migration of the illumination. (c) $k = 74$: mainly two neighboring pulses are used to form the output pattern. (d) $k = 86$: in this sample occurring during the second Tx-event induced gap, several pulses are combined, degrading the SNR.

In each case, the upper sub-plot shows the illumination (normalized power distribution) at the reflector's surface, as seen from above, for each of the N_{eff} = 31 non-blocked pulses. The color coding indicates the resulting power levels, represented separately for each pulse. The separation in the ordinate axis has no physical meaning, and is only for visualization purposes. The reason is that, as it can be seen from the upper sub-plots, the displacement of the reflector between neighboring pulses is considerably smaller than its size, leading to considerable overlap between the surfaces, hampering visualization. The vertical red dashed line indicates the desired output sample phase center position, which changes from sub-figure to sub-figure. The azimuth sampling as in **Figure 32** is represented below for reference: pulse positions are highlighted by arrows, the individual physical channels' phase centers by blue circles and the desired output phase center by the red crosses. The N_{ch} = 3 physical channels are combined at each time to generate the corresponding illumination, meaning the weight vector of dimension $N_{manifold}$ = 93 is split into 31 sub-sets, so that it can be understood from which pulse position the main contribution to the output patterns arise. It should be noted that the final pattern is a sum of the contribution of all pulses. The surfaces' position in azimuth matches the sequence's $t_{rx}[i]$ (defined in (84)), and is highlighted by a cyan cross and the corresponding pulse number.

The **Figure 38 (a)** show the illumination for output sample k = 4, whereas **Figure 38** (b) corresponds to its neighbor, output sample k = 5. In both cases, the major contribution to the illumination is from a single pulse, the second. The comparison between them shows the migration of the primary beam as the desired phase center changes, and illustrates the physical principle behind the method, described in Section 4.3. **Figure 38 (c)** corresponds to output sample k = 74 and shows a different scenario, in which the contributions to the illumination are evenly split between neighboring pulses, which advocates for the use of the extended manifold. As described in Section 4.4.2, performance is improved (with respect to the pulse-independent steering) by taking advantage of the fact that the signal is oversampled

and thus information from different pulses can be exploited. Finally, **Figure 38 (d)**, corresponding to output sample $k = 84$ shows the worst-case performance, during the second Tx-induced gap. The larger phase center shift means that the correlation between the output pattern and the inputs is smaller, and several pulses are employed to implement the pattern. As visible in **Figure 36 (b)**, this worsens the pattern implementation (meaning higher MSE) and furthermore degrades the SNR performance, though this effect is to a considerable extent countered by the choice of the MSE-SNR method.

5.4.2 Impulse Response Function Analysis

The last section has addressed extensively the patterns of each sample in the regularly sampled output grid, to allow a better understanding of the introduced methods and of the compromises involved. This section takes the same example as in Section 5.2, but turns focus to the data after resampling and the SAR performance after focusing, providing an Impulse Response (IR) analysis for the output of the VBS methods.

Figure 39 shows the magnitude of the simulated azimuth raw data after resampling with the optimal MSE weights. **Figure 39 (a)** depicts (in blue) the channel's magnitude in the time domain, plotted against instantaneous Doppler frequency (which is calculated as a function of the time axis), and its shape shows a combination of the patterns seen in **Figure 35**. $G_{com}(f_{\mathrm{D}}) = G_{sum}(f_{\mathrm{D}})$ is also plotted in dashed red, as a visual aid for comparison. The simulation is noise-free, yet the sidelobe regions appear to be noisy, an effect which is caused by the fast residual variation of the patterns between samples, more pronounced in this region. This variation is more clearly visualized in **Figure 39 (b)**, where three cycles of the output grid are seen, starting from the center of the regularized channel. The abscissa refers to indices of the time axis from which the instantaneous Doppler of **Figure 39 (a)** is calculated, and is meant to highlight the period of $N_{out} = 93$ output samples. The zoom is taken starting from zero Doppler, a region where the modulation effect is seen to be small, as is the case over the main beam and in particular over the processed bandwidth, of

greater importance to the final focused signal quality. The relevance of the effect in the sidelobe region and especially outside the multichannel PRF area is reduced by the low gain levels of this part of the signal, which contributes mostly to residual azimuth ambiguities. At each cycle, magnitude oscilations occur following the patterns seen in **Figure 36 (a)**: the samples around the gaps (indices 5-8 and 87-90) plus the edges of the PRI sequence (indices 0 and 92) show worst performance and larger ripples.

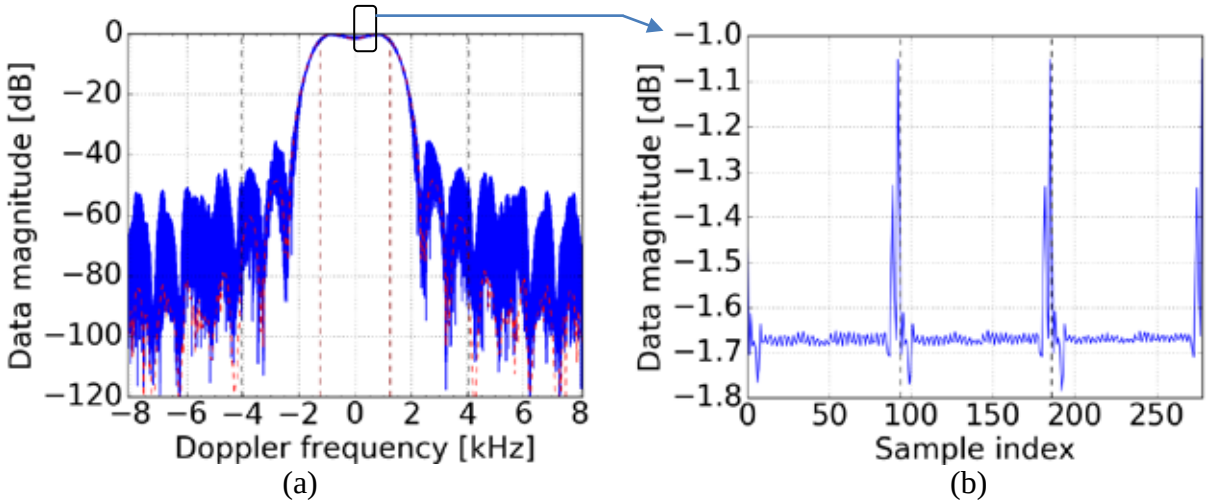

Figure 39. Magnitude of raw data after resampling with the optimal MSE weights. (a) The whole resampled channel in time domain, against instantaneous Doppler frequency (solid blue line) and the reference pattern (dashed red line). The relevant frequency regions Bw_{proc} and PRF_{multi} are marked by red and black dashed lines, respectively. (b) Zoom over three cycles of 93 samples each, starting from the center of the regularized channel, to highlight the residual modulation of the resampled signal.

In **Figure 40**, the focused impulse responses of the data regularized by the MSE-VBS and non-iterative MSE-SNR-VBS methods are plotted versus the instantaneous Doppler frequency. The IR for the iterative MSE-SNR-VBS is not shown due to its similarity to the other plots. Azimuth ambiguities are seen in the impulse responses of the regularized data, which are recognized to occur at multiples of $\overline{PRF}_{eff}$ / N_{eff}, as a result of residual regularization errors. It should be noted that $\overline{PRF}_{eff}$ / N_{eff} = 1 / T_{PRI} is the rate at which the PRI sequence repeats itself, and that the residual deviations between the achieved patterns and the ideal $G_{GOAL}(f_{\mathrm{D}}, k)$ lead to a periodical

modulation of the samples in the output channel at this rate. This residual modulation is also visible in **Figure 39 (b).** Their peak levels are nonetheless very low, indicating successful application of the methods for resampling.

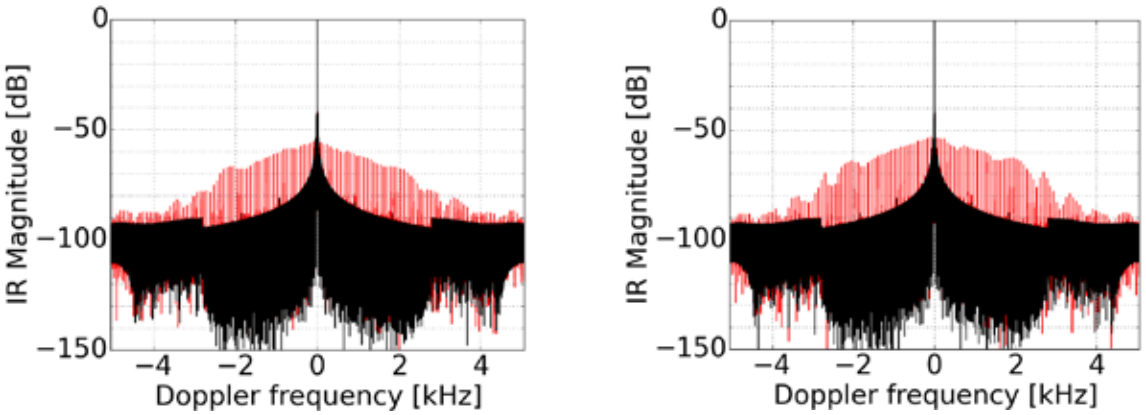

Figure 40. Impulse responses of regularized data (red) and alias-free reference regularly sampled at PRF_{multi} (black), for the MSE-VBS method (a) and (non-iterative) MSE-SNR-VBS method (b).

Figures of merit for the regularizations' output patterns and the impulse responses are summarized in TABLE III, where δ_{AZ} is the 3-dB azimuth resolution, AA_{PEAK} and AASR (cf. Appendix B) describe respectively peak and total azimuth ambiguity levels, while $\overline{MSE}$ and $\overline{\Phi_{SNR}}$ are averages (taken in linear units and then converted to dB) of the quantities in **Figure 36** over the output patterns, i.e.

$$\overline{MSE} = \sum_{k=1}^{N_{out}} \frac{\xi_{MSE}[k]}{N_{out} \cdot p_G}, \tag{139}$$

where $\xi_{MSE}[k]$ is the MSE of the local samples' pattern (defined in (102)), p_G is the goal pattern power (defined in (106)) and

$$\overline{\Phi_{SNR}} = \sum_{k=1}^{N_{out}} \frac{\Phi_{SNR}\left(\underline{\boldsymbol{w}}[k]\right)}{N_{out}}, \tag{140}$$

with $\Phi_{SNR}(\underline{\mathbf{w}})$ from (113). Recall that Φ_{SNR} is a ratio betwenn the achieved SNR and that of the goal pattern (in this case the sum), and therefore negative values indicate a degradation whereas a positive value indicates the SNR is improved with respect to unity beamforming.

TABLE III
COMPARISON BETWEEN VBS METHODS IN TERMS OF
ACHIEVED PATTERN AND IMPULSE RESPONSE FIGURES OF MERIT

Figure of Merit Symbol [unit]	Method		
	MSE-VBS (α = 0.0)	MSE-SNR-VBS (α = 0.6)	Iterative MSE-SNR-VBS (α = 0.6)[23]
δ_{AZ} [m]	2.4	2.4	2.4
AA_{PEAK} [dB]	-55.3	-53.1	-53.3
AASR [dB]	-40.2	-37.3	-36.8
$\overline{MSE}$ [dB]	-28.9	-25.4	-27.6
$\overline{\Phi_{SNR}}$ [dB]	-1.9	1.4	2.2

The resolution goal of 3.0 m is achieved and acceptably low AASR levels are obtained for all methods. Furthermore, the proposed joint optimization (SNR-VBS) is seen to allow a considerable gain in SNR at the expense of an acceptably small loss in MSE and AASR levels. Since the design goal of the MSE cost function (cf. (98)) is to enforce regularity, the MSE and AASR levels are directly linked and the MSE-SNR compromise translates into an AASR-SNR one. It should, however, be noted that $G_{com}(f_{\mathrm{D}})$ also affects the final MSE levels, and the change in this parameter between the two last methods (non-iterative and iterative SNR-VBS) is the reason why the iterative method achieved a slightly worse AASR despite better $\overline{MSE}$.

As a reference, Φ_{SNR} for a frequency-adaptive MVDR beam [40] yields 3.2 dB for regular sampling. This technique requires Doppler-dependent weights and cannot directly be implemented without a regularly sampled input, but may be employed as

[23] The low AASR levels indicate that an even higher azimuth bandwidth could be processed, leading to a better resolution. Section 6.2.2 provides an example with an even higher azimuth resolution.

an SNR upper bound. The proximity of the levels indicates that the performance achieved by means of the joint optimization is also satisfactory with regard to noise rejection, as intended.

5.5 Remarks on Simulation Examples

In this chapter, the sampling scenario of a particular range of a multichannel staggered SAR system (cf. Section 5.2) was used to provide illustrative examples of the application of the methods described in Section 4.4. The impact of the SNR sensitivity parameter on the resampling was analyzed in Section 5.3, focusing on a particular sample of the output grid. Then, Section 5.4 analyzed and compared the output of the different methods over the whole grid, both in terms of the pattern characteristics and the final impact on the SAR system impulse response. In Section 6.2.1, the performance of the SAR system shown here is evaluated over the whole swath.

6 System Design Examples

6.1 Chapter Overview

Chapter 5 provided a first example of the application of the methods in Section 4.4 by means of a simulated point-target response. The analysis was restricted to a single range, to allow an in-depth investigation of the resampling both in terms of the output patterns and the final SAR performance. This allowed emphasizing important aspects of the methods' behavior and the inherent trade-offs involved in the choice of parameters. In this chapter, however, focus is turned to first-order of Multichannel Staggered SAR system design and the prediction of their SAR performance over the whole swath of interest. Reflector systems with single (Section 6.2) and quad (Section 6.3) polarization are presented, as well as a planar system in single polarization (Section 6.4), exemplifying the guidelines in Section 4.5.

All systems operate in L-band and have in common very demanding HRWS operational requirements, detailed in TABLE IV. A comparison of the W_g / δ_{az} ratios (cf. Section 2.3.1) with those of state-of-the-art systems (cf. Section 1.1) in TABLE I shows that these systems outperform current (by an order of magnitude) and even near-future spaceborne systems.

TABLE IV
EXAMPLE HRWS SYSTEMS OVERVIEW

	Section Number			
	6.2.1	6.2.2	6.3	6.4
Antenna architecture	Reflector	Reflector	Reflector	Planar
Polarization	Single-pol	Single-pol	Quad-pol	Single-pol
Goal azimuth resolution δ_{az}	3.0 m	1.0 m	2.0 m	1.5 m
Swath width	350 km	500 km	400 km	400 km
Ratio W_g / δ_{az}	$116.7 \cdot 10^3$	$500 \cdot 10^3$	$200 \cdot 10^3$	$266.7 \cdot 10^3$
Repeat cycle	8 days	6 days	7 days	7 days
Goal NESZ level	-25 dB	-25 dB	-25 dB	-25 dB
Goal azimuth and range ambiguity levels	-25 dB	-25 dB	-25 dB	-25 dB

Part of the material presented in this chapter has been published in [68] and [69].

Section 6.5 turns focus to another important aspect of system design, namely the data rates and a first assessment of the on-board implementation complexity of the multichannel staggered SAR resampling in azimuth.

6.2 Reflector Systems in Single Polarization

6.2.1 Tandem-L High-Resolution 3.0 m Mode

This section complements the example presented in Section 5.2, namely the high-resolution 3.0 m mode alternative for Tandem-L [35], [36]. As described in TABLE V, the mode relies on a 15 m reflector with a multichannel feed, yielding 3 azimuth channels. The goal is to image a 350 km swath from an orbit height of 745 km, which allows a repeat cycle of 8 days.

TABLE V
SIMULATION SCENARIO PARAMETERS: REFLECTOR SINGLE POLARIZATION (TANDEM-L BASED)

Platform and swath parameters		
Parameter	Symbol	Value
Orbit height	h_{orbit}	745 km
Swath width on ground	W_g	350 km
Swath minimum/maximum incidence angle	η_{min}/η_{max}	26.3 / 46.9 deg
Swath minimum/maximum look angle	$\theta_{min}/\theta_{max}$	23.4 / 40.9 deg
Reflector and feed parameters		
Parameter	Symbol	Value
Diameter	D	15.0 m
Focal length	F	13.5 m
Feed offset in elevation	d_{OFF}	9.0 m
Center frequency	f_0	1.2575 GHz
Number of channels in elevation/azimuth	N_{el}/N_{az}	32 / 3
Channel spacing in elevation/azimuth	d_{el}/d_{az}	0.68 λ / 1.2 λ
Feed dimensions (elevation, azimuth)	(L_{el}, L_{az})	(5.2, 0.86) m
Feed losses	L_Ω	3.6 dB
Elevation tilt angle w.r.t. nadir	θ_{tilt}	32.0 deg

Pulse and Tx/Rx hardware parameters		
Parameter	Symbol	Value
Average PRF	$\overline{PRF}$	2700 Hz
Initial PRI	PRI_0	386 μs
PRI sequence step	Δ_{PRI}	-0.98 μs
PRI sequence length	N_{PRI}	33
Duty cycle	T_{dc}	4%
Pulse (chirp) bandwidth	Bw_{chirp}	85 MHz
Peak transmit power of a Transmit-Receive Module (TRM)	P_{TX}	87.0 W
Average transmit power	$\bar{P}_{TX}$	340 W
System noise temperature	T_{noise}	649 K
Transmitted polarizations	-	V
Beamforming and processing parameters		
Parameter	Symbol	Value
Goal azimuth resolution	δ_{az}	3 m
Processed Doppler bandwidth	Bw_{proc}	2494 Hz
Number of simultaneous elevation beams	N_{beams}	4
Elevation beamforming algorithm	–	MVDR
Number of active elements for elevation beamforming	$N_{active_{elev}}$	5
Number of pulses / samples in azimuth beamformer window	N_p / N_{win}	33 / 99
SNR emphasis parameter	α	0.0

Before the azimuth resampling, elevation DBF takes place applying the MVDR algorithm (cf. Appendix A) to form the SCORE beams [36]. At each range, 5 out of the 32 elements are activated to form the beams. In this case, a total of 4 simultaneous elevation beams are required to be formed. The azimuth beamforming is the resampling technique of Section 4.4.2, in this case prioritizing ambiguity suppression. An important difference with respect to Sections 5.2 to 5.4 is that here the restriction that a single PRI cycle is used for resampling — adopted before to make the first example simpler — is removed. Instead, a moving window of N_p = 33 pulses is considered which allows samples from the previous and posterior PRI cycle to be used as input, what considerably improves performance in the output samples at the beginning and end of the cycle.

The predicted SAR performance is summarized in **Figure 41**. The 350 km swath extends from 326 to 678 km ground range.

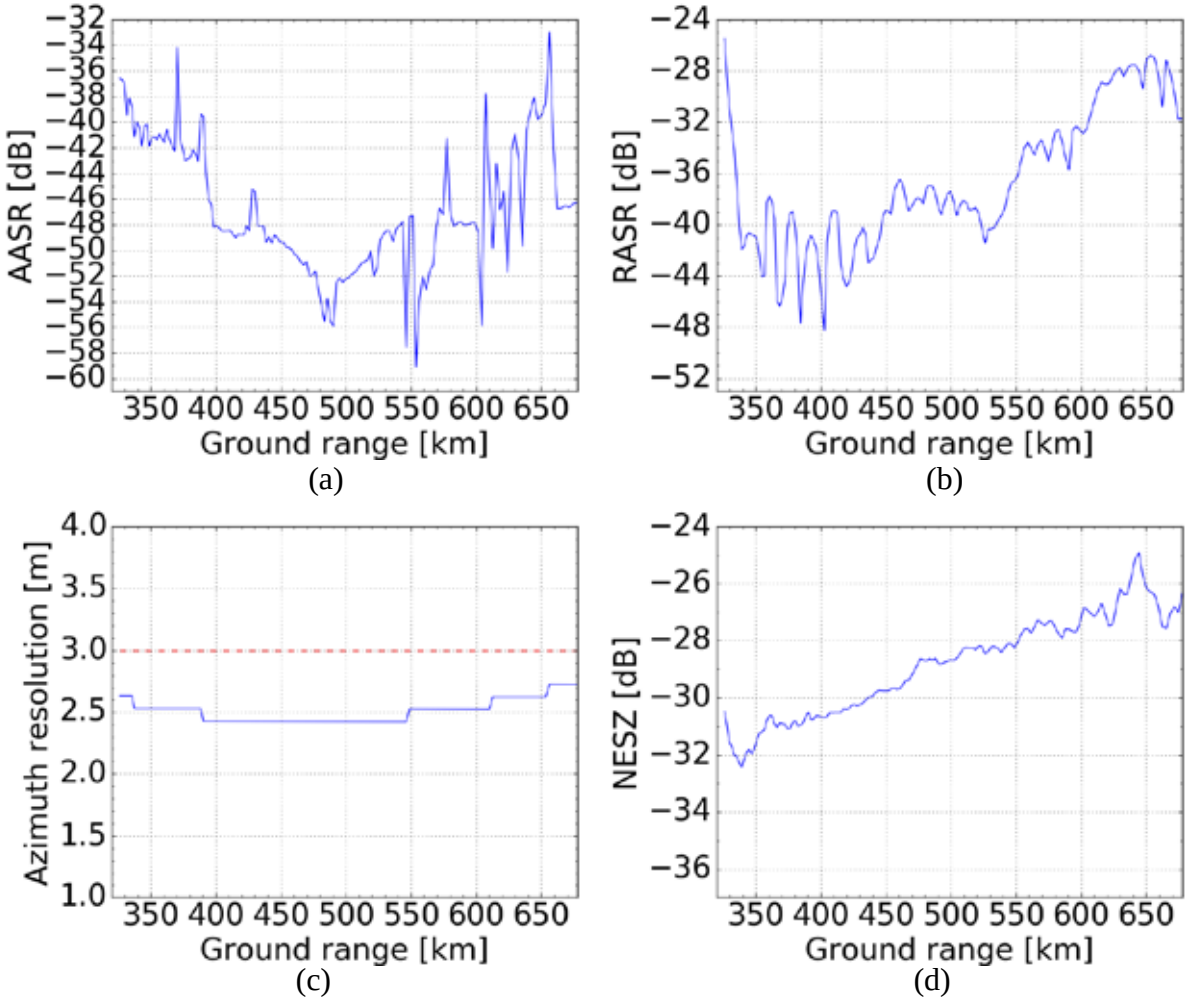

Figure 41. SAR performance over swath for 3.0 m / 350 km single-pol multichannel staggered SAR mode using a 15.0 m reflector with 3 azimuth channels. (a) AASR. (b) RASR. (c) Azimuth resolution. (d) NESZ.

Figure 41 (a) shows the AASR, which is better than -32.9 dB over the swath. The curve is seen to combine an overall concave shape over the swath (with lower levels in middle range) with local performance oscillations. The smooth concave trend can be related to defocusing of the reflector patterns, an effect of the offset with respect to the focal plane [40]. In near or far range, the elements which are active over elevation are positioned at the extremes of the feed, that is, further away from the paraboloid's focus. In contrast, in the center of the swath, the elements are closer to the focus and

the corresponding patterns (both in elevation and azimuth) are narrower and better focused. This characteristic of the antenna patterns in azimuth improves the resampling performance. The second effect, the local variations, can be traced back to the variation of the local sampling conditions according to pulse blocking. In general, gaps of smaller duration lead to smaller required phase center shifts, a more favorable condition that improves performance as well. The very low AASR levels indicate that an even higher azimuth bandwidth could be processed, leading to a better resolution. This motivates the second scenario, described in the following, in Section 6.2.2.

Figure 41 (b) shows the RASR levels, which are below -26.5 dB. The azimuth resolution seen in **Figure 41 (c)** is better than 2.7 m (without any windowing, such as Hamming). The NESZ, plotted in **Figure 41 (d)** is better than -25 dB for the transmitted power of 340 W. The design is thus seen to fulfil the requirements in TABLE IV.

The beamformer's behavior over range in terms of noise amplification and the phase center resampling is considered in **Figure 42**. **Figure 42 (a)** shows the average noise scaling $\overline{\Phi_{SNR}}$ of (140) over range. Recall that a negative value denotes here SNR degradation, and that this factor is included in the NESZ estimation in **Figure 41 (d).** It is shown to illustrate the sensitivity degradation caused by the beamforming (in comparison to unity weights), which in this cases lies between -1.8 and -1.0 dB. **Figure 42 (b)** shows the absolute value of the maximum phase center shift Δx_{eq} between the input and output grid for the given range. It is assumed that δt is chosen to equalize in absolute value the smallest and largest shift, meaning the shifts are in the interval $[-\Delta x_{eq}, \Delta x_{eq}]$ (cf. **Figure 22** and discussion in Section 4.3). The shifts reach ±2.7 m but are seen to be considerably smaller in the regions where no blockage occurs (cf. blockage diagram in **Figure 30**), around ±1.4 m, what is due to the absence of gaps. The red dashed line indicates the maximum shift of the phase centers allowed by the reflector diameter of 15.0 m, ±3.75 m (recall that the shift is done only on Rx and thus the impact on the two way phase center is halved).

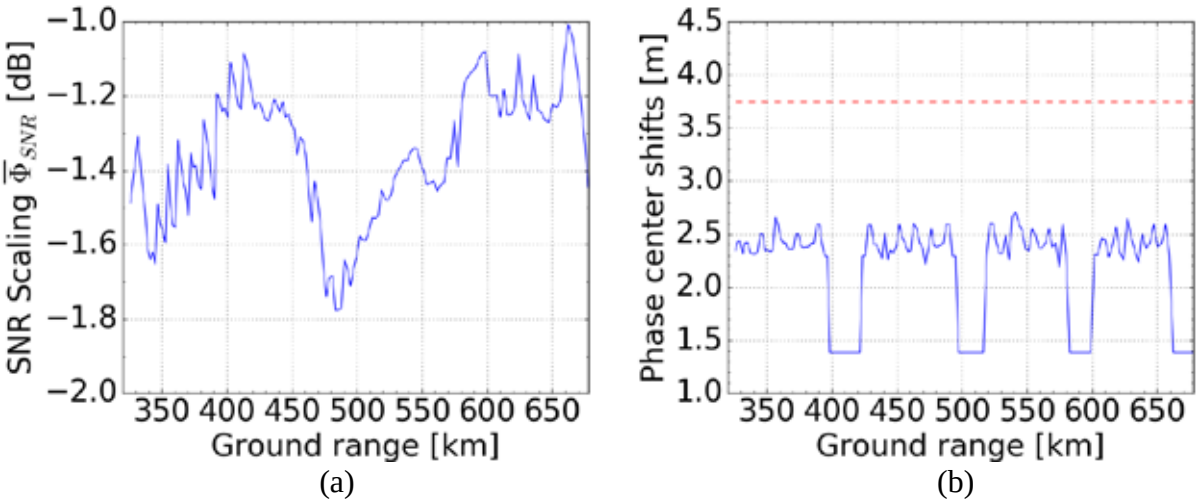

Figure 42. Performance of azimuth beamforming over range. (a) Average noise scaling $\overline{\Phi_{SNR}}$. (b) Absolute value of worst-case shift Δx_{eq} of the phase center between input and output grid.

6.2.2 Very High Resolution Wide Swath Mode

A second example is provided which considers even more demanding requirements, this time allowing deviations from the Tandem-L Mission parameters. As indicated in TABLE IV, this time the goal is to achieve a very fine 1.0 m azimuth resolution over a very wide 500 km swath. The adopted orbit is at a height of 800 km. The reflector and feed design has the one presented in [36] as a starting point, adapted as described below. The antenna system and the mode's operational characteristics are described in TABLE VI. The feed architecture in azimuth still has doublets spaced by 0.6 λ combined pairwise to form channels with 1.2 λ spacing, but the number of channels is increased (in comparison to the design in Section 6.2.1) to 9, to cover the higher Doppler bandwidth required by the azimuth resolution. The patterns are simulated using the GRASP software [113].

The DBF processing of the data starts over the elevation channels, with the goal of forming a high gain SCORE beam for each range. In this case, the sidelobe-constrained beamformer (cf. Appendix A) is employed, with 9 active elements at each time, and a sidelobe region constraint of -36 dB.

TABLE VI
SIMULATION SCENARIO PARAMETERS: REFLECTOR SINGLE POLARIZATION

Platform and Swath Parameters		
Parameter	Symbol	Value
Orbit height	h_{orbit}	800 km
Swath width on ground	W_g	500 km
Swath minimum/maximum incidence angle	η_{min}/η_{max}	23.0 / 50.2 deg
Swath minimum/maximum look angle	$\theta_{min}/\theta_{max}$	20.3 / 43.1 deg
Reflector and Feed Parameters		
Parameter	Symbol	Value
Diameter	D	15.0 m
Focal length	F	15.0 m
Feed offset in elevation	d_{OFF}	10.0 m
Center frequency	f_0	1.2575 GHz
Number of channels in elevation/azimuth	N_{el}/N_{az}	55 / 9
Channel spacing in elevation/azimuth	d_{el}/d_{az}	0.6 λ / 1.2 λ
Feed dimensions (elevation, azimuth)	(L_{el}, L_{az})	(7.88, 2.57) m
Feed losses	L_Ω	2.0 dB
Elevation tilt angle	θ_{tilt}	32.5 deg
Pulse and Tx/Rx Hardware Parameters		
Parameter	Symbol	Value
Average PRF (both polarizations)	$\overline{PRF}$	2120 Hz
Initial PRI	PRI_0	503.5 ms
PRI sequence step (between pulses of same polarization)	Δ_{PRI}	-2.36 ms
PRI sequence length	N_{PRI}	28
Pulse duty cycle	T_{dc}	6%
Pulse (chirp) bandwidth	Bw_{chirp}	85 MHz
Peak transmit power of a Tx/Rx Module	P_{TX}	87.0 W
Average transmit power	$\bar{P}_{TX}$	2584 W
System noise temperature	T_{noise}	649 K
Transmitted polarizations	-	V
Processing Parameters		
Parameter	Symbol	Value
Goal azimuth resolution	δ_{az}	1 m
Processed Doppler bandwidth	Bw_{proc}	7451 Hz
Number of simultaneous elevation beams	N_{beams}	5
Elevation beamforming algorithm	–	Sidelobe-constrained beamformer
Number of active elements for elevation beamforming	$N_{active_{elev}}$	9
Elevation beamforming sidelobe constraint	$20 \cdot \log_{10}(\epsilon_{SDL})$	-36 dB
Number of pulses /samples in azimuth beamformer window	N_p / N_{win}	5 / 45
SNR emphasis parameter	α	0.5

Following the elevation beamforming, azimuth beamforming according to the strategy of Section 4.4.4, with α = 0.5, is applied. In light of the large number of azimuth channels, the pulse vicinity of the extended manifold is limited to 5 pulses, so that N_{win} = 5 · 9 = 45 input samples are used to form each output sample. All these adaptations tend to prioritize the SNR, which is a critical factor in this scenario due to the very wide 500 km swath.

The SAR performance over the swath is depicted in **Figure 43**. The 500 km swath extends from 300 to 800 km ground range.

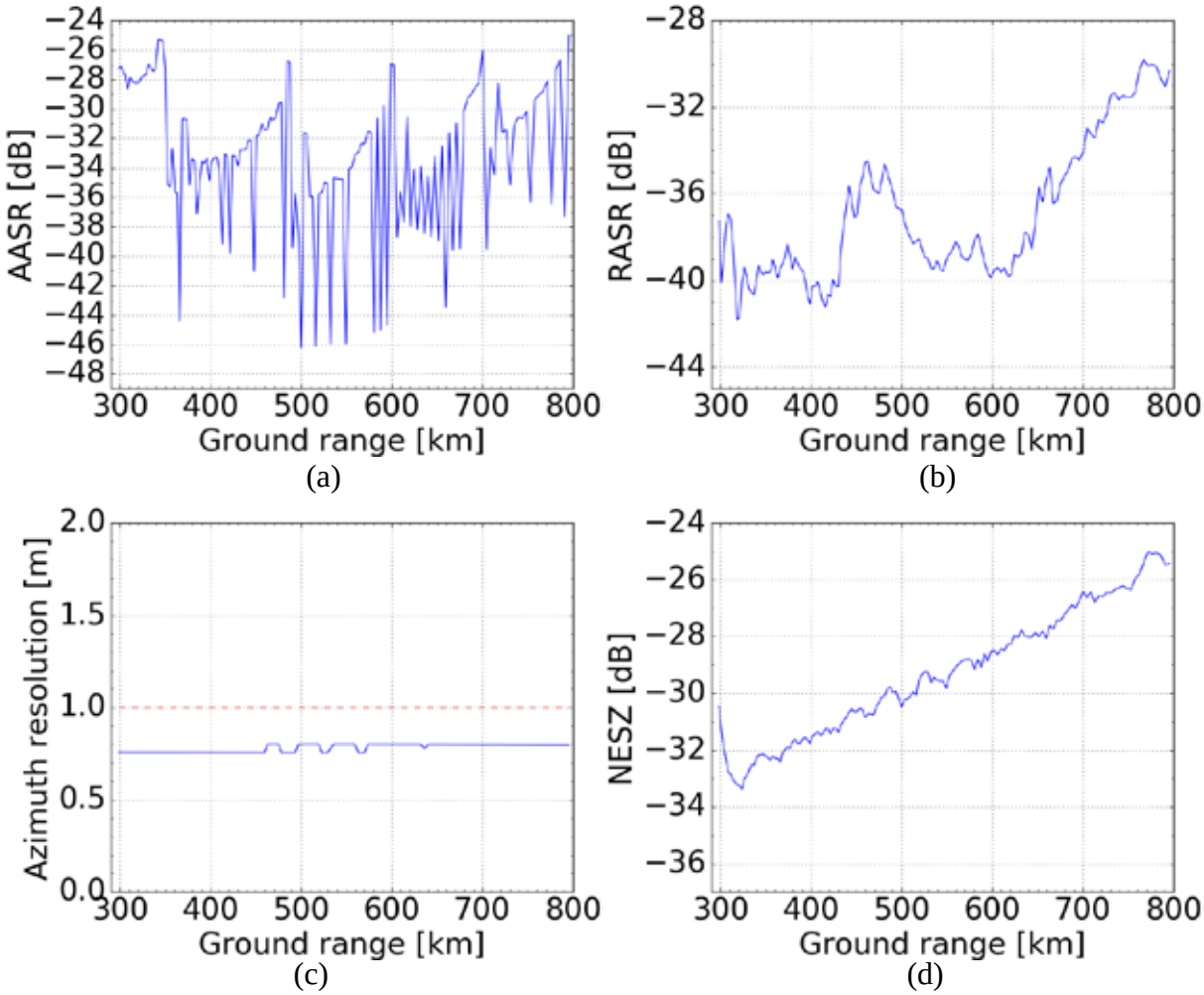

Figure 43. SAR performance over swath for 1.0 m / 500 km single-pol multichannel staggered SAR mode using a 15.0 m reflector with 9 azimuth channels. (a) AASR. (b) RASR. (c) Azimuth resolution. (d) NESZ.

In this example, the AASR (cf. **Figure 43 (a)**) is better than -25.0 dB, therefore fulfilling the requirements but showing no margin with respect to them, unlike in the previous case. This can be traced back to the choice of azimuth beamforming parameters, intentionally prioritizing the SNR. The RASR (cf. **Figure 43 (b))** is better than -29.8 dB, showing very good ambiguity suppression as a consequence of the sidelobe constrained beamformer. The azimuth resolution (cf. **Figure 43 (c)**) is better than 0.8 m over the swath, achieving the goal of 1.0 m with margin for spectral weighting. As seen in **Figure 43 (d)**, the NESZ is better than -25.0 dB for an average transmitted power of 2584 W. The required power is higher than in other scenarios, as a consequence of the very wide swath and the moderate reflector size. (cf. design example in Section 6.3, in which the power requirement is reduced by using a larger reflector)

Beamformer behavior over range is considered in **Figure 44**. The SNR scaling $\overline{\Phi_{SNR}}$ in **Figure 44 (b)** is positive for this case, meaning the DBF performs better than unity weights with respect to gain, a consequence of the α parameter. A gain between 0.5 and 1.5 dB is achieved. The worst-case phase shift in **Figure 44 (b)** is ± 3.5 m, close to the limit of ± 3.75 imposed by the reflector.

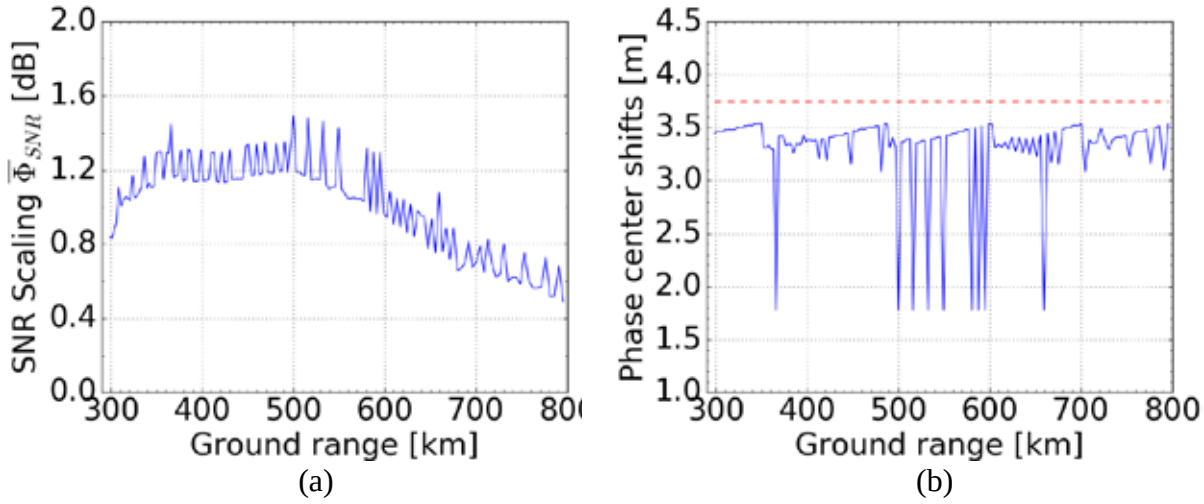

Figure 44. Performance of azimuth beamforming over range. (a) Average noise scaling $\overline{\Phi_{SNR}}$. (b) Absolute value of worst-case shift Δx_{eq} of the phase center between input and output grid.

6.3 Fully Polarimetric Reflector System

Fully polarimetric HRWS operation is especially challenging from a system design perspective. In order to image the swath in quad-pol, the pulses with H and V polarization are interleaved on transmission and received simultaneously. As mentioned in Section 3.3.3, the PRI sequence has to be designed differently for this case: the approach of [53] is followed, meaning the design is performed for a reference single-pol case with half of the mean PRI and then each PRI in the sequence is repeated twice for the interleaved dual-pol transmission sequence.

The interleaved polarization transmission has two noteworthy effects. First, with regard to the azimuth sampling, the spacing of the V (assumed to be the first polarization in the sequence) and the H transmitted pulses differs (namely by Δ_{PRI} between corresponding pulses), making the azimuth performance — notably the AASR levels — dependent on the transmit polarization. Second, the signal is affected by both co-pol (even order) and cross-pol (odd order) range ambiguous returns, with a spacing corresponding to $2 \cdot \overline{PRF}$, which degrades the range ambiguity performance in comparison to an equivalent single-pol case operated at the same $\overline{PRF}$. The cross-pol returns show closer proximity in comparison to the co-pol returns. This means that the former tend to dominate the RASR performance, unless the backscatter levels in cross-pol are much lower than in co-pol and compensate for the differences in range. Considering the L-band backscatter model of [115], the proximity effect is indeed dominant, which leads the cross-pol range ambiguity levels to be the design driver.

In light of the fact that the range ambiguity levels are similar to a single-pol system operated at the double of $\overline{PRF}$, the RASR requirement imposes an upper bound on this parameter. The design guideline is therefore to keep $\overline{PRF}$ as low as possible to counter range ambiguities. The lower $\overline{PRF}$ tends to degrade azimuth performance, but this may be compensated in the antenna design. The antenna system and the mode's operational characteristics are described in TABLE VII.

TABLE VII
SIMULATION SCENARIO PARAMETERS: REFLECTOR QUAD POLARIZATION

Platform and swath parameters		
Parameter	Symbol	Value
Orbit height	h_{orbit}	700 km
Swath width on ground	W_g	400 km
Swath minimum/maximum incidence angle	η_{min}/η_{max}	25.0 / 49.3 deg
Swath minimum/maximum look angle	$\theta_{min}/\theta_{max}$	22.4 / 43.1 deg
Reflector and feed parameters		
Parameter	Symbol	Value
Diameter	D	18.0 m
Focal length	F	18.0 m
Feed offset in elevation	d_{OFF}	12.0 m
Center frequency	f_0	1.2575 GHz
Number of channels in elevation/azimuth	N_{el}/N_{az}	65 / 6
Channel spacing in elevation/azimuth	d_{el}/d_{az}	0.6 λ / 0.8 λ
Feed dimensions (elevation, azimuth)	(L_{el}, L_{az})	(9.30, 1.14) m
Feed ohmic losses	L_Ω	3.5 dB
Elevation tilt angle	θ_{tilt}	34.3 deg
Pulse and Tx/Rx hardware parameters		
Parameter	Symbol	Value
Average PRF (both polarizations)	$\overline{PRF}$	2 x 1750 Hz
Initial PRI	PRI_0	313 μs
PRI sequence step (between pulses of same polarization)	Δ_{PRI}	-1.34 μs
PRI sequence length	N_{PRI}	2 x 41
Pulse length	T_P	22.9 μs
Duty cycle	T_{dc}	2 x 4%
Pulse (chirp) bandwidth	Bw_{chirp}	85 MHz
Peak transmit power of a Transmit-Receive Module (TRM)	P_{TX}	16.0 W
Average transmit power	$\bar{P}_{TX}$	500.0 W
System noise temperature	T_{noise}	649 K
Transmitted polarizations	-	H, V (interleaved)
Beamforming and processing parameters		
Parameter	Symbol	Value
Goal azimuth resolution	δ_{az}	2 m
Processed Doppler bandwidth	Bw_{proc}	3752 Hz
Number of simultaneous elevation beams	N_{beams}	6
Elevation beamforming algorithm	–	Sidelobe-constrained beamformer
Number of active elements for elevation beamforming	$N_{active_{elev}}$	11
Elevation beamforming sidelobe constraint	$20 \cdot \log_{10}(\epsilon_{SDL})$	-40 dB
Number of pulses / samples in azimuth beamformer window	N_p / N_{win}	25 / 150
SNR emphasis parameter	α	0.0

The most relevant design modification with impact on the azimuth performance in comparison to the systems in Section 6.2 is the reduction of the channel spacing and the usage of a larger reflector. The smaller spacing improves the steering capabilities of the feed array and increases the grating-lobe free steering region for the primary beam; whereas the larger reflector increases the maximum possible phase center shift (cf. Sections 4.3 and 4.4). As a consequence, the performance of the resampling (operated by illuminating different areas of the reflector) is improved and a reduction of the mean PRF without severely impairing the azimuth performance levels achieved in the previous configuration is made possible. Another advantage of the large reflector is the large aperture area, which boosts antenna gain and improves the SNR for the same transmitted power. In light of this fact, the MSE-VBS (cf. Section 4.4.2) is chosen as azimuth beamformer, shifting the AASR-SNR trade-off in favor of improved AASR.

In this case, the elevation beamforming for SCORE consists in the sidelobe-constrained beamformer (cf. Appendix A), using 11 elements at a time with a sidelobe constraint of -40 dB.

The SAR performance is summarized in **Figure 45**. The 400 km swath extends from 290 to 690 km ground range. The AASR levels in **Figure 45 (a)** are below -30.2 dB. The good performance shown can be traced back to the large reflector and the improved steering capabilities of the feed, due to the smaller element spacing. The RASR levels in **Figure 45 (b)** are better than -25.7 dB. The cross-pol ambiguities are seen to be clearly dominant. Their level in far range approaches the requirement, and they become as mentioned the design driver for the mode. As seen in **Figure 45 (c)** the goal resolution of 2.0 m is achieved. The NESZ in **Figure 45 (d)** is better than -25.1 dB for an average transmitted power of 500 W, achieving the requirements as well. The average power level is comparable to the case in Section 6.2.1 and considerably reduced in comparison to the case in Section 6.2.2, at the price of the larger reflector, here imposed by the range-ambiguity driven design of $\overline{PRF}$.

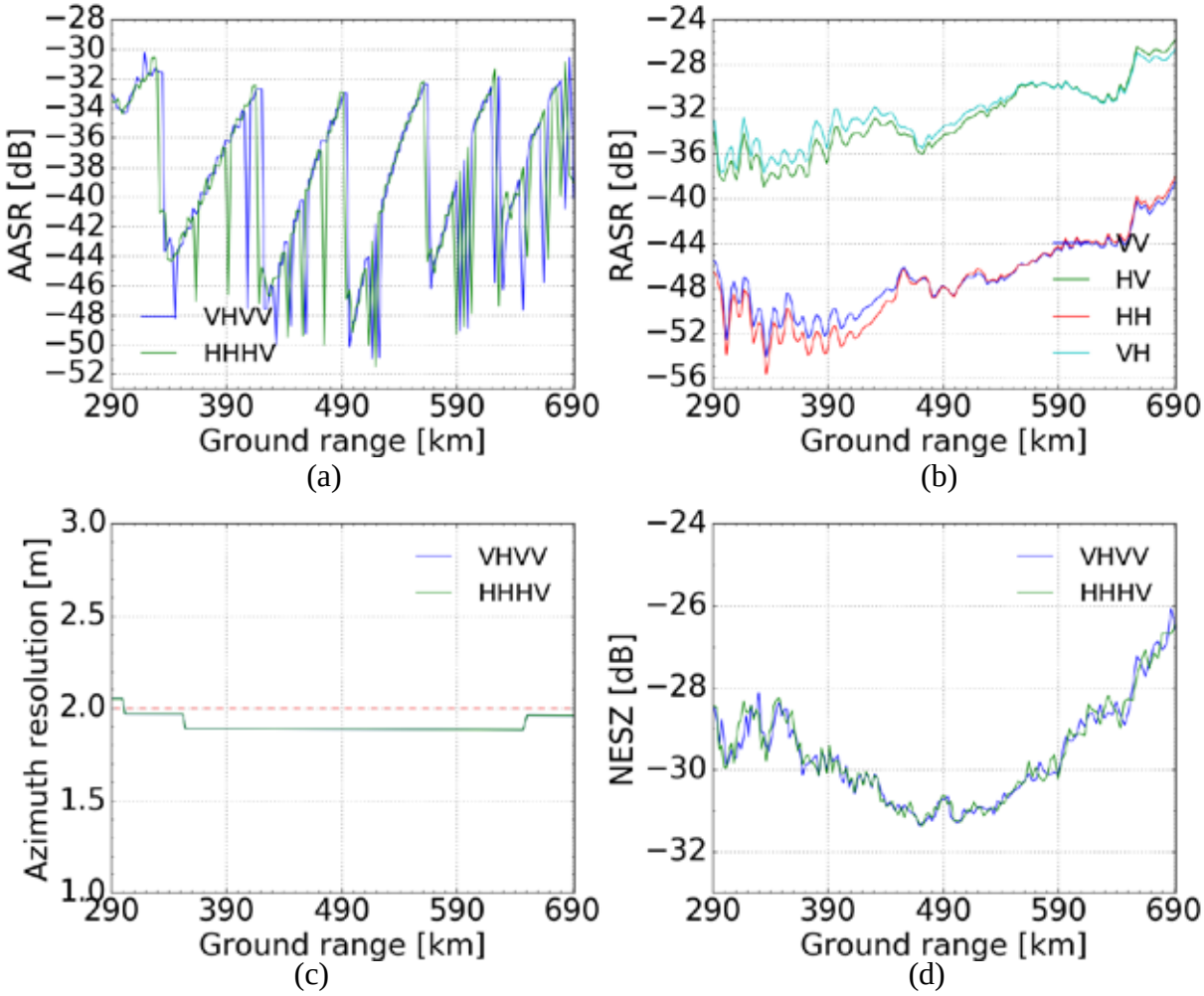

Figure 45. SAR performance over swath for 2.0 m / 400 km quad-pol multichannel staggered SAR mode using a 18.0 m reflector with 6 azimuth channels. (a) AASR. (b) RASR. (c) Azimuth resolution. (d) NESZ.

The beamformer behavior, dependent on the Tx polarization in this case, is seen in **Figure 46**. The noise scaling $\overline{\Phi_{SNR}}$ in **Figure 46 (a)** is seen to cause a relatively high degradation of up to -9.2 dB in near range but to stabilize around -3.5 dB in far range, where the NESZ is critical. This is a consequence of the design of the weights, which privileges ambiguity suppression ($\alpha = 0.0$), but is not critical due to the large reflector aperture. **Figure 46 (a)** also explains the shape of the NESZ curve Figure 45 (d) in near range, where a degradation in sensitivity is seen in spite of the closer proximity to the targets. The phase center shifts in **Figure 46 (b)** are seen to be slightly different between transmit polarization, with a worst-case shift of ± 4.4 m. This value is very

close to the limit of ±4.5 m, indicating that the whole area of the reflector is used for steering, a consequence of the low $\overline{PRF}$ in the design, driven by range ambiguity suppression.

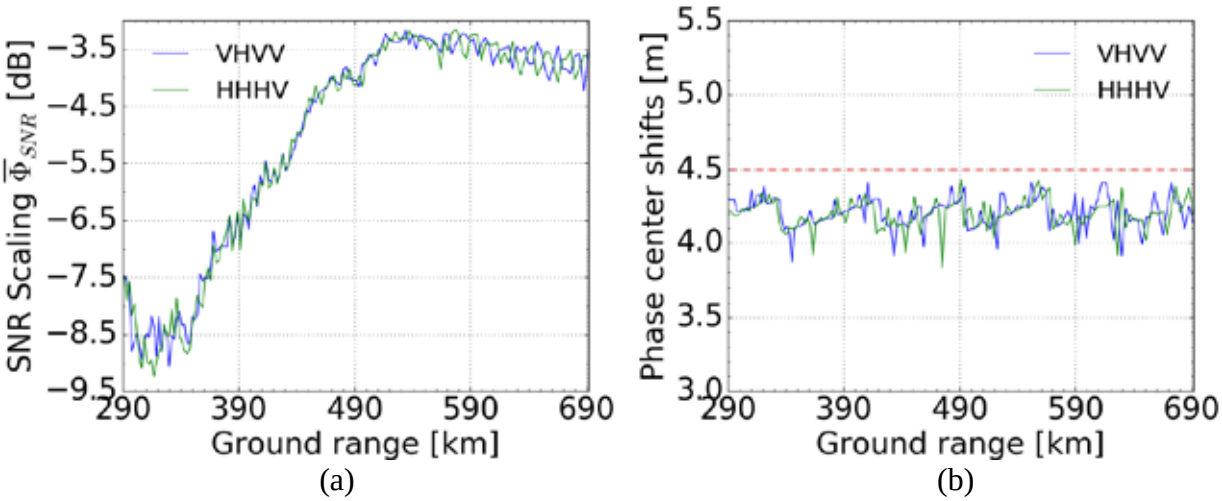

Figure 46. Performance of azimuth beamforming over range. (a) Average noise scaling $\overline{\Phi_{SNR}}$. (b) Absolute value of worst-case shift Δx_{eq} of the phase center between input and output grid.

6.4 Planar System in Single Polarization

As mentioned in Section 4.5, the use of the multichannel staggered SAR technique with planar systems requires special design considerations, as these systems are subject to limitations of the achievable phase centers (and thus phase center shifts) in comparison to the ones with reflector antennas. This section considers the design of a system with a planar direct radiating array to illustrate the procedure.

To assure an adequate performance in spite of the limitations, the design of the azimuth antenna and the PRI sequence must be done simultaneously, taking the sampling into account. The requirements are listed in TABLE IV. In this case, to achieve the resolution of 1.5 m, an antenna of length 3.0 m in azimuth is considered as the sub-set which needs to be activated for each channel, thus determining $G_{com}(f_{\mathrm{D}})$. The total antenna length was chosen to be 15.0 m, due to gain considerations. The simplest case would then be the juxtaposition of five 3 m long panels, each of which

corresponding to a channel. A channel spacing of 3.0 m leads however to relatively high phase center shifts, as illustrated in **Figure 47 (a)**, in which the minimum, mean and maximum (over the swath positions, which have different gaps due to pulse blockage) is portrayed as a function of $\overline{PRF}$. In order to reduce these shifts while keeping a reasonably low $\overline{PRF}$, the desired aperture was split into 3 elements of 1.0 m, leading to the maximum shifts seen in **Figure 47 (b)**. Note that the active aperture is kept the same (3.0 m long), by keeping the same common pattern as design goal. The algorithm will tend to activate 3 elements at a time, but an overlap between the activated apertures is made possible by the subdivision. The effect is a finer sampling in terms of the original channel's phase centers and thus a reduction of the maximum shift for comparable values of $\overline{PRF}$, in comparison to the previous case. The adopted $\overline{PRF}$ of 2050 Hz is indicated as a vertical black dashed line and is seen to lead to small shifts while being reasonably low.

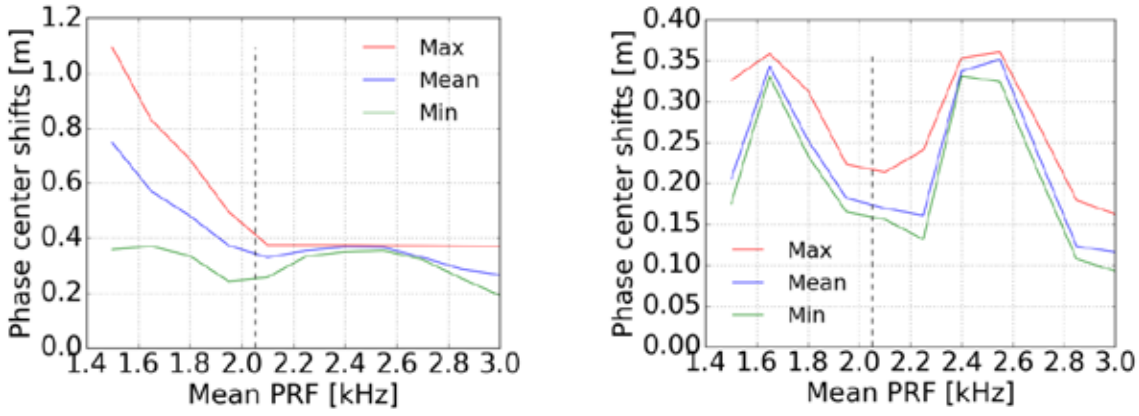

Figure 47. Statistics over the swath's ranges for the required phase center shifts as function of the mean PRF. The total antenna length is l_{az} =15.0 m. In (a) the antenna consists of 5 elements of 3.0 meter length, whereas in (b) 15 elements of 1.0 m length are considered. (In this case the same effective aperture can be achieved by activating 3 elements). The $\overline{PRF}$ of 2050 Hz (vertical dashed line) is chosen to minimize the required phase center shifts with respect to the original sampling.

The parameters for the planar system are summarized in TABLE VIII.

TABLE VIII
SIMULATION SCENARIO PARAMETERS: PLANAR ARRAY SINGLE POLARIZATION

Platform and Swath Parameters		
Parameter	Symbol	Value
Orbit height	h_{orbit}	700 km
Swath width on ground	W_g	400 km
Swath minimum/maximum incidence angle	η_{min}/η_{max}	24.5 / 49.3 deg
Swath minimum/maximum look angle	$\theta_{min}/\theta_{max}$	22.0 / 42.8 deg
Antenna Parameters		
Parameter	Symbol	Value
Antenna height in elevation	h_{el}	6.0 m
Antenna length in azimuth	l_{az}	15.0 m
Center frequency	f_0	1.2575 GHz
Number of channels in elevation/azimuth	N_{el}/N_{az}	36 / 15
Channel spacing in elevation/azimuth	d_{el}/d_{az}	0.7 λ / 1.0 m
Elevation tilt angle	θ_{tilt}	32.6 deg
Antenna system losses	L_{Ω}	2.0 dB
Pulse and Tx/Rx Hardware Parameters		
Parameter	Symbol	Value
Average PRF (both polarizations)	$\overline{PRF}$	2050 Hz
Initial PRI	PRI_0	520 ms
PRI sequence step (between pulses of same polarization)	Δ_{PRI}	-2.7 ms
PRI sequence length	N_{PRI}	25
Pulse duty cycle	T_{dc}	6%
Pulse (chirp) bandwidth	Bw_{chirp}	85 MHz
Peak transmit power of a Transmit-Receive Module	P_{TX}	35.0 W
Average transmit power	$\bar{P}_{TX}$	1134.0 W
System noise temperature	T_{noise}	649 K
Transmitted polarizations	-	V
Processing Parameters		
Parameter	Symbol	Value
Goal azimuth resolution	δ_{az}	1.5 m
Processed Doppler bandwidth	Bw_{proc}	5343 Hz
Number of simultaneous elevation beams	N_{beams}	4
Elevation beamforming algorithm	–	Phase steering with Dolph-Chebyshev amplitude weighting
Number of active elements for elevation beamforming	$N_{active_{elev}}$	36
Elevation beamforming sidelobe constraint (Dolph-Chebyshev weights)	$20 \cdot \log_{10}(\epsilon_{SDL})$	-33 dB
Number of pulses / samples in azimuth beamformer window	N_p / N_{win}	3 / 45
SNR emphasis parameter	α	0.0
Hamming window coefficient (over azimuth)	ϕ_{hamm}	0.9

The beamforming in elevation consists of the use of a phase-only pattern [116] on transmit and SCORE on receive, implemented with phase steering of the patterns (cf. 4.3) plus a Dolph-Chebyshev weighting [106] to control sidelobes (limited to 33 dB below the main signal) and thus improve the range ambiguity rejection. This is analogous to the elevation beamforming strategy used in the reflector cases in Sections 6.2.2 and 6.3, though the weight calculation in the planar case is simpler and does not require a numerical optimization procedure.

The beamforming in azimuth also employs phase-only patterns on transmit — in order to increase the beamwidth without sacrificing the transmitted power — whereas relying on the method of Section 4.4.2 on receive. Following the remarks on Section 4.5, no SNR emphasis was used ($\alpha = 0.0$), but the extended manifold was restricted to a relatively narrow vicinity of 3 pulses (the total of samples is $N_{win} = 3 \cdot 15 = 45$). This limitation indirectly enhances the SNR, compensating the lack of SNR emphasis.

The key results of SAR performance are summarized in **Figure 48**. The 400 km swath extends from 285 to 685 km ground range. The AASR in **Figure 48 (a)** is better than -27.1 dB. It is interesting to compare the shape of the curve to the previous, reflector-based, cases (cf. **Figure 41**, **Figure 43** or **Figure 45**). The local fluctuations over range (which are due to the change in the blockage and therefore the sampling of the input grid) are still present. In contrast, the “concave” behavior (performance degradation at the swath extremes) due to the defocusing of the reflector patterns is not present, as expected. The RASR in **Figure 48 (b)** is lower than -30.4 dB. As seen in **Figure 48 (c),** the goal azimuth resolution of 1.5 m is achieved. The NESZ is better than -25.0 dB, as seen in **Figure 48 (d)**.

The planar antenna scenario in this section is presented in L-band, for consistency and to allow a fairer comparison to the other systems. Nonetheless, the implementation of an antenna of 15.0 m length in this frequency band is recognized to be challenging. A similar design in e.g. C-band, however, could prove a more readily implementable

option, after certain adaptations. The antenna length is fact comparable to that already in use in ESA's Sentinel-1 [117] and actually the same as the one used by the Canadian Space Agency's RADARSAT [118] C-band radar mission.

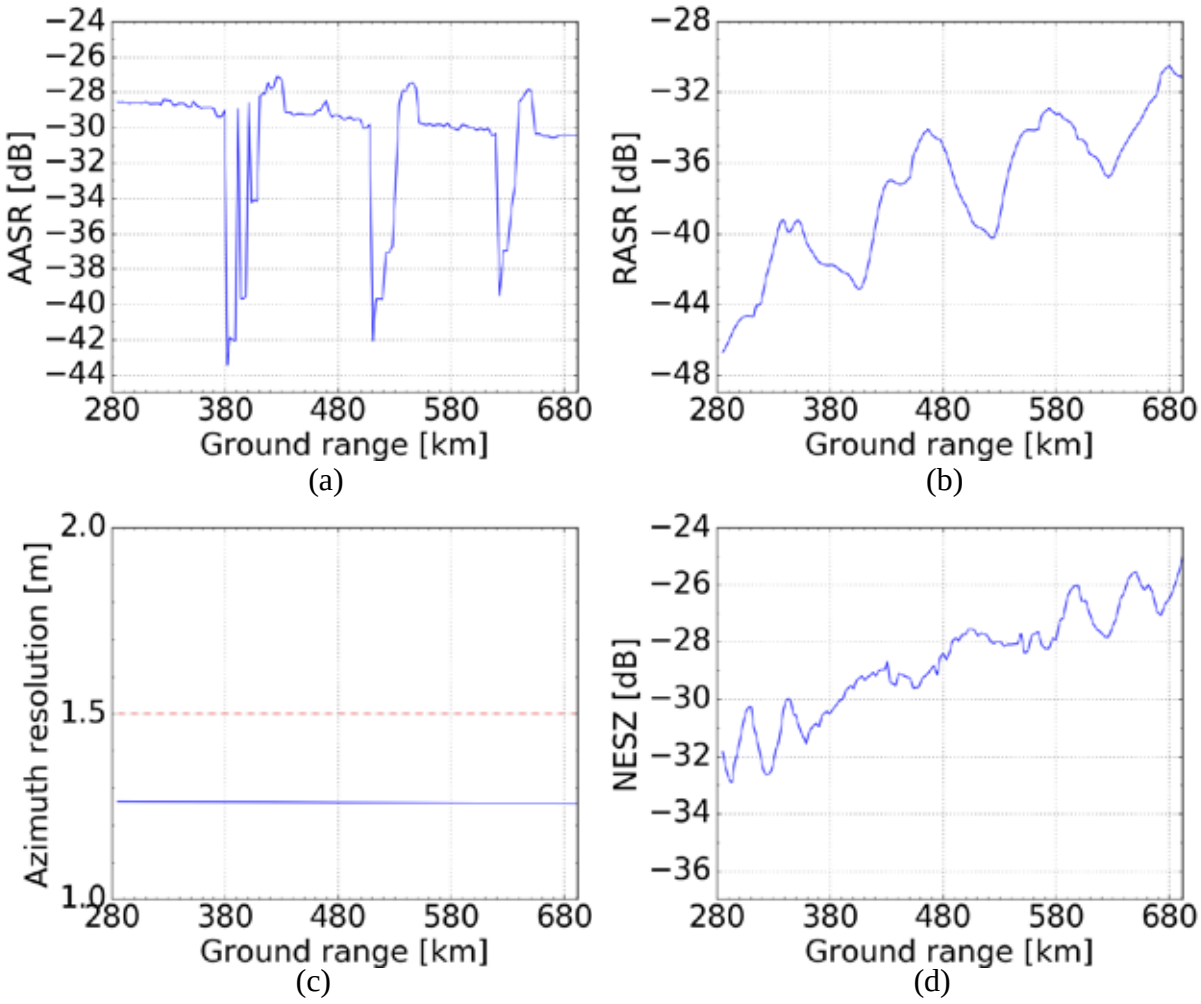

Figure 48. SAR performance over swath for 1.5 m / 400 km single-pol multichannel staggered SAR mode using a planar direct radiating array with 15 azimuth channels. (a) AASR. (b) RASR. (c) Azimuth resolution. (d) NESZ.

Finally, beamformer behavior is depicted in **Figure 49**. The noise scaling $\overline{\Phi_{SNR}}$ in **Figure 49 (a)** shows degradation of the SNR between -2.2 dB and -1.3 dB in comparison to the *element patterns* (cf. Section 4.5), which is kept under control despite α = 0 due to the limitation in the number of pulses for beamforming N_p, reducing decorrelation effects. **Figure 49 (b)** shows shifts smaller than ±0.26 m, kept low by design. The 1.0 m line indicate the element spacing, as a reference.

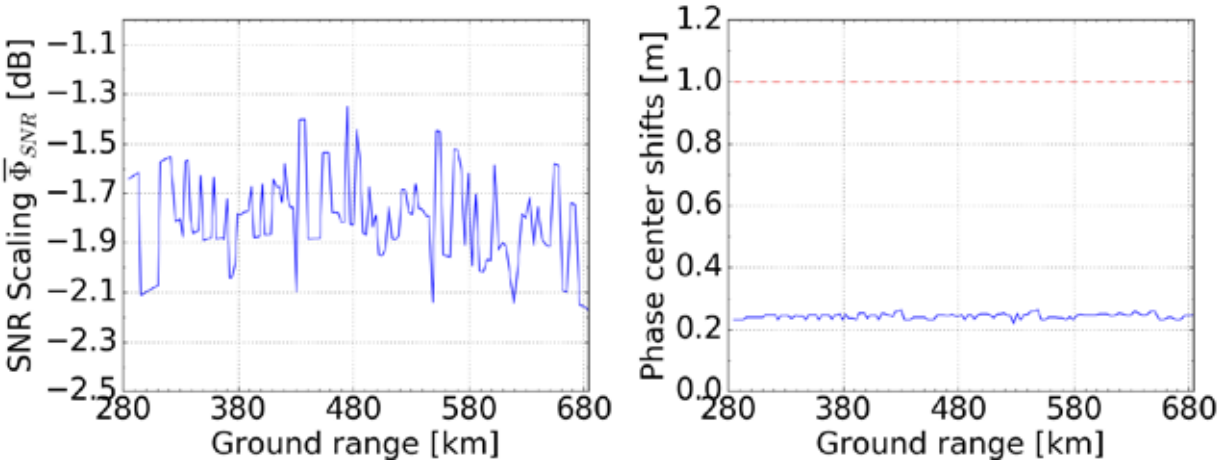

Figure 49. Performance of azimuth beamforming over range. (a) Average noise scaling $\overline{\Phi_{SNR}}$. (b) Absolute value of worst-case shift Δx_{eq} of the phase center between input and output grid.

6.5 Data Rates and Onboard Implementation Complexity

An important aspect in the operation of multichannel SAR systems is the resulting data rate. Clearly, the digitization of the individual channels bears a great potential, both for elevation and azimuth beamforming. It allows the implementation of complex DBF techniques that may greatly increase performance in comparison to conventional systems. The price for this flexibility and improved performance is, alongside the more complex hardware (larger number of ADCs, for instance), a potentially larger data rate, which can become a bottleneck if left unchecked [71].

The approach envisioned for multichannel SAR systems [51], [60] has been so far to perform on-board processing over elevation, for instance to implement the SCORE beamforming, but broadcast the individual azimuth channels for ground processing. One reason for this is namely that, in such systems, the individual channels are expected to be undersampled and subject to aliasing, whereas the full sampling rate — considering all N_{ch} azimuth channels — is designed to be enough to cover the required Doppler bandwidth. In other words, $PRF < Bw_{az}$, even though $N_{ch} \cdot PRF > Bw_{az}$. In light of this, fundamentally no further data reduction is

possible by merely independently processing the individual data streams. They are therefore expected to be broadcast as acquired. Only after combining the channels in some sense, and thus making use of the full sampling, should any data reduction be possible. Since the frequency domain processing approaches (cf. Section 3.2) are computationally costly, broadcasting for on-ground processing is considered more realistic than on-board processing and no data reduction with respect to $N_{ch} \cdot PRF$ is applied. It should be noted that this fact is not critical for this class of system, as the oversampling with respect to $N_{ch} \cdot PRF$ is not required to be particularly high.

For staggered SAR system, in contrast, on-board data rate reduction [53], [72] has been considered as baseline. On the one hand, the fact that the resampling takes the form of a finite-length digital filter in time domain[24] — meaning no FFTs and frequency domain processing are required — makes the computational cost feasible for on-board implementation. On the other hand, the fact that staggered SAR systems require a certain degree of oversampling in azimuth [41], [53] — to make the interpolation to a regular grid with adequate performance feasible — makes data rate reduction desirable. Therefore, since a considerable reduction in the data rate can be achieved at a feasible computational cost, on-board resampling followed by (or simultaneously with) low-pass filtering and decimation is proposed in [53], [72]. The basic idea is to apply a conventional low-pass filter (acting as an anti-alias filter for the decimation stage) to the resampled data, which are uniformly sampled.

A multichannel Staggered SAR system inherits characteristics from both of the aforementioned cases. Whereas the individual data streams sampled at PRF are as a rule undersampled, oversampling with respect to $N_{ch} \cdot PRF$ is expected for good performance. This is illustrated by the system design examples in this chapter. Data rate reduction is hence desirable in this case as well. It remains nonetheless true that any form of possible reduction should consider the multichannel data, whereas little or

[24] The solution is analoguous to a finite impulse response (FIR) filter, except for the non-uniformity of the samples.

no gain is possible from the independent processing of the data streams. A relatively straightforward manner to achieve this is to actually do the sampling to the uniform grid *on-board*, allowing conventional low-pass filtering and decimation to follow. The most complex operation involved is the resampling itself, which fortunately is also a FIR filter, even though more costly than a single-channel staggered SAR resampling by roughly a factor of N_{ch}, for the same sequence.

In this context, a trade-off between the data rate and the on-board implementation complexity presents itself. In the following, the data rate for the examples mentioned in Sections 6.2 to 6.4 is estimated, alongside the computational complexity in terms of the number of operations and amount of memory required to store the weights.

To estimate the data rate, consider that the echo window length EWL required for full range resolution is given by

$$EWL = \frac{2}{\mathrm{c}} \cdot (R_{max} - R_{min}) + T_p, \tag{141}$$

which is roughly the time span of the raw data from the echoes of a single pulse. As indicated in the examples in Sections 6.2 to 6.4, the echo window lengths for the HRWS systems considered therein span several PRI cycles, and multiple simultaneous elevation beams are assumed to be synthesized to overcome the range ambiguity. Even though it is recognized that this has implications for the hardware complexity — since N_{beams} beamforming networks with access to the same data have to be implemented — (141) assumes the beamforming and sorting of the data has been done and ignores blockage effects due to the transmission events. The data rate can then be expressed as

$$R_{data} = 2 \cdot N_{bits}^{data} \cdot \left(N_{pols} \cdot N_{ch}\right) \cdot \left(Bw_{chirp} \cdot \gamma_{rg} \cdot f_{s_{az}}\right) \cdot EWL. \tag{142}$$

The factor 2 accounts for the I/Q channels of the complex data, whereas N_{bits} describes the Block Adaptive Quantization (BAQ) number of bits for real data. N_{pols}

describes the number of polarizations and N_{ch} the number of azimuth channels, each of which is an individual data stream. Their product, the quantity within the first set of parenthesis, is the total number of complex data streams. Bw_{chirp} is the pulse bandwidth and $f_{s_{az}}$ is the azimuth sampling rate. If no post-processing is done, this rate corresponds to the PRF, but may be reduced up to $\gamma_{az} \cdot Bw_{proc}$ (the processed bandwidth plus an oversampling factor γ_{az}) if suitable filtering and decimation are applied. Both scenarios will be compared later on. γ_{rg} is a factor accounting for range oversampling, and accounts for guard times and data headers, among other factors. The product of the last four quantities, the quantity within the second set of parenthesis, is the product of the combined sampling rates in both dimensions.

To estimate the implementation complexity in terms of the number of operations, note that the resampling strategy in (96) describes a FIR filter with N_{win} taps. In a simple implementation, a FIR filter with N_{win} taps consists of basically N_{win} complex multiplications and additions. In turn [119], a complex multiplication consists of four real multiplications and two real additions, whereas a complex addition consists of two real ones. Therefore, one may write for the FIR filter

$$N_{multiplications,\ Re} = 4 \cdot N_{win},$$
$$N_{additions,\ Re} = 4 \cdot N_{win}; \tag{143}$$

which varies linearly with the number of taps.

Further basic memory requirements can be derived by considering the total amount of data that has to be stored to implement a look-up table for the resampling coefficients. It should be noted that they are range-dependent and need to span a whole PRI cycle of the output grid. As discussed in Section 4.2, the maximum amount of samples in the output grid within a PRI cycle — and therefore of coefficients — is given by $N_{out} = N_{ch} \cdot N_{PRI}$. The worst case is assumed, i.e., no Tx blockage, with all PRIs available, which is generally not true for all ranges. The weights for each output sample are N_{win} complex numbers, also assumed to be stored with

$N_{bits}^{storage}$ bits precision, which should match the ADC precision for real data, not considering BAQ. Finally, it should be taken into account that the input grid and therefore the coefficients vary with range. The total number of range bins is given by

$$N_{rbins} = EWL \cdot (\gamma_{rg} \cdot Bw_{chirp}), \tag{144}$$

however, the coefficients do not necessarily need to be updated for every new range bin. At this point, it should be recalled that the input manifold (cf. (97)) and therefore the weights are a function of two main components: the sampling conditions (input and output grids) and the antenna patterns.

The first condition requiring an update is that the sampling conditions induced by Tx blockage change, since this alters the input grid and the local $\overline{PRF}_{eff}$ (cf. (83)). Specifically, what is relevant are changes in the indices of blocked pulses, which define the possible gap configurations, inherently limited due to discrete nature of the indices. Recalling the blockage condition (55) for an order k:

$$\frac{c}{2} \cdot (t_0 + d_{i,k}) \leq R_0 \leq \frac{c}{2} \cdot (t_1 + d_{i,k}), \tag{145}$$

and that the indices i are integers within $1 \leq i \leq N_{PRI}$, it is clear that the blocked ranges do not change within intervals of length

$$\frac{c}{2} \cdot (t_1 - t_0) = \frac{c}{2} \cdot \Delta b. \tag{146}$$

For the resampling of complex data, $\Delta b = T_p$ [63], except possibly for guard intervals, and therefore a quantization of the sampling conditions with respect to lengths proportional to this size occurs. It is also interesting to recall that the blockage diagram spans a region in slant range proportional to the maximum span of $d_{i,k}$, given by $\Delta d(k)$ in (51). This is illustrated in **Figure 51**, which represents schematically a blockage diagram, emphasizing the discrete nature of the indices and the corresponding quantization of the blockage regions in terms of slant range R_0.

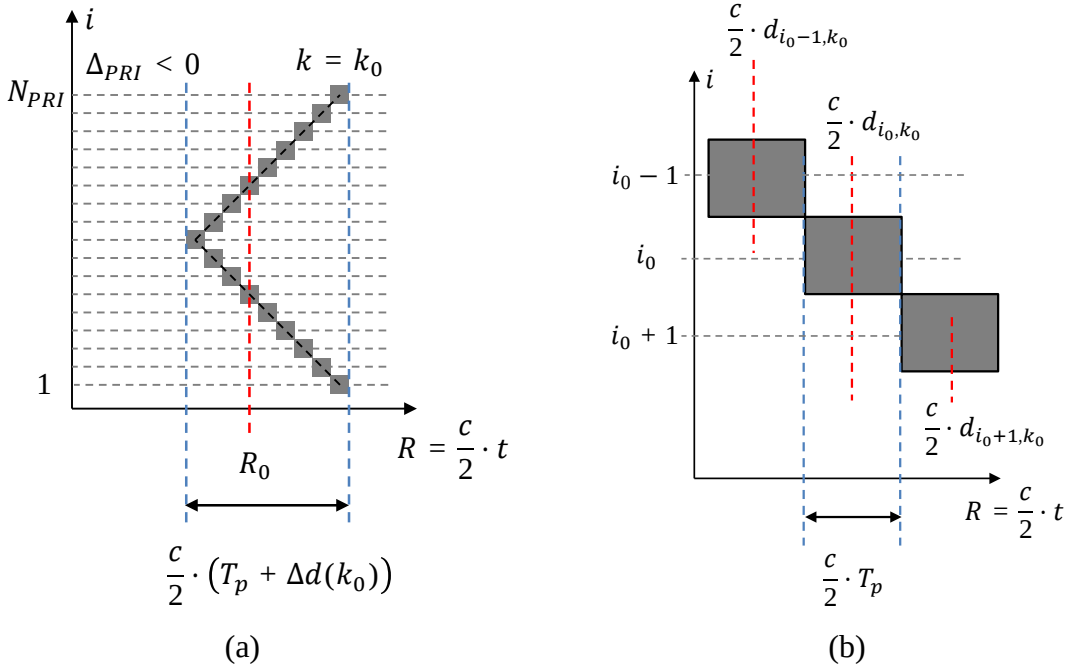

Figure 50. Schematic representation of blockage diagram, emphasizing index discretization. $\Delta b = T_p$ and $\Delta_{PRI} < 0$ are assumed for the example. (a) Overview emphasizing the span of a given order k_0. (b) Close-up emphasizing the quantization effect with respect to the ranges, subject to the same gap configuration within regions proportional to the pulse length.

As represented in the overview in **Figure 51 (a)**, the maximum span of the blockage diagram for a given order k_0 is given by

$$\Delta R(k_0) = \frac{\mathrm{c}}{2} \cdot \left(T_p + \Delta d(k_0)\right) = \frac{\mathrm{c}}{2} \cdot \left(T_p + |\Delta_{PRI}| \cdot (N_{PRI} - k_0) \cdot k_0\right). \tag{147}$$

As indicated in the zoom of the diagram in **Figure 51 (b)**, the slant ranges in which gaps are found are quantized, in the sense that the whole diagram is divided into a set of regions with length $\frac{\mathrm{c}}{2} \cdot T_p$, within which the same blockage occurs for all ranges. For a fixed k_0, therefore, the number of configurations can be estimated by

$$N_{gap\ sets}(k_0) = \frac{\Delta R(k_0)}{\frac{\mathrm{c}}{2} \cdot T_p} = \left(1 + \frac{|\Delta_{PRI}|}{T_p} \cdot (N_{PRI} - k_0) \cdot k_0\right). \tag{148}$$

The total number of gap configurations, considering all the orders within the swath, is

$$\mathrm{N}_{gap\ sets} = 1 + \sum_{k=k_{min}}^{k_{max}} N_{gap\ sets}(k), \tag{149}$$

where the additional configuration is namely the one in which no blockage occurs. It is assumed that (cf. **Figure 30 (a)**) the different orders are separated by regions without any blockage, for which the sampling configuration is always the same. (149) also assumes that the full blockage region is contained within the swath of interest for all orders k, which is not necessarily true in the swath borders. The gaps for k_{min}, k_{max} may be partially outside of the swath and thus not be relevant, making (149) an upper bound for the amount of relevant sets of weights.

The second condition requiring an update of the indices is a change in the azimuth antenna patterns over range. In the case of planar arrays, where the patterns are separable [100], the variation of the azimuth patterns with range is merely a scaling and phase delay, or a complex constant. Such a factor has no effect over the correlations used for calculating the weights or the final weight values, considering the weight normalization. Therefore, the same set of weights can be used for all ranges without any blockage for instance and (149) describes the total number of weights over range: $N_{rg} = N_{gap\ sets}$. No additional weight updates are necessary because of the azimuth patterns. This is however not true for reflector antennas, for which the patterns are non-separable [100] between azimuth and elevation. This means that, even with the same sampling configuration, the input azimuth patterns change shape with range and a new set of weights is necessary. The need for an update is actually dependent on how fast the patterns change. For simplicity one may extend the quantization of the swath with $\frac{\mathrm{c}}{2} \cdot T_p$ — as was the case in the blockage regions — to the regions without blockage. This means the update is done at the same rate over the swath regardless of the blockage region position, implicitly assuming that the sampling is the dominant factor in the changes of the weights. This assumption will be examined by means of simulations in Section 8.3. In that case,

$$N_{rg} = \frac{R_{max} - R_{min}}{\frac{c}{2} \cdot T_p}. \tag{150}$$

In conclusion, the total memory needed to store the coefficients, for all N_{pol} polarizations[25], amounts to

$$MEM_{coef} = 2 \cdot N_{pol} \cdot N_{rg} \cdot N_{bits}^{storage} \cdot N_{out} \cdot N_{win}. \tag{151}$$

The parameters pertinent to the data rate estimation and first-order on-board implementation complexity analysis are summarized in TABLE IX. For the data rate estimation, oversampling factors γ_{rg} = 1.265 (20% oversampling and 6.5% header and guard time overhead) and γ_{az} = 1.2 are assumed in range and azimuth, respectively. For all cases, Bw_{chirp} = 85 MHz and the bit precisions are assumed to be $N_{bits}^{storage}$ = 8 bit (ADC) and N_{bits}^{data} = 4 bit (after BAQ). In the calculations, a Mbps is considered to be 2^{10} bps.

As the values in TABLE IX show, on-board processing has the potential to lead to a considerable reduction in the data rate in all scenarios. A reduction by at least a factor of 2 is seen to be possible. This is especially true for systems with a larger number of channels as e.g. the planar case in Section 6.4, which has the highest reduction factor of 4.8 owing to the presence of 15 channels. Nonetheless, even the filtered data rate $R_{data_{min}}$ is seen to be relatively high, due to the very wide swaths and fine resolution, which require a correspondently high processed bandwidth. The system of Section 6.2.2 for instance has $R_{data_{min}}$ = 14990 Mbps owing to the very wide 500 km swath imaged with 1 m resolution. Quad-pol operation is also seen to considerably impact the data rate, as the amount of data increases fourfold: for instance the system of Section 6.3 shows the highest data rate of $R_{data_{min}}$ = 23940 Mbps in spite of the

[25] The sampling configuration of the inputs (pulse position and gaps) only depends on the Tx polarization (cf. Section 3.3.2) but the antenna patterns are as a rule dependent on the Rx polarization, so that the coefficients are in general unique for each polarization pair.

less stringent (even though still currently not yet achieved) HRWS requirements of a 400 km swath imaged with 2 m. That is to stress that future HRWS missions are also expected to pose challenging requirements in terms of broadcast rates and data storage.

TABLE IX
ANALYSIS OF ON-BOARD IMPLEMENTATION COMPLEXITY FOR EXAMPLE HRWS SYSTEMS

	Section Number			
	6.2.1	6.2.2	6.3	6.4
System basic parameters and requirements				
Antenna architecture	Reflector	Reflector	Reflector	Planar
Polarization	Single-pol	Single-pol	Quad-pol	Single-pol
Goal azimuth resolution	3.0 m	1.0 m	2.0 m	1.5 m
Swath width	350 km	500 km	400 km	400 km
Repeat cycle	8 days	6 days	7 days	7 days
Goal NESZ level	-25 dB	-25 dB	-25 dB	-25 dB
Goal azimuth and range ambiguity levels	-25 dB	-25 dB	-25 dB	-25 dB
Data rate estimation parameters				
Echo window Length (EWL)	1.43 ms	2.04 ms	1.64 ms	1.68 ms
Number of polarizations N_{pol}	1	1	4	1
Number of azimuth channels N_{ch}	3	9	6	15
Staggered Sequence $\overline{PRF}$	2700 Hz	2120 Hz	2 x 1750 Hz	2050 Hz
Processed Bandwidth Bw_{proc}	2494 Hz	7451 Hz	3752 Hz	5343 Hz
Unfiltered data rate $R_{data_{orig}}$	9494 Mbps	31984 Mbps	55829 Mbps	42492 Mbps
Filtered data rate $R_{data_{min}}$	3508 Mbps	14990 Mbps	23940 Mbps	8859 Mbps
Potential data rate reduction factor $R_{data_{orig}}/R_{data_{min}}$	2.7	2.1	2.3	4.8
On-board resampling FIR filter parameters				
Total of input samples N_{win} (FIR taps)	99	45	150	45
$N_{\text{multiplications, Re}}$	396	180	600	180
$N_{\text{additions, Re}}$	396	180	600	180
On-board coefficient storage parameters				
Pulse length T_p	14.8 μs	28.3 μs	22.9 μs	29.3 μs
Number of output samples N_{out}	102	252	246	375
Number of range bins N_{rbins}	153,630	219,721	176,455	181,121
Number of weight sets over range N_{rg}	64	72	72	54
Total memory for coefficients MEM_{coef}	1300 kB	1555 kB	20756 kB	1780 kB

The requirements of processing power and memory for coefficient storage are considered not to be critical, especially considering the projected computational power of near-future hardware. The system example from Section 6.3 has the most complex

FIR filter, owing to the fully polarimetric operation, which doubles the sequence length and requires storage of polarization-dependent weights.

This fact, combined with the considerable improvement in the data rate, makes the on-board processing alternative potentially attractive.

An important aspect with this regard is however that this alternative has as side-effect the imposition of potentially very stringent calibration requirements. The reason is that, for the on-board resampling to be effective, the patterns assumed for weight calculation should match the actual patterns of the channels. Channel imbalances (or in general mismatches between the nominal patterns and the data) have been shown to have the potential to considerably hamper the performance of multichannel reconstruction algorithms (cf. [120], [121], [122]). The on-board processing option combined with a limited maximum data rate implies a considerable reduction of the possibilities for a posteriori compensation of pattern discrepancies. The broadcast of the individual channels for on-ground processing, despite the obviously higher requirement on data rate, provides a more robust alternative (alongside other advantages as e.g. scene-adaptive choice of parameters for the resampling that can boost or equalize performance[26]). This also relaxes the calibration requirements, which might also prove costly or technologically challenging by requiring complex calibration networks that outweigh the data rate advantages. In this context, Chapter 8 complements this chapter by providing an analysis of several factors contributing to mismatches between signal and weight calculation parameters, including the restriction of the number of weight sets over range according to (149), (150). Their impact on some of the system design examples shown here is assessed by means of simulations to allow a better understanding of their impact and the corresponding

[26] Scene-dependent resampling could be achieved on-ground by e.g. adapting the parameter α according to the imaged region and/or the intended application. For instance, in a more homogeneous scene, the AASR requirements could be relaxed without considering disturbing the output image quality, and a better SNR could be obtained by using a higher α. Conversely, a scene with dominant scatterers and higher contrast shows more visible artifacts due to ambiguity, making the AASR more relevant, and in this case a better suppression could be attained at the cost of certain SNR degradation.

requirements that keeping the performance within acceptable levels would have on system calibration.

6.6 Remarks on System Design Examples

This chapter provided examples of multichannel staggered systems designed to use the techniques in Chapter 4 to achieve unprecedentedly demanding HRWS imaging requirements. Systems with reflector antennas in single- (cf. Section 6.2) and quad-polarization (cf. Section 6.3) have been contemplated, as well as a planar system in single-polarization (cf. Section 6.4). In Section 6.5, the same examples were analyzed in terms of the data rate and the implementation complexity, focusing on computational power. A trade-off between data rate and on-board processing power was made clear, which has however implications for calibration and pattern determination accuracy, left to be further analyzed in Chapter 8, which addresses the impact of several modelling mismatches for the weight calculation. Before that, Chapter 7 presents next material on a proof of concept of the techniques in Chapter 4 using experimental data from a ground-based radar system.

7 Proof of Concept with Ground Based Radar Demonstrator

7.1 Chapter Overview

Novel DBF algorithms and techniques are an important line of research at the Microwaves and Radar Institute of DLR. An experimental multichannel ground based radar system [73], [74] was developed and built at the institute, as part of the effort to allow experimental demonstrations of these techniques. The system is very flexible and allows, in particular, the usage of reflector antennas with a multichannel feed for DBF [75]. This makes this system suitable for the demonstration of the multichannel staggered SAR resampling described in Section 4.4.

This chapter adresses a proof of concept of multichannel staggered SAR using data in X-band acquired from an example scene. Section 7.2 briefly describes the system parameters and the experimental setup, whereas Section 7.3 describes the signal processing chain and the procedures adopted for calibration and azimuth antenna pattern characterization. Finally, Section 7.4 describes the results and assesses the quality achieved by means of the reconstruction. The material presented was published as part of [68], [69].

7.2 The MIMO Demonstrator and the Experimental Setup

The experimental data take was performed with a reflector antenna, using a multichannel feed architecture. The system employs an X-band reflector antenna with 8 azimuth feed elements on receive, whereas a separate horn antenna is used for transmit. The most important system parameters are summarized in TABLE X.

Figure 51 summarizes the setup and illustrates its most important elements. As indicated in the overview in **Figure 51 (a),** the imaged scene consists of a calibration corner reflector, plus additional targets: a formation of four other corners and a metal wire fence. The radar system is mounted atop a mast of 6.34 m height on a rail car, which propelled by a step motor at the constant velocity of 8.5 cm/s. The system has 8

channels in azimuth that illuminate different Doppler regions, as schematically indicated by the color-coded beams.

TABLE X
MIMO DEMONSTRATOR SYSTEM AND EXPERIMENT PARAMETERS

Antenna, Pulse and Tx/Rx Hardware Parameters		
Parameter	Symbol	Value
Center frequency	f_0	9.58 GHz
Chirp bandwidth	BW_{chirp}	300 MHz
Intermediate center frequency	f_{IF}	205 MHz
Peak output power	P_{Tx}	18 dBm
ADC sampling rate (real data)	f_s	1 GS/s
ADC resolution	r_{ADC}	10 bit
Elliptical reflector major axis	D_{maj}	1.0 m
Elliptical reflector minor axis	D_{min}	0.7 m
Reflector focal length	F_{ref}	0.5 m
Reflector offset in elevation	O_{ref}	0.35 m
Feed element (horn antenna) spacing	d_{az}	4.4 cm
Pulse length	T_P	10.0 μs
System PRF	PRF	10.0 Hz
Transmitted/Received polarization	$-$	VV
No. of channels in elevation/azimuth	N_{el}/N_{az}	1 / 8
Target/Platform Parameters		
Parameter	Symbol	Value
Antenna height above ground	h_{el}	6.34 m
Platform (rail car) velocity	v_{plat}	8.5 cm/s
Calibration corner's ground / slant range	g_0 / r_0	9.0 m / 11.0 m

Figure 51 (b) shows the rail car, which also carries the radar electronics, the mast and the reflector antenna. **Figure 51 (c)** shows a close-up of the Rx reflector and its feed (the tripod is however not part of the experimental setup). The feed system consists of 8 horn antennas of dimension 4.4 cm placed adjacent to each other, as visible in **Figure 51 (d)**. Their signals are individually digitized constituting 8 channels over azimuth. **Figure 51 (e)** shows the calibration corner — a target used for azimuth antenna pattern characterization and calibration — placed in the edge of a sandbox. Finally, **Figure 51 (f)** shows the remaining elements of the scene in the additional target area, namely four corner reflectors in formation and a metal wire fence.

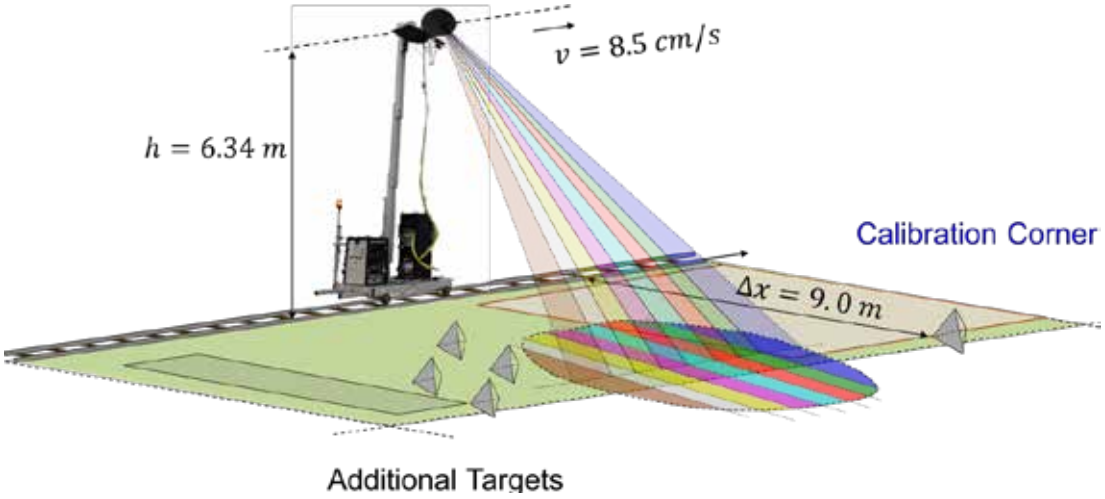

(a)

(b)

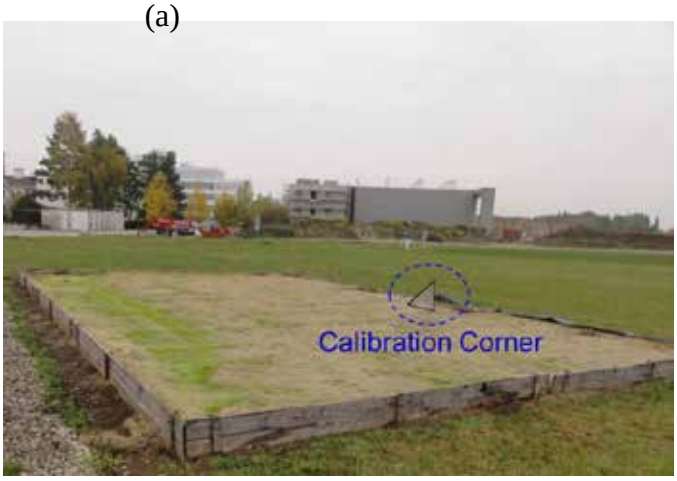

(e)

(c)

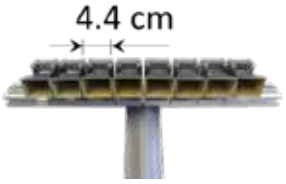

(d)

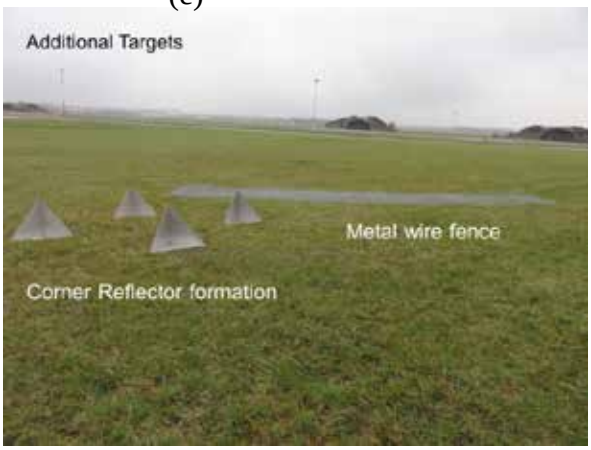

(f)

Figure 51. Illustration of experimental setup. (a) Schematic representation and overview of the experiment's geometry. (b) Close-up of the rail car and the radar system. (c) Rx reflector antenna and its feed. (d) Close-up of the feed, which consists of 8 horn antennas of 4.4 cm. (d) The calibration corner mounted at the edge of the sandbox. (f) Additional target area with a formation of 4 corner reflectors and a metal wire fence.

In a first step, the data were acquired at the relatively high sampling rate of 10.0 Hz (the Doppler bandwidth for each feed channel is around 1.0 Hz — cf. **Figure 53 (c)** for the antenna gain patterns derived from the data) and at uniform sampling. This is intended to allow first a characterization of the antenna patterns from the calibration corner's response, as detailed in Section 7.3. The pattern information derived from this step is used to compensate phase imbalances between the channels and also to define the system's array manifold ($G_n(f_\mathrm{D})$ in (92), (97)), necessary for the second step: the proof of concept itself, described in the following.

The staggered PRI acquisition is simulated via interpolation (which also benefits from the oversampling) and posterior reconstruction of the regularly sampled data from the simulated non-uniform grid. In this case, the original regularly sampled data are also available, and can be directly compared to the output of the beamforming to evaluate the success of the approach. The PRI sequence used for the demonstration is described in TABLE XI, alongside the beamforming parameters for the demonstration.

TABLE XI
PROOF OF CONCEPT PARAMETERS

Staggered PRI Sequence Parameters (used for interpolation/reconstruction)		
Parameter	Symbol	Value
Average PRF	$\overline{PRF}$	1.25 Hz
Initial PRI	PRI_0	0.891 s
PRI sequence step	Δ_{PRI}	-5.31 ms
Sequence length	N_{PRI}	33
Grid, Reconstruction and Processing Parameters		
Parameter	Symbol	Value
Output sampling rate	PRF	10.0 Hz
Number of samples in azimuth beamformer window	N_{win}	56
SNR emphasis parameter	α	0.1 / 0.5
Maximum phase center shift from input to output grid	Δx_{max}	3.63 cm
Processed Doppler Bandwidth	BW_{proc}	3.4 Hz

In this geometry, staggering of the PRI to avoid blind ranges is not necessary, and thus a scaled version of a sequence derived for a spaceborne geometry is used, namely the

one for the 350 km swath in TABLE II (cf. Section 5.2). The 33 PRI sequence is scaled here to a mean PRF of 1.25 Hz, so that after reconstruction with the 8 channels the initial sampling of 10.0 Hz may be restored and directly compared to the original data.

The signal processing chain for both steps is explained in detail next, in Section 7.3, whereas Section 7.4 focuses on the analysis of the results.

7.3 Signal Processing and Calibration

The signal processing of the data can be summarized into four basic steps:

i. *Pre-processing*: conversion of the data of each of the channels to complex format and range compression. The pre-processed data are still not azimuth compressed and are used as input to the antenna pattern analysis.

ii. *Azimuth Antenna Pattern Analysis*: the phase and amplitude of the calibration corner's range compressed response is used to estimate the antenna pattern of each of the feed elements.

iii. *Azimuth Calibration:* phase-correction of the data, using the output of the antenna pattern analysis. The data after calibration are ready to be azimuth-compressed or interpolated to simulate the staggered acquisition. More details of the procedure will be explained later in this section.

iv. *Simulation of a Staggered SAR Acquisition*: the calibrated data (uniformly sampled at a high rate) are interpolated and sampled to match a non-uniform grid that corresponds to the staggered PRI sequence (mean sampling rate of 1.25 Hz). Afterwards, all 8 channels are used as input to the beamforming, so that the original 10.0 Hz sampling is restored. The recovered data are then compared to the sum over the azimuth channels (which has the pattern $G_{sum}(f_{\mathrm{D}})$ of (93)) of the original data, sampled at 10.0 Hz.

The processing chain, starting from the raw data, is detailed in **Figure 52**. The processing done on each azimuth channel independently is represented inside the dashed line box, and afterwards the various channels are combined for beamforming.

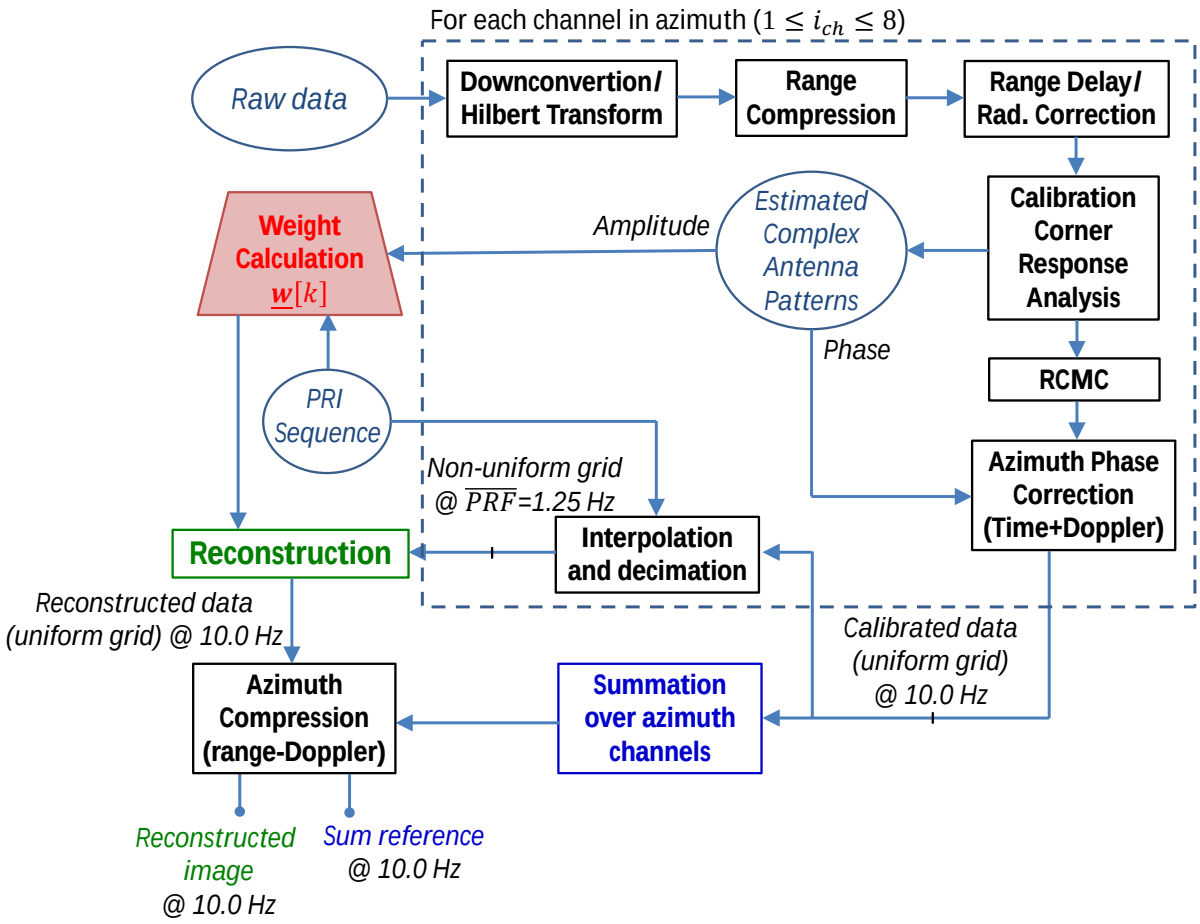

Figure 52. Block diagram detailing the raw data processing chain for the proof of concept.

The *pre-processing* steps include down-conversion to baseband and conversion to complex I/Q format; range compression; correction of the range delays induced by different paths (e.g. different cable lengths and microwave junctions) plus a basic radiometric calibration (data magnitude compensation following range R^4 curve). Next, the *azimuth antenna pattern analysis* by means of the calibration corner's response is performed. After Range Cell Migration Correction (RCMC), the *azimuth calibration* takes place, yielding the calibrated data, still not azimuth compressed and in the original uniform grid. These data are used as input to the *simulation of a staggered SAR acquisition*, forming both the reference with pattern $G_{sum}(f_{\mathrm{D}})$ — the

ideal input of the reconstruction — and non-uniformly sampled data which are reconstructed using the beamforming algorithm in Section 4.4.

First, each recorded channel (real data sampled at 1 GS/s) is converted from the intermediate frequency f_{IF} = 205 MHz to baseband and represented in complex I/Q format. Second, the data are range compressed with a replica of the transmitted pulse. The differences in the signal paths between the channels are corrected, by correlating calibration signals with the replicas of each channel (cf. [74] for more details on system calibration). A basic radiometric correction is performed by compensating the range to the forth power curve at each range bin, which compensates the free-space attenuation of signal power for the non-azimuth compressed data. The range compressed data of the corner reflector are used to determine the complex antenna patterns, as will be further explained shortly. Their amplitude information is used to calculate the manifold for beamforming (cf. (97), whereas the phase information is used to form a correction that compensates the phase differences between the channels. This follows the assumption that ideally no phase differences are expected between the feed elements (cf. [100]).

The calibration corner response analysis and the resulting data-based calibration procedure are detailed in **Figure 53**.

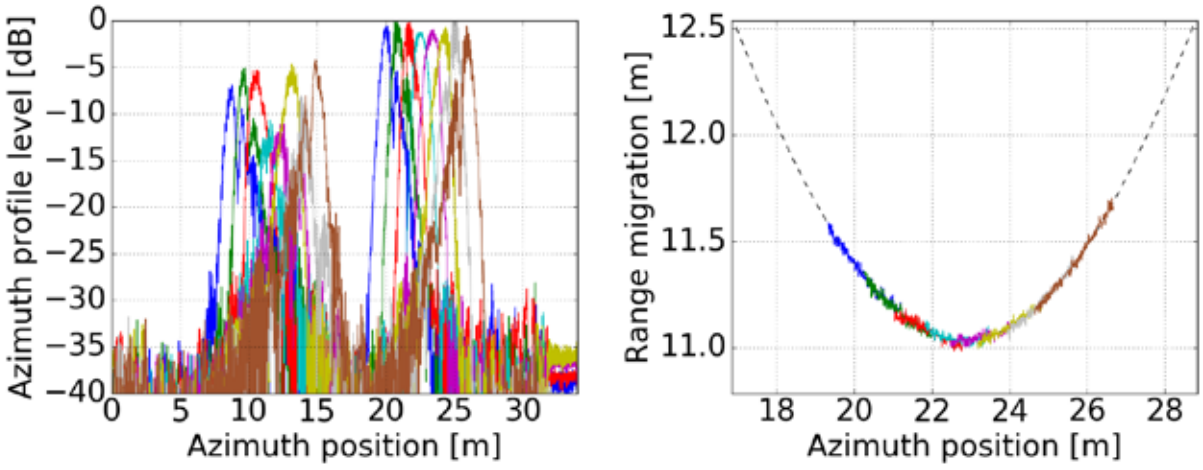

(a) (b)

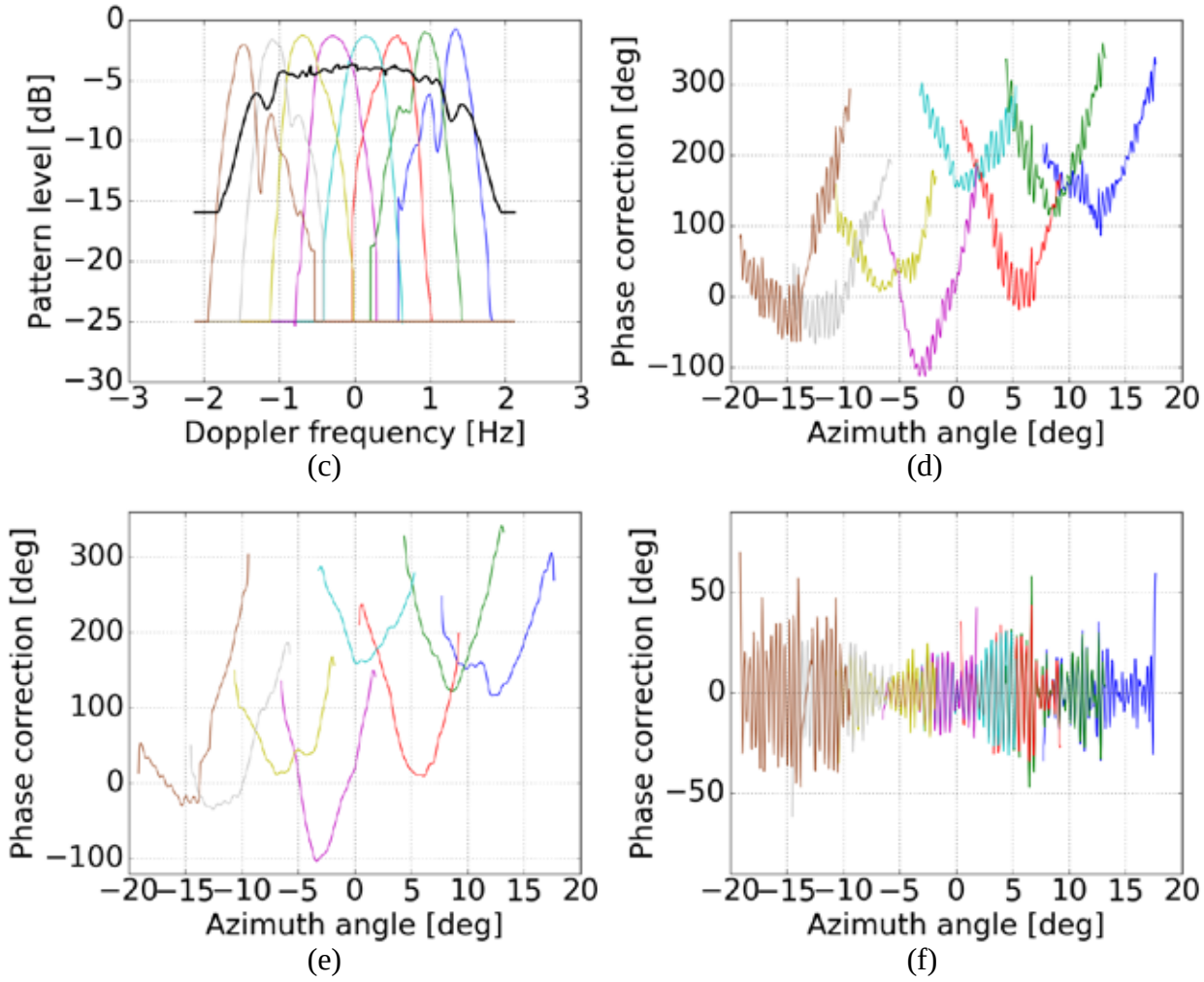

Figure 53. Data-based calibration plots, color-coded as in **Figure 51 (a)**. (a) Profiles over azimuth position — at the maxima over range — of the feed channels. (b) Range cell migration (RCM) of the calibration corner's maxima over range, showing the feed elements individually and a reference RCM in the nominal position of the target (black dashed line). (c) Magnitude of the patterns derived from the calibration corner's response, with resampling to an azimuth Doppler frequency grid (cf. (153)), after low-pass filtering. The black line corresponds to the sum of all feed elements $G_{sum}(f_{\mathrm{D}})$. (d) Azimuth phase correction derived from the phase expected from the geometry. (e) Low pass component of the phase correction (effect of the antenna patterns). (f) Remaining high-pass component, attributed to platform motion, namely the vibration of the mast holding the reflector antenna.

Figure 53 (a) shows the azimuth profiles (maximum over range, for each position of the platform) for the feed channels, color coded consistently with **Figure 51 (a)** (e.g. the fore channel in brown and the aft in blue), as throughout the other plots in this

chapter. The first half of the image contains the corner formation, whereas the second half has the calibration corner as main feature.

Figure 53 (b) shows the range cell migration of the calibration corner in each of the channels (color-coded plots), compared to the ideal trajectory (dashed black line), i.e.

$$R(t_{az}) = \sqrt{\left(v_{plat} \cdot t_{az} - x_{tgt}\right)^2 + r_0^2}\,, \tag{152}$$

where x_{tgt} is the target's position in along-track; the platform velocity v_{plat} and the corner's slant range position[27] r_0 are listed in TABLE X. A good match is observed, and moreover the effect of the different azimuth antenna patterns — with each feed element viewing the target at a given Doppler region with limited overlap between neighboring feed elements — is clearly visible.

Figure 53 (c) shows the gain of the antenna patterns derived from the profiles after interpolation of the response and low-pass filtering to remove artifacts, resampled to an instantaneous Doppler frequency grid, which relates to the slow (along track) time t_{az} according to [26]

$$f_{\mathrm{D}}(t_{az}) = \frac{2 \cdot v_{plat}}{\lambda} \cdot \frac{v_{plat} \cdot t_{az} - x_{tgt}}{R(t_{az})}, \tag{153}$$

where λ is the wavelength.

The black line shows the sum $G_{sum}(f_{\mathrm{D}})$ of the patterns, assuming no phase difference between them, and has a combined bandwidth of circa 3 Hz. Each feed channel is independently normalized to its maximum after range compression, which causes the peaks of all patterns to be similar, though the outermost elements are expected to show lower gains w.r.t. the central ones due to defocusing.

[27] The value is estimated from the data, as the actual position of the phase center is expected to be over the reflector's surface [100].

Figure 53 (d) shows the unwrapped phase difference between the maximum of the corner's response (over range) at each azimuth position and an ideal point-target response calculated from the geometry (the range corresponding to (152)), mapped to an azimuth angle grid. This phase has two noteworthy components: first the phase imposed by the uncompensated azimuth antenna pattern of the k^{th} feed element $\phi_{pattern}(k, \theta_{az})$, where θ_{az} is the azimuth angle; and second a phase arising from non-compensated cross-track motion of the platform $\Delta R_{plat}(t_{az})$. One may write for the k^{th} feed element

$$\phi_k(t_{az}) = \phi_{pattern}\big(k, \theta_{az}(t_{az})\big) + 4 \cdot \frac{\pi}{\lambda} \cdot \Delta R(t_{az}). \tag{154}$$

These contributions are separated using the following approach: the low-pass component [28] seen in **Figure 53 (d)** is attributed to the antenna patterns[29], whereas the remaining high-pass component in **Figure 53 (e)** is attributed to platform motion. In fact, closer analysis reveals that the phase oscillation in **Figure 53 (e)** occurs in phase between feed channels (being hence feed element independent, as expected) with a peak amplitude corresponding to circa 2.0 mm. Spectral analysis of the oscillations by means of a power spectral density estimation shows a main component at a frequency of around 1.0 Hz. As a reference, the fundamental frequency of a simple pendulum of length L is given by

$$f_{fund} \cong \frac{1}{2 \cdot \pi} \cdot \sqrt{\frac{g}{L_p}}, \tag{155}$$

where g is the acceleration due to Earth gravity. For a pendulum with $L_p = h_{el}$ = 6.34 m (corresponding to the nominal mast length), f_{fund} = 1.2 Hz. The results are thus

[28] A rectangular low-pass filter was applied with an empirically determined cut-off frequency of 0.6 Hz to separate the two components in this case.

[29] In [75], an anechoic chamber measurement of the individual feed element's antenna patterns in amplitude and phase is documented. Even though the patterns measured at that time do not directly apply to the current setup, since the system hardware was dismounted and rearranged, the results shown there bear great resemblance to **Figure 53**. In the latter, the maxima of each channel are however equalized by a normalization step after range compression of the individual channels.

considered to be consistent with small periodical oscillations of the mast holding the reflector during the motion of the rail car, due to, e.g., step motor vibration. The small amplitude is moreover consistent with the nearly wind-free meteorological conditions during the data take.

Carrying on the description of the block diagram in **Figure 52**, the next step is the correction of the range cell migration (RCMC), which takes place in range-Doppler domain. The phase calibration of the feed channel's data follows. It comprises two steps in different domains, to reflect the nature of the two main error sources mentioned above. The correction of the time-dependent motion contribution (high pass component in **Figure 53 (e)**, as estimate of the term proportional to $\Delta R(t_{az})$ in (154)) is done in time domain, whereas the azimuth-angle dependent antenna contribution (low pass component in **Figure 53 (d)**, which estimates $\phi_{pattern}\left(k, \theta_{az}(t_{az})\right)$ is done in frequency domain. This explores the relation between Doppler-frequency and squint, and allows performing the correction for all targets simultaneously. In the end of the process, the calibrated data show the amplitude patterns in **Figure 53 (c)** and nearly no phase distortions between the feed elements, corresponding to the nominal behavior of a reflector system.

The calibrated data, sampled at 10.0 Hz, are used to simulate a staggered PRI acquisition at the sampling instants of the PRI sequence described in TABLE XI. This is done by zero-padding the data in frequency domain to an even higher sampling rate (factor 128) and then applying linear interpolation in time domain to achieve the periodically non-uniform grid, on average sampled at $\overline{PRF}$ = 1.25 Hz. As indicated in **Figure 52**, this step is done individually for each channel. The calibrated data are also used to create a reference dataset by summing up over the channels. These data are regularly sampled at 10.0 Hz with an azimuth antenna pattern described by $G_{sum}(f_{\mathrm{D}})$ and are referred to as the *sum reference* (cf. **Figure 52**), a meaningful reference since it represents the ideal output of the reconstruction. The reconstruction process is the beamforming from Section 4.4.4. The results are addressed in detail in Section 7.4. As

seen in **Figure 52**, comparison takes place after azimuth compression with a classic range-Doppler processor [26], [27].

7.4 Results and Reconstruction Quality Assessment

7.4.1 Resampling and Reconstruction of original data

The reconstruction of the regular grid data sampled at $N_{ch} \cdot \overline{PRF}$ = 10.0 Hz requires the combination of all channels over a window of several pulses (cf. Section 4.4.1). Parameters of the input and output grids, as well as the reconstruction algorithm's parameters (cf. Section 4.4.4) are summarized in TABLE XI.

The weights are calculated using the pattern information seen in **Figure 51 (c)** as $G_n(f_\mathrm{D})$, $1 \leq n \leq N_{ch}$ and the phase center positions, which are a consequence of the PRI sequence parameters. The black curve in the same figure is $G_{sum}(f_\mathrm{D})$, adopted as $G_{com}(f_\mathrm{D})$. We choose N_{win} = 56 (meaning a window of N_p = 7 pulses is used for resampling), but consider two scenarios for the choice of the sensitivity parameter α — namely 0.1 and 0.5 — to compare the results with a relatively low and a relatively high SNR emphasis and to better illustrate the trade-offs involved. The maximum distance in azimuth between any sample in the input grid and its closest neighbor in the output grid is, in this case, Δx_{max} = 3.63 cm. The results are summarized in **Figure 54**.

Figure 54 (a) shows the impulse responses for the two reconstructed images (α = 0.1 and α = 0.5) and the sum reference. The impulse responses are stable around the main target position but show differences in the sidelobe region, both with respect to the reference and to each other. It should be pointed out that the effect of resampling errors due to the imperfect goal pattern implementation (cf. Section 5.4.1) is twofold: On the one hand, the residual "non-regularity" due to phase center position errors (meaning the output grid is not exactly uniform in the sense of showing residual phase errors) leads to residual ambiguities, whose levels (which can be estimated from the difference to the reference) are seen to be small. On the other hand, the deviations

of each output sample's pattern from $G_{sum}(f_{\mathrm{D}})$ mean that also the average antenna pattern is not exactly that of the reference. This is not a cause of aliasing per se, but it means that the reconstructed data have a different spectral weighting then the reference, which changes the shape of the impulse response as a whole. **Figure 54 (b)** is a zoom of the main beam showing that this effect is small. All profiles achieve a 3 dB resolution of 2.5 cm. **Figure 54 (c)** shows the result of azimuth compressing the sum over the feed channels of the non-uniformly sampled data, which is highly ambiguous. The approach is equivalent to ignoring the non-uniformity and is not a meaningful processing strategy, but is intended as a lower quality bound to highlight the importance of the resampling. **Figure 54 (d)** in turn shows the upper quality bound, i.e. the sum reference of **Figure 52**. The azimuth position axis has its origin at the position of the calibration corner. The corner constellation is visible in the azimuth region [-15, -10] m. The narrow elevation pattern — a consequence of the usage of a single element of the feed array — is also clearly observable and is the cause for the attenuation of the response of the corner in near range. **Figure 54 (e)** is the reconstructed image with α = 0.1, showing in general great similarity to the reference. The effect of the sidelobe distortions is visible as "clutter", in the region below -30 dB.

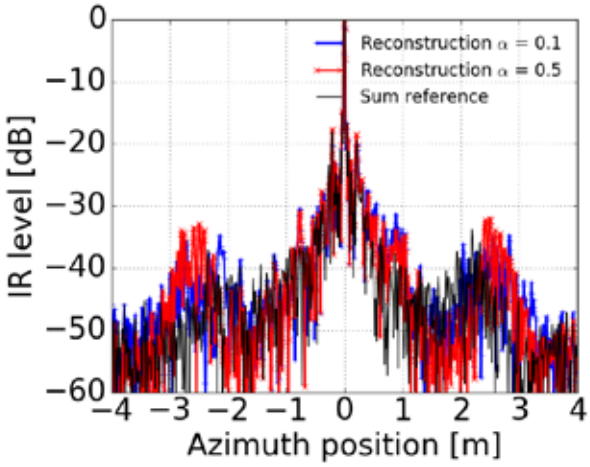

(a)

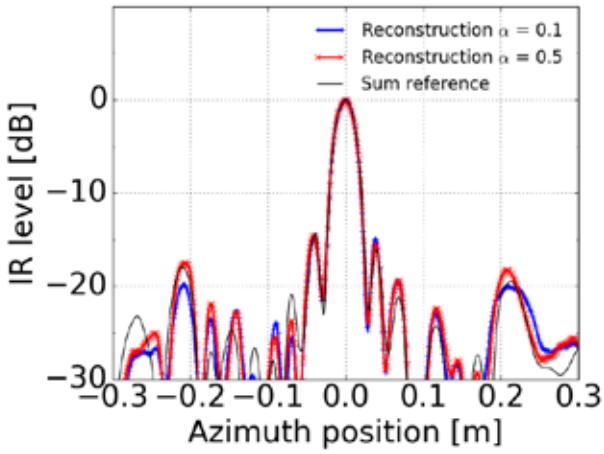

(b)

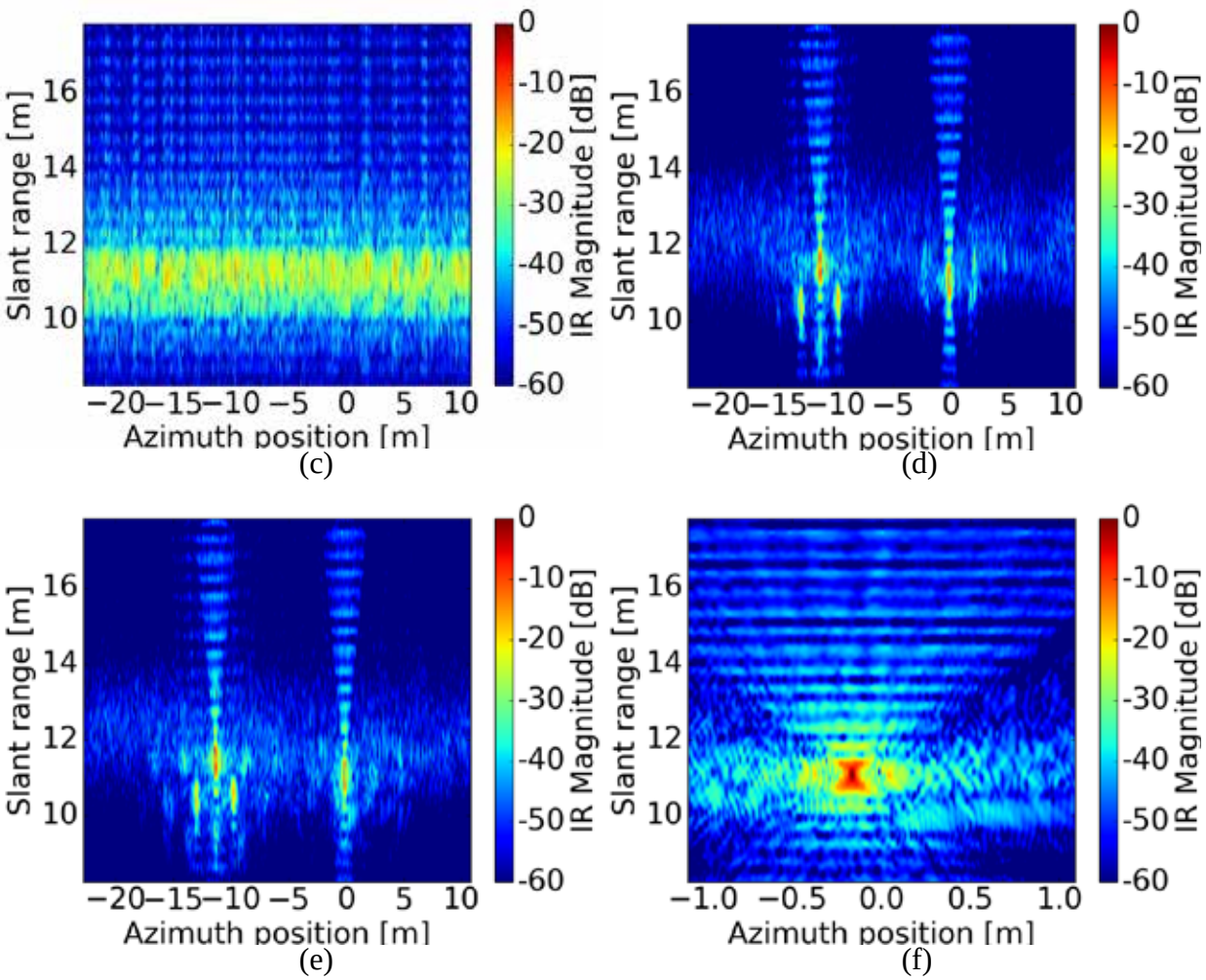

Figure 54. Images after reconstruction and azimuth compression. (a) Calibration corner's azimuth profile after compression, comparing the result of the two sets of reconstruction weights with the *sum reference*. (b) Zoom of the same impulse responses to highlight the fine 2.5 cm resolution achieved. (c) Result of simply azimuth compressing the non-uniformly sampled data (low quality reference). (d) Image of the sum reference channel at the uniform grid with 10.0 Hz sampling (upper quality bound). (e) Reconstructed image obtained with the low SNR emphasis set of weights (α = 0.1) (f) Zoom around the calibration corner reflector for the high SNR emphasis set of weights (α = 0.5).

Figure 54 (f) shows a zoom around the calibration corner's response for the image reconstructed with α = 0.5. As was the case in **Figure 54 (a)**, no major image artifacts are observed. All images were normalized to their respective maximum magnitude.

To better illustrate the residual reconstruction errors, **Figure 55 (a)** and **Figure 55 (b)** show the squared magnitude of the (complex) difference between the reconstructed

and reference images, respectively for $\alpha = 0.1$ and $\alpha = 0.5$. The area is again a zoom around the calibration corner. The sidelobe distortions are visible at peaks below -22 dB and in most regions the error level lies below -25 dB, a level expected due to the limited accuracy of the radar system setup and calibration. In **Figure 55 (c)** and **Figure 55 (d)**, the magnitude of the reconstruction error is shown in more detail, respectively for $\alpha = 0.1$ and $\alpha = 0.5$. The contour lines in **(c), (d)** refer to the magnitude levels of the sum reference, as a visual aid to indicate the main region of the impulse response.

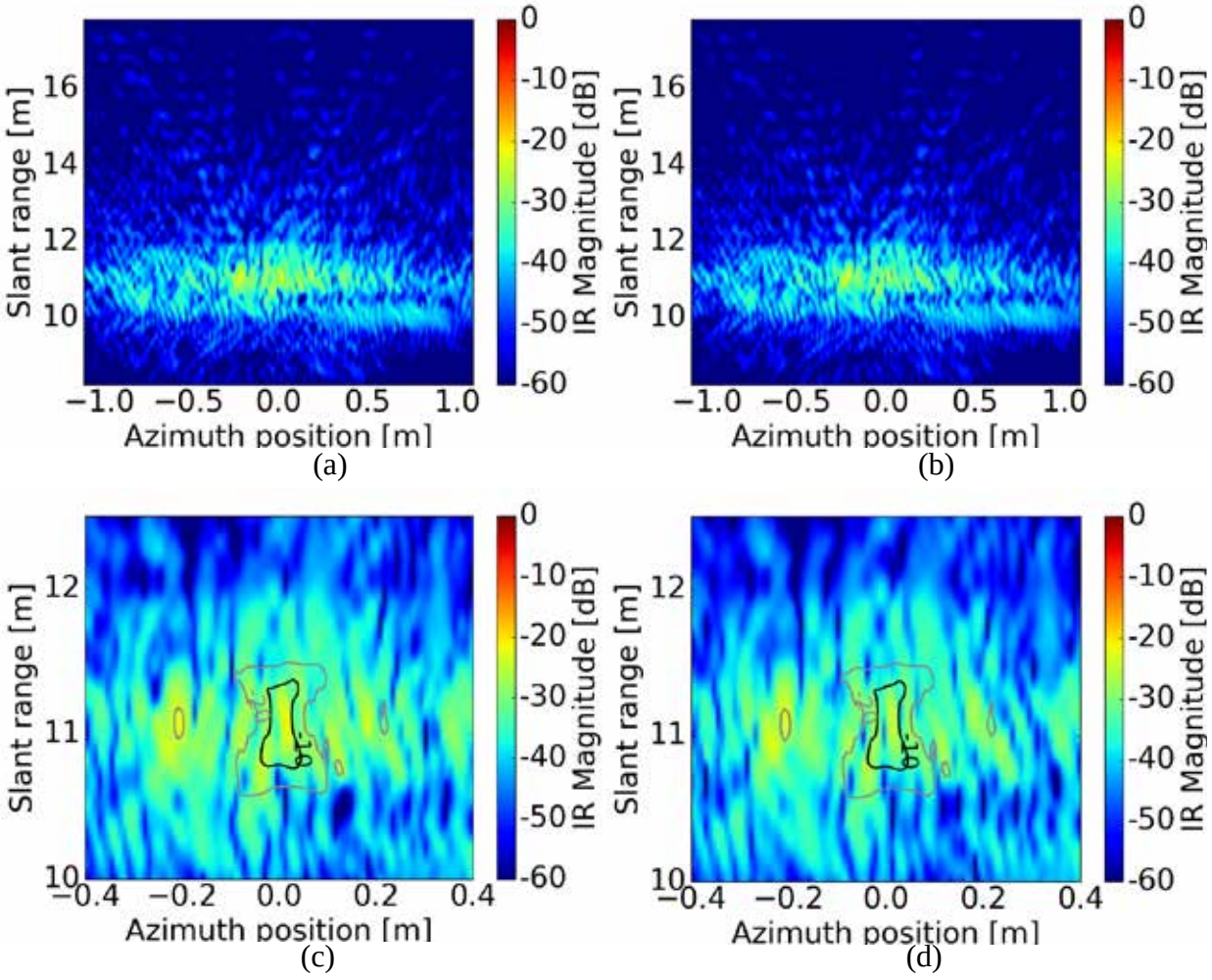

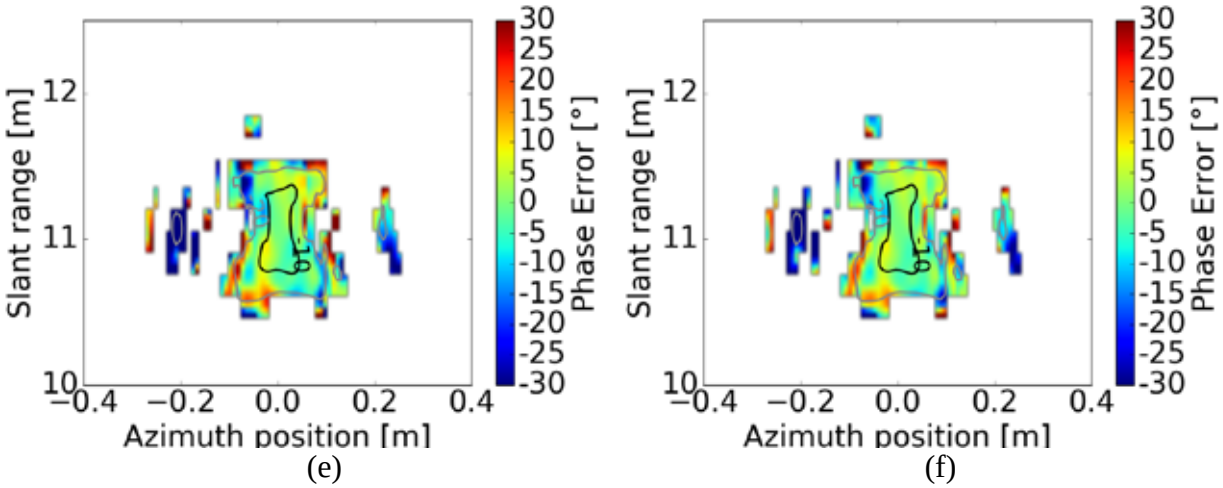

Figure 55. Residual reconstruction errors after azimuth compression, measured by means of the difference to the reference image. (a) Magnitude squared difference between the reconstructed image with α = 0.1 and the sum reference. (b) Magnitude squared difference to the reference for the case α = 0.5. (c) Zoom of the magnitude of reconstruction error, normalized to the maximum of the sum reference, for α = 0.1. (d) Zoom of the magnitude of reconstruction error, normalized to the maximum of the sum reference, for α = 0.5. (e) Zoom of the phase of reconstruction error, masked to include only regions where the sum reference's amplitude is greater than -25 dB, for α = 0.1. (f) Zoom of the phase of reconstruction error, for α = 0.5.

Figure 55 (e) and **Figure 55 (f)** shows the phase of the complex difference to the reference image, respectively for α = 0.1 and α = 0.5 . The region where the magnitude of the sum reference is below -25 dB is masked out. The same contour lines are repeated, indicating a stable phase with small residual errors in the region of dominant magnitude, which is the most relevant for the signal.

Reconstruction with both α = 0.1 and α = 0.5 showed similar results, which is interesting as an indication that the increased SNR emphasis does not severely degrade the ambiguity suppression. The main difference between the two sets of weights and motivation for the mixed form of the cost-function (117) is however the achieved SNR scaling Φ_{SNR} (cf. (113)). In the case of α = 0.1, Φ_{SNR} = −3.9 dB; whereas for α = 0.5, Φ_{SNR} = −0.9 dB. In the latter case, the very high SNR of the data did not allow this considerable difference of the achieved SNR scaling to be

observed. Therefore, to better illustrate the noise behavior of the processing strategies, a final case study is explained, employing the addition of synthetic white noise. This is done in the following, in Section 7.4.2.

7.4.2 Resampling with added Synthetic Noise

A block diagram describing the procedure in this section is provided in **Figure 56 (a)**. As indicated, noise was added to the interpolated irregularly sampled data before the azimuth beamforming and compression (compare to block diagram in **Figure 52**). The level is intended to establish a noise floor of around -30 dB. The noisy data are reconstructed with the two sets of weights, leading to two different reconstructed images and the achieved noise levels are analyzed in the further plots of **Figure 56**.

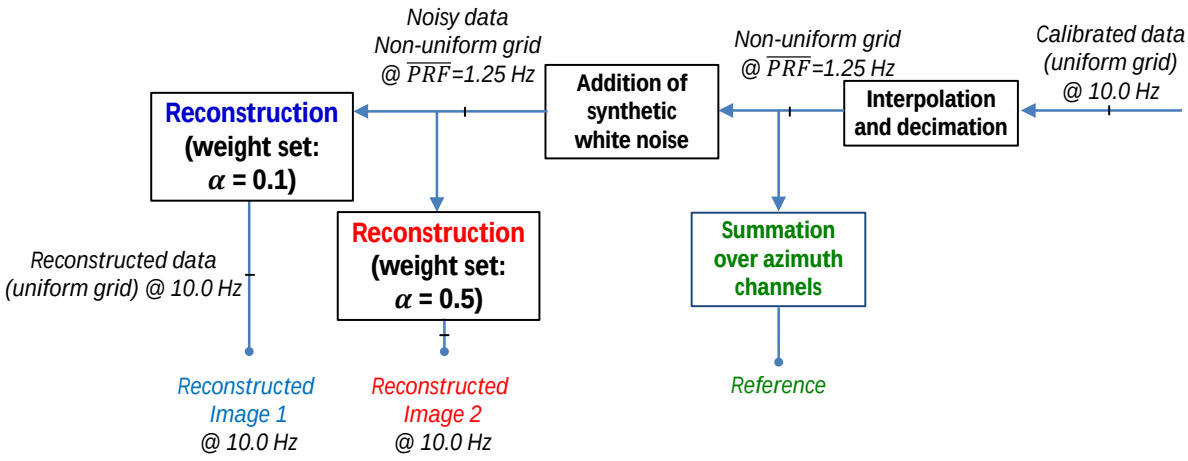

(a)

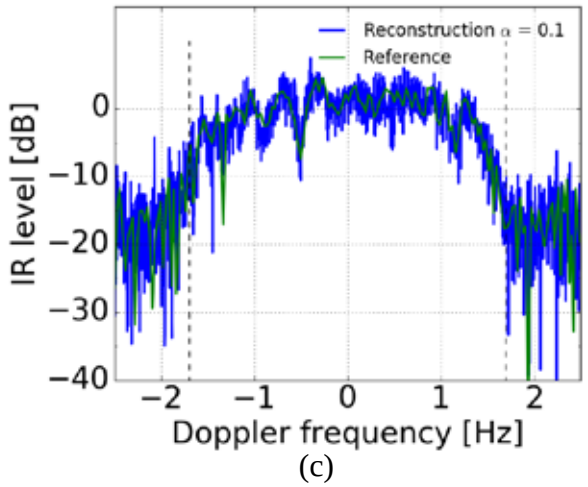

(c)

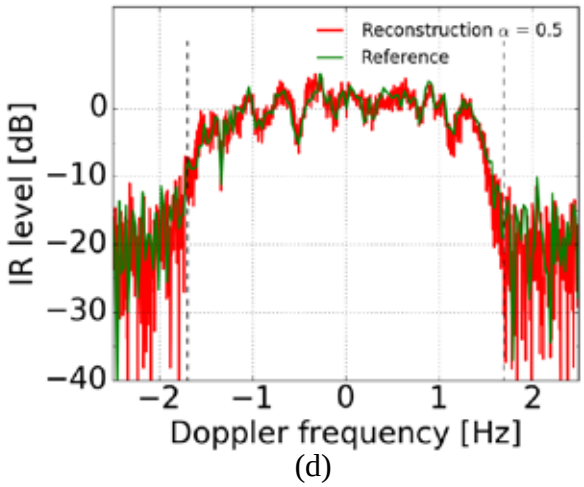

(d)

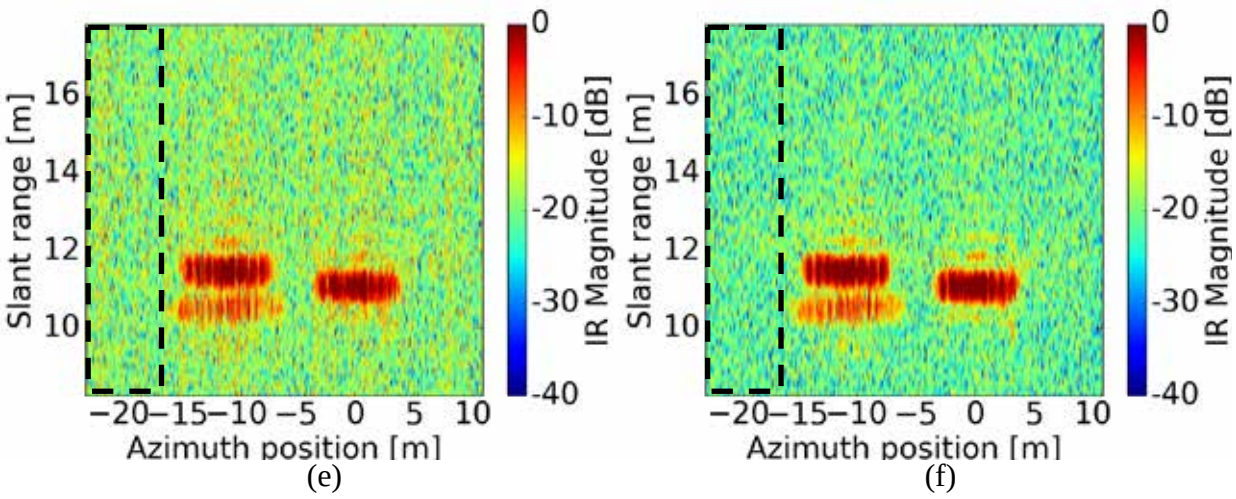

Figure 56. Analysis of noise scaling properties of reconstruction. (a) Block diagram for the performed analysis, indicating the addition of synthetic white noise before the reconstruction to compare the scaling of the two set of weights, leading to two reconstructed images. The reference formed by summing the channels in the irregular grid is provided as a visual aid for the profiles to be shown. (b) Profile of the calibration corner after reconstruction for the low SNR emphasis set of weights (α = 0.1, corresponding to the first reconstructed image) plotted against instantaneous Doppler, resembling the sum pattern. (c) Profile of the calibration corner after reconstruction for the higher SNR emphasis set of weights (α = 0.5, corresponding to the second reconstructed image). (d) First reconstructed image, before azimuth compression, including an indication of the "noise-only" area used for variance estimation to access noise levels (black dashed line box). (e) Second reconstructed image, also before azimuth compression.

An important difference is that all the analysis is done *before performing the azimuth compression*, in order to emphasize the impact on the output patterns, without masking due to posterior filtering steps.

Figure 56 (b) shows the profile of the calibration corner of the first reconstructed image, i.e., with the low SNR emphasis set of weights (α = 0.1) against instantaneous Doppler. The reference shown is derived from the non-uniformly sampled data by summing over the channels and intended as a visual aid. Both profiles are normalized to their respective mean levels within the processed bandwidth (highlighted by the vertical dashed lines) and resemble the sum pattern $G_{sum}(f_{\mathrm{D}})$, as expected. **Figure 56 (c)** shows the same profile for the high SNR emphasis set of weights (α = 0.5), and the

reference is repeated. The second profile is visibly less contaminated by noise. **Figure 56 (d)** shows the first reconstructed image, and the responses of the four-corner formation (left of plot), as well as the calibration corner (around the origin of the axis) are visible.

The box (dashed black line) indicates a region which contains mostly noise, and is used for a variance estimation to validate the noise scaling prediction. **Figure 56 (e)** shows the second reconstructed image, which is seen to show a lower noise floor, due to the higher SNR emphasis of the weights. To quantify the improvement, the variance of the images in the region highlighted in **Figure 56 (d)**, **(e)** was estimated and compared. The ratio of the variances between **Figure 56 (d)** and **Figure 56 (e)** was found to be 3.2 dB, which validates the predicted difference in Φ_{SNR}.

7.5 Remarks on the Proof of Concept

This chapter described a proof of concept of the multichannel staggered SAR resampling, using experimental data from the MIMO ground-based radar demonstrator. The system was operated in X-band with a multichannel feed, yielding 8 independently digitized channels, initially acquired at a high, uniform, sampling rate of 10 Hz, over a scene consisting of a calibration corner reflector and additional targets (cf. Section 7.2). As described in Section 7.3, the corner's response was used to characterize the azimuth antenna patterns from the data and compensate for phase differences, both due to imbalances and motion effects. These calibrated data were interpolated and down-sampled to simulate a staggered PRI acquisition and then reconstructed. As the analysis in Section 7.4 showed, the reconstruction achieved good quality. Furthermore, an additional analysis with added synthetic noise confirmed the expected SNR scaling behavior. The resampling concept was thus validated, provided that proper calibration of the system is applied, and the antenna manifold is known. The next chapter addresses several cases of errors and mismatches between the expected manifold and the actual one, assessing performance degradation due to these effects.

8 Analysis of Errors and Mismatches

8.1 Chapter Overview

This chapter complements the discussion on the implementation by analyzing nonidealities in the resampling of Multichannel Staggered SAR data. Simulations are used to assess the impact of different effects contributing to mismatches between the signal model (notably the array manifolds) assumed for DBF weight calculation (cf. Section 4.2) and the actual properties of the signals being reconstructed. As a rule, these discrepancies worsen the SAR performance. The goal of the analysis is to estimate the magnitude of these effects and identify the driving factors, as a general guideline. Examples from the HRWS systems designed in Chapter 6 are used to this end. The image performance degradation caused by the different sources of error is also compared to the requirements set at that point, to help identify quantitatively the most relevant effects.

The first part of the analysis is deterministic and encompasses sources of error due to properties of the signal in the range dimension. Section 8.2 considers the pulse extension over range, which means that at any given time returns from different ranges are recorded and thus a mismatch between the nominal and the actual range arises, at least before range compression. The range offset translates into an elevation angle offset and causes an antenna pattern mismatch. Another form of elevation angle mismatch is considered Section 8.3, namely the limitation of the number of sets of coefficients over range, which introduces a quantization effect on the elevation angles assumed for pattern modeling and weight calculation. The impact of this quantization — discussed in Section 6.5 in the estimation of the minimum on-board memory requirements — is investigated. In Section 8.4, pattern mismatch due to the signal is considered. It is taken into account that monochromatic antenna patterns are assumed for the weight calculation, whereas in reality the transmitted signal has a given bandwidth. Finally, Section 8.5 considers along-track mispointing as a final source of mismatch, with the aim of providing an estimate of the pointing accuracy requirements for this class of system.

The second part makes use of Monte Carlo simulations as a first order estimation of further hardware and calibration requirements for the HRWS systems. Section 8.6 introduces a simple model for pattern uncertainty, considering the fact that antenna pattern characterization is a measurement with limited precision and also that antenna properties change over time. The approach is to impose a varying degree of mismatch between the nominal antenna pattern (used for DBF weight calculation) and the actual one (used to simulate the signal), to estimate how precisely the patterns need to be known. The analysis complements Section 6.5 in the sense of providing an overview of the feasibility of on-board processing in terms of the required calibration accuracy. Finally, Section 8.7 models amplitude and phase errors on the implementation of the weights, rather than in their design. This is intended to model the effect of limited amplitude and phase accuracy on the TRM modules, which causes the weights applied to be non-ideal, even if the patterns were known with arbitrary precision.

8.2 Pattern Mismatch due to Pulse Extension over Range

In the spaceborne SAR geometry [26], the delays caused by the distance to the ground, as well as the corresponding echo duration (which depends on the difference between the minimum and maximum ranges) are as a rule much larger than the pulse duration T_p. Portraying the radar pulses as very short Dirac pulses for simplicity is thus a very widespread approximation and often accurate enough for timing analysis. As discussed in [123], however, the pulse extension is relevant for the performance (particularly SNR and absolute calibration) of narrow beam systems, in particular those employing the SCORE technique. Considering that the signal transmission starts at time instant t_0 and that the round trip delay for a target at slant range R is given by $\frac{2}{\mathrm{c}} \cdot R$, the time for signal reception is given by

$$t_{RX} = t_{TX} + \frac{2}{\mathrm{c}} \cdot R. \tag{156}$$

Considering that for the whole waveform of the pulse to be transmitted t_{TX} varies within $0 \leq t_{TX} \leq T_p$, it is clear that different ranges, from R_1 to $R_0 = R_1 - \frac{\mathrm{c}}{2} \cdot T_p$, lead

to the same t_{RX}. In other words, before pulse compression, at any given time, the echoes contain backscatter from targets located within the footprint of the pulse with extension $\frac{c}{2} \cdot T_p$ in slant range, as illustrated in **Figure 57**.

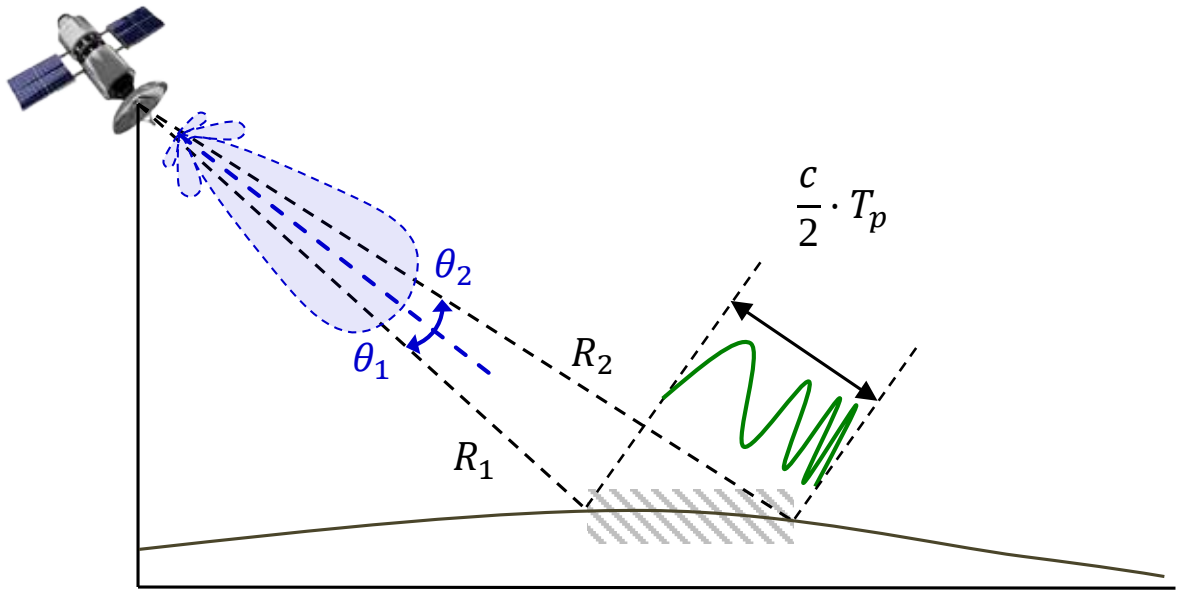

Figure 57. Schematic representation of the region visible at any given time for a pulse of duration T_p, before pulse compression. The visible region extends from R_1 to R_2, corresponding to elevation angles θ_1 to θ_2.

As indicated in the figure, the different ranges translate into an elevation angle region from θ_1 to θ_2. The main effect of the pulse extension is namely a weighting (modulation) of the signal according to the antenna pattern in elevation within this interval. If the elevation pattern is broad, so that the pattern gain doesn't change considerably within $[\theta_1, \theta_2]$, the effect is negligible and the Dirac pulse approximation holds. Nonetheless, if the pattern is narrow (as intended in SCORE operation), the attenuation can mean loss of SNR (or even range resolution), what motivates the definition and analysis of the Pulse Extension Loss (PEL) in [123].

In the context of Multichannel Staggered SAR data resampling, the parameter t_{RX} defines the input grid and plays a central role in the signal modeling and weight calculation (cf. Section 4.2). The implication of the pulse extension in this case is that,

if the resampling is applied to data before range compression, a mismatch of up to $\frac{c}{2} \cdot T_p$ in range[30] between the nominal and actual ranges of the signal is to be expected. This corresponds to process data originating from R_2, θ_2 with weights derived for R_1, θ_1. Particularly in the case of reflector antennas, the elevation mismatch leads to errors in the modeling of the azimuth patterns as well, and these are relevant for the DBF weight calculation (cf. (97)). Note however that, as t_{RX} is the same for all ranges within the pulse extension, the recorded signals are subject to the same blockage effects, even though originating from different ranges.

In order to assess the magnitude of the performance degradation due to this effect, the SAR performance of the system of Section 6.2.1 (cf. TABLE V) is calculated considering a range mismatch of $\frac{c}{2} \cdot T_p$ = 2.2 km. This corresponds to an angular deviation $\theta_2 - \theta_1$ between 0.3° (in near range) and 0.1° (in far range). At each range R_1, the nominal parameters are considered for the weight calculation, whereas the simulated signal matches a point target located at $R_2 = R_1 + \frac{c}{2} \cdot T_p$, except for the timing and blockage considerations, which are dependent on t_{RX} of the nominal range. In [123], the analytic expression relating θ_2 and θ_1 is derived.

In **Figure 58**, the degraded performance is compared to the nominal performance (cf. **Figure 41**), showing that the azimuth performance is the most affected. **Figure 58 (a)** shows the AASR, whose worst-case is degraded by 4.3 dB, reaching -28.6 dB. The difference is larger in near range, where the offset is larger with respect to the local range. The variation of the RASR in **Figure 58 (b)** consists mostly of local oscillations, and the worst-case is changed by only 0.2 dB. In this case, the elevation patterns — the most important factors for the ambiguity ratio — remain fairly unchanged, due to the stability of the MVDR beamformer [40]. Moreover, the range offset (which is minor in comparison to the original ranges) shifts the position of the

[30] Note that here a pessimistic assumption is made. If the weight calculation is matched to the center of the area illuminated by the pulse on ground, the maximum offset could be reduced to $\frac{c}{4} \cdot T_p$.

signal and ambiguities only slightly. In certain cases, especially when the ambiguities are close to pattern minima, considerable variations occur, which however do not change the overall scenario performance. **Figure 58 (c)** shows the azimuth resolution, whose curve is shifted, but changes by less than 0.1 m, still satisfying the 3.0 m goal. Finally, **Figure 58 (d)** shows the NESZ, which is affected especially by the variation in the noise scaling of the azimuth beamforming (cf. Section 4.4.3 and (113)). The degradation of the worst-case is 0.3 dB, and in the case shown the NESZ is better than -24.7 dB. The largest impact is seen in near range, were degradation in the order of 1 dB occurs.

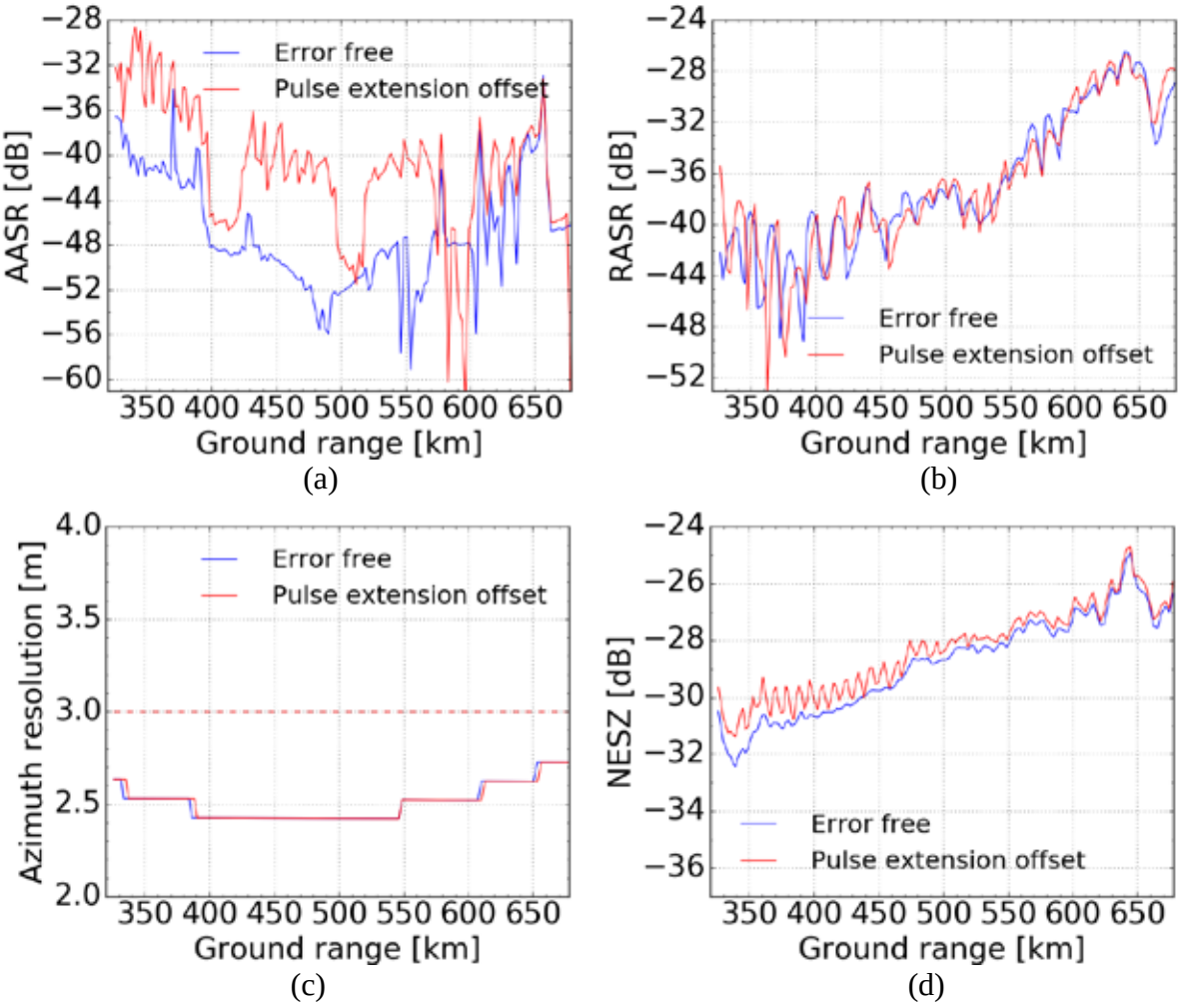

Figure 58. SAR performance with range mismatch due to pulse extension. Example for 3.0 m / 350 km single-pol multichannel staggered SAR mode using a 15.0 m reflector with 3 azimuth channels (cf. 6.2.1). (a) AASR. (b) RASR. (c) Azimuth resolution. (d) NESZ.

It should be noted that, as discussed in [123], the pulse extension effect itself is not visible in the NESZ calculation. This motivates the definition of the Pulse Extension Loss as a separate quantity, of special interest for narrownbeam systems as e.g. those using SCORE.

In this case, the degradation was found to be non-critical in terms of the fulfilment of the requirements. A compensation of this effect is however possible if necessary by separating the signal into RF sub-bands and applying sub-band dependent beamforming weights [40], [52]. This technique is referred to as *dispersive frequency beamforming* and exploits the variation of the RF frequency of the chirp in time, which leads to a correspondence of the instantaneous frequency and the delay of the locally illuminated area on ground. The potential implications for the hardware are the need to implement additional filters and an increase of the number of digital data streams to be handled by the on-board electronics.

8.3 Pattern Mismatch due to Limited Set of Weights over Range

In Section 6.5, during the assessment of the minimum memory requirements for on-board processing, it was made clear that the amount of data to be stored is directly proportional to the number of sets of coefficients over range. As mentioned, an update of the coefficients whenever a change in the blockage configuration occurs is critical, since this represents a major change in the input grid configuration (cf. **Figure 50**). A different situation occurs for the regions over range in which no blockage occurs[31]. Within these, the sampling configuration remains the same. Updates of the weights are nonetheless necessary, at least in reflector systems, due to the variation of the azimuth antenna patterns with range. In (150), a criterion was proposed to extend the update rate of the regions with blockage to the whole swath, to account for this effect. In this case, the assumption is that the pattern information is only available in a discrete set of N_{rg} elevation angles. These are equally spaced within the swath, corresponding to a slant range quantization with step $\frac{c}{2} \cdot T_p$. As

[31] These regions appear in the current examples due to the fact that relatively short sequences are used, which allow the delay orders $d_{i,k}$ not to overlap for neighboring k within the swath. As discussed in [53], [62], longer sequences tend to lead to overlap between orders, and thus these regions disappear. This can be imposed intentionally by the use of the *more elaborate* (composite) *sequences* [53] – which allow equalization of the performance over range at the cost of increased complexity – but also tends to happen as a consequence of a e.g. a higher $\overline{PRF}$ in the design.

also discussed in Section 6.5, this is enough to cover every possible blockage configuration. Thus, at every given range, even though the local blockage is respected, the antenna patterns assumed for weight calculation correspond to the nearest range within this set of N_{rg} patterns. This leads to a total amount of required memory matching (150).

The restriction on the number of range sets effectively leads to another form of range mismatch, with effects similar to the ones discussed in Section 8.2.The purpose of this section is to evaluate the validity of this approach, by assessing the corresponding performance degradation. In **Figure 59**, the performance of the system in Section 6.2.1 considering a quantization to $N_{rg} = 64$ (cf. TABLE IX) sets of weights is simulated.

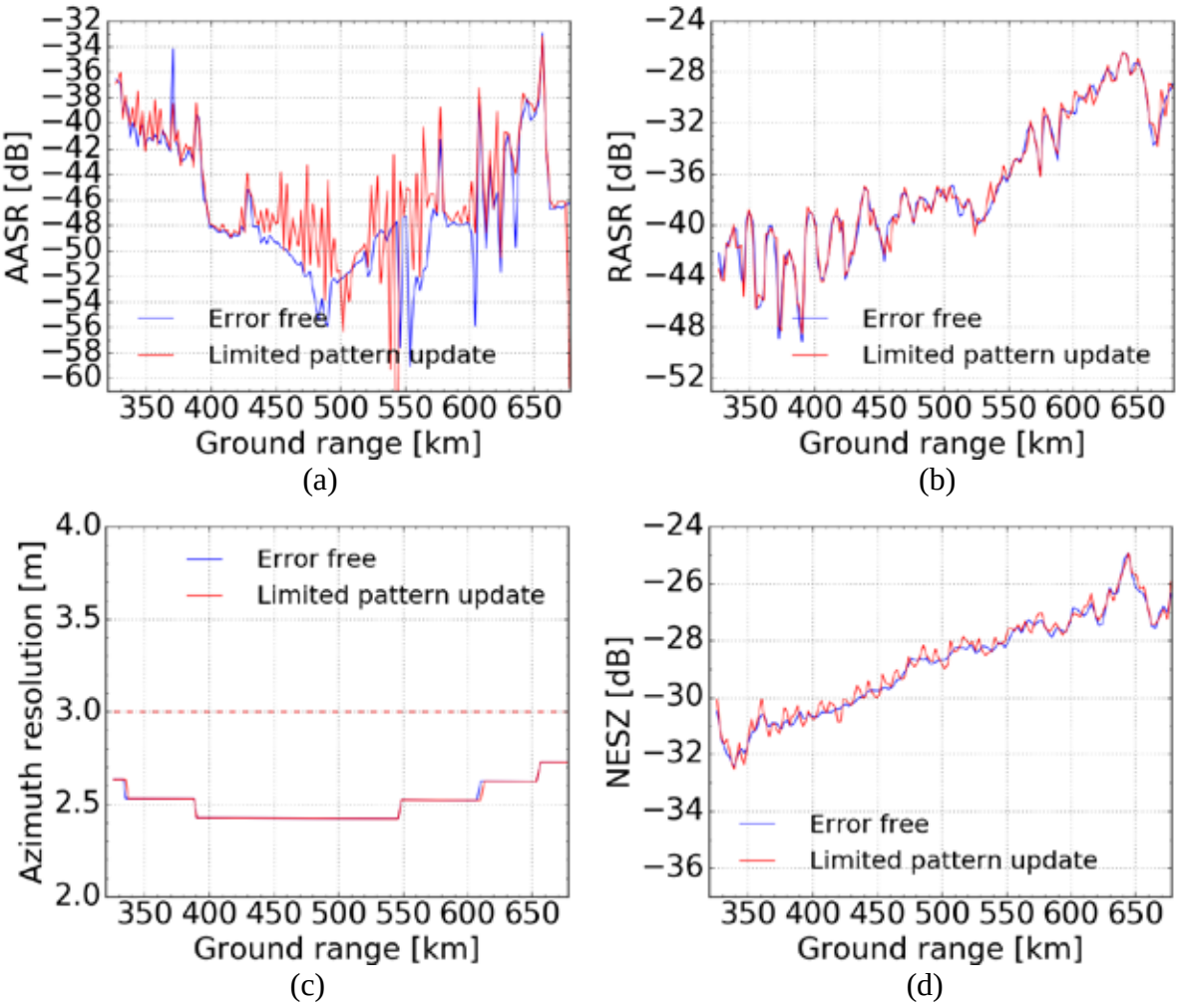

Figure 59. SAR performance with range mismatch due to restriction on the number of sets of weights over range. Example for 3.0 m / 350 km single-pol multichannel staggered SAR mode using a 15.0 m reflector with 3 azimuth channels (cf. 6.2.1). (a) AASR. (b) RASR. (c) Azimuth resolution. (d) NESZ.

The AASR in **Figure 59 (a)** shows mostly local oscillations, and the worst-case is changed by -0.25 dB, due to the disturbance of the peak in far range. The RASR in **Figure 59 (b)** also shows small local fluctuations[32] which however do not change the worst-case. The azimuth resolution in **Figure 59 (c)** is equally virtually unchanged. The NESZ in **Figure 59 (d)** shows local variations induced by the noise scaling, but again the worst-case variation is negligible.

8.4 Pattern Mismatch due to Pulse Bandwidth

In this section, another source of antenna pattern mismatch is considered, namely the antenna pattern variation with frequency. So far, the pattern simulations have been monochromatic (in the examples, at the carrier frequency $f_0 = 1.2575$ GHz). It should however be noted that, regardless of the carrier frequency, the transmitted signals in practice possess a bandwidth. Within it, the antenna pattern as a rule varies with the RF frequency. As represented schematically in **Figure 60**, the worst-case deviation in terms of frequency, which also translates into pattern mismatch, is given by $f_{offset} = f_0 - \frac{BW_{chirp}}{2}$. The magnitude of $\frac{BW_{chirp}}{f_0}$ dictates the maximum degradation.

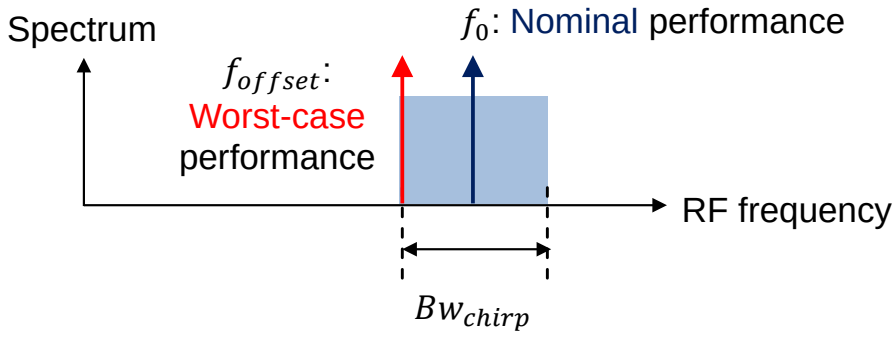

Figure 60. Schematic representation of the system bandwidth the worst-case deviation in terms of pattern mismatch at $f_{offset} = f_0 - BW_{chirp} / 2$.

[32] Considerable robustness with respect to weight mismatches [40] is an advatange of the SCORE beams with the MVDR beamformer.

As an example, in L-band, international regulations (Recommendation ITU-R RS.577-7 (02/2009) [124]), dictate that the bandwidth for active spaceborne system for remote sensing should be limited to $Bw_{chirp} \leq 85$ MHz. The frequency deviation in that case would amount to $f_{offset} = f_0 - \frac{BW_{chirp}}{2} \geq 1.2150$ GHz.

The change in the RF frequency obviously means a change in the wavelength λ. Since the physical dimensions of the antenna do not change, the d/λ ratio of the feed array changes. This affects the steering properties of the primary beam (cf. (87))[33]. Given that the physical principle behind the phase center resampling for the beamformer in Section 4.4 is the steering of the primary beams (cf. Section 4.3), the azimuth performance is expected to be affected. The change in d/λ over the RF bandwidth causes mispointing of the beams with respect to the intended positions, introducing errors in the sampling of the output grid. Since a higher d/λ degrades steering performance[34] [100], [106], f_{offset} in the lower part of spectrum leads to the poorest performance, motivating its choice for the worst-case analysis.

Another factor which influences the robustness to misspointing is the distance from the feed to the reflector, directly proportional to the reflector size[35]. The same angular error leads to a larger displacement if the feed is further away. In this context, this means that when the reflector size increases, for the same element spacing d, the system is expected to show larger deviations from the desired output grid.

[33] This is true under the assumption of beamforming with phase shifts. Means to counter this effect such as *true time delay* beamforming (which achieves an ensamble delay instead of a frequency-dependent phase shift) exist in phased array technology. The underlying operation is however no longer described by a mere complex weighting.

[34] A larger d/λ can be regarded as a lower spatial sampling of the signals within the array and makes the array more prone to e.g. grating lobes.

[35] The analysis here is under the assumption that other geometric properties of the reflector, including the focal lengh to diameter (F/D) ratio, remain constant. A constant angular error thus leads to a linear positioning error which scales linearly with the distance from the feed to reflector, proportional to D in this case.

The effects of the bandwidth will be investigated in the following by means of examples. In **Figure 61** the far-field patterns of the 15.0 m reflector system of Section 6.2.1 (cf. parameters in TABLE V) simulated using the GRASP software [113] at f_0 = 1.2575 GHz and f_{offset} = 1.2150 GHz are compared.

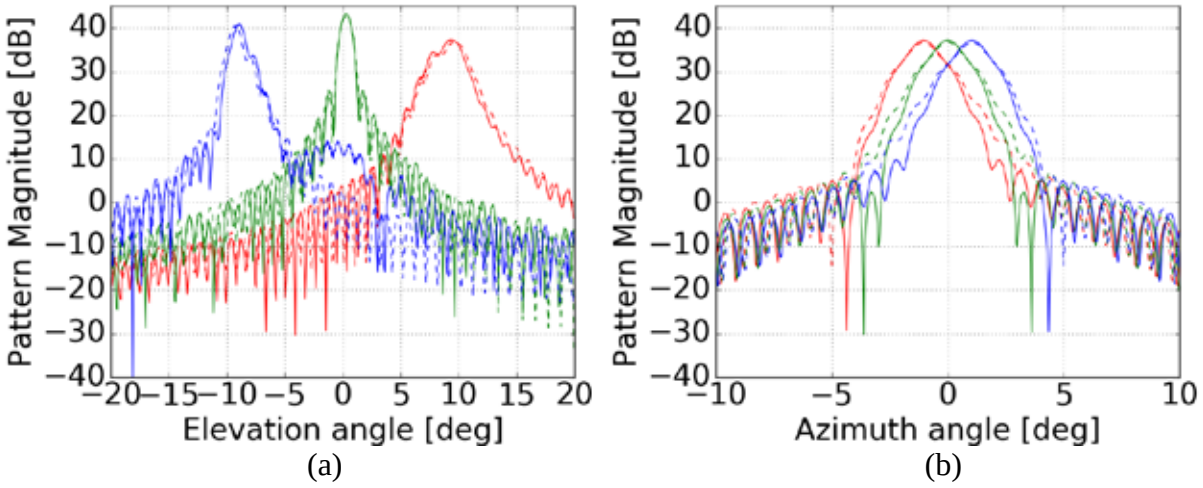

(a) (b)

Figure 61. Reflector pattern modification due to RF frequency offset. Example of 15.0 m reflector with 3 azimuth channels (cf. 6.2.1). (a) Elevation patterns of central azimuth element for different elevation elements (first element, with maximum at far range, in red; central element in green and last element, with maximum at near range, in blue). The patterns at the nominal frequency f_0 are shown in solid lines and the ones at f_{offset} by dashed lines, in the corresponding colors. (b) Azimuth patterns of the first elevation element (maximum at far range). The 3 azimuth elements are shown in different colors. Again the patterns at the nominal frequency f_0 are represented by solid lines whereas the patterns at the frequency f_{offset} are seen in dashed lines. The effect of the frequency offset is a broadening of the patterns and a change in the position of the maximum which is proportional to the distance to the feed center.

Figure 61 (a) shows 3 of the 32 elevation patterns of the central feed elements in azimuth. The first (maximum at far range), central (maximum at the center of the swath) and last (maximum at near range) patterns are chosen as an example, seen in different colors. The patterns are plotted with solid lines for for f_0 and dashed for $f_{offset,}$ respectively. The patterns from the elements at the extremes of the feed are clearly more defocused and also show a larger variation due to the frequency offset. **Figure 61 (b)** shows the 3 azimuth patterns of the first elevation element of the feed (maximum at far range). The different azimuth feed channels are seen in different

colors, and again for f_0 and f_{offset} in different linestyles. In both cases, the effect of the frequency offset of 45 MHz is a slight broadening of the main beams and a displacement of the maxima of the non-central feed elements, which is in the order of 0.05° in elevation for the elements in the feed's edges.

In **Figure 62**, the result of processing a signal generated with the patterns at f_{offset} with DBF weights matched to the patterns at f_0 is considered. It is meant as an illustration of the worst-case degradation expected due to the pattern variation within the bandwidth for the case study.

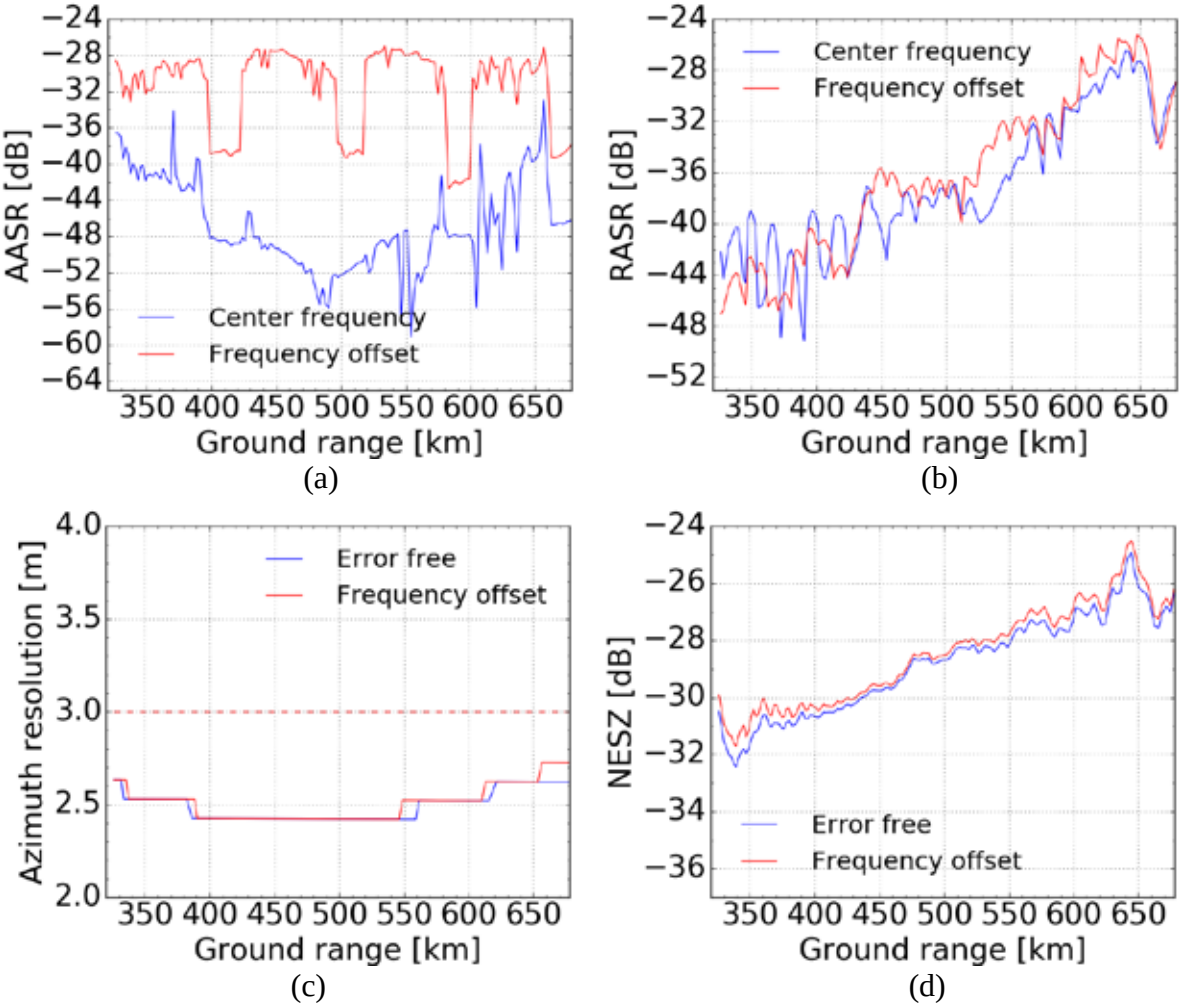

Figure 62. SAR performance with pattern mismatch due to RF frequency offset. Example for 3.0 m / 350 km single-pol multichannel staggered SAR mode using a 15.0 m reflector with 3 azimuth channels (cf. Section 6.2.1). (a) AASR. (b) RASR. (c) Azimuth resolution. (d) NESZ.

The AASR in **Figure 62 (a)** shows the greatest degradation, with the worst-case level over the swath increasing by 5.9 dB to -27.0 dB. The RASR in **Figure 62 (b)** shows a degradation of the worst-case of circa 1.3 dB, and the levels are better than -25.2 dB. The change in the azimuth resolution in **Figure 62 (c)** is in the order of 0.1 m and does not change the worst-case. The NESZ in **Figure 62 (d)** degrades by circa 0.5 dB, and in the curve with frequency offset has as peak value -24.5 dB. In this example, this violates the sensitivity requirement set at Chapter 6, but compliance can however be restored by a non-critical increase of the transmitted power to 380 W.

In this case, therefore, the performance degradation caused by the effect of the antenna pattern change within the RF bandwidth is not a critical factor. A different scenario is however found for the quad-pol mode in Section 6.3, as shown in **Figure 63**. To limit the number of plots, only the polarizations showing the worst performance are represented. The AASR of the HH/HV polarizations, seen in **Figure 63 (a)**, is considerably degraded, reaching -18.3 dB in the worst case, what represents a 12 dB increase in comparison to the nominal performance. Other performance parameters are however not considerably affected. The RASR in **Figure 63 (b)** suffers only local oscillations and has a peak increase of 4.9 dB in near range (cf. first peak of red curve in near range), thought the worst case across the swath changes by less than 0.8 dB. Neither the azimuth resolution in **Figure 63 (c)** nor the NESZ in **Figure 63 (d)** are changed appreciably as well.

As in the previous case, the AASR degradation is the critical factor. An importance difference is however that in this scenario the level of performance degradation is considerably higher (12 dB instead of 5.9 dB). This can be traced back to two main factors. First, the larger reflector of diameter D = 18.0 m (against 15.0 m in the previous example) means the feed is further away from the reflector, and thus the angular errors project as larger displacements of the illuminated region, what affects the output grid more strongly. Second, the larger number of channels in azimuth N_{ch} = 6 (instead of N_{ch} = 3 in the previous example) also plays a role, since more

error sources contribute to the overall deviation. The combination of all these effects leads to the worsened performance.

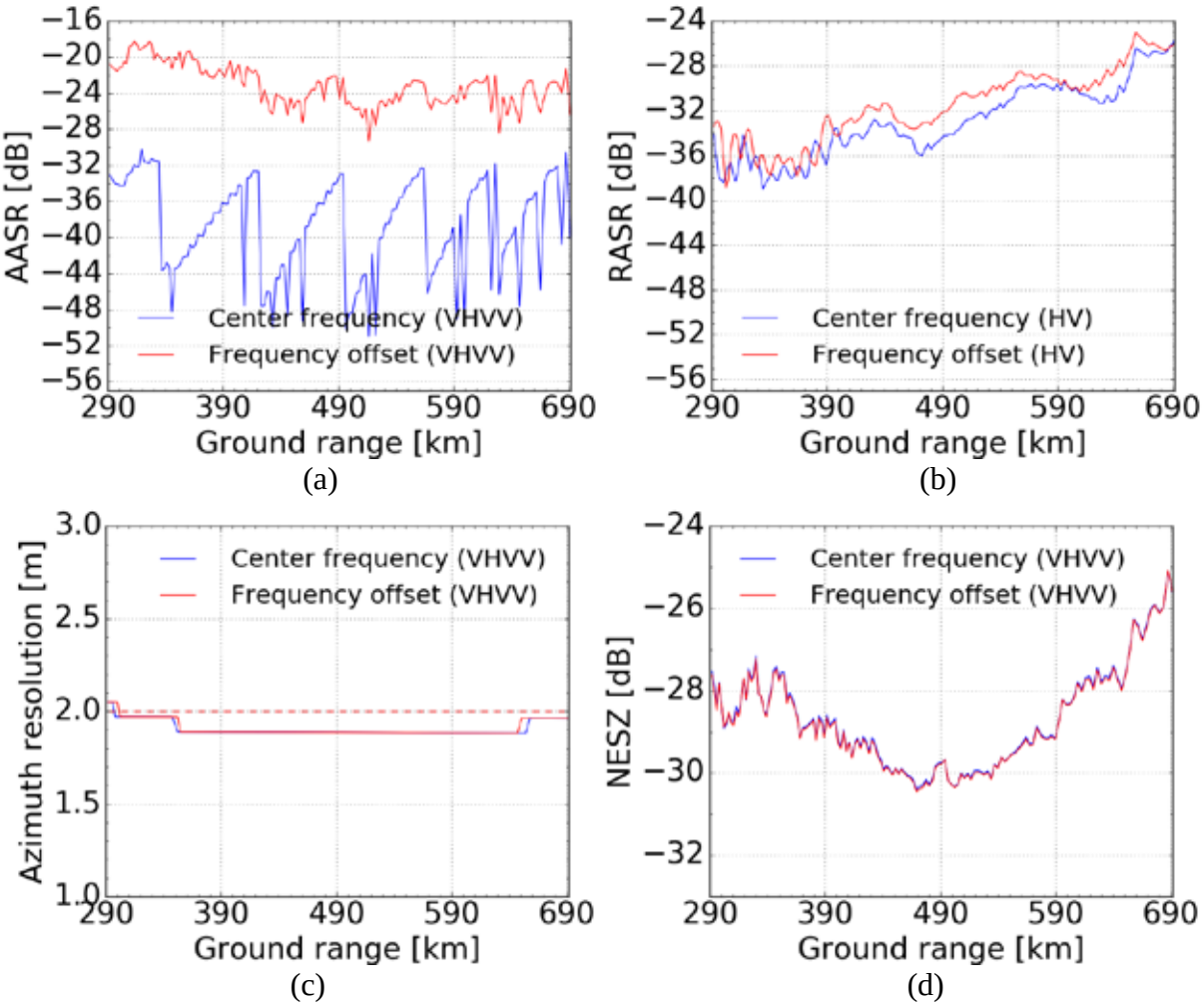

Figure 63. SAR performance with pattern mismatch due to RF frequency offset. Example for 2.0 m / 400 km quad-pol multichannel staggered SAR mode using a 18.0 m reflector with 6 azimuth channels (cf. Section 6.3). (a) AASR. (b) RASR. (c) Azimuth resolution. (d) NESZ.

A Possible Compensation: Beamforming with Division into RF Sub-bands

Even though expected, the worsening in the AASR levels of the last scenario is considerable and must be compensated. A simple way of achieving this is to divide the signal into N_{sb}^{RF} sub-bands with a smaller RF bandwidth. An example with $N_{sb} = 3$ is schematized in **Figure 64**.

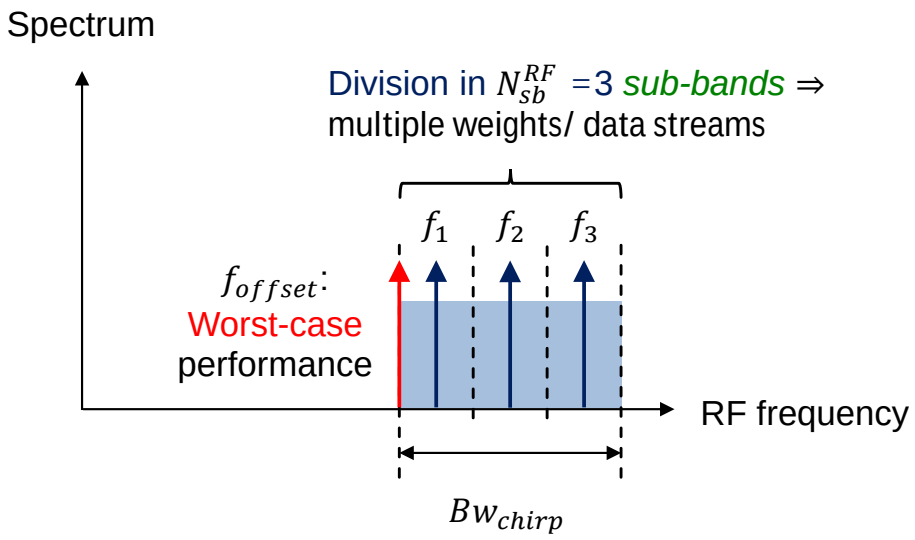

Figure 64. Schematic representation of the division of the system bandwidth into 3 sub-bands to reduce pattern mismatch at $f_{offset} = f_0 - BW_{chirp}/2 = f_1 - BW_{chirp}/6$.

The maximum offset in terms of frequency is reduced by a factor of N_{sb}^{RF}, at the cost of additional filtering and handling of N_{sb}^{RF} separate data streams. In the case of ground processing, this can be straightforwardly implemented by an FFT over the range samples. There are however implications for the on-board processing scenario.

In a radar system, RF filtering and bandwidth control need to be applied simultaneouly with the demodulation of the signal to baseband. One option would be to do the bandpass filtering analogically and acquire the sub-bands as individual data streams. This approach requires only adjustments in the radar's intermediate frequency (IF) sub-system rather than new sub-systems. An increase the number of filters and ADCs would however be necessary. The multiplicity of the weights and data streams increases as well the system complexity, scaling it also by a factor N_{sb}^{RF} in the worst-case. Keeping N_{sb}^{RF} as low as possible is therefore highly desirable in this context. Depending on the processing power on board, digital filtering of a single data stream with the full RF bandwidth could also be used to split it into different RF sub-bands. This could be done using e.g. a range FFT or a bank of bandpass filters. This as a rule would result in an increase in the number (and/or complexity) of the digital processing elements.

The quad-pol system performance at f_{offset} is reexamined in the case of $N_{sb}^{RF} = 3$ in the following. This is simulated by assuming that the weights are calculated with knowledge of the patterns at $f_1 = f_{offset} + BW_{chirp}/6$, instead of $f_0 = f_{offset} + BW_{chirp}/2$, as in **Figure 63**. The performance in **Figure 65** thus applies to the worst-case deviation of the first sub-band. The nominal performance at f_0 is repeated as a reference in the plots for comparison, labeled "center frequency".

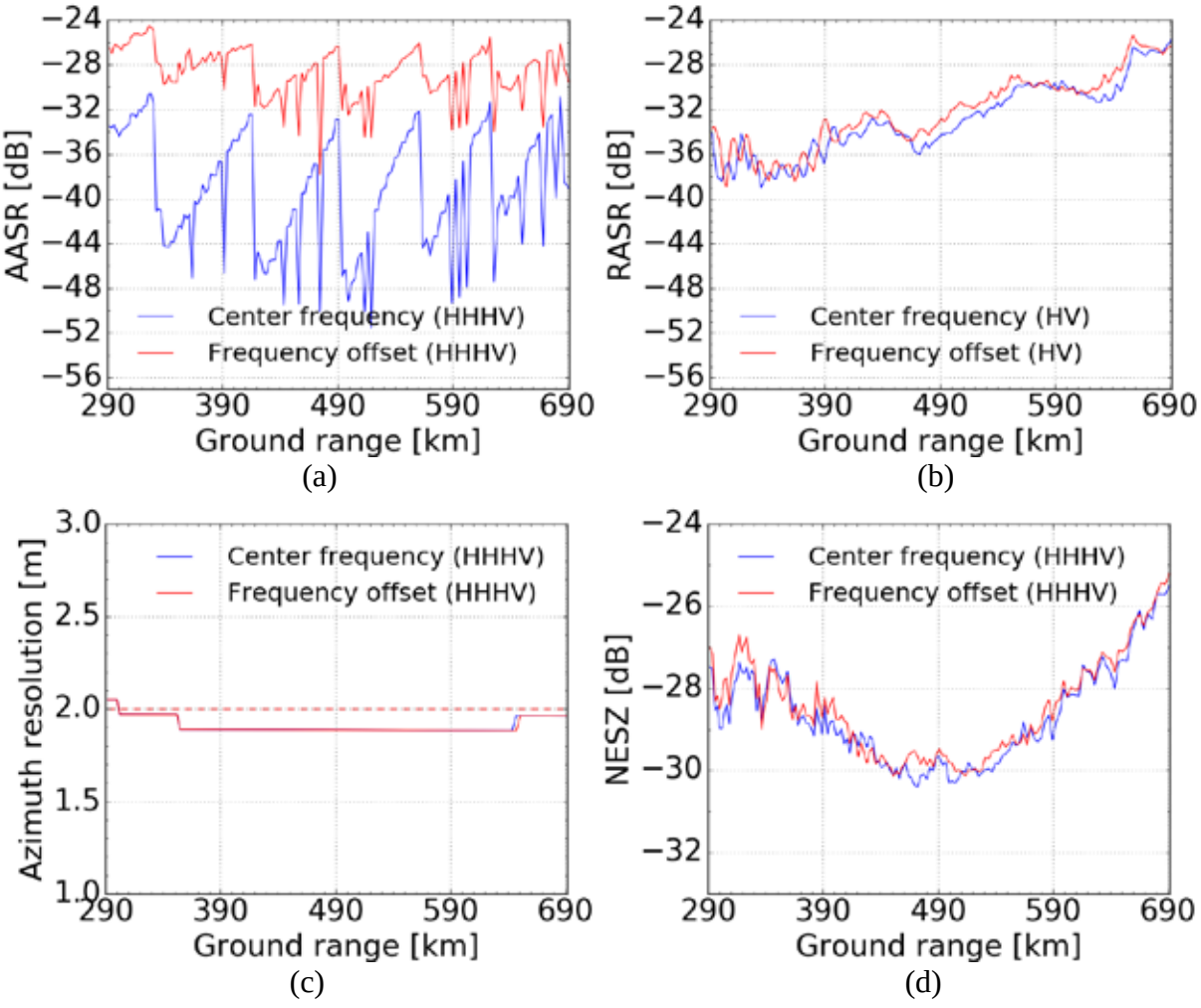

Figure 65. SAR performance with pattern mismatch due to RF frequency offset, assuming 2 RF sub-bands. Example for 2.0 m / 400 km quad-pol multichannel staggered SAR mode using a 18.0 m reflector with 6 azimuth channels (cf. Section 6.3). (a) AASR. (b) RASR. (c) Azimuth resolution. (d) NESZ.

The critical performance parameter, the AASR in **Figure 65 (a)**, achieves a peak level of -24.6 dB. This represents a considerable improvement over the single-band case

and nears the specification of -25 dB. The RASR in **Figure 65 (b)** is similar to the previous case and suffers mostly local oscillations (2.8 dB at most), without changing the worst-case levels over the swath (which rises 0.4 dB, to -25.4 dB). The azimuth resolution in **Figure 65 (c),** as well as the NESZ in **Figure 65 (d)**, do not change considerably.

8.5 Pattern Mismatch due to Mispointing

A final form of deterministic pattern mismatch to be investigated in this section is the one due to mispointing of the patterns in along-track. The aim of the analysis is, as before, to establish an assessment of the sensitivity as a means to the estimation of the hardware and calibration requirements. These are considered as relevant information for analyzing the system feasibility.

The mispointing is this case can be simulated by simply shifting the antenna patterns in azimuth by a deterministic amount. The nominal (shift-free) patterns are used for weight calculation whereas the signal is simulated with the shifted one. The first scenario to be considered is the more sensitive 18.0 m reflector of Section 8.3. The azimuth patterns of the six channels are illustrated in **Figure 66 (a)**.

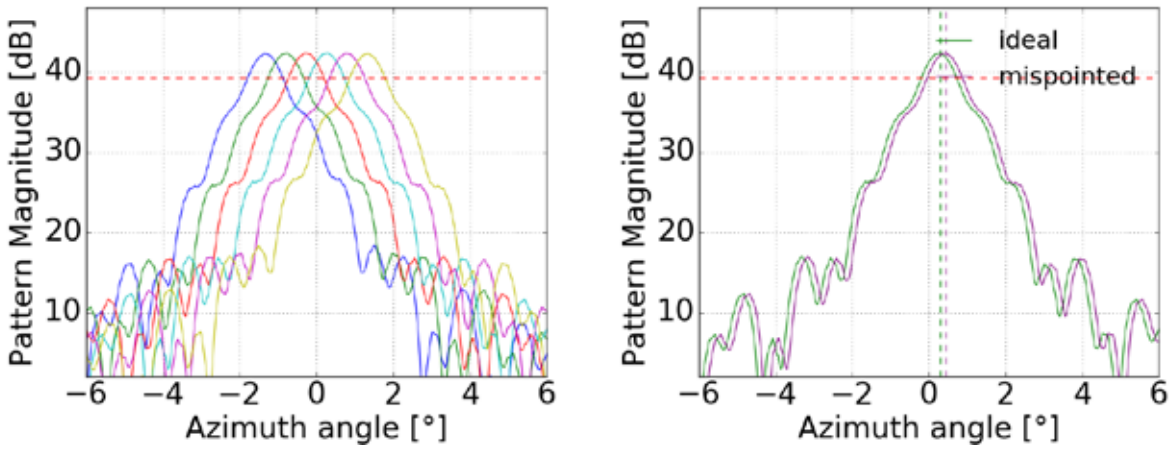

Figure 66. Azimuth patterns and illustration of along-track mispointing, at the range of worst AASR in Section 6.3. (a) Azimuth patterns of the several channels, after elevation DBF. (b) Nominal pattern (green, used for weight calculation) and actual pattern (purple, applied to the simulated data) with mispointing of 75 mdeg.

The red dashed line indicates the 3 dB attenuation line, to give a better perception of their beamwidth, which is of circa 0.9° in this case. The ideal pattern of the forth feed channel and the corresponding pattern mispointed by 75 mdeg is shown in **Figure 66 (b)**, as an example to illustrate the magnitude of the shifts.

The SAR performance as a function of the mispointing of the patterns in the actual manifold with respect to the nominal one is provided in **Figure 67**. Since the patterns are symmetrical with respect to the azimuth angle, it suffices to analyze shifts in a single direction, and positive shifts from zero to 75 mdeg are considered.

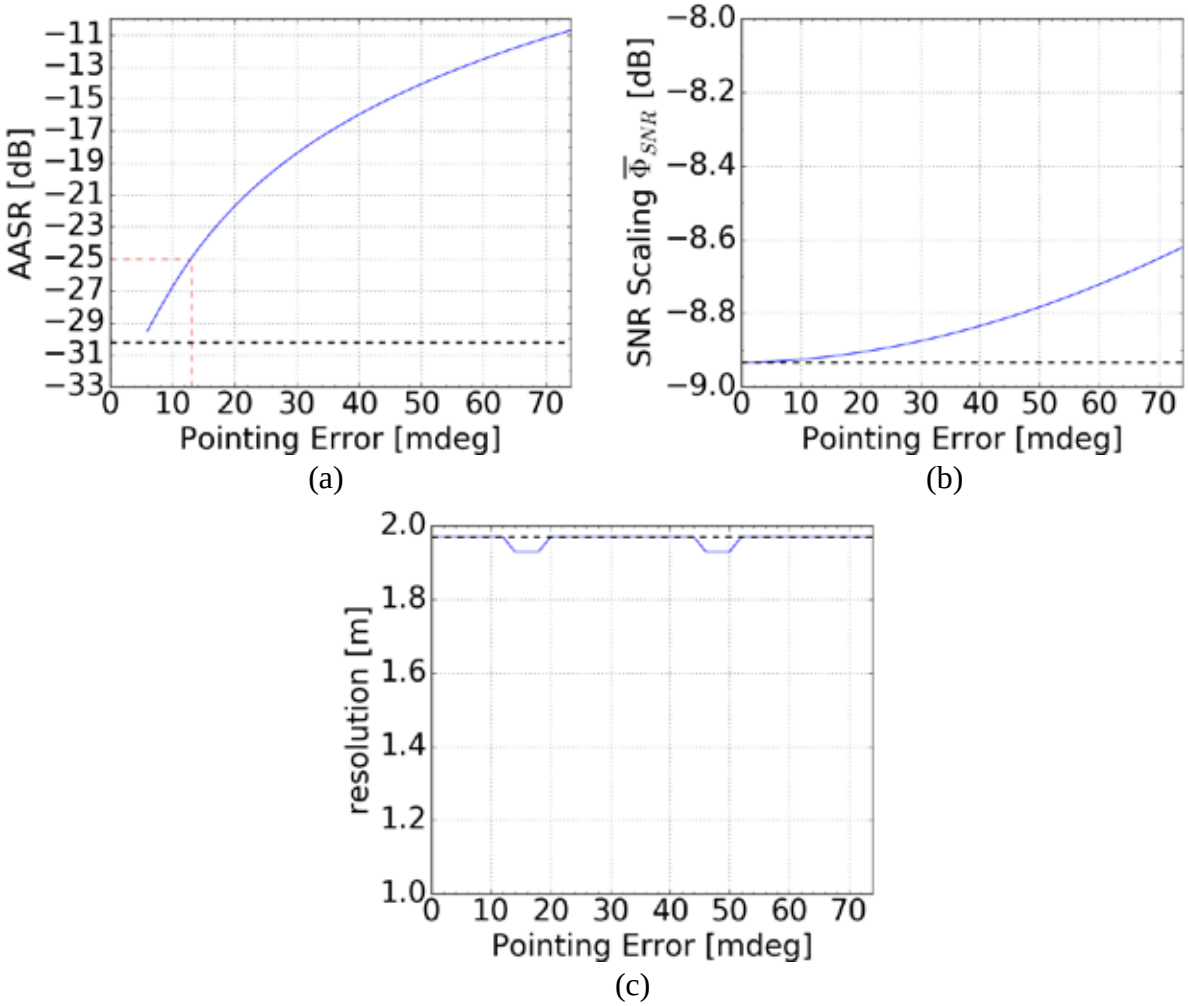

Figure 67. SAR performance with varying level of pattern mispointing in along-track, for the worst-case AASR of the swath in Section 6.3. (a) AASR as a function of mispointing error. (c) Noise scaling $\bar{\Phi}_{SNR}$ of beamformer with nominal weights. (d) Achieved azimuth resolution.

The AASR — the critical performance parameter also for this case — is seen in **Figure 67 (a)** and as expected the levels degrade with increased mispointing, but for a minimum at 2 mdeg which can be attributed to the limited precision of the angle axis. The critical mispointing still allowing the fulfilment of the -25 dB is found to be 13 mdeg. **Figure 67 (b)** shows that the variation of the noise scaling is of less than 0.3 dB over the whole range of shifts, up to 75 mdeg. The azimuth resolution in **Figure 67 (c)** is basically unaffected but for an oscillation which can be traced back to the quantization of the azimuth axis of the simulated signals.

The critical mispointing requirement of 13 mdeg is found to be strict, requiring state-of-the-art calibration schemes, but not necessarily unachievable for near-future systems. An important point for a more in-depth analysis is whether the offset is fixed (due to e.g. the unfurlable reflector's deployment) or time-variant (due to e.g. temperature effects). As a reference value, [125] reports a mispointing accuracy better than 20 mdeg in along-track for the Terra-SAR X [126] system. As mentioned previously in Section 8.4, this system design alternative is especially sensitive to these and other errors affecting the steering of the patterns, due to the larger reflector size (meaning the same angular mispointing error translates into a larger along-track displacement of the illuminated regions over the reflector) and number of channels (which increases the number of error sources).

For comparison, an analogous analysis is performed for the system in Section 6.2.1 in **Figure 68**, leading to a critical mispointing of 75 mdeg in terms of the AASR requirement (cf. **Figure 68 (a)**) for the 15.0 m reflector with 3 channels. In addition to the reduced number of channels, the lower resolution of 3 m in comparison to the 2 m of the previous scenario reduces sensitivity, since a smaller Doppler bandwidth is required. SNR Scaling and azimuth resolution in **Figure 68** (**b)** and **(c)** remain non-critical.

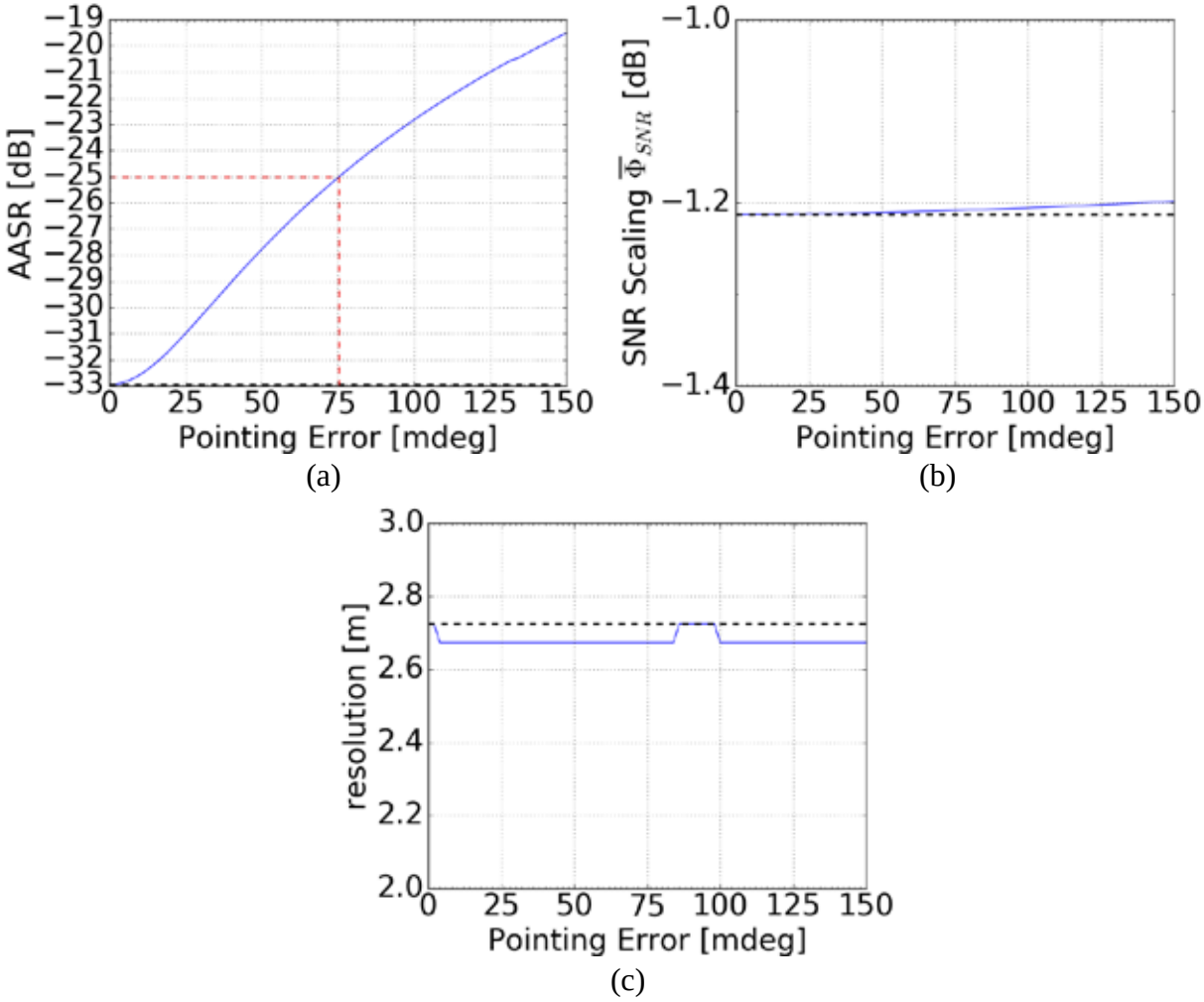

Figure 68. SAR performance with varying level of pattern mispointing in along-track, for the worst-case AASR of the swath in Section 6.2.1. (a) AASR as a function of mispointing error. (c) Noise scaling $\overline{\Phi}_{SNR}$ of beamformer with nominal weights. (d) Achieved azimuth resolution.

8.6 Pattern Mismatch due to Pattern Uncertainty

So far, in Sections 8.2 to 8.5, analyses of deterministic pattern mismatches from different sources have been performed. In this section, focus is turned to a random form of pattern mismatch. The goal is to establish a first estimation of the tolerable degree of pattern mismatch, in order to keep the performance within certain bounds. The results represent a first step towards requirements of pattern measurement accuracy and calibration. This analysis is of great importance for the feasibility of the

on-board resampling approach, (investigated in Section 6.5 in terms of the computational load and memory requirements) since the resampling and broadcast to ground with limited data rate severely limits the possibility of compensating channel imbalances once the data is acquired. In the worst case, should the pattern characterization/calibration requirements prove unfeasibly strict, the broadcast to ground might prove the only option to attain the expected performance, implicating the need to cope with the high data rates shown in Section 6.5. Should they however be within the bounds achievable by a calibration network and/or calibration data acquisition strategy, the cost and complexity of the calibration concept should be weighed against the benefits from the data reduction. In a best-case scenario, non-critical calibration requirements add to the feasibility of the on-board implementation option, attractive in terms of data rate. In any case, this aspect is one of the drivers of the design of future implementation options of such systems.

To characterize the uncertainty in the patterns, which accounts for the combine effect of measurement and residual calibration errors, the model illustrated in **Figure 69** is adopted. The measured antenna pattern (derived from voltage measurements) deviates from the ideal value s_0 by an error of magnitude ϵ_0 (in this case taken as a parameter, related to the noise level) and a random uniform phase. Note that s_0 is a complex quantity, even though represented in the figure with a phase reference of 0.0°. The resulting maximum phase error is given by $\Delta\theta = \arcsin(\epsilon_0 / s_0)$.

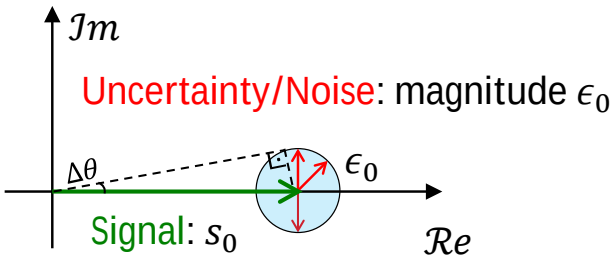

Figure 69. Schematic representation of the error model, which assumes measurement of the deterministic signal phasor s_0 with an error of magnitude ϵ and random phase.

The uncertainty model is applied to the antenna patterns by adding to the *nominal* (error-free) antenna pattern $G_{nom}(f_\mathrm{D})$ (used for weight calculation) a noise term of magnitude described by the normalized noise floor parameter

$$\epsilon = \frac{\epsilon_0}{\max\|G_{nom}(f_\mathrm{D})\|}, \tag{157}$$

which describes the magnitude (in terms of voltage) of the complex errors with respect to the pattern maximum. The addition forms an *actual* antenna pattern $G_{actual}(f_D)$ (used for signal simulation), given by

$$G_{actual}(f_D) = G_{nom}(f_D) + \epsilon \cdot \exp\big(\mathrm{j} \cdot \phi_{uni}(f_D)\big), \tag{158}$$

where $\phi_{uni}(f_D)$ is a random phase uniformly distributed in $[-\pi, \pi]$. Note that a different noise realization is taken for each Doppler frequency. Following this approach, the initial voltage-based error model is translated into an error in the antenna pattern's measurements.

Since the uncertainty is described by the parameter ϵ (which can be interpreted as e.g. a measurement noise floor), normalized by the *maximum* pattern magnitude, the resulting amplitude and phase errors are dependent on the local magnitude of $G_{actual}\ (f_D\ )$. This is illustrated in **Figure 70** for the system in Section 6.3 (cf. TABLE VI), taking the azimuth patterns in the center of the swath (after elevation DBF) as an example.

Figure 70 (a) shows the nominal patterns for all 6 channels and **Figure 70 (b)** the assumed actual patterns, which are disturbed by noise with $20 \cdot \log(\epsilon) = -30$ dB, added independently between channels. The resulting magnitude and phase errors are seen in **Figure 70 (c)** and **Figure 70 (d)**, respectively. Only the two central elements are shown, to improve visibility. Clearly, the error levels in the main beam are smaller than in the sidelobe area, where the SNR degrades due to the reduced pattern gain.

This is considered a desirable property of the error model, in terms of reproducing the expected behavior of real-world measurements.

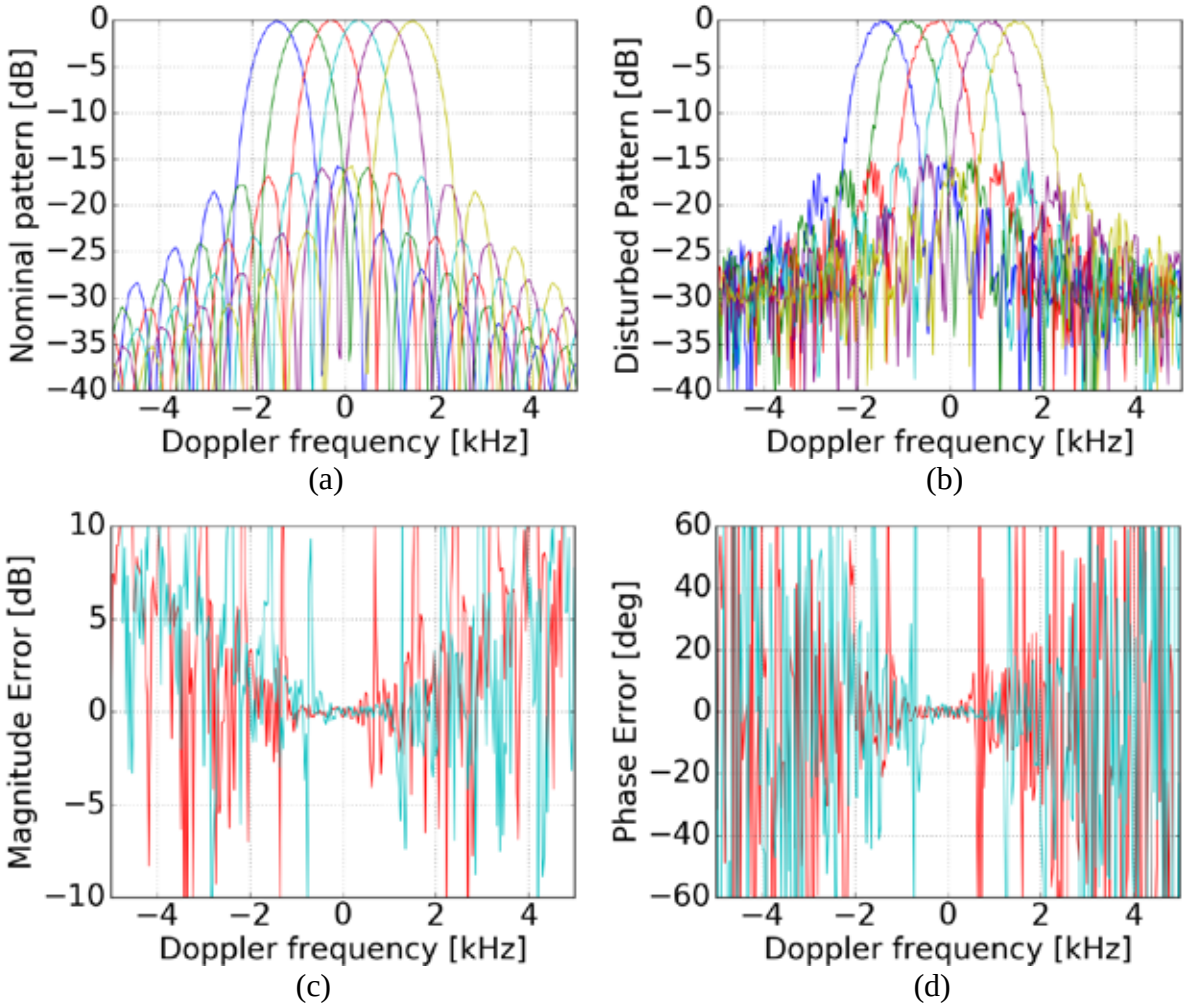

Figure 70. Pattern uncertainty model applied to azimuth patterns of the 6 channel system of Section 6.3. (a) Nominal patterns of all channels. (b) Actual patterns, disturbed by noise/uncertainty of magnitude $20 \cdot \log(\epsilon) = -30$ dB. (c) Magnitude error for two central elements. (d) Phase error for two central elements.

To characterize the sensitivity to the pattern uncertainty, we resort to a Monte Carlo simulation, as described in the block diagram of **Figure 71**.

The parameter ϵ is varied and several realizations of the uniform phase $\phi_{uni}(f_D)$ and thus of the noise are considered for each value. Each of them introduces a mismatch between the signal (simulated with $G_{actual}\ (f_D\ )$) and the DBF weights (calculated for

$G_{nom}(f_D)$), reflecting limited knowledge of the patterns. Once the resampling is done, the AASR, noise scaling and azimuth resolution are measured for the particular realization and an average over realizations forms an estimation of the expected value for each performance index.

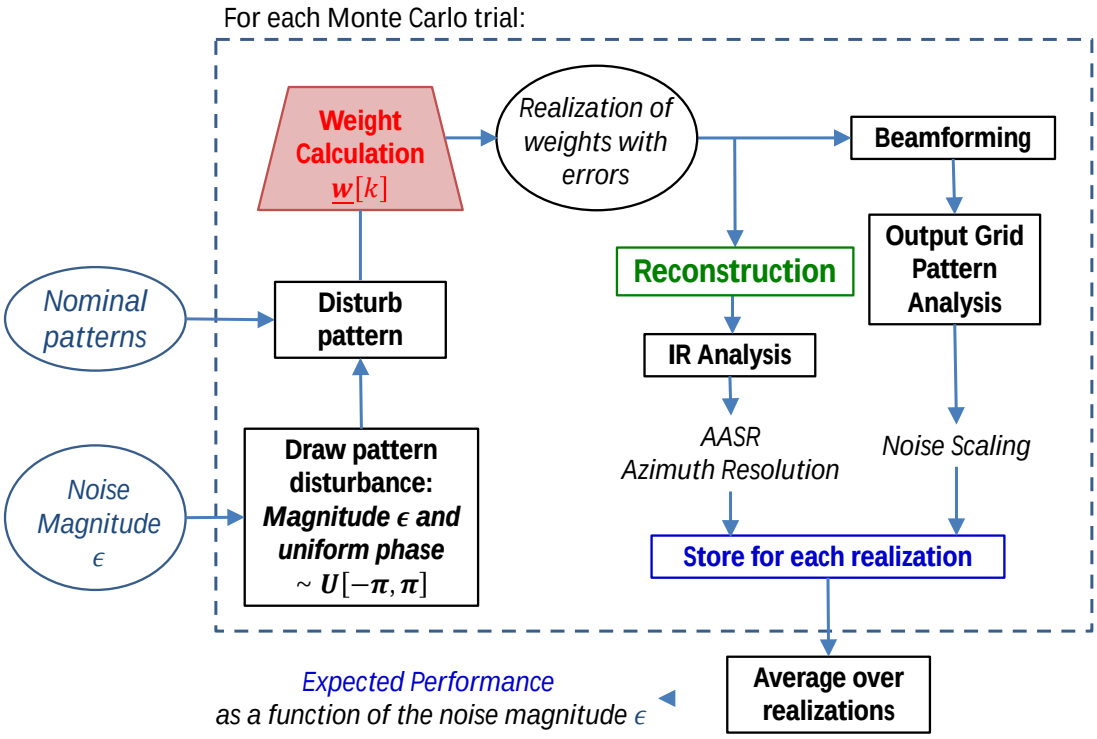

Figure 71. Block diagram of Monte Carlo simulation of errors due to uncertainty/noise magnitude ϵ. The procedure is repeated over a range of values of ϵ to characterize the sensitivity to this parameter.

In a first scenario, the position of lowest AASR within the swath in Section 6.3 is considered. This illustrates a case with very low error-free AASR (cf. **Figure 45**), reaching -51.0 dB. The parameters of TABLE VI apply. The results of the Monte Carlo simulation are depicted in **Figure 72**, for which 128 noise realizations are averaged at each level of the noise/uncertainty floor ϵ. **Figure 72 (a)** shows the AASR as a function of ϵ, and **Figure 72 (b)** the same curve as a function of the maximum main beam phase error $\Delta\theta(\epsilon) = \arcsin(\epsilon)$. The AASR values are seen to rise quickly from the nominal value (indicated by a dashed line), even for small errors. The

performance goal of -25 dB is achieved for $20 \cdot \log(\epsilon) \leq -29.1$ dB [36], or correspondently $\Delta\theta(\epsilon) \leq 2.0°$.

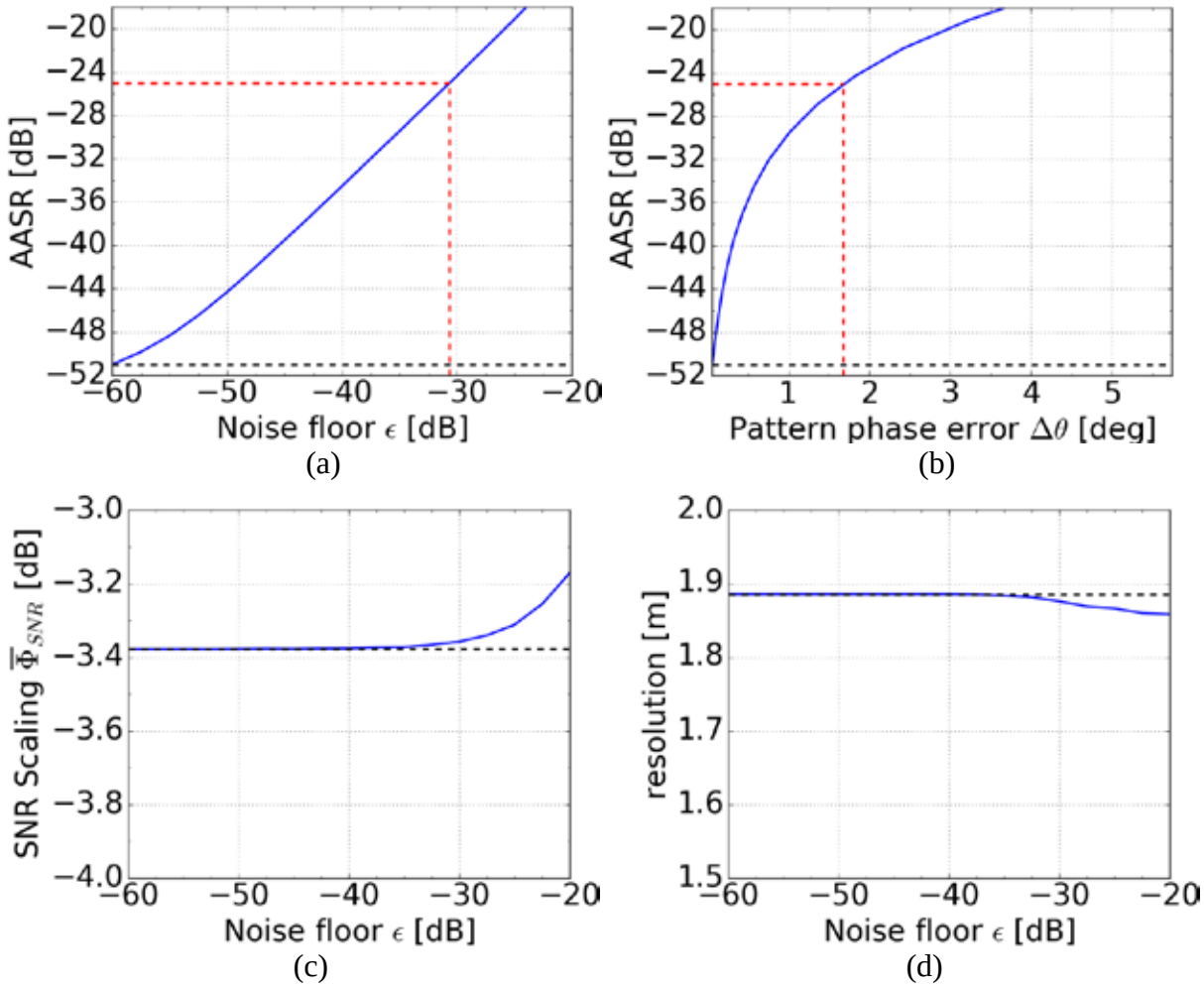

Figure 72. Monte Carlo simulation (128 realizations) of pattern uncertainty, with varying level of uncertainty ϵ, for the signal at the best-case AASR level in Section 6.3. (a) AASR as a function of ϵ. (b) AASR as a function of main beam phase error $\Delta\theta(\epsilon)$. (c) Noise scaling $\overline{\Phi}_{SNR}$ of beamformer with nominal weights. (d) Achieved azimuth resolution.

As indicated in **Figure 72 (c)**, the noise scaling $\overline{\Phi}_{SNR}$ is more robust to errors. The maximum deviation is less than 0.2 dB for $20 \cdot \log(\epsilon) \leq -20$ dB, and visible deviations from the nominal value of -3.38 dB (dashed line) are only seen for errors above $20 \cdot \log(\epsilon) > -35$ dB, for which the AASR requirement is already violated.

[36] Recall that the parameter ϵ has units of normalized field streng/voltage, so that noise power is proportional to $20 \cdot \log(\epsilon)$.

The variation of the azimuth resolution in **Figure 72 (d)** follows a similar behavior, leading to the conclusion that the AASR is the most sensitive and driving factor in terms of pattern uncertainty.

A second scenario is considered to illustrate the behavior starting from a higher error-free AASR. The range position with the highest AASR within the swath in Section 6.3, (cf. **Figure 45**) with AASR = -30.2 dB, is chosen. **Figure 73 (a)** and **Figure 73 (b)** illustrate the AASR degradation with increasing errors, which is less sensitive at the start (below -50 dB) due to the higher initial values.

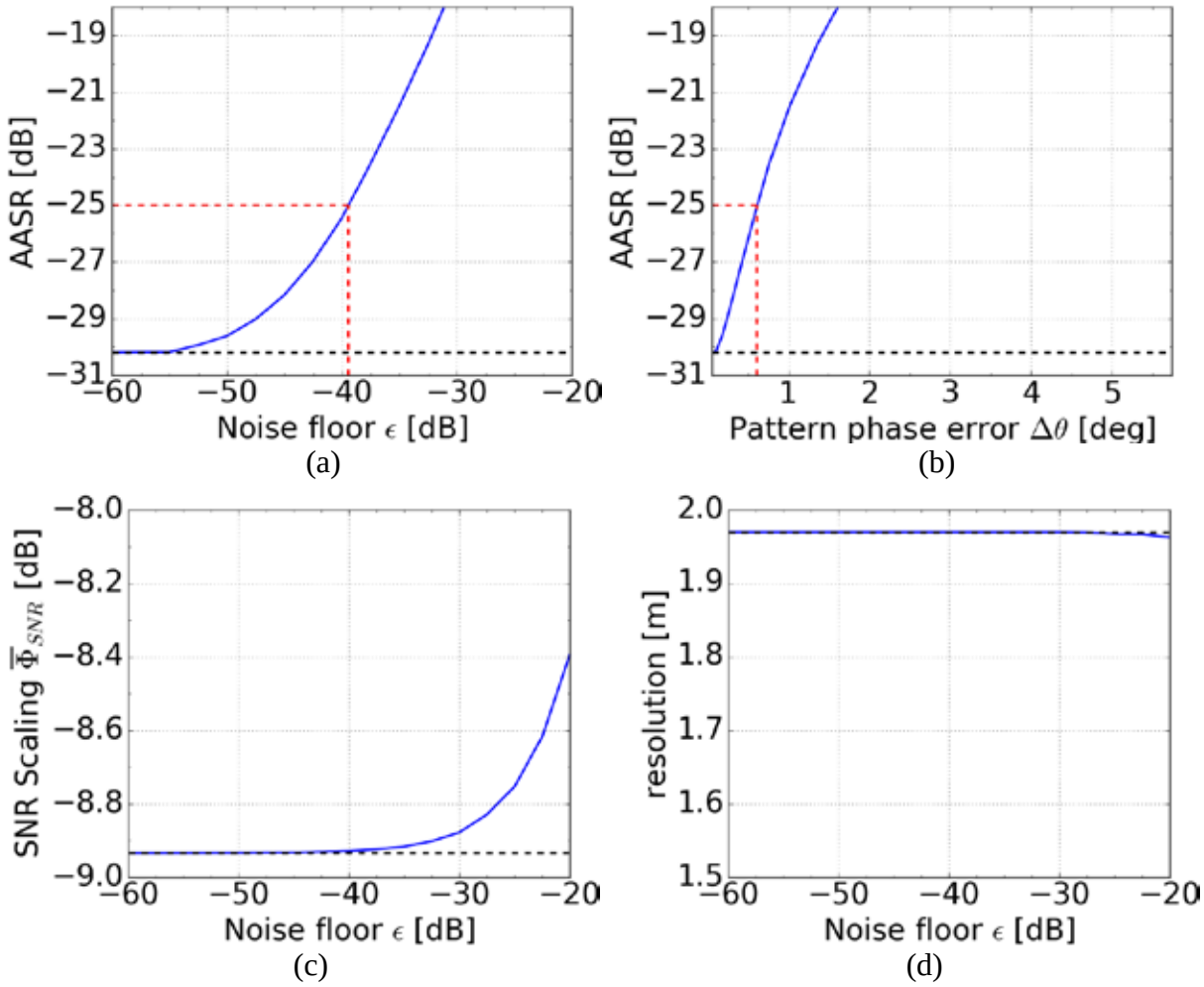

Figure 73. Monte Carlo simulation (128 realizations) of pattern uncertainty, with varying level of uncertainty ϵ, for the worst-case AASR of the swath in Section 6.3. (a) AASR as a function of ϵ. (b) AASR as a function of main beam phase error $\Delta\theta(\epsilon)$. (c) Noise scaling $\overline{\Phi}_{SNR}$ of beamformer with nominal weights. (d) Achieved azimuth resolution.

The critical error level which still allows the achievement of the performance goal of -25 dB is $20 \cdot \log(\epsilon) \leq -40.4$ dB or correspondently $\Delta\theta(\epsilon) \leq 0.6°$, which is more stringent than the previous case. This indicates that this scenario does not only show higher initial levels but is also more sensitive, owing to the patterns and the sampling configuration. Analogously to **Figure 72**, the noise scaling $\overline{\Phi}_{SNR}$ in **Figure 73 (c)** and the resolution in **Figure 73 (d)** show lower sensitivity to the errors than the AASR.

A final scenario is considered to compare the derived pattern calibration requirements between different system designs in **Figure 74**.

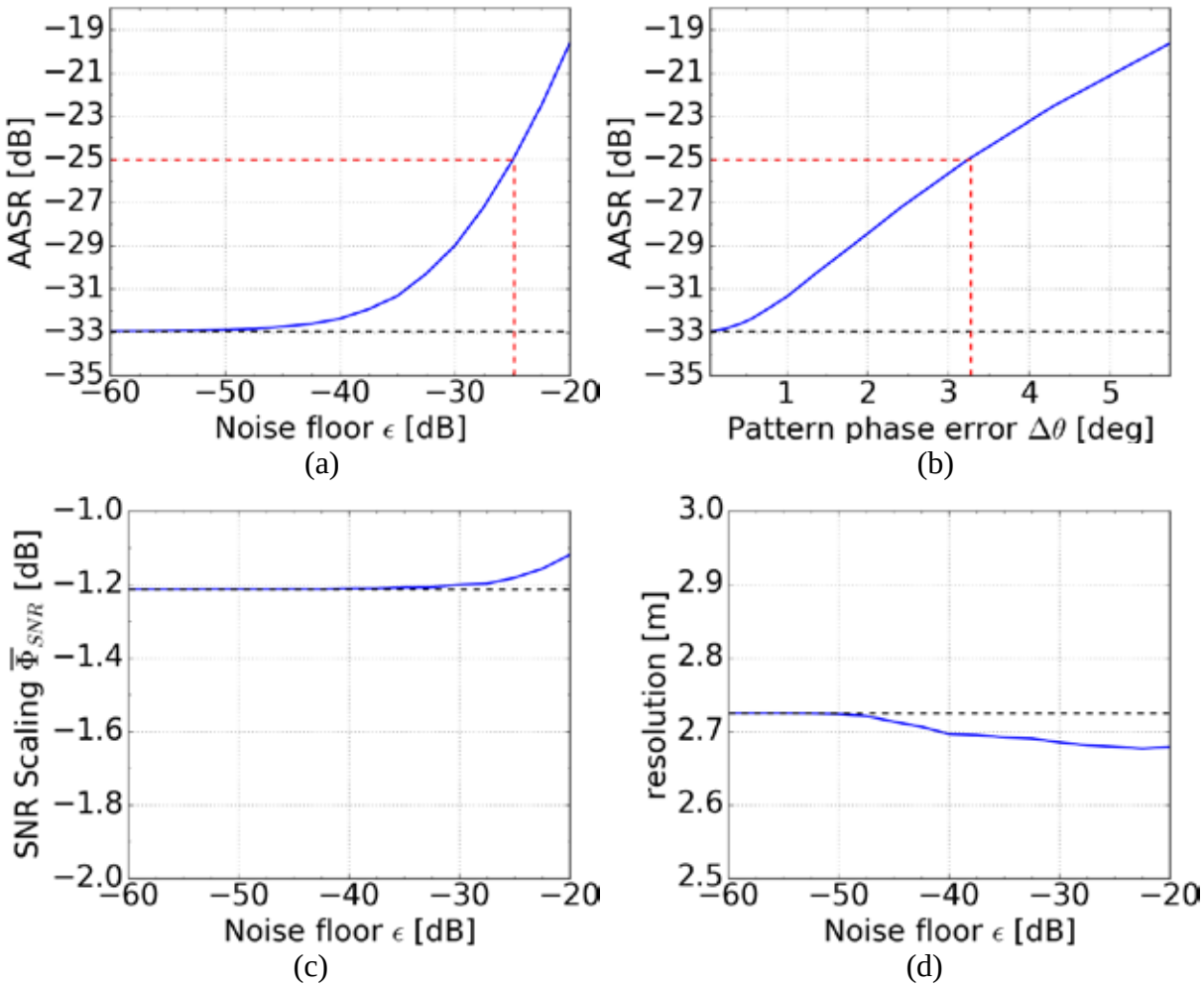

Figure 74. Monte Carlo simulation (128 realizations) of pattern uncertainty, with varying level of uncertainty ϵ, for the worst-case AASR of the swath in Section 6.2.1. (a) AASR as a function of ϵ. (b) AASR as a function of main beam phase error $\Delta\theta(\epsilon)$. (c) Noise scaling $\overline{\Phi}_{SNR}$ of beamformer with nominal weights. (d) Achieved azimuth resolution.

The single-pol system of Section 6.2.1 (350 km swath with 3.0 m resolution using a 15.0 m reflector) is chosen as a last example. The worst-case AASR of the swath, the critical case seen for the previous system, is analyzed. The AASR seen in **Figure 74 (a)** and **(b)** has an error-free level of -32.9 dB and shows critical error levels (still allowing the achievement of the performance goal of -25 dB) of $20 \cdot \log(\epsilon) \leq -24.9$ dB or $\Delta\theta(\epsilon) \leq 3.3°$. The behavior of the noise scaling and azimuth resolution in **Figure 74 (c)** and **(d)**, respectively, remains as expected non-critical. The estimated calibration requirements are thus considerably less strict than in the previous scenario, as discussed (cf. Section 8.4) the most sensitive one, due to the element spacing, the reflector size and the number of channels.

8.7 Effect of Phase and Amplitude Errors on Weights

So far, in Sections 8.2 to 8.6, different sorts of mismatches in the model describing the signal (related to the antenna patterns) were considered. All of those lead to wrong assumptions in the design of the weights and consequently performance degradation. In this section, however, a final form of mismatch is investigated which is related to limitations in the *implementation* of the weights, rather than their design. The goal is to consider the effect of limited precision in the amplification and phase shifting of the signals required to implement in practice the (flawlessly designed) weights. This accounts, for instance, for the limited precision in the amplitude and phase applied by TR-modules, and also drits in the hardware. These errors are not a function of f_{D}.

The error model is described in the following. Assume N_{ch} channels and thus TR-modules exist, each of which shows an amplitude error ϵ_k and a phase error ϕ_k such that, given an input complex coefficient w_{TRM} and an input signal $s_{in}(t)$, the actual output is

$$u_{out}(t) = (1 + \epsilon_k) \cdot u_{in}(t) \cdot \exp(\mathrm{j} \cdot \phi_k), \qquad 1 \leq k \leq N_{ch}; \tag{159}$$

which means that the coefficient that the TR-module actually applies to the signal is $(1 + \epsilon_k) \cdot \exp(\mathrm{j} \cdot \phi_k) \cdot w_{TRM}$.

The errors are assumed to be independent between channels and identically distributed, with $\epsilon_k \sim N(0, \sigma_\epsilon^2)$, i.e., zero-mean Gaussian with standard deviation σ_ϵ, and $\phi_k \sim U\left(\frac{-\xi_u}{2}, \frac{\xi_u}{2}\right)$, uniformly distributed in the interval $\left[-\frac{\xi_u}{2}, \frac{\xi_u}{2}\right]$.

It should be recalled that the beamformer combines the N_{ch} channels over N_p pulses in azimuth (cf. Section 4.4.1), using in total $N_{win} = N_{ch} \cdot N_p$ input samples. Thus, for a given set of (error-free) complex weights $\underline{\boldsymbol{w}}$ of dimension N_{win} and entries $w[i]$, the disturbed set of weights $\underline{\boldsymbol{w}}_{error}$ has entries

$$w_{error}[i] = \left(1 + \epsilon_{i \bmod N_{ch}}\right) \cdot w[i] \cdot \exp\left(\mathrm{j} \cdot \phi_{i \bmod N_{ch}}\right), \qquad 1 \le i \le N_{win}; \qquad (160)$$

which means that the errors are assumed to be the stable over time (the pulses) within the window of length N_p but to vary between channels. The model thus describes a (possible slowly varying) residual bias for each TR-module[37].

As in the previous section, the impact of the errors on the resampling is assessed by means of a Monte Carlo simulation, which is described in the block diagram of **Figure 75**.

Starting from an error-free weight vector $\underline{\boldsymbol{w}}$, the parameters of the error distributions ξ_u or σ_ϵ (for clarity, amplitude and phase errors are analyzed separately in the following) are varied and, for each value, several realizations are drawn from the appropriate distributions to calculate $\underline{\boldsymbol{w}}_{error}$. The resampling is performed for each realization and the average of the performance indices (AASR, noise scaling and azimuth resolution, as before) over them is used to estimate their expected values.

[37] Even though aimed at describing the TR-module behavior, the model can also be used to describe channel imbalances limited to a constant gain and phase offset between the N_{ch} channels. The results of the analysis therefore also apply to this case.

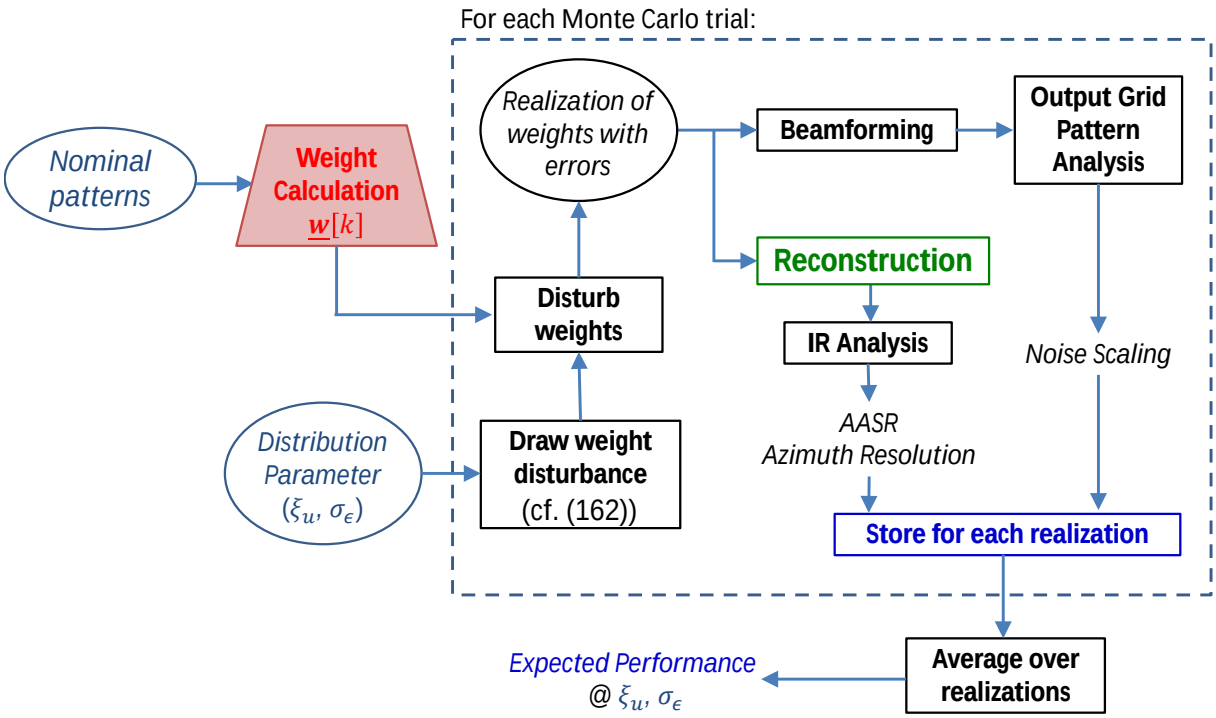

Figure 75. Block diagram of Monte Carlo simulation of errors due to amplitude and phase noise for weight realization (e.g. due to TRMs). The procedure is repeated over a range of values of (ξ_u, σ_ϵ) to characterize the sensitivity to these parameters.

The analysis starts with the scenario of worst-case performance of the larger 18.0 m reflector system of Section 6.3., which was found to be the most sensitive to mismatches. **Figure 76** illustrates the results of the Monte Carlo simulation with varying amplitude error levels σ_ϵ (up to 10%) and ξ_u = 0. For each value of σ_ϵ, represented in percentage with respect to the maximum amplitude of the error-free weights, 128 realizations of the Gaussian disturbances ϵ_k are drawn. **Figure 76 (a)** shows the histograms of the achieved AASR over the realizations, for example values of σ_ϵ. A black vertical line highlights the error-free AASR of -30.2 dB. The histogram for very low disturbances (σ_ϵ = 0.1%) shows a bimodal behavior, indicating some difficulties in the numerical AASR evaluation. These are however not critical for the current analysis, which focuses on higher error levels. The migration of the histograms towards higher AASR with increasing error levels highlights the performance degradation, as expected. The expected AASR levels (average over realizations) are

seen in **Figure 76 (b)**. The requirement of AASR less than -25 dB is satisfied up to σ_ϵ = 2.1%. The noise scaling in **Figure 76 (c)** and the azimuth resolution in **Figure 76 (d)** are seen not to be severely affected by weights errors in the range σ_ϵ < 10%.

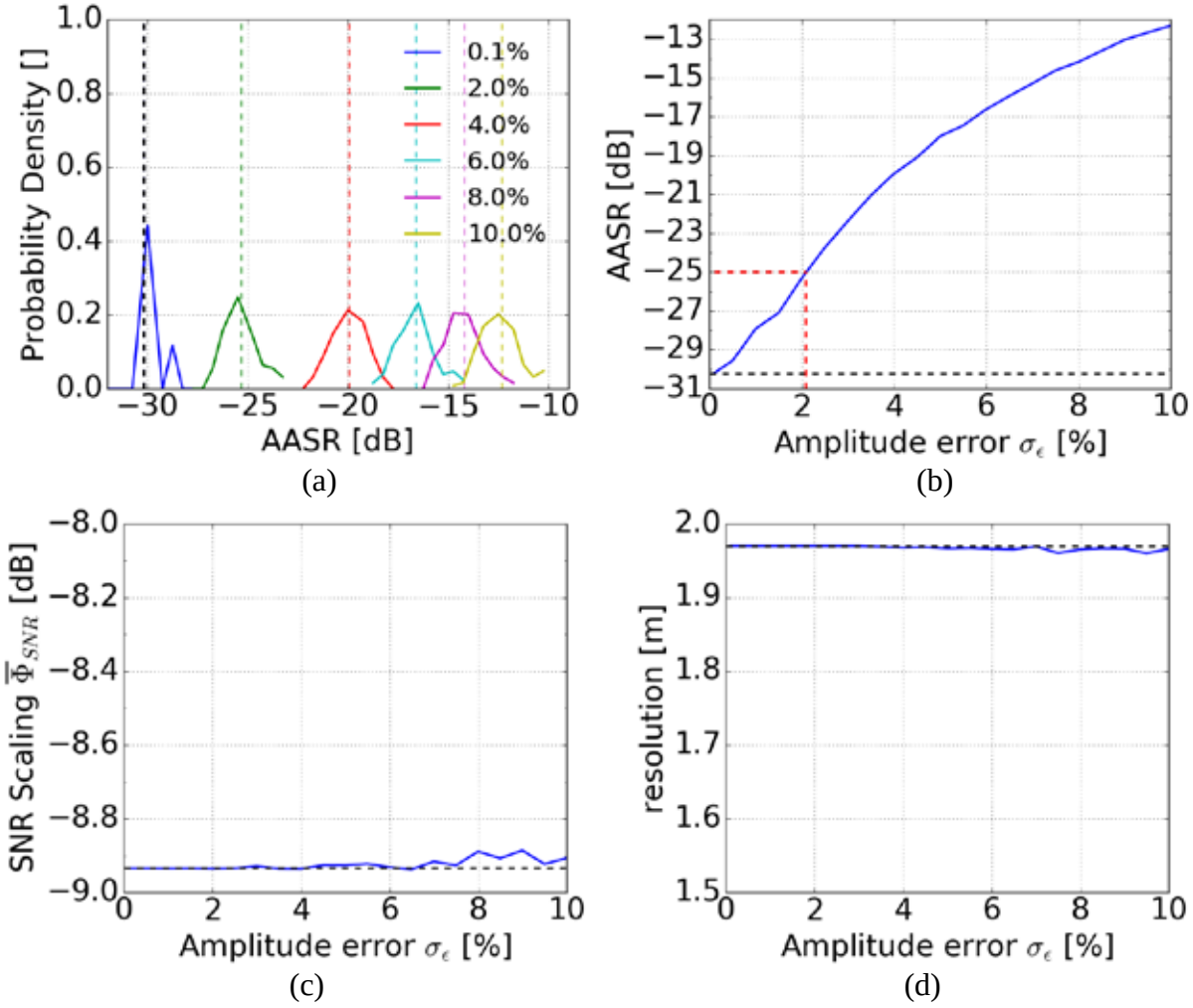

Figure 76. Monte Carlo simulation (128 realizations) of weight errors, with varying level of amplitude error variance σ_ϵ, for the worst-case AASR of the swath in Section 6.3. The error-free value is -30.2 dB. (a) Example histograms of AASR over the realizations, parametrized by σ_ϵ. (b) AASR expectation as a function of σ_ϵ. (c) Noise scaling $\overline{\Phi}_{SNR}$ of beamformer with weight errors. (d) Achieved azimuth resolution.

Figure 77 in turn illustrates the effect of increasing phase error distribution ranges ξ_u (up to 20°), fixing σ_ϵ = 0. The Monte Carlo simulation is performed with 128 realizations of the uniform phase disturbances ϕ_k. **Figure 77 (a)** shows the histograms

of the achieved AASR over the realizations whereas **Figure 77 (b)** shows the expected AASR value.

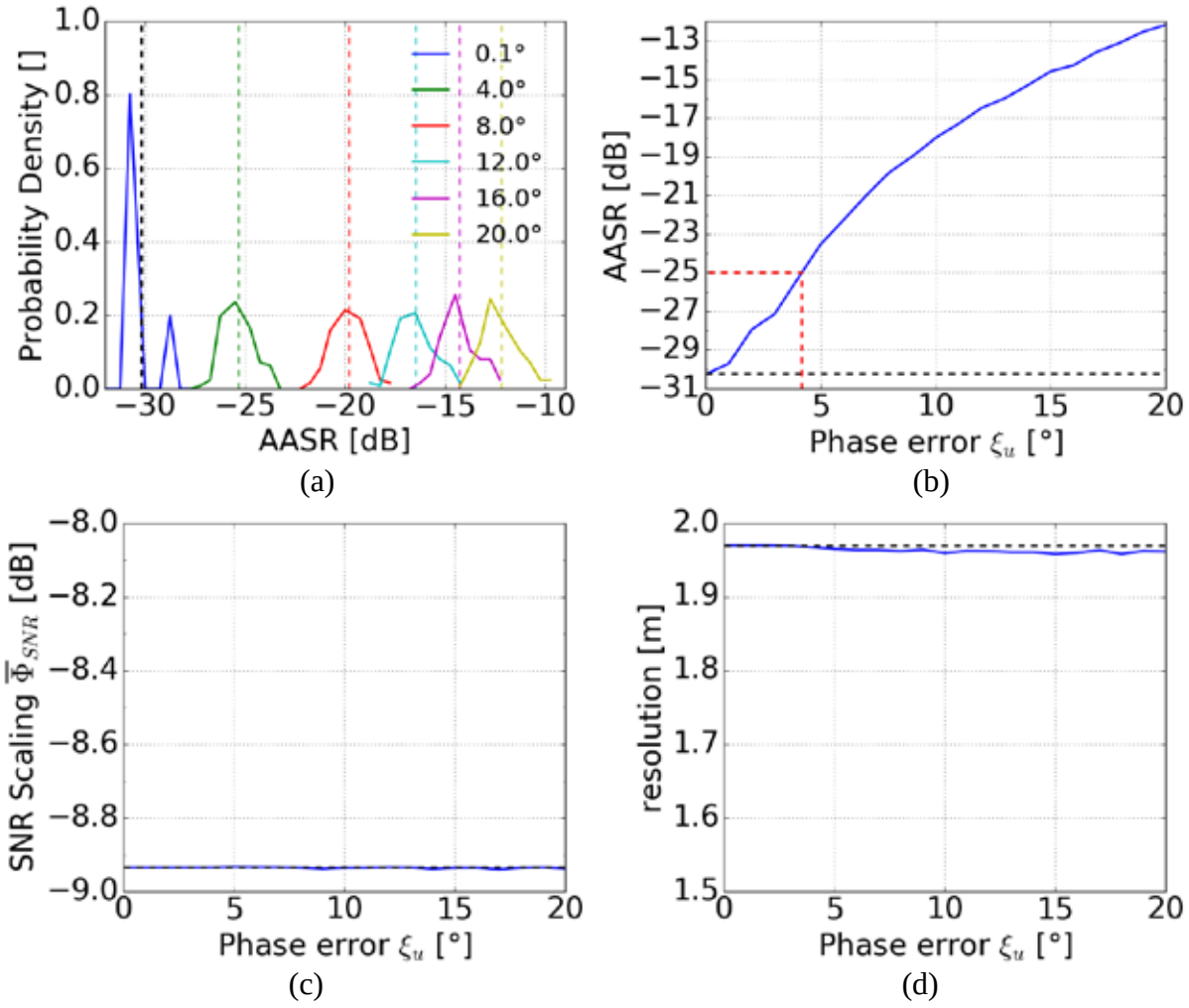

Figure 77. Monte Carlo simulation (128 realizations) of weight errors, with varying level of phase error range ξ_u, for the worst-case AASR of the swath in Section 6.3. The error-free value is -30.2 dB. (a) Example histograms of AASR over the realizations, parametrized by ξ_u. (b) AASR expectation as a function of ξ_u. (c) Noise scaling $\overline{\Phi}_{SNR}$ of beamformer with weight errors. (d) Achieved azimuth resolution.

In this case, the requirement of AASR less than -25 dB is satisfied up to ξ_u = 4.2°, meaning the TR-module's phase is subject to noise within $[-2.1, 2.1]°$. The noise scaling in **Figure 77 (c)** and the azimuth resolution in **Figure 76 (d)** are fairly insensitive to the errors within the analyzed range.

A similar analysis for the 15.0 m reflector system of Section 6.2.1 is provided next in **Figure 78** and **Figure 79**.

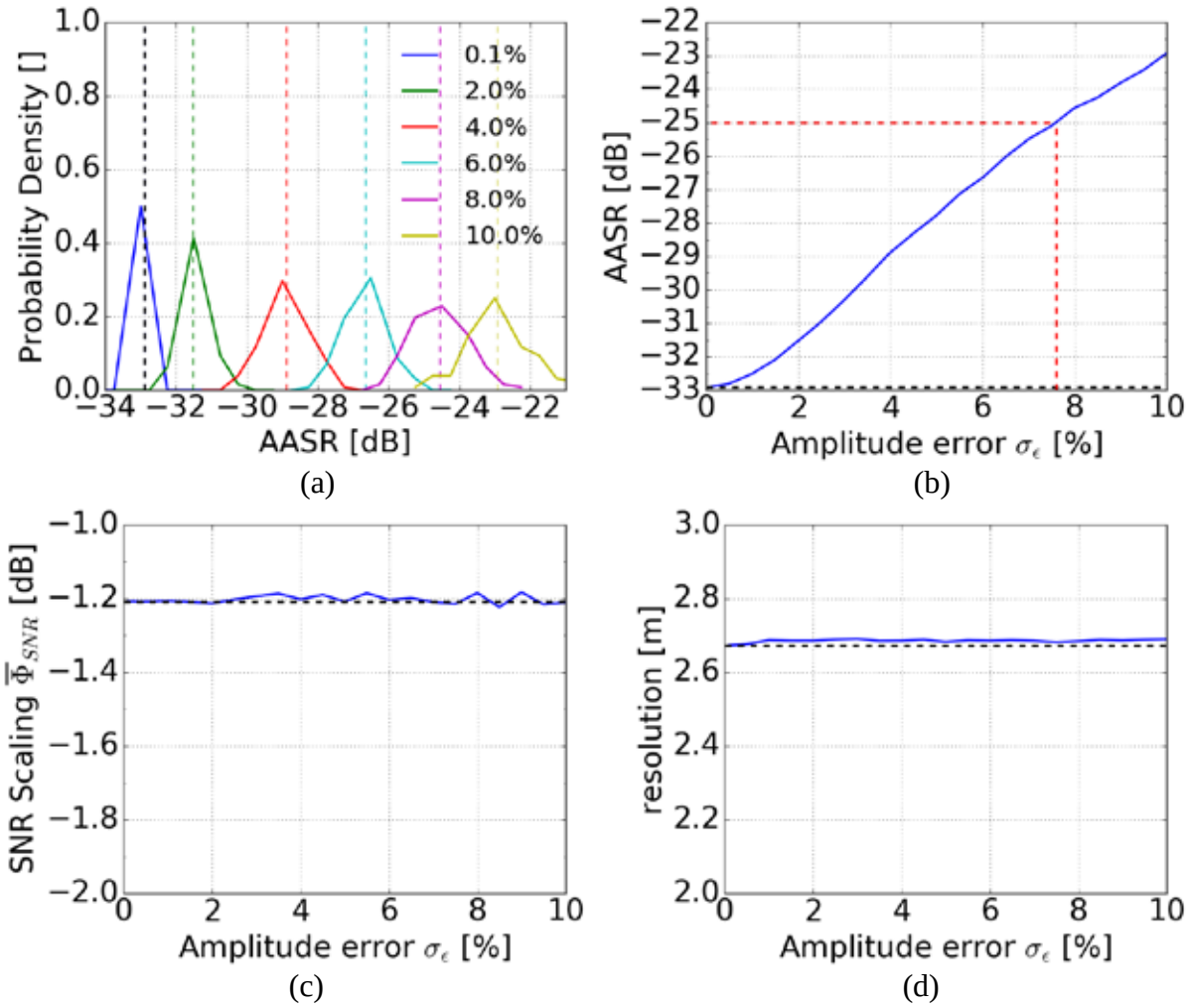

Figure 78. Monte Carlo simulation (128 realizations) of weight errors, with varying level of amplitude error variance σ_ϵ, for the worst-case AASR of the swath in Section 6.2.1. The error-free value is -32.9 dB. (a) Example histograms of AASR over the realizations, parametrized by σ_ϵ. (b) AASR expectation as a function of σ_ϵ. (c) Noise scaling $\overline{\Phi}_{SNR}$ of beamformer with weight errors. (d) Achieved azimuth resolution.

The former shows increasing amplitude errors with σ_ϵ up to 10% and ξ_u = 0° (analogous to **Figure 76**), whereas the latter shows increasing phase errors with ξ_u up to 20° and σ_ϵ = 0 (analogous to **Figure 77**). In this scenario, the error-free AASR level is of -32.9 dB and the critical error levels still satisfying the -25 dB requirement

are $\sigma_\epsilon \leq 7.6\%$ and $\xi_u \leq 14.9°$ (cf. **(b)**). The SNR Scaling and resolution, as before, are not severely affected by the errors.

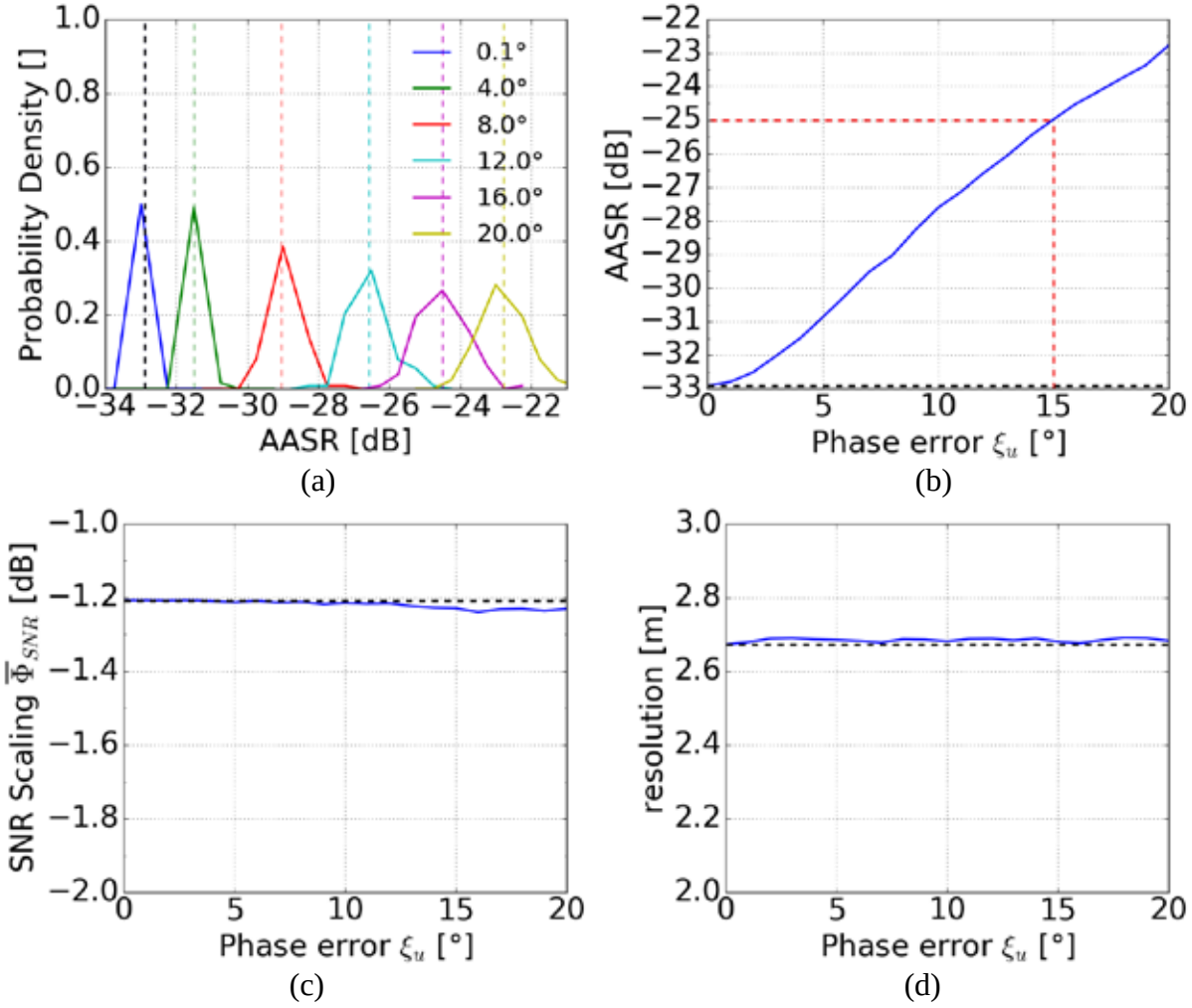

Figure 79. Monte Carlo simulation (128 realizations) of weight errors, with varying level of phase error range ξ_u, for the worst-case AASR of the swath in Section 6.2.1. The error-free value is -32.9 dB. (a) Example histograms of AASR over the realizations, parametrized by ξ_u. (b) AASR expectation as a function of ξ_u. (c) Noise scaling $\overline{\Phi}_{SNR}$ of beamformer with weight errors. (d) Achieved azimuth resolution.

8.8 Remarks on the Analysis of Error and Mismatches

This chapter addressed the effect of wrong assumptions in the calculation and implementation of the Virtual Beam Synthesis weights (cf. Section 4.4), which degrade the

performance with respect to the expected error-free values. Sections 8.2 to 8.6 assumed the signal is acquired with actual patterns different from the nominal ones used for weight design. The mismatch is deterministic up until Section 8.5, whereas the last analysis considers a Monte Carlo approach. Section 8.7 considers a different effect, assuming the weight implementation accuracy is limited by TR-module phase and amplitude fluctuations, even for perfectly designed weights.

Comparing the results of the sensitivity analysis, it is clear that in all cases the AASR is the critical performance parameter, whereas SNR Scaling and azimuth resolution are fairly insensitive to the investigated errors. In Sections 8.2 to 8.4, the approach was to simulate the performance obtained with the respective mismatch (pulse extension, number of coefficients and RF bandwidth) expected from the parameter in Chapter 6. All the error sources are thus deterministic and take fixed values. The effect of the pulse bandwidth (Section 8.4) was found to be most severe, and division into three RF-subbands was required for compliance with the requirements in the case of the 18.0 m reflector in quad-pol operation (cf. Section 6.3). This was not necessary for the 15.0 m reflector in single-pol (cf. Section 6.2.1), but this effect still led to the greatest performance degradation. The effect of the limited update of pattern of elevation (cf. Section 8.3) is in comparison of minor influence, whereas the pulse extension effects (cf. Section 8.2) showed an intermediate behavior. An overview of the results is provided in TABLE XII.

In Sections 8.5 to 8.7, the approach changed in that a sweep of the quantities parametrizing the errors was performed within a range of values, to derive the critical levels still allowing compliance with the requirements. Focus was turned to the AASR, found to be the most sensitive aspect of the performance. Mispointing (cf. Section 8.5) is treated deterministically and was found to play a relevant role, suggesting certain system configurations (especially the larger 18.0 m reflector case) may lead to demanding pointing requirements. The remained sections modelled errors in a statistical sense. Accurate knowledge of the patterns was found to be of crucial importance, as the uncertainty modeled in Section 8.6 showed the potential to severely degrade the expected performance. The effect of weight errors in Section 8.7 is in comparison less critical. The results are summarized in TABLE XIII.

TABLE XII
OVERVIEW AND COMPARISON OF IMPACT OF MISMATCH SOURCES

Mismatch source	Section	Possible compensation/ Implications	Severity	System design example	Nominal/degraded worst-case AASR
Pulse extension	8.2	Reduce pulse length or apply frequency-dispersive DBF [46]	Medium	6.2.1	-32.9 dB → -28.6 dB (4.3 dB worsening)
Limited update over range	8.3	Store more coefficients on board	Minor	6.2.1	-32.9 dB → -32.6 dB (0.25 dB worsening)
Pulse RF bandwidth	8.4	Divide signal into RF sub-bands and adapt weights	**Major**	6.2.1	-32.9 dB → -27.0 dB (5.9 dB worsening)
				6.3 with 1 RF band	-30.2 dB → -18.3 dB (11.9 dB worsening)
				6.3 with *3 RF bands*	-30.2 dB → -24.6 dB (-5.6 dB worsening)

TABLE XIII
PRELIMINARY CALIBRATION REQUIREMENTS DERIVED FROM MISMATCH SOURCES

Mismatch source	Section	Error model	Severity	System Design Example	Critical error level
Mispointing	8.5	Deterministic	Medium	6.2.1	75 mdeg
				6.3	13 mdeg
Pattern measurement uncertainty	8.6	Deterministic noise-to-maximum-signal level ϵ (uncertainty floor) and random uniformly distributed phase for noise affecting pattern	**Major**	6.2.1, worst-case AASR	-24.5 dB uncertainty floor ϵ
				6.3, best-case AASR	-29.1 dB uncertainty floor ϵ
				6.3, worst-case AASR	-40.4 dB uncertainty floor ϵ
Phase and amplitude errors in weight implementation (TR-modules)	8.7	Gaussian amplitude errors for each channel/TR-module $\epsilon_k \sim N(0, \sigma_\epsilon^2)$, Uniform phase errors for each channel/TR-module $\phi_k \sim U\left(\frac{-\xi_u}{2}, \frac{\xi_u}{2}\right)$	Minor	6.2.1	7.6%
				6.3	2.1%
				6.2.1	14.9°
				6.3	4.2°

The next chapter will conclude the dissertation reviewing and commenting the main results.

9 Conclusion

This chapter concludes the thesis with an overview of the achieved results and an outlook on further research.

9.1 Thesis Objectives and Results

SAR sensors are active imaging systems suitable for nearly weather-independent operation. This feature, alongside the growing understanding and acceptance of the wealth of information provided by microwave imaging for many applications, makes them an invaluable component of future remote sensing systems. SAR could provide virtually continuous observation of the Earth, facilitating the monitoring of dynamic processes. However, as discussed in Chapter 2, conventional SAR systems possess limitations which prevent the fulfillment of the current and projected demand for high-resolution imagery with a high temporal resolution.

New imaging concepts and corresponding processing techniques are deemed necessary to achieve the required HRWS SAR imaging performance. In particular, multichannel system architectures in azimuth — discussed in Chapter 3.2 — are a relatively mature concept allowing high resolution imaging with a swath width limited by the maximum antenna size deployable in space. Multichannel ScanSAR/TOPS systems have also been proved to be possible, but the burst nature of operation (which introduces spectral gaps as explained in Section 2.4) introduces considerable performance degradation and makes processing challenging.

Staggered SAR with multiple elevation beams — discussed in Chapter 3.3 — presents itself as another promising alternative, of special interest in the cases were a wide gapless swath is desirable. This is often the case in terms of the application-driven requirements, even though the feature of eliminating the blind ranges has a considerable impact on system complexity. The concept requires multiple channels and time-dependent DBF in elevation to form multiple SCORE beams, plus an azimuth interpolation step to regularize the sampling in along-track. The main

limitation of Staggered SAR so far was the single aperture on azimuth, limiting the maximum achievable performance in terms of azimuth resolution.

The main achievement of the work was to develop a further HRWS imaging concept to overcome the limitations of the previous approaches and combine their strengths. The technique is applicable to a system with multiple channels in elevation and azimuth, and requires range-dependent digital beamforming in both dimensions. The modeling of the multichannel Staggered SAR signal and algorithms for its resampling into a regular grid were introduced in Chapter 4. The resampling operation, the critical processing step for this mode, is performed in time domain (unlike the conventional multichannel techniques with a constant PRF) and employs beamforming concepts applied to an extended manifold, which combines spatial and temporal information. The novel Virtual Beam Synthesis (VBS) algorithm was developed, and variations allowing to also address the problems of controlling the possible SNR loss and making the performance across the output grid more uniform (in spite of the different sampling configurations) were introduced. The chapter also included an analysis of the technique for planar arrays and the adaptations needed for the design of the systems.

Chapter 5 focused on examples which allow a better understanding of the technique and the trade-offs involved in the design of the weights, whereas Chapter 6 showed several systems designs to apply the technique both with reflector and planar antennas. The predicted performance was seen to allow unprecedented HRWS imaging performance: for instance a 500 km wide gapless swath imaged at 1 m azimuth resolution in single polarization and 400 km at 2 m resolution in quad-pol. As pointed out in Chapter 6.5, this comes at the cost of increased complexity of the systems. An important aspect in terms of implementation which was identified is the trade-off between on-board complexity (both in terms of processing power and the stringency of calibration requirements) and the need to cope with a higher data rate.

Chapter 7 shifted focus to a proof of concept employing a ground-based radar system operated with a reflector antenna with a multichannel feed. The results indicated successful implementation of the technique, provided that the system undergoes sufficient pattern characterization and calibration.

The topic of calibration was again the main focus in Chapter 8, which took system examples from Chapter 6 and analyzed the impact of different sources of errors. Systems with larger reflectors and a larger number of channels were shown to be more sensitive to errors. In terms of the error sources, pulse extension and the variation of the patterns with the wavelength were found to have potentially significant effects, requiring frequency dispersive beamforming for the most sensitive system. The most stringent requirements with respect to calibration were identified to be the pattern measurement uncertainty as well as mispointing, especially for very large reflectors.

In light of the presented results, the thesis is considered to be successful in its original objective, having introduced, analyzed and demonstrated a new HRWS technique with potential to enable high-performance SAR imaging modes in the future. Moreover, an initial discussion of the implementation aspects of systems of this class was provided and certain critical points were identified, which is valuable input for further analysis of system implementation.

9.2 Outlook of Further Work

The Virtual Beam Synthesis technique introduced in this thesis has been analyzed in the framework of beamforming on receive [37], therefore leading to a Single Input Multiple Output (SIMO) system. Relying on advanced waveform design and the undergoing developments in hardware and especially processing power, Multiple Input Multiple Output (MIMO) [38], [127], [128] systems are recognized to be an important trend for future radar applications, certainly including remote sensing. The combination of the technique with beamforming on Tx and/or multiple separable waveforms [129] would be a possible alternative to further improve performance.

Furthermore, the VBS techniques were seen to be initially motivated by reflector antenna architectures, for which they are especially suitable. In this context, a promising emerging technology deemed to play an important role in spaceborne communications in the near future is *reflectarrays* [130], [131], [132], [133]. The concept is basically to change the surface impedance of parts of the antenna's reflective surface, which then behave in a way similar to the "elements" of a typical antenna array. By introducing phase shifts between the regions of the reflective surface, another degree of freedom in pattern synthesis is achieved, which can be used to improve fixed beams or even to obtain reconfigurable beams. The Virtual Beam Synthesis could also be used in conjunction with this class of antenna in further developments.

A final aspect which deserves particular attention for multichannel systems in general is the simultaneous need for adequate calibration (and pattern characterization, as addressed in Chapter 8) and reduction of the data rates (as discussed in Section 6.5). Typical internal calibration strategies [134] have limitations in the sense that part of signal's path, notably the RF cables and the antenna itself, are usually not characterized. Moreover, the use of calibration tones — signals of very limited bandwidth in comparison to the actual SAR data — shows some limitations. Data driven calibration schemes [135], [136] are thus deemed necessary at least as a complement of the internal system calibration. This is particularly challenging for multichannels systems in azimuth, since on one hand the individual channels are often undersampled and subject to aliasing, but on the other suffer artifacts from reconstruction in the presence of channel imbalances. Moreover, as a rule the data-driven calibration techniques exploit (and require) correlation between the channels to derive corrections. Some level of oversampling must therefore be preserved, which contradicts the need to keep the data rates, which may quickly become very high for high performance HRWS systems, low. In the interest of an efficient implementation of this class of system in the future, further investigation of data-driven calibration schemes with limited impact on the data-rate (or implementable with on-board

hardware) is an important field of research. Multichannel Staggered SAR systems would benefit especially from techniques applicable in azimuth time domain regardless of aliasing and irregular sampling. An approach using range-compressed data reported in [137] could represent a viable alternative.

Appendix A: Elevation Beamforming Techniques

The main topic of this Thesis is azimuth beamforming, specifically with the aim of the resampling Multichannel Staggered SAR data. Nonetheless, as the system design examples in Chapter 6 show, system performance over range (for instance the RASR and NESZ) is also a fundamental part of system design. Therefore, elevation beamforming techniques also present themselves as a very important topic. This Appendix, containing material published in [69], discusses elevation beamforming techniques suitable for the implementation of the SCORE beams [52], [65] of a multichannel Staggered SAR system. Section A.1 describes a beamforming technique especially suited for range ambiguity suppression of staggered SAR systems [69], here denoted as Sidelobe Constrained Beamformer. A similar approach is referred to as "Digital Sidelobe Canceller" in [52]. Section A.2 provides an example of application of the technique. The implementation of the far range SCORE beams of the system described in Section 6.2.2 is considered and the technique is compared to currently used alternatives [36], [73], highlighting trade-offs and implications for system performance.

Appendix A.1: The Sidelobe Constrained Beamformer

To define the notation, assume the channel's elevation beams to be described by $G_n(\theta)$, $1 \leq n \leq N$. The antenna system is thus described by an array manifold vector [106]

$$\underline{\boldsymbol{v}}_{\boldsymbol{el}}(\theta) = [G_1(\theta) \quad \dots \quad G_N(\theta)]^T, \tag{161}$$

which is analogous to (92), however in the elevation dimension. In this case, θ denotes the elevation angle. Let the N-dimensional complex elevation beamforming weight vector be denoted by $\underline{\boldsymbol{w}}$ and the resulting pattern of the array at a particular elevation angle by $G_{array}(\theta) = \underline{\boldsymbol{w}}^{\boldsymbol{H}} \cdot \underline{\boldsymbol{v}}_{\boldsymbol{el}}(\theta)$. Moreover, allow the statistics of the

noise affecting the system's channels to be described by the N by N noise covariance[38] matrix $\underline{\boldsymbol{R}}_{\boldsymbol{noise}}$.

A beamformer of particular interest in the implementation of SCORE beams is the *Minimum Variance Distortionless Response* (MVDR) [40], [52], [106], [138]. The MVDR is the solution to the constrained optimization problem:

$$\underline{\boldsymbol{w}}_{MVDR} = \begin{array}{c}\operatorname{argmin}\left(\underline{\boldsymbol{w}}^{H} \cdot \underline{\boldsymbol{R}}_{\boldsymbol{noise}} \cdot \underline{\boldsymbol{w}}\right) \\ \text{subject to: } \underline{\boldsymbol{w}}^{H} \cdot \underline{\boldsymbol{v}}(\theta_0) = 1\end{array}. \tag{162}$$

The name MVDR is because the cost function being minimized $\sigma_{noise}^2 = \underline{\boldsymbol{w}}^{H} \cdot \underline{\boldsymbol{R}}_{\boldsymbol{noise}} \cdot \underline{\boldsymbol{w}}$ represents the variance or power of the noise in the output after the weighting, whereas the constraint $\underline{\boldsymbol{w}}^{H} \cdot \underline{\boldsymbol{v}}(\theta_0) = 1$ means the signal is not distorted at the elevation angle of interest θ_0, which is typically the intended maximum of the SCORE beam in this context. The solution to (161) can be derived using Lagrange multipliers and yields [40], [52], [106], [138]

$$\underline{\boldsymbol{w}}_{MVDR} = \frac{\underline{\boldsymbol{R}}_{\boldsymbol{noise}}^{-1} \cdot \underline{\boldsymbol{v}}(\theta_0)}{\underline{\boldsymbol{v}}(\theta_0)^{H} \cdot \underline{\boldsymbol{R}}_{\boldsymbol{noise}}^{-1} \cdot \underline{\boldsymbol{v}}(\theta_0)}. \tag{163}$$

In the particular case of white noise, $\underline{\boldsymbol{R}}_{\boldsymbol{noise}} = \sigma_n^2 \cdot \boldsymbol{I}_N$. The elements are hence weighted by $\underline{\boldsymbol{v}}(\theta_0)^{H} / \left\|\underline{\boldsymbol{v}}(\theta_0)\right\|^2$ and the beamformer has a "matched-filter" behavior, gathering all the available power at θ_0. MVDR thus steers the beam towards the echo signal direction of arrival and aims at maximizing the SNR. It does not, however, consider that the pulse has a non-vanishing extension on the ground (cf. [123]).

Even though the MVDR is very effective at maximizing the output SNR while focusing the maximum beam's gain around a θ_0 of choice, it allows no control over the sidelobes of the achieved beam. Motivated by this, [138] analyses an extension of

[38] In practice it is often unknown, and thus estimated from the data.

the optimization problem with addition of a sidelobe constraint. This is done by introducing a maximum level ϵ_{SDL} for the formed beam at a grid of N_{SDL} elevation angles $\Theta_{SDL} = \bigcup_n \theta_n$, $1 \leq n \leq N_{SDL}$. The resulting problem is:

$$\underline{\boldsymbol{w}}_{SDL} = \begin{array}{c} \operatorname{argmin}\left(\underline{\boldsymbol{w}}^H \cdot \boldsymbol{R}_{noise} \cdot \underline{\boldsymbol{w}}\right) \\ \text{subject to: } \begin{cases} \underline{\boldsymbol{w}}^H \cdot \underline{\boldsymbol{v}}(\theta_0) = 1; \\ \left\| \underline{\boldsymbol{w}}^H \cdot \underline{\boldsymbol{v}}(\theta_n) \right\|^2 < \epsilon_{SDL}, \\ \text{for } 1 \leq n \leq N_{SDL}. \end{cases} \end{array} \tag{164}$$

This means the distortionless constraint is kept, but a maximum level of the sidelobes within $\Theta_{SDL} = \bigcup_n \theta_n$ is specified. The problem (163) does not have a closed form solution in every case and is not necessarily feasible for every choice of pattern or sidelobe level ϵ_{SDL}. Nonetheless, as demonstrated in [138], it can be re-written as a Second-Order Cone (SOC) Optimization problem which can be efficiently solved by existing optimization packages [139]. Moreover, high-level interfaces such as [140] allow the problem to be specified directly in the form (163). An additional interesting feature of the SOC solvers is the capability of testing for feasibility before attempting to solve the problem, which allows adaptive strategies for the threshold ϵ_{SDL}, as e.g. relaxing the constraint until a solution is possible.

The technique is applicable both for reflector antennas and for planar direct radiating arrays, as only knowledge of the manifold is assumed. It should be recalled that a global sidelobe level smaller than a given ϵ_{SDL} in the planar case can be readily achieved by conventional Dolph-Chebyshev weighting [106], with the advantage of a closed-form solution, but the optimization technique allows additional flexibility, since Θ_{SDL} can be chosen freely. A possibility is setting extended minima at specific angular intervals. Another readily available extension are angle-dependent sidelobe levels $\epsilon_{SDL}(\theta_n)$, which can also be handled seamlessly by the numeric solvers and may be of interest for certain scenarios.

The sidelobe control strategy described above is of special interest in the context of SCORE pattern design, and can be used in order to improve the RASR. This is done

by specifying the direction of arrival of the signal as θ_0 and including the angles of arrival of the ambiguities (and their vicinity) within Θ_{SDL}.

The rationale is similar to the use of another beamforming technique described in [40], [52], [106] (employed for the same purpose of improving the RASR), namely the *Linear Constraint Minimum Variance* (LCMV). The latter beamformer solves the problem

$$\underline{\boldsymbol{w}}_{LCMV} = \begin{array}{c}\text{argmin}\left(\underline{\boldsymbol{w}}^H \cdot \underline{\boldsymbol{R}}_{\boldsymbol{noise}} \cdot \underline{\boldsymbol{w}}\right) \\ \text{subject to: } \underline{\boldsymbol{w}}^H \cdot \underline{\boldsymbol{A}} = \underline{\boldsymbol{c}}\end{array}, \tag{165}$$

where the N x N array matrix

$$\underline{\boldsymbol{A}} = [\underline{\boldsymbol{v}}(\theta_0) \quad \underline{\boldsymbol{v}}(\theta_1) \quad \dots \quad \underline{\boldsymbol{v}}(\theta_{N-1})] \tag{166}$$

contains the manifold for the angle of interest θ_0 and $N-1$ other angles for which the pattern level can be specified. Typically, in the case of SCORE beamforming,

$$\underline{\boldsymbol{c}} = [1 \quad \epsilon_{SDL} \quad \cdots \quad \epsilon_{SDL}] \tag{167}$$

and ϵ_{SDL} is chosen to be zero or a very low value creating a grid of nulls or minima $\Theta_{SDL} = \bigcup_n \theta_n$, $1 \leq n \leq N_{el} - 1$. The analogy between (164)-(166) and (163) is thus clear, replacing the "hard" equality constraints by "soft" inequality constraints over the sidelobe grid Θ_{SDL} and adjusting the size of this grid.

The LCMV beamformer has indeed the advantage of a closed form solution [106]

$$\underline{\boldsymbol{w}}_{LCMV} = \underline{\boldsymbol{R}}_{\boldsymbol{noise}}^{-\boldsymbol{1}} \cdot \underline{\boldsymbol{A}} \cdot \left(\underline{\boldsymbol{A}}^H \cdot \underline{\boldsymbol{R}}_{\boldsymbol{noise}}^{-\boldsymbol{1}} \cdot \underline{\boldsymbol{A}}\right)^{-1} \cdot \underline{\boldsymbol{c}}^{\boldsymbol{T}}, \tag{168}$$

but the number of constraints is limited by the number of available elevation channels N.

In the context of staggered SAR, the position of the range ambiguities changes from pulse to pulse [64], meaning that typically several tenths or even hundreds of different

angles of arrival need to be considered for each order of ambiguity. This means that the LCMV is of limited usefulness in this situation, though very effective for a conventional constant-PRI SAR. In contrast, the sidelobe-constrained beamformer of (163) can be used to force a minimum (though not a zero) over a (not necessarily contiguous) broad region, as no a-priori restriction on N_{SDL} exists. In fact, N_{SDL} should ideally be high, since a properly fine grid is necessary to ensure the pattern behavior follows the constraints in the vicinity of the grid points. This allows the creation of "broad minima", again making an LCMV-like approach feasible for mitigation of range ambiguities in staggered SAR.

Appendix A.2: Example and Comparison to Other Methods

With the aim of illustrating the application of the discussed methods and comparing their properties, the implementation of the far range SCORE beams of the reflector antenna system in Section 6.2.2 is considered next. To simplify the discussion, a single azimuth channel is considered (namely the central one out of the nine), and the elevation patterns are taken at an azimuth angle of 0.0°. The combination of the channels over azimuth and the implications for the range ambiguity performance are considered as well.

In the far range region two effects contribute to poorer RASR performance: the range ambiguities are closer to the main beam (in terms of the corresponding elevation angles) and pattern defocusing effects contribute to higher sidelobes. These effects, as will be shown in the following example, may be mitigated by the elevation beamforming. A look angle $\theta_0 = 43.2°$, at the edge of the swath of interest, is considered the desired maximum of the beam (note that the antenna is tilted 32.5° with respect to nadir). Besides, a total of $N = 9$ elevation channels are chosen as part of the input manifold for beamforming, as seen in **Figure 80 (a)**. The plot refers to the *directivity* of the individual feed elements, as simulated by the GRASP software [113]. In the plot, the desired position of the maximum is highlighted by the vertical black dashed line in the center, and the limits of the sidelobe region — where the range

ambiguous contributions begin — by purple vertical dashed lines to its sides. The position of the ambiguities is determined by the geometry and the PRI sequence parameters in TABLE VI. The noise affecting the channels is assumed white, so $\underline{\boldsymbol{R}}_{noise} = \boldsymbol{I}_9$.

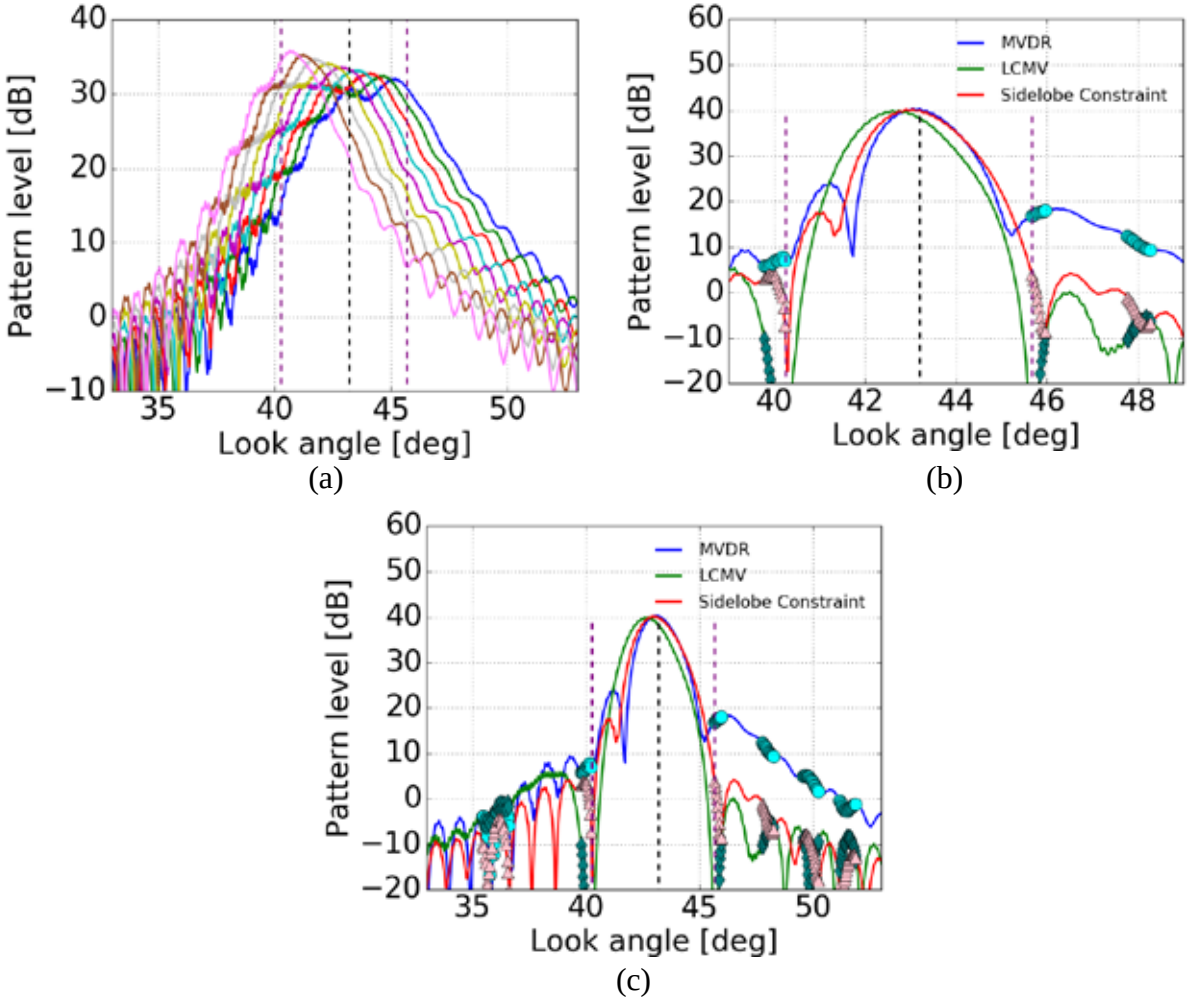

Figure 80. Far-range SCORE elevation beams illustrating the discussed methods of elevation beamforming. (a) Manifold over elevation consisting of the 9 active elements used to form the beams, with vertical lines highlighting main signal and sidelobe region limits. (b) SCORE beams formed by the different methods (MVDR, LCMV and Sidelobe-constrained beamformers respectively in blue, green and red). The markings for signal direction and sidelobe region are repeated, and the location of the range ambiguities is superimposed on the different patterns (circles, diamonds and triangles, respectively); (c) SCORE patterns of (b) over a broader range of angles to better illustrate the behavior of the outermost range ambiguities.

Figure 80 (b) and **(c)** show the patterns (their gain following the convention of [106], cf. (138)) obtained by the algorithms described in the previous section. The first shows a zoom around the main beam whereas the second depicts a broader angular region. The MVDR beam (cf. (161), (162)) is seen in blue, and the levels in the positions of the range ambiguities are highlighted by light blue circles. Note that several positions exist ($N_{PRI} = 28$ per order) due to the staggered PRI operation. This solution effectively maximizes the gain at the goal elevation angle θ_0, but provides no control over the sidelobes. The first ambiguity to the right of the main beam is seen to be at a relatively high level, circa -20 dB below the pattern's maximum. The LCMV beam (cf. (167)) is calculated by setting a linear constraint (cf. (166)) of 1.0 at θ_0 and $\epsilon_{SDL} = 0$ for eight range-ambiguous positions. The pattern is seen in green, and ambiguous positions are highlighted by adjacent green diamonds. Whereas only the aforementioned eight ambiguities can be nulled, the neighboring ones are also seen to be suppressed by the proximity of the deep minima formed (especially visible in **Figure 80 (b)**). However, no control is possible over more distant ones. The same is true regarding the position of the main beam, which is seen to be distorted, showing a maximum at a look angle circa 0.5° smaller than θ_0. Finally, the sidelobe-constrained pattern (cf. (163)) obtained with $20 \cdot \log_{10} \epsilon_{SDL} = -36.0$ dB and Θ_{SDL} corresponding to all angles of the sidelobe grid (i.e. the expected range ambiguity positions) within $[15.3°, 40.3°]$ and $[45.7°, 48.2°]$ (the grid spacing is 0.03°) is seen in red. This time, ambiguities are highlighted by triangles and their maximum is at circa 4 dB. As the maximum gain is at 40 dB, this indicates a successful implementation of the threshold.

The robustness of the beamformers against errors in the coefficients is also a crucial point for their applicability in real-world systems, where effects such as limited phase accuracy play a role. A first assessment and comparison of the methods with this regard is performed by means of a Monte Carlo simulation. This consists of disturbing each element of the complex weight vectors (calculated from the error-free manifolds according to the specific algorithm in Appendix A.1) with a uniform phase draw from a uniform distribution in the interval $[-\xi_u/2, \xi_u/2]$. For a varying ξ_u in the interval

$[0, 45.0]°$, a total of 100 draws of the phases are done, for each of which the disturbed patterns are calculated. For consistency, the same disturbance (realization of the phase errors drawn from the distribution) is used for the three beamforming methods at each trial. For each drawn phase, pattern parameters are assessed, and then the mean over the trials is considered as the expected value.

In **Figure 81 (a)** the expected sidelobe-to-peak ratios of the patterns are analyzed for the three beamforming algorithms, seen in different colors. Solid lines indicate the maximum over the sidelobe regions (i.e. range ambiguities), whereas the dashed lines indicate the mean over these range-ambiguous positions. For the LCMV, the maximum over the desired nulls is also provided as a dotted line. It is clear that the MVDR shows very stable levels, nearly invariant to the phase errors, even though the sidelobe-to-peak levels (which translate into RASR levels) are the highest. Both the LCMV and the sidelobe-constrained beamformer show some sensitivity to errors. Even though the nulling of the patterns does not hold in the presence of errors and the maximum of the controlled ambiguities quickly rises (as indicated by the dotted line), the maximum level of the sidelobe region is dominated by the non-controlled ambiguities until $\xi_u \cong 15°$ and the performance is not severely degraded for small phase errors. Though the sensitivity (inclination of the curve in dB/°) increases for larger errors, the peak level remains the lowest of all methods. The sidelobe-constrained beamformer in turn shows a higher starting point (at the set threshold of -36.0 dB) and a smaller sensitivity (which is influenced by the starting point as well as by the weights themselves). The mean curve indicates that for larger phase errors, the sidelobes are on average lower for the latter method in comparison to LCMV, even though the peak values of both methods converge in the extreme case of $\xi_u \cong 45°$. Both methods are seen to outperform the MVDR beamformer in terms of sidelobe levels, even in the presence of errors.

The influence of the errors over the pattern gain is analyzed in **Figure 81 (b)**, in terms of the gain with respect to the best case, namely that of the error-free MVDR. The plot shows the gain loss — negative values indicate attenuation — of the global maximum

of the patterns (not necessarily in θ_0) in solid lines and the gain loss at θ_0 in dashed lines. The beamformer algorithms are represented by different colors. All methods show relatively small gain sensitivity to the phase errors, with the LCMV method showing the maximum error-induced variation of -0.2 dB. The error-free levels thus dictate the performance. The MVDR shows the highest gains and a very small discrepancy between the maximum and the gain at position θ_0, in this case due to discretization of the elevation grid of the patterns (θ_0 is not necessarily a sample in the grid). In contrast, the LCMV shows considerable main beam distortion (as visible in **Figure 80 (b)** and **(c)**), with an attenuation of 2 dB at θ_0, mainly characterizing mispointing, as the absolute maximum is only 0.4 dB below the MVDR reference. The sidelobe-constrained beamformer shows an intermediate behavior, with a 0.4 dB attenuation at θ_0 and mild mispointing (the global maximum shows 0.16 dB attenuation).

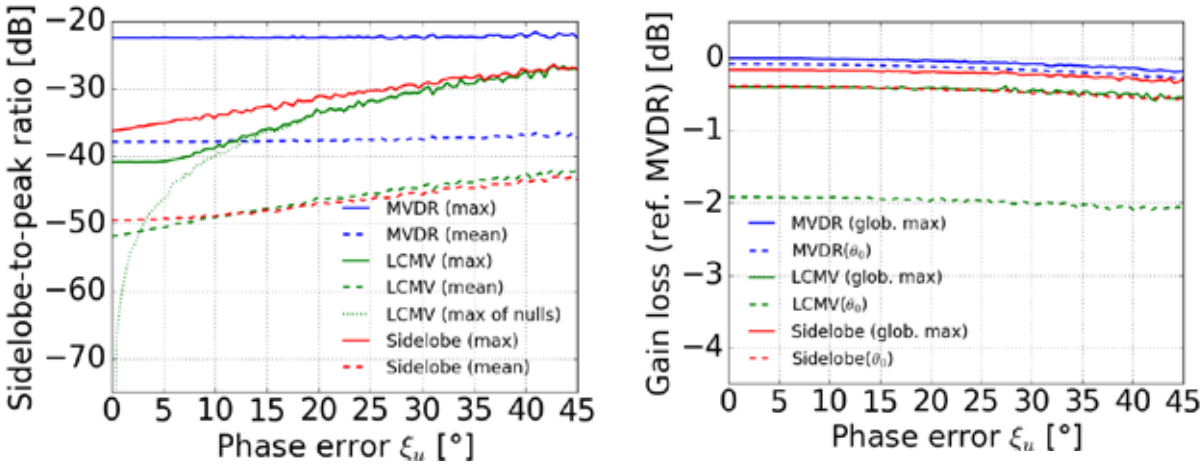

Figure 81. (a) Monte Carlo simulation of sidelobe-to-peak ratio (sidelobes are defined by the sidelobe grid) of the implemented patterns as a function of a uniform phase error in the interval $[-\xi_u/2, \xi_u/2]$. The MVDR, LCMV and Sidelobe-constrained beamformers are represented by blue, green and red lines, respectively, and for each beamformer the maximum and mean over the sidelobe grid are represented by solid and dashed lines, respectively; (b) Monte Carlo simulation of the gain loss (with respect to the maximum gain of the error-free MVDR), as before as a function of the uniform phase error parameter ξ_u.

The comparison shows that, as expected, the sidelobe-constrained beamformer provides a compromise between the pattern's gain and sidelobe levels, presenting characteristics which are in-between those of the MVDR and the LCMV methods. The gain reduction is expected, as the additional constraint in (163) in comparison to (161) means that the achieved minimum noise variance cannot be smaller than in the MVDR case. It should be stressed that the choice of ϵ_{SDL} and Θ_{SDL} is very important for meaningful results: a sidelobe region too close to the main beam or a too low ϵ_{SDL} may severely degrade the achieved gain. With proper design of the parameters, however, the method offers the possibility of avoiding severe main beam distortion (which reduces gain at the signal's direction of arrival) while retaining improved sidelobe suppression.

Further aspects of the elevation beamforming are illustrated in **Figure 82**. In order to assess the impact of the elevation beamforming for SAR performance, the final SCORE beams of all the $N_{ch} = 9$ azimuth channels need to be taken into account. These are plotted in **Figure 82 (a)** in different colors, as function of the look angle. Each pattern is taken at the azimuth angle which represents the maximum of the particular channel (recall that for reflector systems the antenna patterns are not separable in azimuth and elevation, and show different maxima positions due to the feed element's displacement). The patterns cannot be clearly distinguished, indicating great similarity between them, apart from the different azimuth angles of the maxima.

The signal and ambiguity positions, as well as the imposed constraint for the sidelobe region are highlighted by the green and red crosses and the dashed horizontal line, respectively. Θ_{SDL} in this case includes the look angles in the intervals [15.3°, 40.3°] and [45.7°, 48.2°], chosen to include all orders of range ambiguities, assuming the maximum PRI in the sequence, 439.8 μs. As before, the patterns are interpolated to a grid of spacing 0.03°, and the constraint parameter is $20 \cdot \log_{10} \epsilon_{SDL} = -36.0$ dB. Due to the similarity of the patterns from different azimuth elements, the constraint levels are also very similar. The pattern levels below the constraint indicate that the elevation beamforming was successful for all channels. **Figure 82 (b)** shows a pattern

which is the result of the summation over the azimuth elements — relevant as the reference common pattern — taken at an azimuth angle of 0.0°.

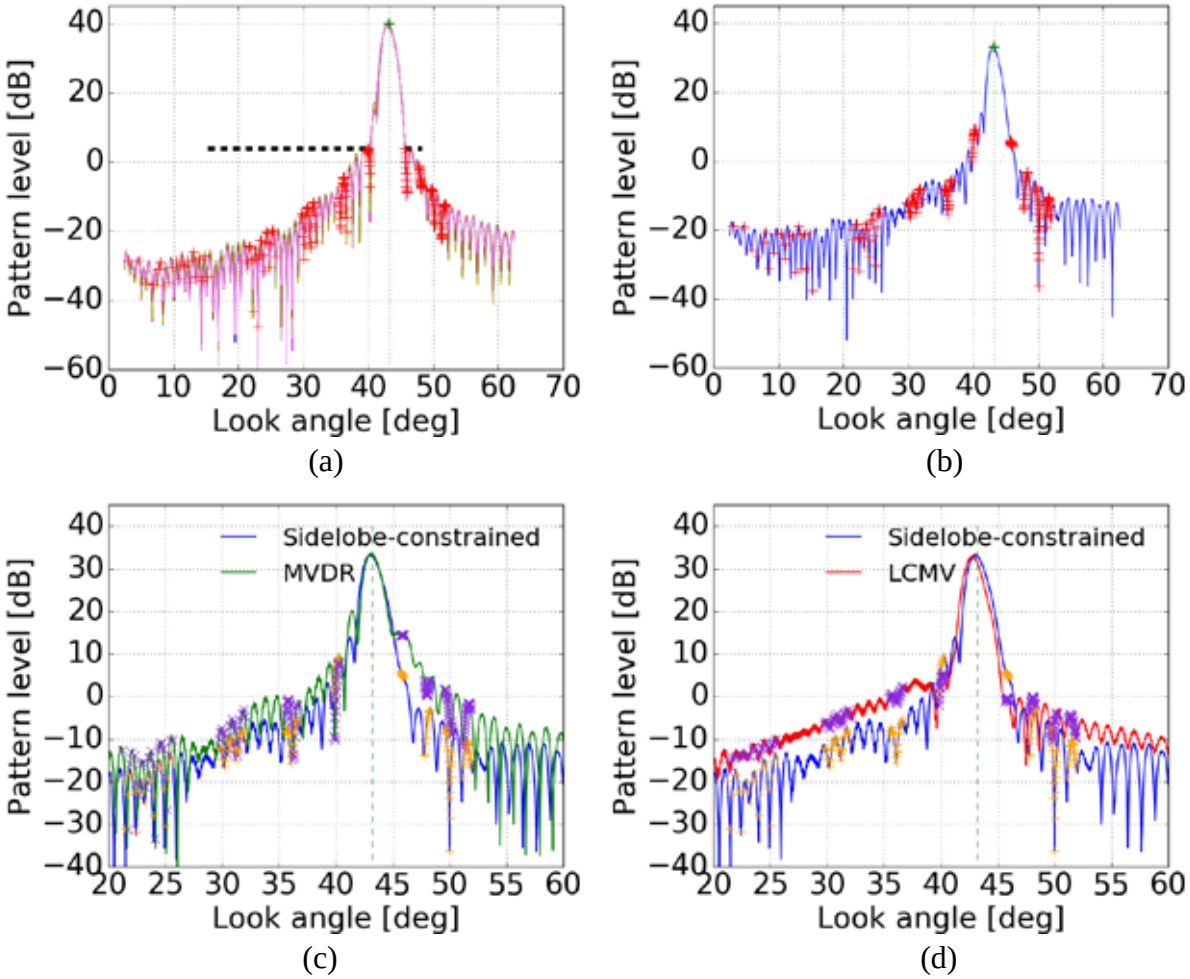

Figure 82. Far-range SCORE elevation beams illustrating some special aspects of the elevation beamformers. (a) SCORE elevation patterns (sidelobe-constrained) for each of the azimuth elements at their maximum position. Green and red crosses mark signal and ambiguity contributions, respectively, and the imposed sidelobe level constraint is indicated by the black horizontal dashed line. (b) Cut of the sum over the azimuth elements of the sidelobe-constrained patterns, at an azimuth angle of 0.0°. (c) Comparison of the SCORE patterns of the sum over the azimuth channels (cut around an azimuth angle of 0.0°) for the sidelobe-constrained beamformer (blue) and the conventional MVDR (green). The signal direction is highlighted by a vertical dashed line and the range ambiguity positions by '+' and 'X' symbols superimposed on the respective patterns. The blue patterns are the same as in (b), repeated to facilitate the comparison; (d) Comparison of the SCORE patterns for the sidelobe-constrained beamformer (blue) and LCMV (red) with respective ambiguities.

The signal and ambiguity positions are marked as well. Note that the constraint is no longer fulfilled, since the azimuth angle is no longer that of the maximum for each channel, but a considerable reduction in sidelobe levels is nevertheless observed, resulting in improved range ambiguity suppression.

To better illustrate this point, **Figure 82 (c)** shows the SCORE pattern of the central azimuth element in far range (look angle of 43.2°) for the sidelobe constrained beamformer (blue) and the conventional MVDR (green). The main beam (centered around the vertical dashed line) is not considerably changed, but sidelobe suppression at the range ambiguity positions (compare the '+'s and 'X's) is notable, especially for the first-order far range ambiguities, as intended. In **Figure 82 (d)** the sidelobe-constrained (blue) elevation beam at 0.0° in azimuth is compared to the LCMV one (red). The latter technique was also applied for each azimuth channel at the location of its maximum, and thus due to the non-separable characteristic of the patterns the deep minima (cf. **Figure 80 (b)**) are not visible for the sum of all patterns, even though a reduced level is obtained.

The impact of the choice of beamformer on system performance in this particular range is summarized in TABLE XIV. The sidelobe-gain compromise mentioned before is seen to be translated into a RASR-NESZ compromise, and the sidelobe-constrained beamformer retains the behavior of an intermediate solution between the MVDR and the LCMV with regard to both parameters. As expected, the MVDR technique yields the optimal NESZ of -26.4 dB and the LCMV the best ambiguity suppression, with an RASR of -30.5 dB. The MVDR shows however the worst RASR, with -23.6 dB, and the LCMV's mispointing with respect to the signal direction leads to a worsened NESZ of -24.6 dB. The sidelobe-constrained beamformer leads to an NESZ of -26.0 dB and an RASR of -29.6 dB, indicating that a considerable gain in range ambiguity suppression could be achieved for the price of a slight SNR degradation if compared to the MVDR beamformer.

TABLE XIV
FAR-RANGE PERFORMANCE OF DIFFERENT ELEVATION BEAMFORMERS

Beamforming Method	RASR [dB]	NESZ [dB]
MVDR (162)	-23.6	-26.4
LCMV (167)	-30.5	-24.6
Sidelobe-constrained (163)	-29.6	-26.0

Appendix B: SAR Performance Indices

The main SAR performance indices considered in this thesis for evaluation of an imaging mode's output quality are azimuth resolution, azimuth ambiguity to signal ratio (AASR), range ambiguity to signal ratio (RASR) and noise equivalent sigma zero (NESZ). The purpose of this appendix is to define these quantities and indicate the methods used for their calculation.

Azimuth Resolution

The azimuth resolution is a fundamental SAR image property, defined as the 3 dB length of the (sinc-like) impulse response, and inversely proportional to the processed Doppler bandwidth [26], [76]. To account for possible distortions introduced by the resampling and/or errors (cf. Chapter 8), this parameter is estimated directly from the focused impulse responses in time domain, after interpolation.

Azimuth Ambiguity to Signal Ratio (AASR)

The azimuth ambiguity to signal ratio (AASR) is defined as the ratio of the power of the azimuth ambiguities (i.e. the aliased part of the Doppler spectrum) to the power of the signal (the part of Doppler spectrum within the processed bandwidth) [26]. This parameter is strongly related to the azimuth antenna patterns, which weight the Doppler spectrum, and the sampling configuration. For multichannel systems, the parameter plays an important role, due to the resampling operation which increases the sampling rate and thus reduces the ambiguity level with respect to the one found in each individual channel. In [39], [51], this parameter is calculated analytically by integration of the antenna patterns, taking into account the (constant PRF) system's transfer functions.

For staggered SAR, [41], [53], [62], [64], [141], the effect of the resampling over the spectrum is more complex, and the favored approach is to estimate the level of residual ambiguous energy from a comparison of the resampled impulse response and an alias-free reference simulated with constant PRI, chosen to implement the desired

(regular) output grid. As detailed in [64], the level is estimated from the difference in Integrated Sidelobe Ratio (ISLR) between the impulse response of the data and that of an alias-free reference. The ISLR is defined as the ratio of the power of the impulse response in the sidelobe region to the power in the main beam. The mainlobe is usually assumed to be the region between the first minima closest to the maximum. This region contains the bulk of the signal energy and does not contain appreciable levels of ambiguous energy. Denoting the contributions to signal power in the sidelobe and mainlobe regions as $P_{sidelobe}$, $P_{mainlobe}$ (where $P_{signal} = P_{sidelobe} + P_{mainlobe}$, but $P_{sidelobe} \ll P_{mainlobe}$) and the ambiguity power as $P_{ambiguity}$, the ISLR difference becomes

$$\begin{aligned} ISLR_{data} - ISLR_{alias-free} &= \frac{P_{sidelobe} + P_{ambiguity}}{P_{mainlobe}} - \frac{P_{sidelobe}}{P_{mainlobe}} \\ &= \frac{P_{ambiguity}}{P_{mainlobe}} \cong \frac{P_{ambiguity}}{P_{signal}}, \end{aligned} \tag{169}$$

which is by definition the AASR.

For this estimation method, matching of the antenna patterns (which strongly influence the shape of the impulse response) between data and reference is important for accurate results. For this reason, the average (over the output grid samples) common pattern $\hat{G}_{com}(f_D)$ (cf. Section 4.4.5, (121)) is used for simulating the reference.

Conceptually, staggering of the PRI has the impact of smearing the azimuth ambiguities [53], [64], [141], which spreads the energy over azimuth and thus reduces the peak values. Note that this of PRI staggering effect over Doppler ambiguities is valid for radar systems in general [76], not being restricted to the SAR case.

Noise Equivalent Sigma Zero (NESZ)

Following the notation and logic of [109], the signal power of a single pulse before azimuth compression can be expressed, employing the Friis transmission equation, as

$$P_{signal} = \iint_{A_{ill}} \frac{P_{TX}}{L_f} \cdot \frac{G_{TX} \cdot |C_{TX}(\theta,\phi)|^2}{4 \cdot \pi \cdot R^2(\theta,\phi)} \cdot \frac{A_{RX} \cdot |C_{RX}(\theta,\phi)|^2}{4 \cdot \pi \cdot R^2(\theta,\phi)} \cdot \sigma(\theta,\phi)\, \mathrm{d}A\,; \tag{170}$$

for the quantities defined in the upper part of TABLE XV. A white scene is assumed, in the sense that the surface reflectivities from non-overlapping patches are uncorrelated.

TABLE XV
DEFINITION OF QUANTITIES RELEVANT FOR SIGNAL AND NOISE POWER

Signal parameters		
Symbol	Parameter	Unit
P_{TX}	Peak Tx power	[W]
L_f	Feed system losses	[]
G_{TX}	Gain of the Tx antenna	[]
θ, ϕ	Elevation and azimuth angles, respectively	[rad]
$C_{TX}(\theta,\phi)$	Normalized Tx antenna pattern ($\lvert C_{TX}(\theta,\phi)\rvert \leq 1$)	[]
A_{RX}	Aperture area of the Rx antenna	[m^2]
G_{RX}	Gain of the Rx antenna	[]
$C_{RX}(\theta,\phi)$	Normalized Rx antenna pattern ($\lvert C_{RX}(\theta,\phi)\rvert \leq 1$)	[]
$C(\theta,\phi) = C_{TX}(\theta,\phi) \cdot C_{RX}(\theta,\phi)$	Two-way normalized antenna pattern	[]
$\sigma(\theta,\phi)$	Radar Cross Section (RCS) per unit area	[]
$R(\theta,\phi)$	Slant range to the area element	[m]
$\mathrm{d}A = R \cdot d\phi \cdot \frac{\mathrm{d}R}{\sin(\eta)}$	Infinitesimal area element	[m^2]
η	Incidence angle	[rad]
A_{ill}	Illuminated area on ground (depends on the azimuth beamwidth ϕ_{AZ} and the pulse extension T_p)	[m^2]
ϕ_{AZ}	Azimuth beamwidth	[rad]
T_p	Pulse duration/extension	[s]
Noise parameters		
Symbol	Parameter	Unit
k_B	Boltzmann constant	[m^2 kg s^{-2} K^{-1}]
T_{noise}	System noise temperature	[K]
Bw_n	System noise bandwidth	[Hz]

If the scene is assumed uniform, the Radar Cross Section (RCS) per unit area is such that $\sigma(\theta,\phi) = \sigma_0$. Moreover, let $A_{RX} = \frac{G_{RX}\cdot\lambda^2}{4\cdot\pi}$ and consider the pattern integration along a iso-range line in $\left[-\frac{\phi_{AZ}}{2},\frac{\phi_{AZ}}{2}\right]$ (i.e. a constant slant range, in no-squint geometry), meaning $R(\theta,\phi) = R(\theta)$. Thus, (169) becomes, expressed explicitly as a function of the local elevation θ,

$$P_{signal}(\theta) = \frac{P_{TX}\cdot G_{TX}\cdot G_{RX}\cdot\lambda^2\cdot\sigma_0}{(4\cdot\pi)^3\cdot L_f}\cdot\int_{\phi_{AZ}}\int_{\frac{c\cdot T_p}{2}}\frac{|C(\theta,\phi)|^2}{R(\theta)^3\cdot\sin(\eta(\theta))}\,\mathrm{d}r\,\mathrm{d}\phi\,; \tag{171}$$

which is analogous to the result in [108]. Note that the integration over range (dr) takes place over the pulse length and that θ, η and the patterns change accordingly, even though the variation is typically small in comparison to $R(\theta)$ (except for very long pulses). In other words, rigorously, $\theta = \theta(r)$ inside the integral but this is avoided not to overload the notation. The noise power, in turn, is simply given by

$$P_{noise} = k_B\cdot T_{noise}\cdot Bw_n, \tag{172}$$

where the symbols are defined at the lower part of TABLE XV.

For a (wide-sense) stationary [142] signal $g(t)$, the Power Spectral Density (PSD) $S(f)$ is the Fourier Transform of the autocorrelation function $E[g(t)\cdot g^*(t-\tau)\,] = R(\tau)$. According to the Wiener-Khinchin Theorem,

$$P_{signal} = R(0) = \int_{-\infty}^{\infty} S(f)\cdot\mathrm{d}f. \tag{173}$$

The SAR signal has a Doppler spectrum which is shaped by the two-way antenna pattern $C(\theta, f_\mathrm{D})$ — where f_D denotes Doppler frequency — and satisfies (172), so one may write

$$S(\theta, f_{\mathrm{D}}) = \frac{|C(\theta, f_{\mathrm{D}})|^2}{\int_{PRF_{multi}} |C(\theta, f_{\mathrm{D}})|^2 \, \mathrm{d}f_{\mathrm{D}}}, \tag{174}$$

where the integration is done over the interval $PRF_{multi} = N_{ch} \cdot PRF$, assuming a multichannel system with N_{ch} channels. The noise is assumed white and uncorrelated between channels, with a flat spectrum of density P_{noise} / PRF_{multi}.

The effect of pulse compression by a focusing filter $H_{az}(f_{\mathrm{D}})$ over the power can be modeled as

$$P_{s,comp}(\theta) = \int_{-\frac{PRF_{multi}}{2}}^{\frac{PRF_{multi}}{2}} S(\theta, f_{\mathrm{D}}) \cdot |H_{az}(f_{\mathrm{D}})|^2 \, \mathrm{d}f_{\mathrm{D}}. \tag{175}$$

The same can be done for the range compression, which is however not the focus of this discussion. Using (173), (174), the power of the signal after compression $P_{s,comp}(\theta)$ thus relates to the power before compression $P_{signal}\,(\theta)$ according to

$$P_{\mathrm{s},comp}(\theta) = \left(\frac{\int_{PRF_{multi}} |C(\theta, f_{\mathrm{D}})|^2 \cdot |H_{az}(f_{\mathrm{D}})|^2 \, \mathrm{d}f_{\mathrm{D}}}{\int_{PRF_{multi}} |C(\theta, f_{\mathrm{D}})|^2 \mathrm{d}f_{\mathrm{D}}} \right) . P_{signal}(\theta) \tag{176}$$

$$P_{s,comp}(\theta) = w_{sig}(\theta) . P_{signal}(\theta),$$

and the signal power scaling due to azimuth compression, the quantity between brackets, is denoted $w_{sig}\,(\theta)$. Analogous considerations apply for the noise, and one may write, recalling the flat spectrum,

$$P_{n,comp} = \left(\frac{\int_{PRF_{multi}} |H_{az}(f)|^2 \, \mathrm{d}f_{\mathrm{D}}}{PRF_{multi}} \right) . P_{noise} \tag{177}$$

$$P_{n,comp} = w_{noise} . P_{noise}.$$

The signal-to-noise ratio (SNR) after azimuth compression may thus be expressed as

$$SNR_{comp}(\theta) = \frac{P_{s,comp}(\theta)}{P_{n,comp}} = \left(\frac{w_{sig}(\theta)}{w_{noise}}\right) \cdot \frac{P_{signal}(\theta)}{P_{noise}}$$

$$SNR_{comp}(\theta) = \left(\frac{\int_{PRF_{multi}} |C(\theta, f_{\mathrm{D}})|^2 \cdot |H_{az}(f)|^2 \, \mathrm{d}f_{\mathrm{D}}}{\int_{PRF_{multi}} |C(\theta, f_{\mathrm{D}})|^2 \mathrm{d}f_{\mathrm{D}}}\right) \cdot \left(\frac{PRF_{multi}}{\int_{PRF_{multi}} |H_{az}(f)|^2 \, \mathrm{d}f_{\mathrm{D}}}\right)$$
$$\cdot \frac{P_{TX} \cdot G_{TX} \cdot G_{RX} \cdot \lambda^2 \cdot \sigma_0}{(4 \cdot \pi)^3 \cdot L_f \cdot \mathrm{k_B} \cdot T_n \cdot Bw_n} \tag{178}$$
$$\cdot \int_{PRF_{multi}} \int_{\frac{\mathrm{c} \cdot T_p}{2}} \frac{|C(\theta, f_{\mathrm{D}})|^2}{R(\theta)^3 \cdot \sin(\eta(\theta))} \, \mathrm{d}r \, \mathrm{d}f_{\mathrm{D}} ;$$

where the integration over azimuth angle ϕ was changed to integration over Doppler frequency f_{D} for consistency with the integrals involved in the calculation of the effect of azimuth compression. The region of integration is changed to PRF_{multi} following the heuristic assumption that the multichannel system's pattern is properly designed, in the sense of negligible pattern energy outside PRF_{multi}, even though the individual channels sampled at PRF may be aliased. For short pulses, the integration over the pulse length can be dropped, further simplifying the expression to

$$SNR_{comp}(\theta) = \left(\frac{\int_{PRF_{multi}} |C(\theta, f_{\mathrm{D}})|^2 \cdot |H_{az}(f)|^2 \, \mathrm{d}f_{\mathrm{D}}}{\int_{PRF_{multi}} |C(\theta, f_{\mathrm{D}})|^2 \mathrm{d}f_{\mathrm{D}}}\right) \cdot \left(\frac{PRF_{multi}}{\int_{PRF_{multi}} |H_{az}(f)|^2 \, \mathrm{d}f_{\mathrm{D}}}\right)$$
$$\cdot \frac{P_{TX} \cdot G_{TX} \cdot G_{RX} \cdot \lambda^2 \cdot \sigma_0}{(4 \cdot \pi)^3 \cdot L_f \cdot \mathrm{k_B} \cdot T_n \cdot Bw_n} \cdot \frac{1}{R(\theta)^3 \cdot \sin(\eta(\theta))} \tag{179}$$
$$\cdot \int_{PRF_{multi}} |C(\theta, f_{\mathrm{D}})|^2 \mathrm{d}f_{\mathrm{D}} ;$$

From (177) it is clear that the azimuth compression may bring a gain corresponding to $(w_{sig}(\theta))/w_{noise}$ to the uncompressed signal SNR, depending on the antenna

patterns and the degree of oversampling. Assume the simple case of a rectangular low-pass filter matched to the processed bandwidth Bw_{proc}, that is, $|H_{az}\,(f_{\mathrm{D}})|^2 = \mathrm{rect}\left(\frac{Bw_{proc}}{PRF_{multi}}\right)$. As is illustrated schematically in **Figure 83**, this filtering keeps $\frac{Bw_{proc}}{PRF_{multi}}$ of the noise power whereas keeping most of the signal power (for typical antenna patterns with mainlobe within Bw_{proc}).

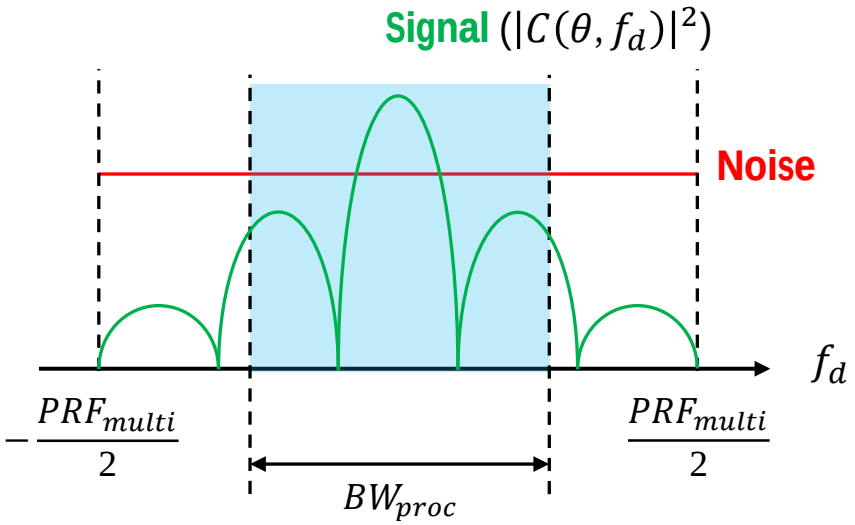

Figure 83. Conceptual illustration of the possible gain due to oversampling of the SAR signal, considering the signal's and the noise's spectral power density after filtering by a low pass filter matched to the processed bandwidth BW_{proc}.

The Noise Equivalent Sigma Zero (NESZ) is defined as the σ_0 which causes the signal power to be the same as the noise power. Equating the SNR in (177) to 1,

$$NESZ(\theta) = \left(\frac{\int_{PRF_{multi}} |C(\theta, f_{\mathrm{D}})|^2 \,\mathrm{d}f_{\mathrm{D}}}{\int_{PRF_{multi}} |C(\theta, f_{\mathrm{D}})|^2 \cdot |H_{az}(f)|^2 \,\mathrm{d}f_{\mathrm{D}}}\right) \cdot \left(\frac{\int_{PRF_{multi}} |H_{az}(f)|^2 \,\mathrm{d}f_{\mathrm{D}}}{PRF_{multi}}\right) \cdot \frac{(4 \cdot \pi)^3 \cdot L_f \cdot \mathrm{k_B} \cdot T_n \cdot Bw_n}{P_{TX} \cdot G_{TX} \cdot G_{RX} \cdot \lambda^2} \cdot \frac{1}{\int_{PRF_{multi}} \int_{\frac{c \cdot T_p}{2}} \frac{|C(\theta, f_{\mathrm{D}})|^2}{R(\theta)^3 \cdot \sin(\eta(\theta))} \,\mathrm{d}r \,\mathrm{d}f_{\mathrm{D}}}; \tag{180}$$

which is seen to depend basically on the system parameters and the antenna patterns.

In order to account for the effect of the azimuth resampling techniques of Section 4.4, the approach adopted thought this thesis is to perform the NESZ calculations (179) for the goal common pattern, i.e., $C(\theta, f_{\mathrm{D}}) = G_{com}(\theta, f_{\mathrm{D}})$ (cf. Section 4.4) and then scale the result by the average (over the output grid) SNR degradation factor with respect to the common pattern, $\bar{\Phi}_{SNR}$ (cf. Section 4.4.3).

Range Ambiguity to Signal Ratio (RASR)

The signal power considerations made previously, based on [109], can be readily applied to the calculation of the Range Ambiguity to Signal Ratio (RASR), by recognizing that the range ambiguities are actually SAR signals from different pulses, thus showing different delays and incidence angles η. As analyzed in [64], [141] in detail, the PRI staggering leads the range ambiguities to show some peculiarities. For a constant PRI SAR at a slant range R, the range ambiguity of order k is the SAR signal arriving from the range

$$R_{amb}(k) = R + k \cdot \frac{\mathrm{c}}{2} \cdot PRI, \tag{181}$$

whereas for staggered SAR, N_{PRI} different positions exist for each order k,

$$R_{amb}(i,k) = R + \frac{\mathrm{c}}{2} \cdot d_{i,k}, \quad 1 \leq i \leq N_{PRI}; \tag{182}$$

where $d_{i,k}$ are the delays from (42), (46). An important implication from the PRI staggering is namely the migration of the positions representing range ambiguities from pulse to pulse, as illustrated in **Figure 84**, in a simplified flat-Earth geometry. The case of constant PRI is illustrated in **Figure 84 (a)**: the resolution cell dimensions (before azimuth compression) are determined by the pulse duration T_p and the incidence angle η over range, and by the azimuth beamwidth ϕ_{az} in along-track; and a range ambiguity of a given order does not change position. The spectral shape and signal correlation properties are thus determined exclusively by the azimuth patterns. In contrast, in the staggered case of **Figure 84 (b)**, the position of a range ambiguity

of a fixed order k changes over azimuth with $R_{amb}(i,k)$, which introduces an additional decorrelation effect. In the example, $k = 1$, and pulses i and $i + \Delta i$ show completely uncorrelated returns, since the resolutions cell do not overlap on ground.

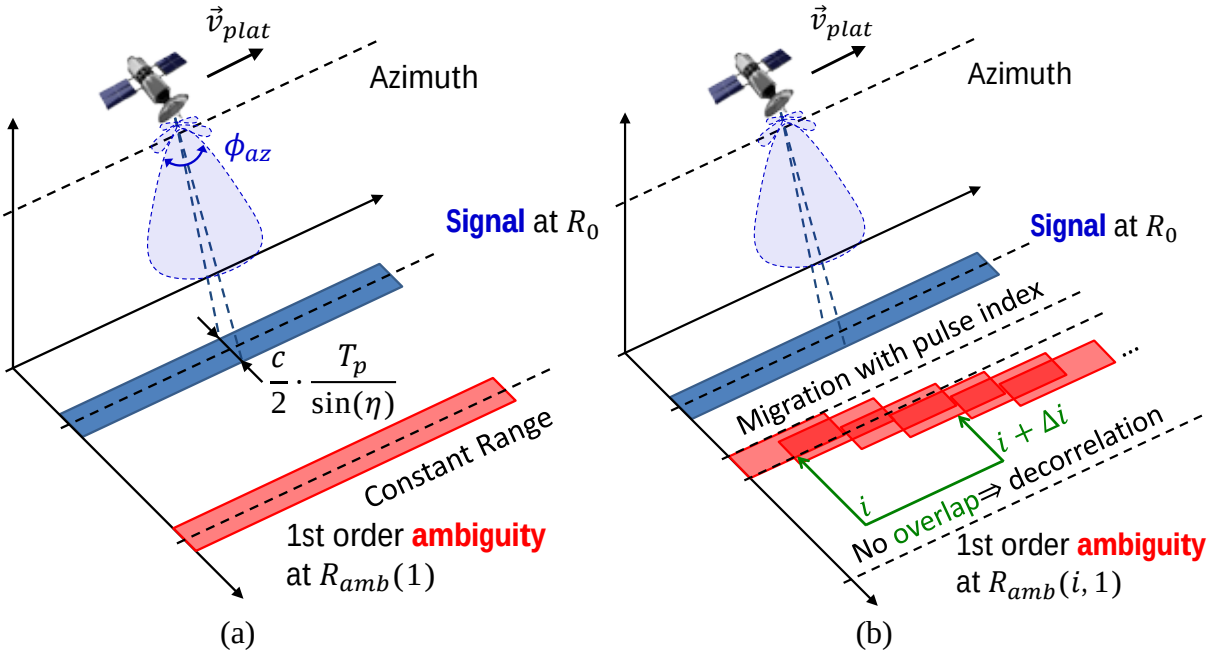

Figure 84. Schematic illustration of the position of range ambiguities, taking a fixed order as an example. (a) Constant PRI case, in which the position of the range ambiguity is constant. (b) Staggered PRI case, in which the ambiguity position changes from pulse to pulse (index i). Following the white scene assumption, this causes decorrelation over time which is complete as the area generating the ambiguity leaves the resolution cell. In the figure this is considered to happen at pulse index $i + \Delta i$.

The magnitude of this migration can be readily calculated from the timing considerations in Section 3.3.2. From (47),

$$\left|d_{i+1,k} - d_{i,k}\right| = \begin{cases} k \cdot |\Delta_{PRI}|, & \text{for } 1 \le i \le N_{PRI} - k; \\ |\Delta_{PRI}| \cdot (N_{PRI} - k), & \text{for } N_{PRI} - k + 1 \le i \le N_{PRI}. \end{cases} \quad (183)$$

This migration has two important implications: first, it is clear that the power of the ambiguities is actually dependent on the azimuth time (represented by the pulse index i, which repeats cyclically) and hence the signal representing the range ambiguities of a given order, unlike in conventional (constant-PRI) SAR, is non-stationary. A power spectrum can however still be defined using the strategy in [143], namely considering

the average over azimuth time of the autocorrelation function. Equivalently, the power of the *mean ambiguous signal* of order k can be calculated by introducing an average over i.

The second implication is related to the changes in the Doppler spectrum (and thus the PSD) of the range ambiguities in comparison to that of the main signal, which will be discussed in the following. Let θ_s, η_s denote the elevation and incidence angles of the main signal (matched to R) and $\theta_{i,k}$, $\eta_{i,k}$ the corresponding angles for the k^{th} order ambiguity, for the i^{th} PRI (matched to $R_{amb}(i,k)$). Applying (178) for a total of N_{ambs} orders and calculating the ratio between signal and mean (over i) ambiguity yields

$$RASR(\theta_s) = \sum_{\substack{k=\frac{-N_{ambs}}{2} \\ k\neq 0}}^{\frac{N_{ambs}}{2}} \sum_{i=1}^{N_{PRI}} \frac{w_{amb}(\theta_{i,k})}{N_{PRI}} \cdot \frac{G_{TX}(\theta_{i,k}) \cdot G_{RX}(\theta_{i,k}) \cdot \sigma_0(\theta_{i,k})}{R(\theta_{i,k})^3 \cdot \sin(\eta_{i,k})} \cdot \int_{PRF_{multi}} \left|C(\theta_{i,k}, f_{\mathrm{D}})\right|^2 \mathrm{d}f_{\mathrm{D}} \cdot \frac{1}{w_{sig}(\theta_s) \cdot \frac{G_{TX}(\theta_s) \cdot G_{RX}(\theta_s) \cdot \sigma_0(\theta_s)}{R(\theta_s)^3 \cdot \sin(\eta_s)} \cdot \int_{PRF_{multi}} |C(\theta_s, f_{\mathrm{D}})|^2 \mathrm{d}f_{\mathrm{D}}}; \quad (184)$$

where the θ dependency was highlighted when applicable. In particular, note that a reflectivity model $\sigma_0(\theta)$ is required from the calculations: in this thesis, the L-band model of [115] is employed. In (183), $w_{sig}(\theta_s)$, $w_{amb}(\theta_{i,k})$ denote the factors corresponding to the contribution of azimuth compression (cf. definition in (177)) for signal and ambiguities, which depend on the shape of the Doppler spectrum. Note that these factors are not the same, as the variation of the range ambiguities' position causes additional decorrelation with respect to the signal. Assuming short pulses, the white scene assumption leads to complete decorrelation between ambiguities from

neighboring pulses and thus a flat spectrum, whereas the signal at θ_s has the usual pattern-induced weighting. One may write in this case

$$w_{sig}(\theta_s) = \frac{\int_{PRF_{multi}} |C(\theta_s, f_\mathrm{D})|^2 \cdot |H_{az}(f_\mathrm{D})|^2 \, \mathrm{d}f_\mathrm{D}}{\int_{PRF_{\mathrm{multi}}} |C(\theta_s, f_\mathrm{D})|^2 \mathrm{d}f_\mathrm{D}}, \qquad (185)$$

$$w_{amb}(\theta_{i,k}) = \frac{\int_{PRF_{multi}} |H_{az}(f_\mathrm{D})|^2 \, \mathrm{d}f_\mathrm{D}}{PRF_{multi}};$$

which implies that the ambiguities behave as the noise in **Figure 83** and a gain $w_{amb}\left(\theta_{i,k}\right) = \frac{Bw_{proc}}{PRF_{multi}}$ can be achieved for a rectangular filter in the RASR. This is the result in [64], [141].

Closer examination of (182) shows that the migration rate varies proportionally to the ambiguity order k. Thus, ambiguities of a higher order tend to show a faster rate of decorrelation. The worst-case occurs for the 1st order ambiguities (k = 1), for which the delay variation is of the order of $|\Delta_{PRI}|$. From (75), a sequence designed according to the *fast PRI variation* criterion satisfies

$$|\Delta_{PRI}| \geq \frac{T_p}{k_{min}}, \qquad (186)$$

where k_{min} is the minimum order of blind range within the swath $[R_{min}, R_{max}]$. It thus takes several pulses, in the order of k_{min}, for the range ambiguity to leave the initial resolution cell (of width proportional to T_p in range) and lose correlation completely due to this effect alone. Another important effect which introduces decorrelation for the range ambiguities are the angle fluctuations induced by $d_{i,k}$, which modify the resulting pattern for the ambiguities and also increase in magnitude as the order k increases. The impact of these decorrelation effects are examined for an example in **Figure 85**. The parameters correspond to the center of the swath of the system in 6.2.1 (cf. TABLE V).

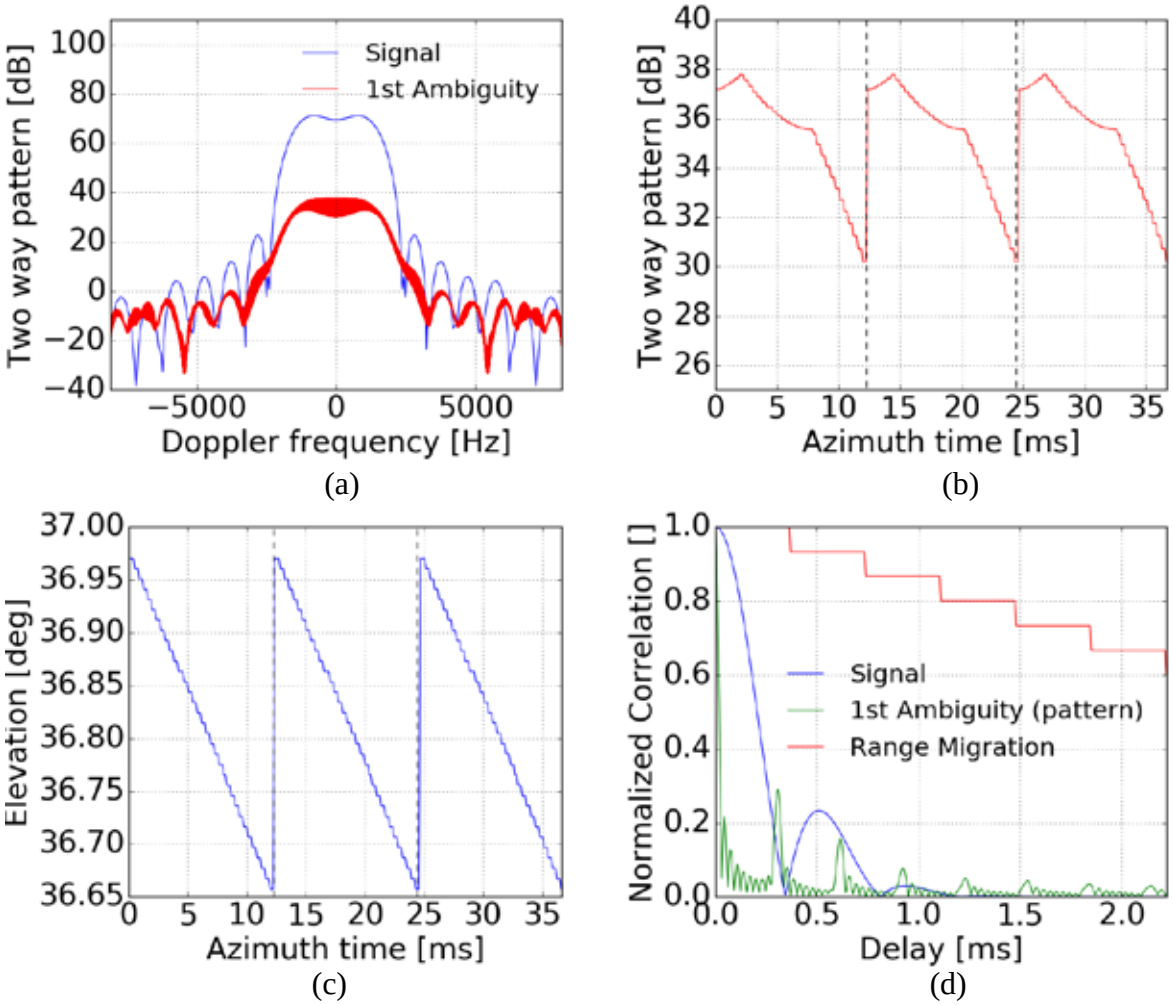

Figure 85. Analysis of patterns and resulting power spectral density (PSD) for first order range ambiguity in the center of the swath of Section 6.2.1. (a) Signal and ambiguity patterns against Doppler of the signal. (b) Zoom of the ambiguity's pattern for three PRI cycles, separated by vertical dashed lines. (c) Look angle of the first range ambiguity over azimuth time. (d) Magnitude of autocorrelation following PSD proportional to square of the signal's (blue) and ambiguity (green) patterns. The red stepped line models decorrelation over time due to range migration of the range ambiguity (cf. (182)), reaching zero after k_{min} = 15 pulses.

In **Figure 85 (a)** the pattern for the signal (blue) and for the 1st order range ambiguity (red) are plotted. The Doppler frequency axis refers to the Doppler of the main target. In **Figure 85 (b)** the ambiguity's pattern is plotted against azimuth time for three PRI cycles of duration T_{PRI} = 12.2 ms, separated by the vertical dashed lines. The fluctuations explain the "noisy" look of the previous plot. The reason for the

fluctuations is the variation of the look angle from which the ambiguous signal arises, represented in **Figure 85 (c)** for the same time interval of three cycles. In **Figure 85 (d)** the autocorrelation function is calculated as the inverse Fourier transform of the power spectral density (PSD), assumed to satisfy (173), both for the signal's pattern and for the ambiguities pattern**.** Note that this does not consider the decorrelation effect of the range migration, but illustrates how the fluctuations induce decorrelation, modifying the power spectrum. In this scenario, T_p = 14.8 μs and Δ_{PRI} = −0.98 μs, with k_c = k_{min} = 15. The stepped line in red models the decorrelation due to the migration of the position of the first ambiguity over range. It stays constant over intervals of $\overline{PRI}$ = 370.4 ms (the average interval over which the position of the ambiguities remain constant) and decreases from 1 to 0 in steps of magnitude $T_p/|\Delta_{PRI}|$ (cf. (182)), so that the correlation reaches zero after k_{min} = 15 pulses. This is when the range migration causes the area from which the first orders range ambiguities come to show no overlap with the original resolution cell (cf. **Figure 84 (b)**). The contribution of the pattern fluctuation is seen to be dominant for this order of ambiguity.

The added contribution of the range migration effect is considered in **Figure 86**. **Figure 86 (a)** shows the PSD of the autocorrelation functions in **Figure 85 (d).** The green curve is the inverse Fourier Transform of the green one in the latter figure, amounting for the effect of the pattern fluctuations. The red one is the PSD corresponding to the product of autocorrelation functions (the green and red curves) in **Figure 85 (d)**, and represents the impact of the additional source of decorrelation over the PSD. A further flattening of the spectrum is seen to occur. All curves in **Figure 86** are normalized to the maximum of the green PSD (which is outside of the plotted region). The black vertical dashed lines mark $N_{ch} \cdot PRF_{mean}$ and the red ones, Bw_{proc}, which are the relevant integration intervals. **Figure 86 (b)** compares the PDS of different orders k, considering the autocorrelation of the pattern with fluctuations multiplied by the stepped curve of the corresponding order (with a step $k \cdot T_p/|\Delta_{PRI}|$ as in (182)). The PSDs show similar behavior, with considerable impact from the

decorrelation, even though the PSD is not completely flat, showing some oscillations induced by the look angle variation over time.

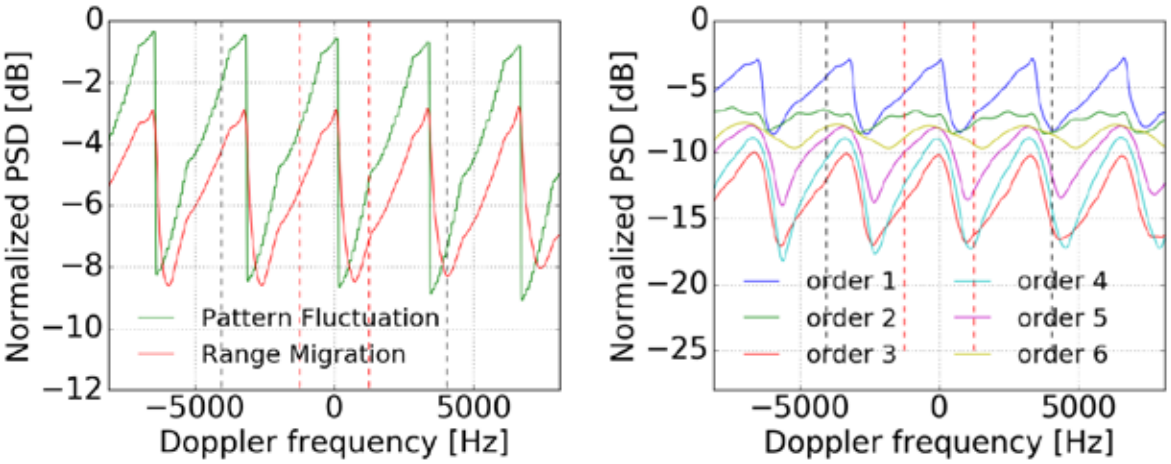

Figure 86. Analysis of power spectral density (PSD) for different orders of range ambiguities, in the center of the swath of Section 6.2.1. (a) PSD of the first order range ambiguity, considering only the pattern fluctuation (green) and the superposition of the pattern fluctuation and the decorrelation due to range migration (red). The superposition is modeled by multiplying the autocorrelation functions. (b) PSD of the combined effect from patterns and decorrelation due to range migration for different orders of ambiguity.

To assess the impact of the oscillations on the RASR estimation and the possible deviation with respect to the flat spectrum assumption of (184), the azimuth compression factor was evaluated using the estimated PSDs, i.e.,

$$w_{amb}\left(\theta_{i,k}\right) = \frac{\int_{PRF_{multi}} S(f_{\mathrm{D}}) \cdot |H_{az}(f_{\mathrm{D}})|^2 \, \mathrm{d}f_{\mathrm{D}}}{\int_{PRF_{multi}} S(f_{\mathrm{D}}) \, \mathrm{d}f_{\mathrm{D}}}, \tag{187}$$

and compared to the factor $\frac{Bw_{proc}}{PRF_{multi}}$ obtained using (184) and assuming $|H_{az}\,(f_{\mathrm{D}})|^2 = \mathrm{rect}\left(\frac{Bw_{proc}}{PRF_{multi}}\right)$. That is, the ratio

$$\Delta w_{amb}(\theta_{i,k}) = \left(\frac{\int_{PRF_{multi}} S(f_\mathrm{D}) \cdot |H_{az}(f_\mathrm{D})|^2 \, \mathrm{d}f_\mathrm{D}}{\int_{PRF_{multi}} S(f_\mathrm{D}) \, \mathrm{d}f_\mathrm{D}} \right) \cdot \left(\frac{PRF_{multi}}{Bw_{proc}} \right) \tag{188}$$

was calculated for all ambiguities shown in **Figure 87 (b)**. The deviation was smaller than 0.3 dB for all cases, indicating that the flat spectrum assumption does not yield considerably different RASR estimates in comparison to the PSD model just described. Since the former has the advantage of a simpler implementation, (183), (184) is the method of choice for the results shown in this thesis.

Simulation Chain

In conclusion of this appendix, an overview of the simulation chain is described in the block diagram of **Figure 87**, highlighting the estimation of the SAR performance indices discussed in the previous sub-sections. The system parameters and antenna patterns are the main inputs for the performance estimation, performed for each slant range *R* across the swath of interest. At each range, elevation DBF is performed (cf. Appendix A) to form the SCORE beams for each of the N_{ch} azimuth channels, which are the basic inputs for the following performance estimation steps. As described in the sub-sections of this appendix, the AASR and azimuth resolution are estimated from the time-domain impulse responses (cf. (168)), whereas the NESZ and the RASR are estimated from the patterns (cf. (179), (183) and (184)).

On the one hand, the SCORE beams are used as inputs for the simulation of the staggered SAR data, which is resampled in time domain using the VBD algorithm (yielding data sampled at $N_{ch} \cdot \overline{PRF}_{eff}$), zero-padded to a rate of $N_{ch} \cdot \overline{PRF}$ (which leads to the same grid independently of range) and compressed in azimuth to yield the *regularized impulse response*, from which the azimuth resolution is estimated after interpolation. A reference impulse response is also generated, which is uniformly sampled at $N_{ch} \cdot \overline{PRF}$ and employs the mean patterns $\hat{G}_{com}(f_\mathrm{D})$ achieved by the regularization. This is used for AASR estimation following the ISLR approach. The

VBS weights are also used to estimate the mean SNR scaling with respect to the common pattern, $\bar{\phi}_{SNR}$, which is part of the NESZ calculation.

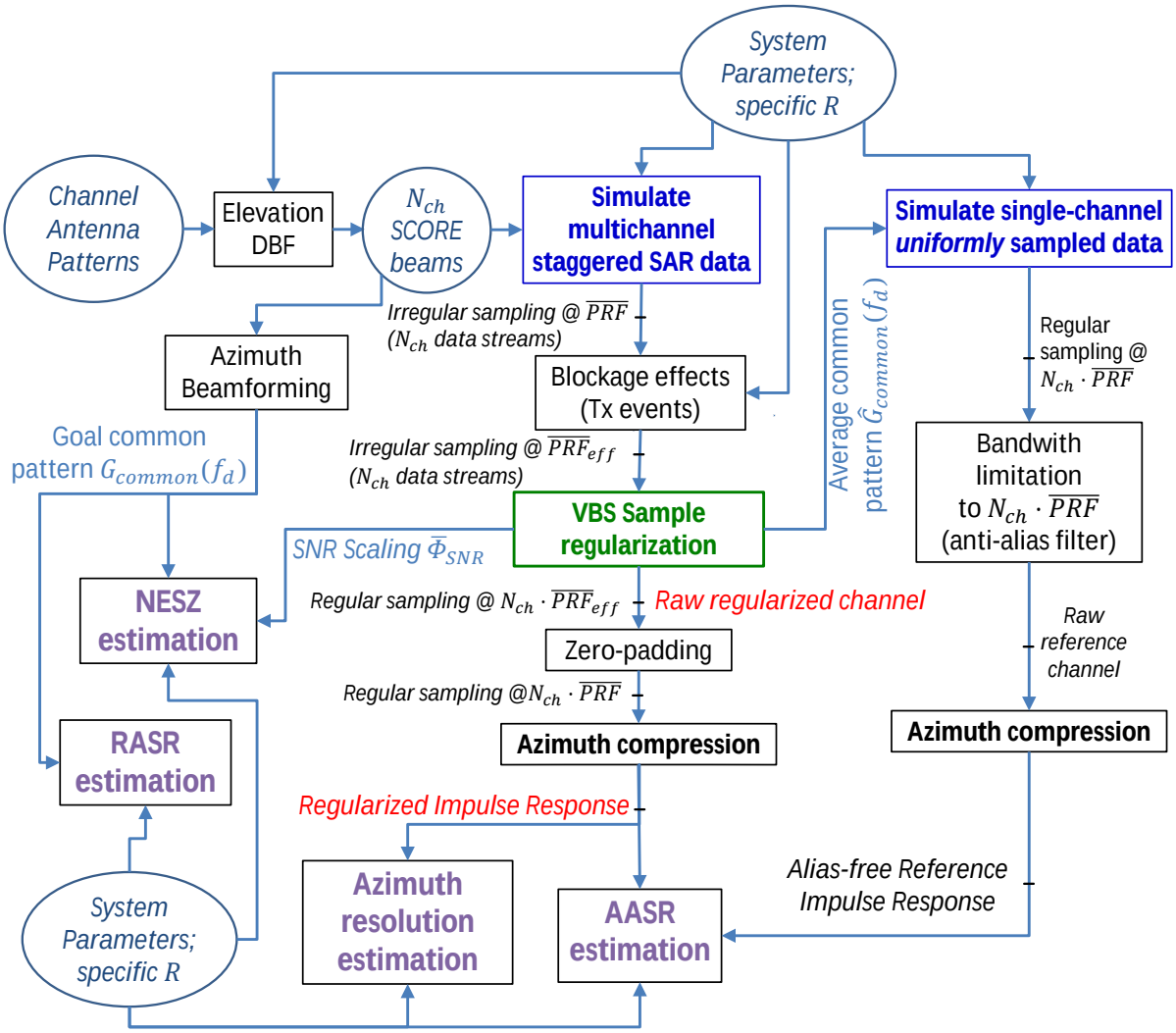

Figure 87. Simulation chain for SAR performance estimation highlighting the inputs for estimation of the SAR performance figures: AASR, azimuth resolution (estimated from simulated impulse responses in time domain); NESR and RASR (estimated from the antenna patterns).

On the other hand, the beams are subject to azimuth beamforming to form the desired common pattern $G_{com}(\theta, f_{\mathrm{D}})$ (unity beamforming in the case of reflectors; selection of a single element for planar arrays, as described in Section 4.5), which serves as input to the calculation of RASR and NESZ (to which the SNR scaling $\bar{\phi}_{SNR}$ is added). The patterns are integrated according to (178), (183) to yield the estimations.

10 Bibliography

[1] Fraunhofer Institute, W. Holpp, (August, 2017) “A Century of Radar”. [Online]. Available at: https://www.100-jahre-radar.fraunhofer.de/vortraege/Holpp-The_Century_of_Radar.pdf.

[2] C. Hülsmeyer. *Verfahren, um entfernte metallische Gegenstände mittels elektrischer wellen einem Beobachter zu melden*, German Patent 165546, filed 1904, published 1905.

[3] C.A. Wiley, *Pulsed Doppler Radar Methods and Apparatus*, US Patent 3196436, filed 1954, published 1965.

[4] L. J. Cutrona, W. E. Vivian, E. N. Leith and G. O. Hall, “A High-Resolution Radar Combat-Surveillance System”, in *IRE Transactions on Military Electronics*, vol. MIL-5, no. 2, pp. 127-131, April 1961.

[5] C. W. Sherwin, J. P. Ruina and R. D. Rawcliffe, “Some Early Developments in Synthetic Aperture Radar Systems”, in *IRE Transactions on Military Electronics*, vol. MIL-6, no. 2, pp. 111-115, April 1962.

[6] W. M. Brown, “Synthetic Aperture Radar”, in *IEEE Transactions on Aerospace and Electronic Systems*, vol. AES-3, no. 2, pp. 217-229, March 1967.

[7] H.P. Groll, J. Detlefsen, “History of Automotive Anticollision Radars and Final Experimental results of a MM-Wave Car Radar Developed by the Technical University of Munich”, in *IEEE Aerospace and Electronic Systems Magazine*, vol. 12, issue 8, pp. 15 – 19, Aug 1997.

[8] C. Waldschmidt and H. Meinel, “Future Trends and Directions in Radar Concerning the Application for Autonomous Driving”, in *2014 44th European Microwave Conference*, Rome, pp. 1719-1722, 2014.

[9] M. Köhler, F. Gumbmann, J. Schür, L. P. Schmidt and H. L. Blöcher, “Considerations for Future Automotive Radar in the Frequency Range Above 100 GHz”, in *German Microwave Conference Digest of Papers*, Berlin, pp. 284-287, 2010.

[10] H. Iqbal, M. B. Sajjad, M. Mueller and C. Waldschmidt, “SAR Imaging in an Automotive Scenario”, in *2015 IEEE 15th Mediterranean Microwave Symposium (MMS)*, Lecce, pp. 1-4, 2015.

[11] M. Nezadal, J. Schür and L. P. Schmidt, "Non-destructive Testing of Glass Fibre Reinforced Plastics With a Full Polarimetric Imaging System", in *2014 39th International Conference on Infrared, Millimeter, and Terahertz waves (IRMMW-THz)*, Tucson, AZ, pp. 1-2, 2014.

[12] F. Gumbmann and L. P. Schmidt, "Millimeter-Wave Imaging With Optimized Sparse Periodic Array for Short-Range Applications", in *IEEE Transactions on Geoscience and Remote Sensing*, vol. 49, no. 10, pp. 3629-3638, Oct. 2011.

[13] United Stated National Reconnaissance Office (October, 2017), "Declassified Records: QUILL" [Online] Available at: http://www.nro.gov/foia/declass/QUILL.html

[14] NASA Jet Propulsion Laboratory (August, 2017), "Seasat" [Online]. Available at: https://www.jpl.nasa.gov/missions/seasat/.

[15] ESA Earth Observation Portal, (August, 2017) "SeaSat Mission – the World's First Satellite Mission Dedicated to Oceanography" [Online]. Available at: https://directory.eoportal.org/web/eoportal/satellite-missions/s/seasat.

[16] NASA Jet Propulsion Laboratory (August, 2017) "Shuttle Imaging Radar-A" [Online]. Available at: https://www.jpl.nasa.gov/missions/shuttle-imaging-radar-a-sir-a/.

[17] NASA Jet Propulsion Laboratory (August, 2017) "Shuttle Imaging Radar-B" [Online]. Available at: https://www.jpl.nasa.gov/missions/shuttle-imaging-radar-b-sir-b/.

[18] ESA Earth Observation Portal, (August, 2017) "European Remote Sensing Satellite" [Online]. Available at: https://earth.esa.int/web/guest/missions/esa-operational-eo-missions/ers.

[19] ESA Earth Observation Portal, (August, 2017) "Almaz-1 Mission" [Online]. Available at: https://directory.eoportal.org/web/eoportal/satellite-missions/a/almaz.

[20] JAXA, (August, 2017), "Japanese Earth Resources Satellite "FUYO-1" (JERS-1)" [Online]. Available at: http://global.jaxa.jp/projects/sat/jers1/index.html.

[21] United States Geological Survey, (August, 2017) "Spaceborne Imaging Radar C-band". [Online]. Available at: https://lta.cr.usgs.gov/SIRC.

[22] NASA Jet Propulsion Laboratory, (August, 2017) "Shuttle Radar Topography Mission" [Online]. Available at: https://www2.jpl.nasa.gov/srtm/index.html.

[23] ESA Earth Observation Portal, (August, 2017), "Tandem-X Mission". [Online]. Available at: https://directory.eoportal.org/web/eoportal/satellite-missions/t/terrasar-x

[24] DLR (August, 2017), "New 3D World Map – TanDEM-X Global Elevation Model Completed" [Online]. Available at: http://www.dlr.de/dlr/en/desktopdefault.aspx/tabid-10081/151_read-19509/#/gallery/24516

[25] A. Moreira, P. Prats-Iraola, M. Younis, G. Krieger, I. Hajnsek and K. P. Papathanassiou, "A Tutorial on Synthetic Aperture Radar", in *IEEE Geoscience and Remote Sensing Magazine*, vol. 1, no. 1, pp. 6-43, March 2013.

[26] J. C. Curlander and R. N. McDonough, *Synthetic Aperture Radar: Systems and Signal Processing*, New York: John Wiley & Sons Inc., 1992.

[27] I. G. Cumming and F.H. Wong, *Digital Processing of Synthetic Aperture Radar Data – Algorithms and Implementation*, Boston: Artech House, 2011.

[28] F. Henderson and A. Lewis, *Manual of Remote Sensing: Principles and Applications of Imaging Radar*. New York: Wiley, 1998.

[29] P. A. Rosen *et al*., "Synthetic Aperture Radar Interferometry", in *Proceedings of the IEEE*, vol. 88, no. 3, pp. 333-382, March 2000.

[30] K. P. Papathanassiou and S. R. Cloude, "Single-Baseline Polarimetric SAR Interferometry", in *IEEE Transactions on Geoscience and Remote Sensing*, vol. 39, no. 11, pp. 2352-2363, Nov 2001.

[31] A. Ferretti, C. Prati and F. Rocca, "Permanent Scatterers in SAR Interferometry", in *IEEE Transactions on Geoscience and Remote Sensing*, vol. 39, no. 1, pp. 8-20, Jan 2001.

[32] A. Reigber and A. Moreira, "First Demonstration of Airborne SAR Tomography Using Multibaseline L-Band Data", in *IEEE Transactions on Geoscience and Remote Sensing*, vol. 38, no. 5, pp. 2142-2152, Sep 2000.

[33] European Space Agency, (July, 2017) "The CEOS Database: Missions, Instruments and Measurements" [Online]. Available at: http://database.eohandbook.com/database/instrumenttable.aspx.

[34] European Space Agency, (July, 2017) "Earth Observation Portal: Satellite Missions Database" [Online]. Available at: https://directory.eoportal.org/web/eoportal/satellite-missions.

[35] A. Moreira et al., "Tandem-L: A Highly Innovative Bistatic SAR Mission for Global Observation of Dynamic Processes on the Earth's Surface", in *IEEE Geoscience and Remote Sensing Magazine*, vol. 3, no. 2, pp.8-23, 2015.

[36] S. Huber et al. "Tandem-L: A Technical Perspective on Future Spaceborne SAR Sensors for Earth Observation", submitted for publication in *IEEE Transactions on Geoscience and Remote Sensing*, 2016.

[37] G. Krieger, N. Gebert, M. Younis, F. Bordoni, A. Patyuchenko and A. Moreira, "Advanced Concepts for Ultra-Wide-Swath SAR Imaging", in *7th European Conference on Synthetic Aperture Radar (EUSAR 2008)*, pp. 1-4, Friedrichshafen, Germany, 2008.

[38] G. Krieger, N. Gebert, and A. Moreira, "Multidimensional Waveform Encoding: A New Digital Beamforming Technique for Synthetic Aperture Radar Remote Sensing", in *IEEE Transactions on Geoscience and Remote Sensing*, vol. 46, no. 1, pp. 31–46, January 2008.

[39] N. Gebert, G. Krieger and A. Moreira, "Digital Beamforming on Receive: Techniques and Optimization Strategies for High-Resolution Wide-Swath SAR Imaging", in *IEEE Transactions on Aerospace and Electronic Systems*, vol. 45, no. 2, pp. 564-592, April 2009.

[40] S. Huber, A. Patyuchenko, G. Krieger and A. Moreira, "Spaceborne Reflector SAR Systems With Digital Beamforming", in *IEEE Transactions on Aerospace and Electronic Systems*, vol. 48, no. 4, pp.3473-3493, 2012.

[41] M. Villano, G. Krieger and A. Moreira, "Staggered SAR: High-Resolution Wide-Swath Imaging by Continuous PRI Variation", in *IEEE Transactions on Geoscience and Remote Sensing*, vol. 52, no.7, pp.4462-4479, 2014.

[42] G. Krieger et al., "Advanced Concepts for Ultra-Wide-Swath SAR Imaging", in *7th European Conference on Synthetic Aperture Radar (EUSAR 2008)*, Friedrichshafen, Germany, pp.1-4, 2008.

[43] G. Krieger *et al.*, "SIMO and MIMO System Architectures and Modes for High-Resolution Ultra-Wide-Swath SAR Imaging", in *11th European Conference on Synthetic Aperture Radar (EUSAR 2016)*, pp. 1-6., Hamburg, Germany, 2016.

[44] M. Younis *et al.*, "Techniques and Modes for Multi-Channel SAR Instruments", in *11th European Conference on Synthetic Aperture Radar (EUSAR 2016)*, pp. 1-6, Hamburg, Germany, 2016.

[45] G. Krieger et al., "Advanced L-Band SAR System Concepts for High-Resolution Ultra-Wide-Swath SAR Imaging", in *5th Workshop on Advanced RF Sensors and Remote Sensing Instruments (ARSI 2017)*, Noordwijk, The Netherlands, 2017.

[46] M. Suess, B. Grafmueller, and R. Zahn, "A Novel High Resolution, Wide Swath SAR System", in *International Geoscience and Remote Sensing Symposium (IGARSS '01)*, vol. 3, pp. 1013–1015, Sydney, Australia, July 2001.

[47] G. Krieger, N. Gebert and A. Moreira, "Unambiguous SAR Signal Reconstruction From Nonuniform Displaced Phase Center Sampling", in *IEEE Geoscience and Remote Sensing Letters*, vol. 1, no. 4, pp. 260-264, 2004.

[48] I. Sikaneta, C. H. Gierull and D. Cerutti-Maori, "Optimum Signal Processing for Multichannel SAR: With Application to High-Resolution Wide-Swath Imaging", in *IEEE Transactions on Geoscience and Remote Sensing*, vol. 52, no. 10, pp. 6095-6109, 2014.

[49] D. Cerutti-Maori, I. Sikaneta, J. Klare and C. H. Gierull, "MIMO SAR Processing for Multichannel High-Resolution Wide-Swath Radars", in *IEEE Transactions on Geoscience and Remote Sensing*, vol. 52, no. 8, pp. 5034-5055, 2014.

[50] C. Qian, L. Yadong, D. Yunkai and R. Wang, X. Wei, "Investigation on an Ultra–Wide-Swath, Multiple-Elevation-Beam SAR Based on Sweep-PRI Mode", in *IEEE Transactions on Aerospace and Electronic Systems*, vol. 50, no. 4, pp.2998-3020, 2014.

[51] N. Gebert, "Multi-Channel Azimuth Processing for High-Resolution Wide-Swath SAR Imaging", Ph.D. dissertation, Institute of Radio Frequency Engineering and Electronics (IHE), Karlsruhe Institute of Technology (KIT), Karlsruhe, Germany, June 2009.

[52] S. Huber, "Spaceborne SAR Systems With Digital Beamforming and Reflector Antenna", Ph.D. dissertation, Institute of Radio Frequency Engineering and Electronics (IHE), Karlsruhe Institute of Technology (KIT), Karlsruhe, Germany, February 2014.

[53] M. Villano, "Staggered Synthetic Aperture Radar", Ph.D. dissertation, Institute of Radio Frequency Engineering and Electronics (IHE), Karlsruhe Institute of Technology (KIT), Karlsruhe, Germany, February 2016.

[54] J. Bechter, K. Eid, F. Roos and C. Waldschmidt, "Digital Beamforming to Mitigate Automotive Radar Interference", in *2016 IEEE MTT-S International Conference on Microwaves for Intelligent Mobility (ICMIM)*, San Diego, CA, pp. 1-4, 2016.

[55] European Space Agency, (July, 2017) "Sentinel 1: Instrument and Payload" [Online]. Available at: https://sentinel.esa.int/web/sentinel/missions/sentinel-1/instrument-payload.

[56] European Space Agency, (July, 2017) "Sentinel-1 ESA's Radar Observatory Mission for GMeS Operational Services", Report SP-1322/1, 2012. [Online]. Available at: https://sentinel.esa.int/documents/247904/349449/S1_SP-1322_1.pdf.

[57] C. Fischer, C. Heer and R. Werninghaus, "X-Band HRWS Demonstrator: Digital Beamforming Test Results", in *9th European Conference on Synthetic Aperture Radar (EUSAR 2012)*, pp. 1-4, Nuremberg, Germany, 2012.

[58] G. Adamiuk, T. Fuegen, C. Fischer, B. Grafmueller, F. Rostan and C. Heer, "Verification of Scan-On-Receive Beamforming for X-Band HRWS Applications", in *IEEE International Geoscience and Remote Sensing Symposium (IGARSS 2016)*, pp. 2120-2122, Beijing, China, 2016.

[59] G. Adamiuk, C. Heer and M. Ludwig, "DBF Technology Development for Next Generation of ESA C-Band SAR mission", in *11th European Conference on Synthetic Aperture Radar (EUSAR 2016)*, pp. 1-4, Hamburg, Germany, 2016.

[60] M. Ludwig, J-C. Angevain, C. Buck and D. Petrolati. "Multi-Channel Synthetic Aperture Radar in Europe", in *2017 IEEE International Geoscience and Remote Sensing Symposium*, pp. 3828-3831, Fort Worth, Texas, 2017.

[61] N. Gebert and G. Krieger, "Ultra-Wide Swath SAR Imaging With Continuous PRF Variation", in *8th European Conference of Synthetic Aperture Radar (EUSAR 2010)*, pp.1-4, Aachen, Germany, 2010.

[62] M. Villano, G. Krieger and A. Moreira, "Staggered-SAR for High-Resolution Wide-Swath Imaging", in *IET International Conference on Radar Systems*, pp.1-6, 22-25 October 2012.

[63] M. Villano, G. Krieger and A. Moreira, "A Novel Processing Strategy for Staggered SAR", in *IEEE Geoscience and Remote Sensing Letters*, vol. 11, no. 11, pp.1891-1895, 2014

[64] M. Villano, G. Krieger and A. Moreira "Ambiguities and Image Quality in Staggered SAR", in *5th Asia-Pacific Conference on Synthetic Aperture Radar (APSAR)*, pp. 204-209, Singapore, 2015.

[65] M. Suess and W. Wiesbeck, *Side-Looking Synthetic Aperture Radar System*, European Patent EP 1 241487, filed 2001, published 2002.

[66] F. Queiroz de Almeida and G. Krieger, "Multichannel Staggered SAR Azimuth Sample Regularization", in *11th European Conference on Synthetic Aperture Radar (EUSAR 2016)*, pp. 1-6, Hamburg, Germany, 2016.

[67] F. Queiroz de Almeida, M. Younis, G. Krieger and A. Moreira, "Multichannel Staggered SAR Azimuth Processing", in *IEEE Transactions on Geoscience and Remote Sensing*, vol. 56, no. 5, 2018.

[68] F. Queiroz de Almeida, M. Younis, G. Krieger and A. Moreira, "Multichannel Staggered SAR With Reflector Antennas: Discussion and Proof of Concept", in *2017 18th International Radar Symposium (IRS)*, pp. 1-10, Prague, Czech Republic, 2017.

[69] F. Queiroz de Almeida, T. Rommel, M. Younis, G. Krieger and A. Moreira, "Multichannel Staggered SAR: System Concepts With Reflector and Planar Antennas", submitted for publication in *IEEE Transactions on Aerospace and Electronic Systems*, 2017.

[70] F. Queiroz de Almeida, M. Younis, G. Krieger, F. López-Dekker and A. Moreira, *Synthetik-Apertur-Radarverfahren und Synthetik-Apertur-Radarvorrichtung*, German Patent 102016208899, filed 2016, published 2017.

[71] M. Villano, G. Krieger and V. Del Zoppo, "On-board Doppler Filtering for Data Volume Reduction in Spaceborne SAR Systems", in *2014 15th International Radar Symposium (IRS)*, pp. 1-6, Gdansk, 2014.

[72] M. Villano, G. Krieger and A. Moreira, "Onboard Processing for Data Volume Reduction in High-Resolution Wide-Swath SAR", in *IEEE Geoscience and Remote Sensing Letters*, vol. 13, no. 8, pp. 1173-1177, Aug. 2016.

[73] A. Patyuchenko, T. Rommel, P. Laskowski, M. Younis, and G. Krieger, "Digital Beam-Forming Reconfigurable Radar System Demonstrator", in *IEEE International Geoscience and Remote Sensing Symposium (IGARSS 2012)*, pp. 1541–1544, Munich, Germany, 2012.

[74] T. Rommel, A. Patyuchenko, P. Laskowski, M. Younis and G. Krieger, "Development of a MIMO Radar System Demonstrator - Calibration and Demonstration of First Results", in *2012 13th International Radar Symposium (IRS)*, pp. 113-118, Warsaw, Poland, 2012.

[75] S. Huber, T. Rommel, A. Patyuchenko and P. Laskowski, "A Reflector Based Digital Beamforming Demonstrator", in *10th European Conference on Synthetic Aperture Radar (EUSAR 2014)*, pp. 1-4, Berlin, Germany, 2014.

[76] A. W. Rihaczek, *Principles of High Resolution Radar*, Boston: Artech House, 1996.

[77] A. W. Rihaczek, "Radar Signal Design for Target Resolution", in *Proceedings of the IEEE*, vol. 53, no. 2, pp. 116-128, Feb. 1965.

[78] A. Freeman et al., "The "Myth" of the Minimum SAR Antenna Area Constraint", in *IEEE Transactions on Geoscience and Remote Sensing*, vol. 38, no. 1, pp. 320-324, Jan 2000.

[79] O. Montenbruck, E. Gill, *Satellite Orbits: Models, Methods and Applications*, Berlin: Springer Verlag, 2012.

[80] W.G. Carrara, R.S. Goodman, and R.M. Majewski, *Spotlight Synthetic Aperture Radar Signal Processing Algorithms*, Boston: Artech House, 1995.

[81] M. Soumekh, "Reconnaissance With Slant Plane Circular SAR Imaging", in *IEEE Transactions on Image Processing*, vol. 5, no. 8, pp. 1252-1265, August 1996.

[82] O. Ponce, P. Prats, M. Rodriguez-Cassola, R. Scheiber and A. Reigber, "Processing of Circular SAR trajectories With Fast Factorized Back-Projection", in *IEEE International Geoscience and Remote Sensing Symposium (IGARSS 2011)*, Vancouver, BC, pp. 3692-3695, 2011.

[83] O. Ponce *et al*., "Fully Polarimetric High-Resolution 3-D Imaging With Circular SAR at L-Band", in *IEEE Transactions on Geoscience and Remote Sensing*, vol. 52, no. 6, pp. 3074-3090, June 2014.

[84] D. P. Belcher and C. J. Baker, "High Resolution Processing of Hybrid Strip-Map/Spotlight Mode SAR", in *IEE Proceedings - Radar, Sonar and Navigation*, vol. 143, no. 6, pp. 366-374, Dec 1996.

[85] J. Mittermayer, R. Lord and E. Borner, "Sliding Spotlight SAR Processing for TerraSAR-X Using a New Formulation of the Extended Chirp Scaling Algorithm", in *IEEE International Geoscience and Remote Sensing Symposium (IGARSS 2003) (IEEE Cat. No.03CH37477)*, pp. 1462-1464, Toulose, France, 2003.

[86] P. Prats, R. Scheiber, J. Mittermayer, A. Meta and A. Moreira, "Processing of Sliding Spotlight and TOPS SAR Data Using Baseband Azimuth Scaling", in *IEEE Transactions on Geoscience and Remote Sensing*, vol. 48, no. 2, pp. 770-780, Feb. 2010.

[87] K. Tomiyasu, "Conceptual Performance of a Satellite Borne, Wide Swath Synthetic Aperture Radar", in *IEEE Transactions on Geoscience and Remote Sensing*, vol. GRS-19, no. 2, pp. 108–116, 1981.

[88] R. K. Moore, J. P. Claassen, and Y. H. Lin, "A Scanning Spaceborne Synthetic Aperture Radar With Integrated Radiometer", in *IEEE Transactions on Aerospace and Electronic Systems*, vol. AES-17, no. 3, pp. 410–421, May 1981.

[89] F. De Zan and A. M. Monti Guarnieri, "TOPSAR: Terrain Observation by Progressive Scans", in *IEEE Transactions on Geoscience and Remote Sensing*, vol. 44, no. 9, pp. 2352–2360, September 2006.

[90] N. Gebert, G. Krieger and A. Moreira, "Multichannel Azimuth Processing in ScanSAR and TOPS Mode Operation", in *IEEE Transactions on Geoscience and Remote Sensing*, vol. 48, no. 7, pp. 2994-3008, July 2010.

[91] A. Freeman *et al*., "SweepSAR: Beam-Forming on Receive Using a Reflector-Phased Array Feed Combination for Spaceborne SAR", in *2009 IEEE Radar Conference*, Pasadena, CA, pp. 1-9, 2009.

[92] J.H. Blythe, *Radar Systems*, US Patent 4253098, filed 1978, published 1981.

[93] Ramanujam, P., Law, P. H., Lane, S. O., *Multi-Beam Reflector With a Simple Beamforming Network*, US Patent 6366256, filed 2000, published 2002.

[94] J.T. Kare, *Moving Receive Beam Method and Apparatus for Synthetic Aperture Radar*, US Patent 6175326 B1, filed 1998, published 2001.

[95] M. Younis and W. Wiesbeck, "SAR With Digital Beamforming on Receive Only", in *International Geoscience and Remote Sensing Symposium (IGARSS '99)*, Hamburg, pp. 1773-1775 vol.3, 1999.

[96] M. Younis, C. Fischer and W. Wiesbeck, "Digital Beamforming in SAR Systems", in *IEEE Transactions on Geoscience and Remote Sensing*, vol. 41, no. 7, pp. 1735-1739, July 2003.

[97] F. Queiroz de Almeida and G. Krieger, "A Novel High-Resolution Wide-Swath SAR Imaging Mode Employing Multichannel Slow PRI Variation", submitted to *12th European Conference on Synthetic Aperture Radar (EUSAR 2018)*, Aachen, Germany, 2018.

[98] A. Papoulis, "Generalized Sampling Expansion", in *IEEE Transactions on Circuits and Systems*, vol. 24, no. 11, pp. 652-654, November 1977.

[99] J. L. Brown, "Multi-Channel Sampling of Low-Pass Signals", in *IEEE Transactions on Circuits and Systems*, vol. 28, no. 2, pp. 101-106, February 1981.

[100] C. Balanis, *Antenna Theory: Analysis and Design*, New York: John Wiley & Sons Inc., 1997.

[101] D. Seidner and M. Feder. “Vector Sampling Expansion”, in *IEEE Transactions on Signal Processing*, vol. 48, no. 5, pp. 1401–1416, 2000.

[102] D. Seidner and M. Feder, “Noise Amplification of Periodic Nonuniform Sampling”, in *IEEE Transactions on Signal Processing*, vol.48, no.1, pp.275-277, 2000.

[103] J. Yen, “On Nonuniform Sampling of Bandwidth-Limited Signals”, in *IRE Transactions on Circuit Theory*, vol. 3, no.4, pp.251-257, December 1956.

[104] S. Bertl, P. Lopez-Dekker, M. Younis and G. Krieger, “Along-track SAR interferometry using a single reflector antenna”, in *IET Radar, Sonar & Navigation*, vol. 9, no. 8, pp. 942 – 947, October 2015.

[105] A. Papoulis, *The Fourier Integral and its Applications*, New York: McGraw-Hill Co., 1962.

[106] H. L. V. Trees, *Optimum Array Processing*, New York: John Wiley & Sons Inc., 2002.

[107] D. H. Brandwood, “A Complex Gradient Operator and Its Application in Adaptive Array Theory”, in *IEE Proceedings in Communications, Radar and Signal Processing*, vol. 130, no. 1, pp. 11-16, 1983.

[108] R. K. Raney, “SNR in SAR”, in *International Geoscience and Remote Sensing Symposium (IGARSS 1985)*, pp.994-999, 1985.

[109] M. Younis, P. López-Dekker and G. Krieger, “Signal and Noise Considerations in Multi-Channel SAR”, in *2015 16th International Radar Symposium (IRS)*, Dresden, pp. 434-439., 2015.

[110] M. Younis, S. Huber, A. Patyuchenko, F. Bordoni, and G. Krieger, “Performance Comparison of Reflector- and Planar-Antenna Based Digital Beam-Forming SAR”, in *International Journal of Antennas and Propagation*, vol. 2009, Article ID 614931, 2009.

[111] N. Gebert and G. Krieger, “Azimuth Phase Center Adaptation on Transmit for High-Resolution Wide-Swath SAR Imaging”, in *IEEE Geoscience and Remote Sensing Letters*, vol. 6, no. 4, pp. 782-786, Oct. 2009.

[112] N. Gebert and G. Krieger, *Synthetik-Apertur-Radarsystem*, German Patent DE 10 2007 041 373.6, filed 2007, published 2009.

[113] TICRA (August, 2017), “GRASP”, Copenhagen, Denmark. [Online]. Available at: http://www.ticra.com/products/software/grasp.

[114] L. Lei, G. Zhang and R. J. Doviak, "Bias Correction for Polarimetric Phased-Array Radar With Idealized Aperture and Patch Antenna Elements", in *IEEE Transactions on Geoscience and Remote Sensing*, vol. 51, no. 1, pp. 473-486, Jan. 2013.

[115] D. D'Aria et al., "A Wide Swath, Full Polarimetric, L band Spaceborne SAR", in *IEEE Radar Conference*, Rome, pp. 1-4, 2008.

[116] M. Villano, G. Krieger and A. Moreira, "An Analytical Phase-Only Beam Shaping Method for High-Resolution Wide-Swath SAR", submitted for publication in *IEEE Geoscience and Remote Sensing Letters*, 2016.

[117] European Space Agency (June, 2017), "Sentinel-1 ESA's Radar Observatory Mission for GMeS Operational Services", Report SP-1322/1, 2012. [Online]. Available at: https://sentinel.esa.int/documents/247904/349449/S1_SP-1322_1.pdf.

[118] Canadian Space Agency (October, 2017), "RADARSAT: Satellite Characteristics", [Online]. Available at: http://www.asc-csa.gc.ca/eng/satellites/radarsat/radarsat-tableau.asp, 2017.

[119] B. Porat, *A Course in Digital Signal Processing*, New York: John Wiley & Sons Inc., 1997.

[120] N. Gebert, F. Queiroz de Almeida and G. Krieger, "Airborne Demonstration of Multichannel SAR Imaging", in *IEEE Geoscience and Remote Sensing Letters*, vol. 8, no. 5, pp. 963-967, 2011.

[121] P. Laskowski, F. Bordoni and M. Younis, "Multi-Channel SAR Performance Analysis in the Presence of Antenna Excitation Errors", in *2013 14th International Radar Symposium (IRS)*, Dresden, pp. 491-496, 2013.

[122] F. Queiroz de Almeida, M. Younis, G. Krieger and A. Moreira, "An Analytical Error Model for Spaceborne SAR Multichannel Azimuth Reconstruction", in *2017 IET Radar Conference*, Belfast, Northern Ireland, 2017.

[123] M. Younis, T. Rommel, F. Bordoni, G. Krieger and A. Moreira, "On the Pulse Extension Loss in Digital Beamforming SAR", in *IEEE Geoscience and Remote Sensing Letters*, vol. 12, no. 7, pp. 1436-1440, 2015.

[124] International Telecommunication Union (ITU) (July, 2017) "Recommendation ITU-R RS.577-7 (02/2009): Frequency Bands and Required Bandwidths Used for Spaceborne Active Sensors Operating in the Earth Exploration-Satellite (Active) and Space Research (Active) Services". [Online]. Available at: https://www.itu.int/rec/R-REC-RS.577-7-200902-I/en.

[125] M. Schwerdt, M. Bachmann, B. Brautigam and B. Doring, “Antenna Characterization Approach for High Accuracy of Active Phased Array Antennas on Spaceborne SAR Systems”, in *2009 3rd European Conference on Antennas and Propagation*, Berlin, pp. 3385-3388, 2009.

[126] S. Buckreuss, R. Werninghaus and W. Pitz, “The German Satellite Mission TerraSAR-X”, in *2008 IEEE Radar Conference*, pp. 1-5, Rome, Italy, 2008.

[127] W. Wiesbeck, L. Sit, M. Younis, T. Rommel, G. Krieger and A. Moreira, “Radar 2020: The Future of Radar Systems”, in *IEEE International Geoscience and Remote Sensing Symposium (IGARSS) 2015*, Milano, Italy, July 2015.

[128] W. Wiesbeck, “Radar of the Future”, *in Proceedings of the 10th European Radar Conference*, Nuremberg, Germany, pp. 137-140, 9-11 October 2013.

[129] J.-H. Kim, M. Younis, A. Moreira, and W. Wiesbeck, “A Novel OFDM Chirp Waveform Scheme for Use of Multiple Transmitters in SAR”, in *IEEE Geoscience and Remote Sensing Letters*, vol. 10, no. 3, pp. 568-572, May 2013.

[130] A. G. Roederer, “Reflectarray Antennas”, in *2009 3rd European Conference on Antennas and Propagation*, pp. 18-22, Berlin, Germany, 2009.

[131] R. A. Bauer, R. C. Reinhart, D.R. Hilderman and P. E. Paulsen, (August, 2017) “Space Communications and Data Systems Technologies for Next Generation Earth Science Measurements”, Technical Memorandum NASA/TM-2003-212616 [Online]. Available at: https://ntrs.nasa.gov/archive/nasa/casi.ntrs.nasa.gov/20040000792.pdf, 2003.

[132] J. Huang, "Analysis of a Microstrip Reflectarray Antenna for Microspacecraft Applications", in *Telecommunications and Data Acquisition Progress Report*, pp. 153-173, February 1995.

[133] C. Tienda, J. A. Encinar, M. Arrebola, M. Barba and E. Carrasco, “Design, Manufacturing and Test of a Dual-Reflectarray Antenna With Improved Bandwidth and Reduced Cross-Polarization”, in *IEEE Transactions on Antennas and Propagation*, vol. 61, no. 3, pp. 1180-1190, March 2013.

[134] M. Younis, C. Laux, N. Al-Kahachi, P. Lopez-Dekker, G. Krieger and A. Moreira, “Calibration of Multi-Channel Spaceborne SAR - Challenges and Strategies”, in *10th European Conference on Synthetic Aperture Radar (EUSAR 2014)*, pp. 1-4, Berlin, Germany, 2014.

[135] E. Attia and B. Steinberg, "Self-Cohering Large Antenna Arrays Using the Spatial Correlation Properties of Radar Clutter", in *IEEE Transactions on Antennas and Propagation*, vol. 37, no. 1, January 1989.

[136] G. Farquharson, P. Lopez-Dekker and S. J. Frasier, "Contrast-Based Phase Calibration for Remote Sensing Systems With Digital Beamforming Antennas", in *IEEE Transactions on Geoscience and Remote Sensing*, vol. 51, no. 3, pp. 1744-1754, March 2013.

[137] M. Jäger and R. Scheiber, "A Novel Approach to the External Calibration of Multi-Channel SAR Sensors Based on Range Compressed Data," in *Earth Observation Summit 2017*, Montreal, Canada, 20-23 Jun 2017.

[138] J. Liu *et al*., "Adaptive Beamforming With Sidelobe Control: a Second-Order Cone Programming Approach," in *IEEE Signal Processing Letters*, vol. 10, no. 11, pp. 331-334, 2003.

[139] M. S. Andersen, J. Dahl, and L. Vandenberghe, (May, 2017) "CVXOPT: A Python Package for Convex Optimization", version 1.1.8. [Online]. Available at cvxopt.org.

[140] G. Sagnol, *et al*, (May, 2017) "PICOS: A Python Interface for Conic Optimization Solvers", version 1.1.2. [Online]. Available at: picos.zib.de.

[141] M. Villano, G. Krieger and A. Moreira, "New Insights Into Ambiguities in Quad-Pol SAR," in *IEEE Transactions on Geoscience and Remote Sensing*, vol. 55, no. 6, pp. 3287-3308, June 2017.

[142] A. Papoulis, *Probability, Random Variables, and Stochastic Processes*, 4th ed. New York: McGraw-Hill, 2002.

[143] W. Lu and N. Vaswani, (July, 2017) "The Wiener-Khinchin Theorem for Non-wide Sense Stationary Random Processes", Cornel University Library, arXiv:0904.0602. [Online]. Available at: https://arxiv.org/abs/0904.0602, 2009.